Machine Learning for Emission Modeling of Fossil-fueled and Hydrogen-fueled Internal Combustion Engines

by

Saeid Shahpouri

A thesis submitted in partial fulfillment of the requirements for the degree of

Doctor of Philosophy

Department of Mechanical Engineering
University of Alberta

Abstract

Development of fast and accurate emission models for engine-out and tailpipe of internal combustion engines (ICEs) using machine learning (ML) and hybrid methods are the focus of this thesis. The application is on medium and heavy-duty vehicles powered by both fossil fuels and alternative fuels like hydrogen. This thesis is structured in three interconnected phases that sequentially build upon each other to establish steady-state and transient emission models for fossil-fueled and hydrogen-fueled engines.

The first phase proposes a new approach for physics-based combustion modeling of low-carbon fuels, by replacing traditional thermo-kinetic combustion mechanisms with computationally efficient ML models for laminar flame speed (LFS) calculation. LFS is a crucial input for physics-based pre-mixed combustion models. The LFS models are developed by creating a large dataset of LFS through combustion mechanism simulations and training ML methods using this dataset. The results are models that can predict LFS for blends of low carbon fuels including hydrogen, methanol, and ammonia over wide range of temperature, pressure, exhaust gas recirculation (EGR) and air-fuel equivalence ratio that represents combustion conditions in ICEs. These models are hundreds of thousands times faster than traditional thermo-kinetic models in LFS calculation.

To optimize steady-state operation of an engine it is important to model and predict engine-out emissions. The second phase of this research focuses on developing steady-state emission models for both fossil-fueled and hydrogen-fueled engines. Physics-based, black-box (BB), and gray-box (GB) emission models are created and

compared against each other to predict emissions from a compression ignition (CI) diesel engine. Subsequently, steady-state BB and GB NOx and soot emissions models for the hydrogen-diesel engine are developed. The resulting BB and GB models can predict NOx and soot emissions for both fossil-fueled and hydrogen-fueled engine with R^2 between 0.95 and 0.99 considering the trade-off between accuracy and computational cost.

The third phase focuses on transient emission modeling. First, transient emission models of the dual-fuel hydrogen-diesel engine are developed using the experimental transient data of engine-out emissions. Training models using steady-state data and directly training models with transient data are investigated. Classic ML algorithms and deep-learning (DL) time-series networks are utilized for GB and BB transient emission modeling. The models developed using transient data and times series network showed the best performance, predicting transient NOx emissions with R^2 between 0.96 and 0.97. Next, transient tailpipe emissions from a heavy-duty truck are investigated using real-driving on-road emission data from a Class 8 truck, from over 10000 Km of driving. This data is employed to develop various time-series DL algorithms with different input feature sets, complexity levels, and training dataset sizes. The best developed model can predict tailpipe real driving instantaneous NOx emissions with R^2 of 0.91 and cumulative NOx emissions with less than 2% error.

The computationally efficient BB emission models developed in this study can predict over 10000 cases per second which makes them suitable for engine and aftertreatment system model-based control. On the other hand, the GB models provide higher accuracy but require more computational power, which makes them suitable for diagnostics, calibration, and hardware-in-the-loop (HIL) setups for performance optimization and tailpipe emission reduction without requiring expensive experimental tests. These techniques can contribute to mitigating emissions from the transportation sector.

Preface

This thesis is an original work by Saeid Shahpouri. The research was conducted utilizing available computing systems and experimental setups at the University of Alberta Energy Mechatronics Lab (EML) led by Dr. Mahdi Shahbakhti and the Advanced Combustion Engine Lab led by Dr. Bob Koch.

The content of each chapter is either fully or partially based on published or submitted papers in peer-reviewed journals and conference proceedings [1–6]. The experimental setups, including the fossil-fueled diesel engine and hydrogen-diesel engine emission measurement system, were prepared in collaboration with Dr. David Gordon, Jakub McNally, and Dr. Armin Nourozi. Furthermore, the measured data for the spark ignition hydrogen engine was provided by IAV Company in Germany. Additionally, Luo Jiang was responsible for collecting on-road heavy-duty diesel truck data.

As the lead author, I made substantial contributions to all the peer-reviewed published papers referenced throughout this thesis. The contributions of co-authors in each paper are listed below.

In Chapter 3, [1], Dr. Armin Nourozi, Christopher Hayduk, Dr. Alexander Fandakov, and Dr. Reza Rezaei provided valuable insights regarding combustion mechanisms and the optimization of machine learning algorithms.

In Chapter 4 [2, 3], Dr. Armin Nourozi assisted with experimental data measurement and the development of machine learning models. Christopher Hayduk and Dr. Reza Rezaei contributed through insightful discussions on physics-based model development and emission modeling.

In Chapter 5, [4], Dr. David Gordon helped with the experimental data measurement, while Christopher Hayduk and Dr. Reza Rezaei provided the experimental data for the single cylinder SI engine and engaged in insightful discussions on emission modeling.

In Chapter 6, [5], Dr. David Gordon and Jakub McNally contributed to the experimental data measurements.

In Chapter 7, [6], Luo Jiang contributed by collecting on-road heavy-duty diesel truck data.

Acknowledgments

First and foremost, I would like to express my genuine appreciation to Dr. Mahdi Shahbakhti and Dr. Bob Koch for their overarching guidance, encouragement, and support throughout my study. Your advice always puts things in perspective, and I am deeply indebted to you.

I would like to thank Dr. Reza Rezaei and Dr. Alexander Fandakov, and Christopher Hayduk for their valuable feedback for our joint publications.

Thanks to all of my friends and colleagues in both the University of Alberta and IAV company. I would like to especially thank Dr. Armin Norouzi, Dr. David Gordon, Jakub McNally and Luo Jiang for their contributions to my projects.

Finally, I would like to express my deepest gratitude to my parents, Fatemeh and Ali, my brother Mohammad, my fiancee Carolyn, and my dear friends. Your unwavering support and encouragement throughout my Journey have been truly invaluable. I am forever grateful to have such incredible people in my life.

Table of Contents

List of Tables

List of Figures

Abbreviations and Acronyms

0D   Zero-Dimensional

1D   One-Dimensional

2D   Two-Dimensional

3D   Three-Dimensional

aTDC   after Top Dead Center

AI   Artificial Intelligence

ACT   Advanced Combustion Toolset

ANN   Artificial Neural Network

bTDC   before Top Dead Center

BNN   Beysian Neural Network

BB   Black-Box

BMEP   Break Mean Effective Pressure

CA50   Crank Angle by which 50% of fuel is burnt

CAD   Crank Angle Degree

CART   Classification and Regression Trees

CH3OH   Methanol

CL1	Complexity Level 1
CL2	Complexity Level 2
CL3	Complexity Level 3
CL4	Complexity Level 4
CO2	Carbon Dioxide
CO	Carbon Monoxide
CNG	Compressed Natural Gas
CI	Compression Ignition
CFD	Computational Fluid Dynamics
DL	Deep Learning
DOC	Diesel Oxidation Catalyst
DOE	Design of Experiments
DPF	Diesel Particulate Filter
DOI	Duration of Injection
DS1	Dataset 1
DS2	Dataset 2
DS3	Dataset 3
DS4	Dataset 4
DT	Decision Tree
ECU	Engine Control Unit

EI	Expected Improvement
ESM	Engine Simulation Model
ERT	Ensemble of Regression Trees
EGR	Exhaust Gas Recirculation
ELM	Extreme Learning Machines
ES	Expert Selection
EV	Electric Vehicle
FS	Feature Selection
FS1	Feature Set 1
FS2	Feature Set 2
FS3	Feature Set 3
FC	Fully Connected Layer
GA	Genetic Algorithm
GB	Gray-Box
GHG	Greenhouse gas
GPR	Gaussian Process Regression
GRU	Gated Recurrent Unit
LFS	Laminar Flame Speed
H2	Hydrogen
HCCI	Homogeneous Charge Compression Ignition

HIL	Hardware-In-the-Loop
HL	Hidden Layer
IMEP	Indicated Mean Effective Pressure
ICE	Internal Combustion Engine
LASSO	Least Absolute Shrinkage and Selection Operator
LCF	Low Carbon Fuel
LSTM	Long-Short Term Memory
LNT	Lean-Burn Trap
MAPE	Mean Absolute Percentage Error
MCC	Model-based Combustion Control
ML	Machine Learning
MLR	Multiple Linear Regression
MPC	Model Predictive Control
MPRR	Maximum Pressure Rise Rate
MRE	Mean Relative Error
MRMR	Minimum Redundancy Maximum Relevance
MSE	Mean Squared Error
MSL	Minimum Samples Leaf
NH3	Ammonia
NN	Neural Network

NOx	Nitrogen Oxides
PCCI	Pre-mixed Charge Compression Ignition
PHY	Physical insight features
PM	Particulate Matter
PMLS	Physics-based Models with Machine Learning Laminar Flame Speed
PN	Particulate Number
PR	Polynomial Regressor
QSSM	Quasi Steady-State Model
RDE	Real Driving Emissions
ReLU	Rectified Linear Unit
RF	Random Forest
RT	Regression Tree
RMSE	Root Mean Square of Error
SCR	Selective Catalytic Reduction Catalyst
SI	Spark Ignition
SNR	Sensor to Noise Ratio
SOI	Start of Injection
SSM	Steady-State Model
SVM	Support Vector Machine
TSM	Transient Sequential Model

UHC	Unburnt Hydrocarbons
VGT	Variable Geometric Turbine
WB	White-Box
WHO	World Health Organization

PART I: Introduction and Experimental setup

Chapter 1

Introduction and Background[1]

Internal combustion engines output emissions

Transportation sector is a major source of Carbon Dioxide (CO_2) greenhouse gas (GHG) emissions worldwide and this sector is dominated by internal combustion engines (ICEs). Between 1990 and 2019, the transportation sector experienced the largest increase in GHG emissions production [7]. Furthermore, ICEs are significant sources of other pollutants, including Nitrogen Oxides (NOx), CO_2, Soot, Carbon Monoxide (CO), and unburned Hydrocarbon (UHC) [8].

NOx refers to a group of gaseous compounds comprising nitrogen and oxygen atoms, primarily formed as byproducts during the combustion of fossil fuels. Burning fossil fuels in combustion chambers results in high temperature which contribute to the formation of NOx emissions. Exposure to NOx can lead to adverse health effects, especially in the respiratory and cardiovascular systems. According to the world health organization (WHO) [9], elevated levels of NOx can exacerbate asthma, bronchitis, and other respiratory conditions while increasing susceptibility to respiratory infections. Furthermore, NOx emissions not only affect air quality but also contribute to the formation of ground-level ozone and fine particulate matter, both of which have detrimental effects on human health and the environment [10]. The transportation sector, particularly heavy-duty trucks, plays a significant role in producing NOx emissions. Environment and Climate Change Canada [11] reported that

---

[1] This chapter is partially based on [1–6]

the road transportation and mobile equipment sector are responsible for about 47% (682 kt) of the total NOx emissions. Notably, the combined emissions from heavy-duty diesel vehicles, off-road diesel vehicles and equipment, and rail transportation constitute 32% (461 kt) of the total NOx emissions, highlighting their substantial share of emissions [11].

Soot emissions are byproducts of the combustion process and consist of fine particles primarily composed of carbon. Soot forms during the incomplete combustion of hydrocarbon fuels, undergoing processes including nucleation, particle growth, agglomeration, and oxidation [12]. Accurate soot emissions modeling is important due to three factors: i) Soot emissions can cause serious health problems [12], ii) Soot emissions have a complex formation and oxidation mechanism that makes soot modeling the most challenging of all emissions [12], and iii) Soot emissions regulations are becoming increasingly strict [13], particularly for real driving emissions (RDE). Soot emissions depend on various factors, including fuel properties and fuel blending [14, 15]. Soot emissions regulations have progressively reduced the maximum soot mass that can be produced. More recent emission standards restrict both particle sizes and particulate number (PN) [12].

Carbon dioxide (CO_2) emissions account for over 80% of all greenhouse gas emissions generated by human activity in Canada [16]. From 1990 to 2020, CO_2 emissions from light-duty gasoline vehicles dropped by 40%, whereas CO_2 emissions from light-duty gasoline trucks and heavy-duty diesel trucks increased by 120% and 240%, respectively [16]. The transportation sector is the second major source of CO_2 production, accounting for over 28% of the total CO_2 emissions production [16]. Medium and heavy-duty vehicles are almost exclusively powered by compression ignition (CI) diesel engines burning diesel fuel. Diesel engines are responsible for 25% of the fuel consumption and CO_2 emissions production in the transportation sector, and in recent years this share has been constantly increasing [16]. Additionally, electrification, which is progressing rapidly in light-duty vehicles, is more challenging for the medium

and heavy-duty sector [17]. The increasing share of CO_2 production, electrification challenges, and stricter emission regulations for medium and heavy-duty vehicles necessitate searching for alternative solutions. This is especially important in the short and medium terms as despite the progress in electrification, ICEs will continue to power the majority of transportation vehicles in the near future as it is depicted in Figures 1.1 and 1.2 [17]. Emissions regulations have become more stringent, particularly for NO_x and soot emissions in vehicles [18]. Figure 1.3 illustrates the evolution of European heavy-duty legislated particle matter (consist of soot, UHC, and other particles) and NO_x emissions limits.
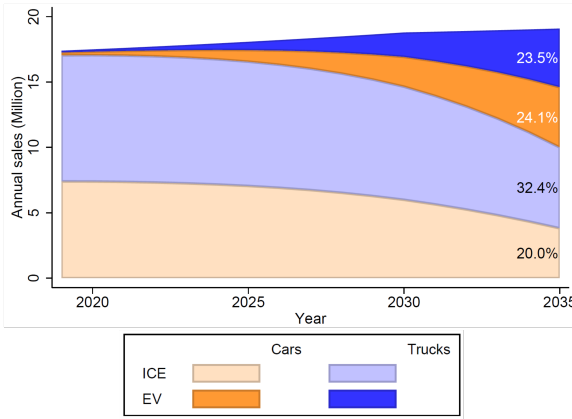
Figure 1.1: Market share of newly sold light-duty vehicles based on the best case scenario for electric cars [17]
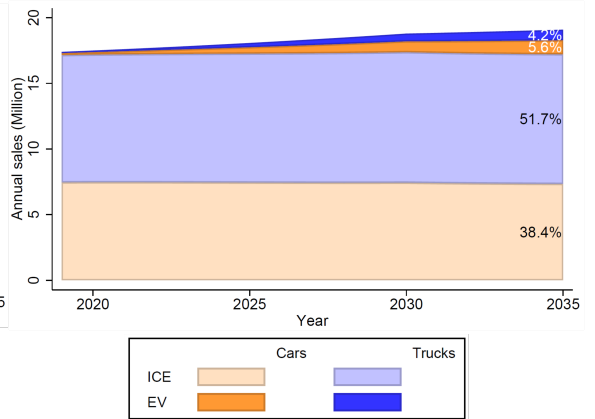
Figure 1.2: Market share of newly sold light-duty vehicles based on worst case scenario for electric cars [17]

Emission reduction techniques in internal combustion engines

Methods to reduce NO_x and soot emissions from ICEs can be broadly classified into two main categories. The first approach focuses on minimizing in-cylinder emission formation by reducing peak combustion temperatures. Techniques commonly employed in this approach include exhaust gas recirculation (EGR) [20, 21], water injection [22, 23], multi-phase fuel injection [3, 21], homogeneous charge compression ignition (HCCI) [24], and pre-mixed charge compression ignition (PCCI) [25]. However, the implementation of some of these techniques may cause higher emissions
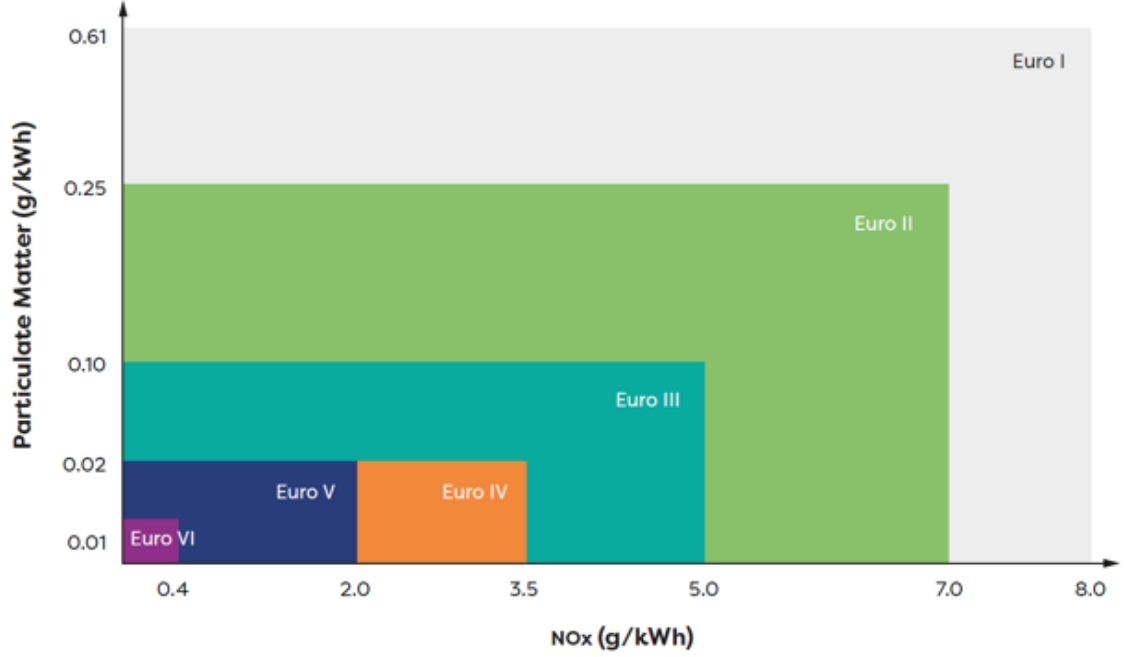
Figure 1.3: Development of European heavy-duty legislated emission limits [19]

of other pollutants like soot. To optimize the performance of these methods and maintain minimal emission levels, precise combustion control is crucial and can be achieved using engine model-based combustion control [26, 27]. Employing engine model-based combustion control for emission regulation requires accurate emission models, which can be provided by data-driven and hybrid methodologies [28].

The second approach to reduce tailpipe emissions involves the use of after-treatment systems to reduce the produced emissions in combustion engines to be released into the environment [29]. Some of the most common soot, UHC and CO after-treatment technologies include: diesel particulate filters (DPFs) and diesel oxidation catalysts (DOCs). DPFs are the most widely used soot after-treatment technology. They physically trap and collect particulate matter from the exhaust gas stream. Over time, the trapped soot accumulates, and the DPF undergoes a regeneration process to burn off the collected particulates, converting them into less harmful gases. DOCs use a catalytic process to oxidize soot particles and other pollutants

such as UHC and CO into less harmful compounds like CO_2 and water. While DOCs are less effective in removing soot compared to DPFs, they are commonly used in combination with DPFs to improve overall soot reduction.

Lean-burn NOx traps (LNT) and selective catalytic reduction (SCR) are among the most widely used after-treatment technologies for mitigating NOx emissions [30]. The LNT system functions as a NOx emissions capture mechanism, absorbing NOx emissions during engine lean operating conditions. During engine rich operating conditions, the captured emissions are released and converted to nitrogen via reactions with intermediate compounds generated during fuel combustion processes [31]. However, the LNT's performance is limited in diesel engines, often leading to increased fuel consumption [32]. So, a rich-lean engine control strategy that minimizes the NOx emissions is required.

SCR technology is extensively used in various sectors, including power generation, transportation, and industry, to reduce NOx emissions in exhaust gases. This system uses a catalyst and a reducing agent (typically ammonia) to transform NOx into nitrogen and water vapor. The reducing agent must be properly added using a control strategy. SCR has demonstrated effective performance, reducing NOx emissions by more than 95%, and its popularity has grown due to its high efficiency and reliability [30, 31]. While SCR technology's effectiveness decreases at low temperatures [33], it still outperforms EGR and LNT systems in reducing on-road tailpipe NOx emissions, in both cumulative and peak values [34]. Fast and accurate emission models are essential for optimal exhaust after-treatment techniques. It can also help to minimize the need for costly experimental tests to evaluate emission reduction techniques effectiveness.

To decrease CO_2 emissions, one potential solution is modifying existing engines to burn alternative zero-carbon fuels, substantially reducing diesel engine carbon tailpipe emissions, including net CO_2, soot, CO, and unburned hydrocarbons [35, 36]. Emission modeling is also crucial for these ICEs that utilize alternative fuels like hydrogen

or a combination of alternative and fossil fuels, in order to optimize, calibrate, and control them. This is particularly important for engines burning hydrogen, as hydrogen addition can increase NO_x emissions [36, 37]. Modeling engine-out emissions is vital for model-based engine control, engine control unit (ECU) calibration, and fault diagnostics [38–41]. Employing machine learning (ML) methods for emission modeling in ICEs is a promising approach that can provide fast and accurate emission models for engine control and diagnostics real-time applications [42].

To comply with stricter emission standards, including RDE standards, and at the same time reducing tailpipe carbon foot print of ICEs, a promising approach is to use alternative fuels in ICEs and control the engine using artificial intelligence (AI) emission control strategies based on predictive emission models [43]. This approach enables the simultaneous reduction of NO_x, soot, CO_2, and other emissions without requiring extensive modifications to traditional ICEs.

This chapter provides an overview of the literature on ICE combustion modeling, steady-state and transient engine-out and tailpipe emission modeling, and the application of alternative fuels in ICEs. Following this review and identification of research gaps, the scope and novel solutions from this thesis will be presented.

1.1   Physics-Based Combustion Modeling

Physics-based combustion modeling in ICEs employs mathematical models to simulate the intricate processes that occur within the engine. These models can vary from one dimensional (1D) to three dimensional (3D) simulations, depending on the required level of detail. When combined with reaction mechanisms, these models can also predict emissions. While 1D models offer a simplified representation of engine processes and are computationally efficient, they often lack accuracy in emission prediction [12]. In contrast, 3D computational fluid dynamic (CFD) models provide a more comprehensive and detailed analysis, capturing complex phenomena such as turbulence, flame propagation, and heat transfer. Although these models can accu-

rately predict emissions, they are computationally expensive and time-consuming [12]. Physics-based models have been widely used for combustion modeling and emission prediction of diesel engines [44, 45].

The accuracy of physics-based combustion models relies on several factors, one of which is the correct laminar flame speed (LFS) estimation. LFS plays a crucial role in the physics-based combustion modeling of premixed combustion processes, as it influences the overall performance and emission characteristics of the engine.

1.1.1 Laminar flame speed modeling

A physics-based combustion model, that does not require excessive computation, relies on flamelet assumptions which needs the LFS value as an essential input for premixed combustion [46]. The hydrogen LFS model is therefore critical for modeling hydrogen fueled engines with premixed combustion (port hydrogen injection), including both spark ignition (SI) engines running on 100% hydrogen and dual-fuel CI hydrogen-diesel engines. The accuracy of the LFS model plays a significant role in the performance of the physics-based combustion models. An accurate LFS calculation is needed at each crank angle in a physics-based model. This can be accomplished using thermo-kinetic combustion mechanisms, but this is a time-consuming process. The fast estimation of LFS is one of the most challenging aspects of developing gray-box emission models for hydrogen engines as the physical model needs the LFS value for each crank angle. LFS is a fundamental property of premixed combustion and is an estimation of how fast a flame propagates through quiescent mixture of unburned reactants in an adiabatic process [47]. Mixture properties including reactivity, diffusivity, and exothermicity all affect LFS values [48]. LFS is closely related to the fuel-burning rate in the combustion chamber, which influences combustion efficiency and emissions production. Thus, an accurate LFS estimation is important for characterising the fuel combustion behaviour in combustion engines. In turbulent combustion models, LFS values may be utilized directly or indirectly for the validation of

chemical kinetic models [49]. Introduced in 1883, the first theoretical model for the determination of the LFS was based on the assumption that combustion is sustained by upward propagation of heat through the layers of unburned gas up to the ignition temperature [50]. Since 1883, a lot of improvements in LFS modelling have occurred which are discussed next.

LFS for different types of hydrocarbon fuels have been investigated experimentally in the literature [51–53]. There are also a number of studies that experimentally investigated LFS for H_2 fuel [54–56], but fewer studies have focused on ammonia (NH_3) [56–58] and methanol (CH_3OH) [59, 60]. However, these experimental methods can only measure LFS for relatively low pressures and temperatures compared to the typical temperatures and pressures at which ICEs operate. Thus, LFS models based on experimental data need to extrapolate the LFS for the entire engine working conditions [61]. Thermo-kinetic combustion mechanisms can be used to calculate LFS at high temperatures and pressures which occur in the in-cylinder gases at the end of compression. These thermo-kinetic mechanisms that consider the effects of different parameters on LFS, often consist of many reactions and are computationally expensive. Even though LFS can only be measured experimentally for low pressures and temperatures, these limited experimental values of LFS are used as a main criterion for validating combustion mechanisms for different fuels [54, 62, 63]. Using detailed combustion mechanisms is computationally demanding and impractical for use in models required for engine model-based control.

ML methods can be used to accelerate LFS calculation in 0D and 1D engine models [64]. ML methods have been applied for different applications in combustion engines, including improving the combustion modeling [65, 66], engine-out emission modeling [67, 68], engine control [27], and diagnostics [42]. It is also possible to predict LFS for fuel blends using ML methods. This is specially important because with the growing emphasis on low-carbon fuels, a more various range of these fuels for ICEs is expected. Future engines may be designed to run on a range of low-carbon fuels

and their combinations, depending on the availability of these fuels in the particular geographical location.

ML methods have been applied for LFS prediction and to investigate LFS dependency on a variety of different factors in the literature. The effect of underlying fuel structure and the physical conditions on LFS have been investigated using artificial neural network (ANN) [69]. The effect of octane number and fuel sensitivity as well as physical conditions on gasoline LFS was studied using four ML methods [70]. Experimental data of LFS for H_2 and propane were used to train an ANN model [71], and the results show that ANN is more accurate than the analytical formula for LFS calculations over the entire range of combustion in an ICE engine. ML methods have also been used for developing empirical LFS models [72], and it has been shown that using ANN model for LFS prediction is more accurate than using empirical LFS models [73]. Using a 1D laminar flamelet code to predict LFS for methane-hydrogen-air mixture, an ANN model was trained with 10,000 LFS simulation points [74]. The temperature and pressure were limited to 800 K and 30 bar, which is much lower than the temperature and pressure ranges for an H_2 fuelled engine at end of compression and during the combustion. The results showed that the addition of H_2 increases LFS values. A classification of selected relevant studies is shown in Figure 1.4. Two main limitations of all these studies are: i) they are limited to low temperature and pressure ranges in comparison to the pressure and temperature ranges of an ICE, ii) the number of simulated or experimentally measured data points is relatively small, since only a limited range of physical conditions (pressure, temperature, and equivalence ratio) was used. As a result, the developed models in the previous studies require extrapolation to represent ICE conditions, which may result in inaccurate LFS prediction. As shown in Figure 1.4, ML methods have been mostly applied to LFS modeling where a mixture of fuels is used instead of a single fuel. Existing multiple fuel studies use a combination of a low carbon fuel (LCF) and a fossil fuel while the combination of LCFs hasn't been studied.
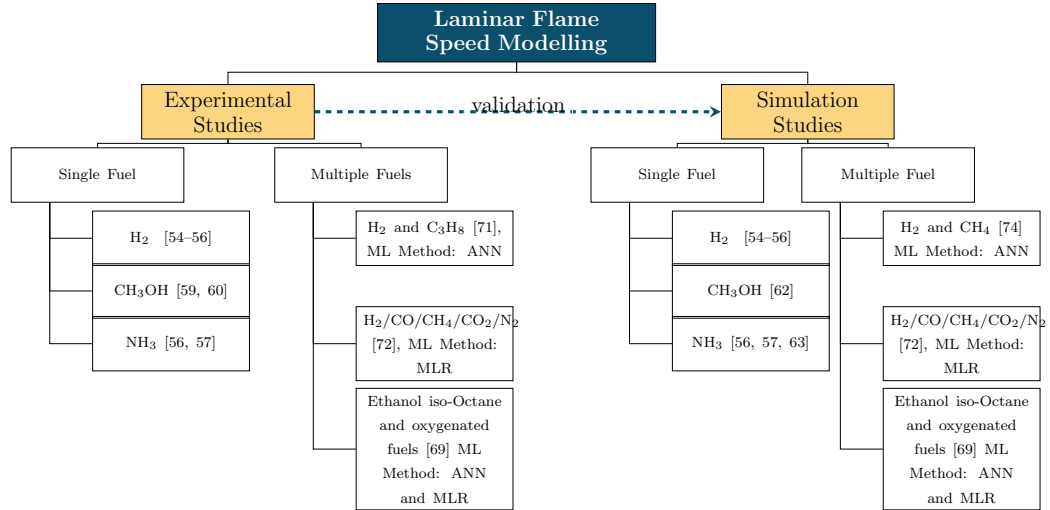
Figure 1.4: Prior laminar flame speed modeling studies. MLR stands for multiple linear regression.

1.2 Steady-State Engine-Out Emission Modeling

While the physics-based combustion modeling is useful for producing physical insight, a detailed 3D combustion simulation model is computationally expensive [22, 23], which makes it impractical for model-based calibration and real-time model-based control. Physical models are accurate for predicting NO_x emissions, but these models are less accurate in predicting soot, HC, and CO emissions [12, 28]. It is especially difficult to physically model soot, since the oxidation and formation mechanisms are still not fully understood [12, 75] and only detailed physical models are reasonably accurate [12]. Physical emission models could also be used for investigating the most important parameters in soot oxidation and formation process [76].

1.2.1 Steady-state emission modeling for fossil-fueled engines

Engine control units (ECUs) are currently not capable of doing the computation that is required for detailed physical emission models in real time. Thus, these models cannot be used to control emissions in real-time in model-based control. Data-driven black-box (BB) models that use measurement data directly for training ML methods are an alternative approach for modeling emissions. These models could be as accu-

rate as 3D CFD physical models but require significantly less processing time that is desired for implementation of model-based controllers in ECUs. The BB emission modeling can be carried out by selecting appropriate ML methods, such as: ANN, support vector machine (SVM), regression tree (RT), ensemble of regression trees (ERT), or Gaussian process regression (GPR) [77]. Similar to physical models, the prediction error is usually higher for soot emissions compared to other emission species for BB emission modeling [78]. The most popular ML method for soot emissions modeling is ANN [77], while some studies showed the advantage of other methods. In [79], SVM and ANN were used for BB emission modeling of a diesel engine using limited amount of data. Results showed that SVM shows better performance in emission modeling including soot emissions for limited amount of experimental data.

Data-driven BB models require fewer computations than detailed physical models, but since they do not contain physical models, they require data when physical conditions change. The need for large and rich set of experimental data in BB models makes them only suitable for engine control and calibration and for examining the effects of different engine components if sufficient experimental data is available. In addition, BB models are generally not suitable for studies that require modeling of a large number of cases since it is often difficult to obtain enough experimental engine data that span over all engine operating conditions. Extrapolation in the BB models typically results in poor accuracy. Gray-box (GB) models attempt to address these problems with BB models. A GB approach combines the benefits of physical modeling with supervised data-driven analysis. Thus to employ a GB model, a virtual engine (a 0D or 1D simulation model) is paired with an ML method. The ML method is trained using the input-output data of this virtual engine. In the virtual engine simulations, many parameters are produced, some are difficult or expensive to measure directly, e.g., in-cylinder parameters. The requirements to run the real engine and get experimental data is reduced in GB modeling. This makes the GB models appropriate for calibration. GB models are typically more reliable than BB models

for extrapolation and transient analysis because underlying physics is embedded in the simulation model.

GB models were used to predict NOx, CO, HC, and soot emissions in [80]. A combination of a 1D-CFD model and a GPR ML method with a fixed input feature set were used in [81] for emission modeling including NOx and soot emissions. Using only GPR method as the data driven part of the GB model is the limitation of this study. These results showed that the prediction error is generally larger for soot emissions in comparison with NOx emissions. The same trend was observed in other studies [28, 68]. The GB emission modeling for a wide range of emissions was investigated in [28]. A physical model was used, and different data-driven algorithms with fixed input feature sets for different emissions were used. For more complicated emissions including soot and HC, two 3-layer ANN methods were used, whereas other emissions were modelled by GPR method. This study showed that soot is the most difficult emission to model with hybrid and classical emission modeling methods. Although a more advanced ML method (ANN) was used in this study, there are still other ML methods that could be used for the data driven part. For GB and BB emission modeling, ANN and SVM methods were trained with the selected features [68]. This study also showed that soot is a challenging emission to model. In addition, soot emissions are more accurately modeled with SVM in comparison with ANN. In both of these studies [28, 68], input feature sets have not been analysed and only physical knowledge about the emissions formation and oxidation process were used to choose the fixed input feature sets for emission modeling. Using physical knowledge to select the input feature set, some of the crucial parameters might be missed because our physical knowledge about soot emissions is not complete.

An alternative way for choosing the input feature set is using ML feature selection methods. Data can be categorized according to their similarity to different groups using unsupervised clustering methods. Clustering can be used as a pre-processing or post-processing tool. As a pre-processing tool, clustering enables us to divide input

data into groups based on their similarity. In that case, each group will be considered a separate data set and analyzed separately. A well known ML clustering algorithm is K-means clustering algorithm. In [82], the K-means clustering algorithm is used to divide vehicles into clusters based on emission production level. Different ML methods were applied to each cluster, and then the methods offering the highest performance were selected. The study in [82] shows that clustering of the data in advance can lead to an improvement in the prediction accuracy. The same approach was used to classify the combustion events inside an engine cylinder [83]. Clustering has also been used as a post-processing tool by categorizing the output data of a simulation into different groups making the data easier to analyze. A CFD simulation was used to calculate the soot formation inside the combustion chamber of a diesel engine [84]. Then, on the basis of the soot formation rate in the engine combustor, the K-means clustering algorithm was used to partition the combustor into different zones. The low soot areas were distinguished from the high soot areas, helping in the soot formation analysis and to facilitate finding solutions to reduce soot production in high soot areas.

1.2.2 Steady-state emission modeling for hydrogen-fueled engines

One effective and economic way to reduce tailpipe carbon foot-print in the transportation sector is to switch to alternative fuels with zero carbon content like hydrogen. Hydrogen can be used in two primary ways in vehicles: as fuel in internal combustion engines (ICEs) or as an energy source in electric vehicles (EVs) through the use of fuel cells, which convert hydrogen into electricity.

Hydrogen-based ICEs offer several advantages over fuel cell technologies. They are less expensive to produce, have a longer service life, and do not require special hydrogen fuel purity standards [85]. Moreover, ICEs can be adapted to use multiple fuels, making them more versatile and convenient in terms of fuel availability [85].

Current ICEs can be converted into hydrogen engines or dual-fuel hydrogen engines with minimal changes and costs, which allows manufacturers to use the existing infrastructure for mass production of these engines with minimal modifications [85]. Dual-fuel hydrogen engines can play a significant role in the transition to a pure carbon-free hydrogen transportation system, especially as the number of active ICEs is expected to continue to increase over the next 15 years [86]. In particular, the dual-fuel hydrogen-diesel engine is an alternative powertrain for medium and heavy-duty tasks. This is because vehicles in these sectors often have longer service life and may need to operate in remote areas where the infrastructure for alternative fuels may not be available in near or mid term.

The most popular forms of using hydrogen in SI engines are: as the only fuel [74, 87–94], as the secondary fuel with gasoline [95–103], and as the secondary fuel with natural gas [74, 104–108]. Compression ignition engines can not run using hydrogen as the only fuel because the compression temperature in these engines is typically insufficient to initiate hydrogen combustion. A second high cetane fuel, like diesel or bio-diesel fuel is needed in CI engines to ignite the hydrogen-air mixture and operate using a dual-fuel mode [37]. The combination of hydrogen and other zero carbon fuels like NH_3 have also been investigated [109] to further reduce CO_2 emissions. Adding hydrogen to CI diesel engines and converting them to dual-fuel hydrogen-diesel engines is promising for two main reasons: i) diesel engines produce higher amounts of CO_2 and other emissions compared to gasoline engines per liter of fuel [16, 37] and ii) diesel engines are being used mainly for medium and heavy-duty tasks where the market for converting to battery electric is slow [17].

To assess the impact of hydrogen usage in ICEs and its associated emissions, experimental testing and modeling methods can be employed. Three main types of models can be utilized for emission prediction in ICEs: physics-based models (also referred to as white-box (WB) models), data-driven models or black-box (BB models), and hybrid models (GB models). Physics-based modeling of combustion involves utilizing

zero dimensional (0D) to three dimensional (3D) numerical models that are based on fundamental principles and mathematical equations. In contrast, BB models utilize a supervised ML method that is trained using training data (typically collected from experimental setup) to predict outcomes. GB models combine the strengths of both WB and BB models by simulating each engine case using a physical model, and then employing the outputs of the physical model along with experimental data for ML algorithm training. The additional information provided by the physical model, in the form of extra features, enhances the ML algorithm's prediction accuracy and incorporates physics into the prediction process. Studies concentrating on the emissions of hydrogen ICEs in terms of fuels and methodology have been summarized in Figure 1.5. Most of these studies have focused on experimental testing, and physics-based numerical modeling has been more commonly employed than ML methods for emission modeling in hydrogen ICEs. To the best of author's knowledge, GB modeling has not been investigated in the context of hydrogen engines in the literature.

The majority of the experimental studies reported that adding hydrogen into diesel engines and converting them to dual-fuel hydrogen-diesel engines can reduce soot (or particular matter PM), CO and UHC emissions. These engines typically have higher NO_x emissions production as a result of higher combustion temperatures [36, 37]. However, some studies reported that NO_x emission production remains constant [110] or can even be decreased [112–114, 118] when converting a diesel engine to dual-fuel hydrogen-diesel, depending on the hydrogen-diesel energy ratio and engine load. In [118], NO_x has a direct relationship with the hydrogen-diesel energy ratio and for high loads an inverse relationship exists, while in [112], the exact opposite is observed. Some studies concluded that increasing the hydrogen substitution ratio up to a certain point decreases NO_x emissions and then increases it at higher replacement amounts [113, 122]. In summary, converting diesel engines to hydrogen-diesel dual-fuel can generally result in decrease of all of the engine-out emissions including CO_2 except for NO_x emissions. The NO_x emissions depend on the engine configura-
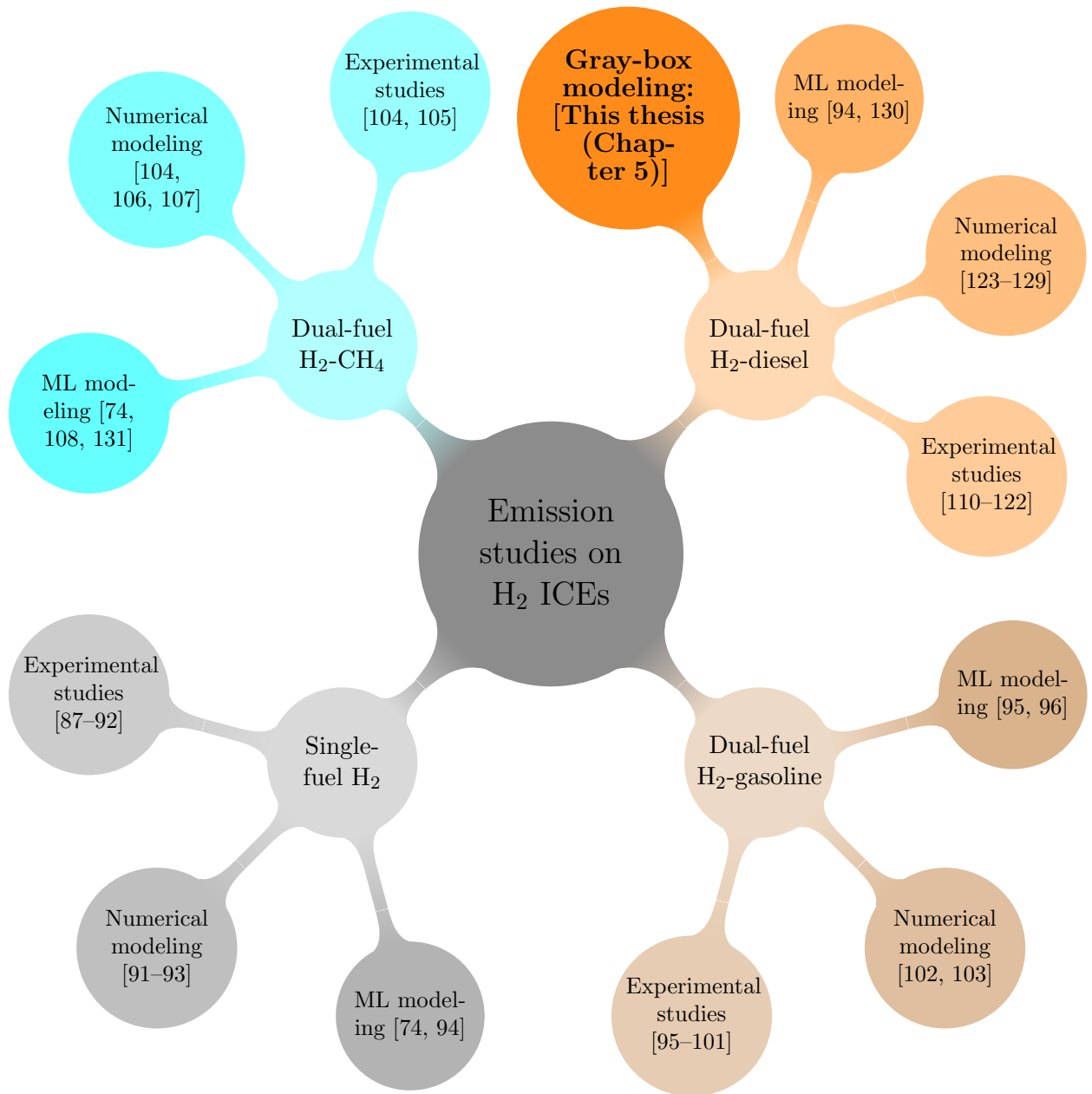
Figure 1.5: Prior emission studies on hydrogen fueled internal combustion engines (ICEs): Experimental, numerical, and machine learning (ML) modeling classified by fuel type and number of fuels used. The research gap addressed by this thesis is highlighted by "This thesis (Chapter 5)" in the diagram.

tion including available combustion control knobs such as exhaust gas recirculation (EGR) [119, 120], hydrogen injection location (port or direct injection) [121], engine operating conditions [112, 118], hydrogen substitution ratio [113, 122], and diesel injection timing [26].

Physical models that use detailed 3D CFD models can be highly accurate for predicting emissions [12, 22, 23]. However, these models are computationally expensive and therefore more suitable for offline applications such as investigating the effects of different parameters [123–126, 128, 129] and parameter optimization [127] for dual-fuel hydrogen-diesel combustion. In general, 3D CFD studies focusing on the effect of hydrogen addition to diesel engines and predicting emissions production are in agreement with experimental studies. These studies reported that adding hydrogen to diesel engines increases brake thermal efficiency [124, 125, 127, 129] and the hydrogen-diesel energy ratio has a direct relationship with NO_x emissions and an inverse relationship with soot emissions [123–126, 129].

To meet the tailpipe emissions and fuel economy regulations [132], modern engine controllers must provide high thermal efficiency while minimizing engine emissions for a wide range of real driving conditions. This may be done using model predictive control (MPC) techniques [8] where a model of the system is embedded for the real time combustion control. Since usual ECUs do not possess the computation power required for managing detailed physical emission models in real-time, these models are not suitable for real-time emission control. Alternative approaches for modeling include data-driven models or BB models that consist of trained ML methods. Using these models, model-based controllers in ECUs can be implemented with significantly less required computation time. The most popular ML method for emissions modeling in ICEs is ANN algorithm [77]. Although BB emission modeling has been studied extensively for traditional ICEs that burn fossil fuels [8, 42], this method has not been used as extensively for hydrogen ICEs. Experimental data was used to develop ANN and SVM models for NO_x emission prediction in a dual-fuel hydrogen-

18

diesel engine [94]. The results showed that ANN outperformed SVM in NO_x emission prediction with an R^2 of 0.94.

Using experimental data from a hydrogen blended natural gas engine, quadratic polynomial, ANN and SVM ML models were developed in [108] for NO_x emission prediction. The results showed that SVM outperforms ANN and quadratic polynomial methods with an average error of around 15% and the maximum error of approximately 60% [108]. Using experimental engine data, an SVM model was developed for NO_x emission prediction of a hydrogen blended compressed natural gas engine [131]. Although systematic optimization methods were not used [131], their results showed the importance of finding the optimal model parameters. The best SVM model when compared to the original SVM model reduced the mean absolute percentage error from 13% to 8% and the maximum relative prediction error from 57% to 26%.

GB or hybrid models can be created by integrating physics into BB models to improve model performance [28, 68]. Combining the physical knowledge in the form of fast physics-based models and BB models can result in a fast and accurate GB model that at least partially encompass physics. GB emission modeling for hydrogen engines are lacking so far. Previous studies of GB emission modeling for ICEs running with fossil fuels showed enhanced emission prediction performance compared to BB models [68]. Usually 1D and 0D physical models are used in GB emission modeling because high dimensional physical models are too computationally expensive.

1.3   Transient Emission Modeling

The investigation of transient emissions from vehicles can be broadly categorized into two distinct areas: engine-out emissions and tailpipe emission modeling studies. Both laboratory measurements and real on-road driving tests are employed in the literature to assess these transient emissions accurately. It is important to note that emissions measured during real driving conditions not only provide a more realistic evaluation but also account for the influence of environmental factors.

1.3.1 Transient engine-out emission modeling

ML algorithms can be utilized for transient engine-out emission modeling through GB and BB models in three distinct ways, depending on the algorithm type and the source of the training data. The most straightforward approach in transient emission modeling is to utilize steady-state models (SSM). These models consist of a classical ML algorithm that has been trained using steady-state emission data, and are now applied for the prediction of transient emissions. Due to the lack of transient emission data in the training process, these models have limited capacity to accurately predict the emissions. GB version of these models can perform better to a certain extent depending on the accuracy of the physical model. This is because the physical model can provide additional information and and incorporate certain elements of the transient nature of transient emissions into the ML method. In [133, 134], support vector machine (SVM) algorithm was trained using steady-state data for predicting NO_x emissions from a diesel engine (SSM methodology). Two models are developed, a low order model with 9 features and a high order model with 29 features. Results showed that the more complex high order model performs better in predicting transient NO_x emissions. The developed models then were used for model-based control of the engine.

The second approach for utilizing ML in transient emission modeling involves training classical ML algorithms with transient emission data. In this methodology, the emission value at each time step is treated as an individual steady-state case during the training process. These models are referred to as quasi steady-state models (QSSMs) and have the advantage of using the same type of data for both training and testing. However, the disadvantage of these models is that they cannot account for the sequential nature of transient emissions. This means for predicting each case algorithm only relies on the current state and not the previous states, which does not reflect the reality of transient emissions. Similar to SSMs, the performance of QSSMs

can be improved through the implementation of a GB version, as the physical model can provide additional information and capture some aspects of the transient behavior. In [135], QSSM models for NO_x emissions are developed using different classical ML methods including ANN, extreme gradient boosting (XG-Boost), random forest (RF), SVM, and decision tree (DT) using in-cylinder pressure data as the input. Results showed that all of the ML models are accurate ($R^2_{val} > 0.89$) and can be used as the virtual sensors. However, the study had a drawback in that it lacked an assessment of the models on new test data, and only the validation error terms were reported. This could result in a discrepancy between the performance of the models on validation data and on unseen test data. In [136], NO_x emissions data from a SI engine for six RDE cycles were used to develop QSSMs using ANN, SVM, polynomial regressor (PR), RF, light gradient boosting regressor ML models. Both steady-state and transient performance of the developed QSSMs were tested using two other RDE cycles and a steady-state map of NO_x emissions. Results showed that QSSMs can predict NO_x emissions for both steady-state and transient condition with R^2_{test} greater than 0.9. It was also found that the QSSMs are more accurate in predicting transient emissions compared to steady-state emission, as they were specifically trained using transient emission data.

The third strategy for modeling transient emissions using ML methods involves the use of transient sequential models (TSMs). In this approach, a deep learning (DL) recurrent neural network (RNN) is trained using transient emission data. RNNs have the capability to capture the sequential nature of transient emissions, meaning that the emission value at each time step depends on both the inputs at the current time step and the previous time steps. Two of the most widely used types of RNNs are long short-term memory (LSTM) and gated recurrent unit (GRU). These models can effectively handle the time-series nature of the data and can provide improved predictions of transient emissions compared to traditional models [137]. In [138], both QSSM and TSM are developed for predicting transient NO_x emissions of a SI engine. Clas-

sical ANN and LSTM algorithms were used for developing QSSM and TSM. Results showed that the TSM model outperform the QSSM which is due to the advantage of LSTM model in TSM that enables it to consider sequential behaviour of the data in prediction. In [139], RF and SVM algorithms were used to develop QSSM and LSTM algorithm was used to develop TSM for NO_x emissions of a CI engine. Results showed that the mean absolute error for the TSM is over 20% less than the QSSMs. In [140], QSSMs and TSMs are developed for NO_x emissions of two CI engines. SVM and RF algorithms were used for QSSM development, while the TSMs were developed using LSTM and GRU algorithms. In addition, noise reduction techniques were used to improve model performance. The results showed that the TSMs achieved around 10% lower MAE compared to the QSSMs. Furthermore, the application of noise reduction techniques resulted in a further improvement in the performance of the models. In the previous work [27], an LSTM TSM model was trained using transient simulation data obtained from a physical model of a CI engine to predict NO_x emissions. The resulting TSM model was then utilized to develop a model-based controller for the engine. However, relying solely on simulation data as the training and test data for the TSM model is the limitation of this work. Incorporating extra information from the physical model with the experimentally measured emission values can provide better training for the ML method in the forms of GB models. Figure 1.6 provides a summary of the studies on NOx emission modeling in ICEs. Given the large number of studies on steady-state NOx emission modeling, only sample representations (i.e. dual-fuel hydrogen-diesel engines) are highlighted in the steady-state section of the figure. As it is seen in Figure 1.6, most of the studies use some forms of physical models for engine model-based control and using data-driven models is a new approach in this field.
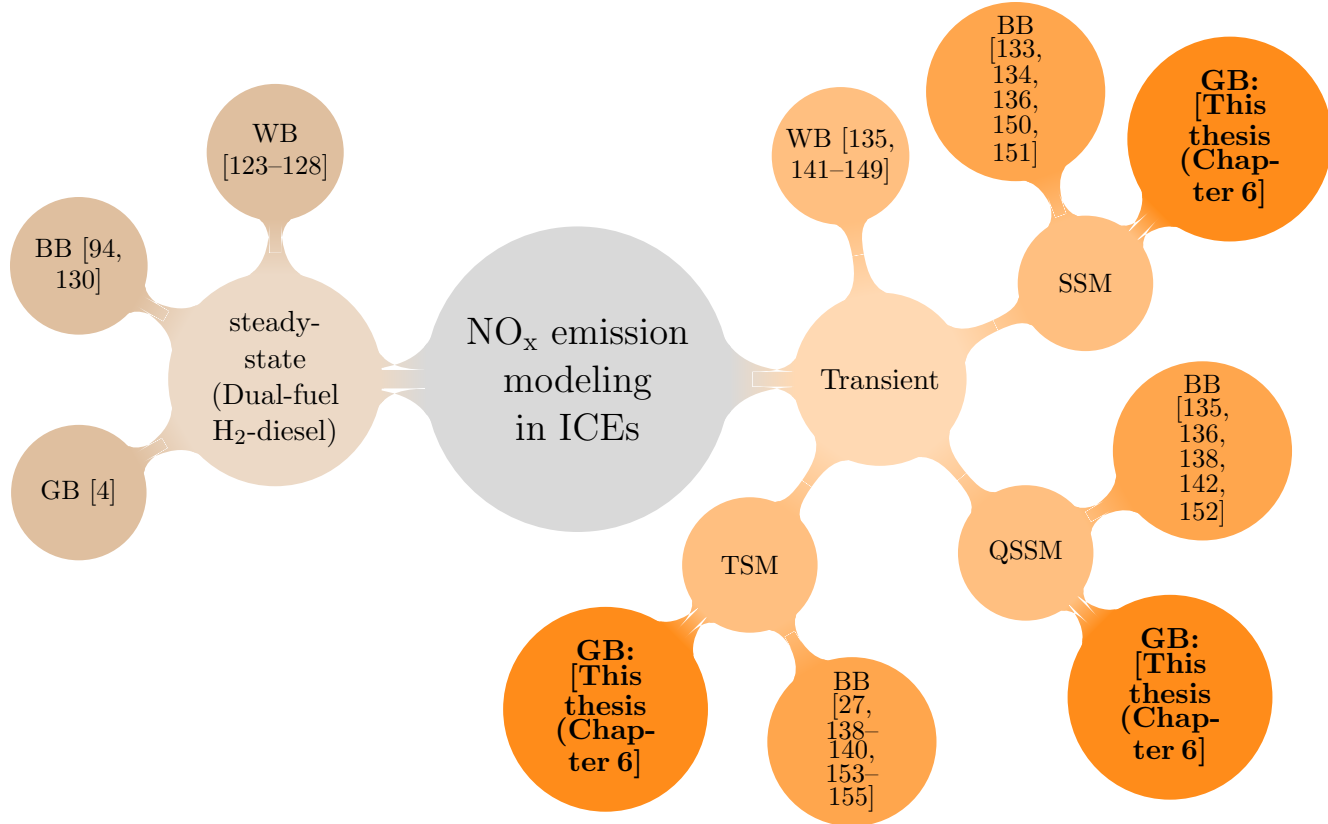
Figure 1.6: Prior NO_x emission modeling studies on internal combustion engines (ICEs): Steady-state and transient studies classified by modeling method (white-box (WB), black-box (BB) and gray-box (GB)), and methodology (steady-state models (SSM), quasi steady-state models (QSSM), and transient sequential models (TSM)). The research gaps addressed by this thesis is highlighted by "This thesis (Chapter 6)" in the diagram.

1.3.2 Transient tailpipe emission modeling

Due to importance of tailpipe NOx emissions and stringent regulations, a number of the studies in the literature have focused on tailpipe NOx emissions prediction. Predicting tailpipe NOx emissions is also important as for optimal SCR system performance, it is crucial to inject the appropriate amount of ammonia at the correct time. Delayed or excessive ammonia injection can lead to ammonia being present downstream of the SCR (ammonia slip), resulting in the formation of corrosive byproducts, air preheater blocking, and reduced efficiency and longevity of the SCR system [31, 156]. The SCR control system adjusts the timing and quantity of ammonia injection

based on the NOx emissions concentration measured at the SCR reactor's output. This concentration can be obtained using sensors installed at the output or "virtual sensors" that can predict the output NOx emissions concentration. The "virtual sensor" is a NOx emission model that predicts the tailpipe NOx emissions value. The tailpipe NOx emissions model can be employed for: i) model-based SCR system control to accurately adjust the timing and quantity of ammonia injection [157], ii) engine model-based control to decrease NOx emissions formation by modifying engine control parameters [27], iii) diagnosing SCR systems and NOx emission sensor [158, 159], and iv) on-road vehicle simulation applications [160].

Tailpipe NOx emissions can be modeled using either physical mechanism-based SCR models or data-driven ML and DL models. Physical SCR models predict output NOx emissions by simulating the chemical reactions between injected ammonia and the exhaust gas within the SCR system. More complex physical models, with a higher number of chemical reactions, provide a more accurate representation of the SCR system [161]. Three SCR physical models with different complexity levels were investigated in [162]. The most complex model considered both diffusion and reaction kinetics, while the other two models focused solely on reaction kinetics. The results indicated that only the complex model, with an RMSE lower than 20 ppm, was accurate enough for SCR model-based control in a production ECU. A combination of one-dimensional (1D) engine models and after-treatment models, including SCR, has been utilized for real-time engine control [163] and hardware-in-the-loop (HIL) setups [164, 165], which can be employed for engine optimization to achieve lower emissions. These models can accurately predict cumulative NOx emissions (95% accuracy), but they have reduced accuracy when predicting instantaneous NOx emissions [163]. Another application of physical SCR models is to investigate the internal processes of the SCR systems in detail, which can be used to enhance SCR performance in reducing NOx emissions [29, 166]. A combination of physical SCR models and CFD has been used to study the urea injector shape [167] and analyze the effects of different

parameters on urea spray within the SCR system [168], to optimize its performance. The most critical parameter was found to be the SCR intake gas temperature.

One primary limitation of studies on physics-based modeling of SCR systems is that none of the developed models have been tested in real-driving situations. The experimental data generated in the lab that is used in modeling studies may not accurately represent on-road conditions. Another issue with these models is the required complexity to achieve sufficient accuracy. This results in computational costs that are unsuitable for model-based SCR control.

Data-driven NOx emissions models offer the benefit of fast prediction. Further, the ability to be trained with real on-road driving data, enables these models to consider crucial parameters for predicting emissions in actual driving situations. A simple form of these models, known as look-up tables, is employed for tailpipe NOx emissions prediction [169, 170]. They make use of multi-dimensional tables, generated from experimental data, to correlate input variables with output values, specifically tailpipe NOx emissions. When predicting new cases, the models interpolate between the nearest data points in the table. Although look-up table models are effective in examining the impact of various factors on tailpipe NOx emissions and estimating cumulative emissions with approximately a 10% error [169]. Their accuracy in estimating instantaneous NOx emissions is lower than cumulative NOx emissions prediction due to the complex transient processes within the SCR system [169, 170]. As a result, they are unsuitable for transient NOx emissions modeling.

DL algorithms can capture complex physical processes [4], making them appropriate for representing the complexity within the SCR system. DL models were developed to predict engine out and tailpipe NOx emissions from a heavy-duty diesel engine and a diesel-electric engine [159]. The results showed that engine-out NOx could be predicted more accurately than tailpipe NOx. However, using SCR parameters such as inlet NOx, temperature, and mass flow rate, tailpipe NOx could still be predicted with high accuracy, with test $R^2 > 0.90$. The main limitation of this study [159]

is that only the lab-generated experimental data were used for model development and testing, whereas predicting tailpipe NOx emissions during real on-road driving is more difficult due to changing test conditions. Another limitation is that the developed deep networks only consist of fully connected layers [157], which cannot consider the dynamic (sequential) nature of the transient emissions in prediction. Time series networks, can capture this nature and can be used to improve prediction accuracy. Sequential models with LSTM networks, as well as SVM and back-propagation neural networks, were employed to predict SCR system output NOx emissions for a power plant [157]. Classic ML algorithms, including SVM and back propagation neural networks, were unable to capture the SCR NOx emissions trend and were highly inaccurate while the time series LSTM network prediction matched the experimental SCR NOx emissions with test mean absolute percentage error (MAPE) lower than 5%. A classification of existing studies in the literature that focus on tailpipe NOx emissions modeling in ICEs equipped with SCR after-treatment systems is shown in Figure 1.7.

1.4 Problem Identification and Proposed Solutions

As discussed above, the transportation sector predominantly relies on internal combustion engine (ICE)-powered vehicles, a trend that is expected to persist, especially for medium and heavy-duty trucks that primarily utilize diesel engines [17]. However, these trucks emit harmful pollutants such as CO, soot, UHC, and NO_x, which pose significant risks to human health. Emissions from ICEs, excluding CO_2, can be substantially reduced through various methods, including supercharging, exhaust after-treatment techniques, proper calibration, optimization of engine components, and the implementation of efficient engine and exhaust after-treatment control strategies [8]. Developing fast and accurate emission models is a crucial prerequisite for success of the techniques that rely on real-time control.
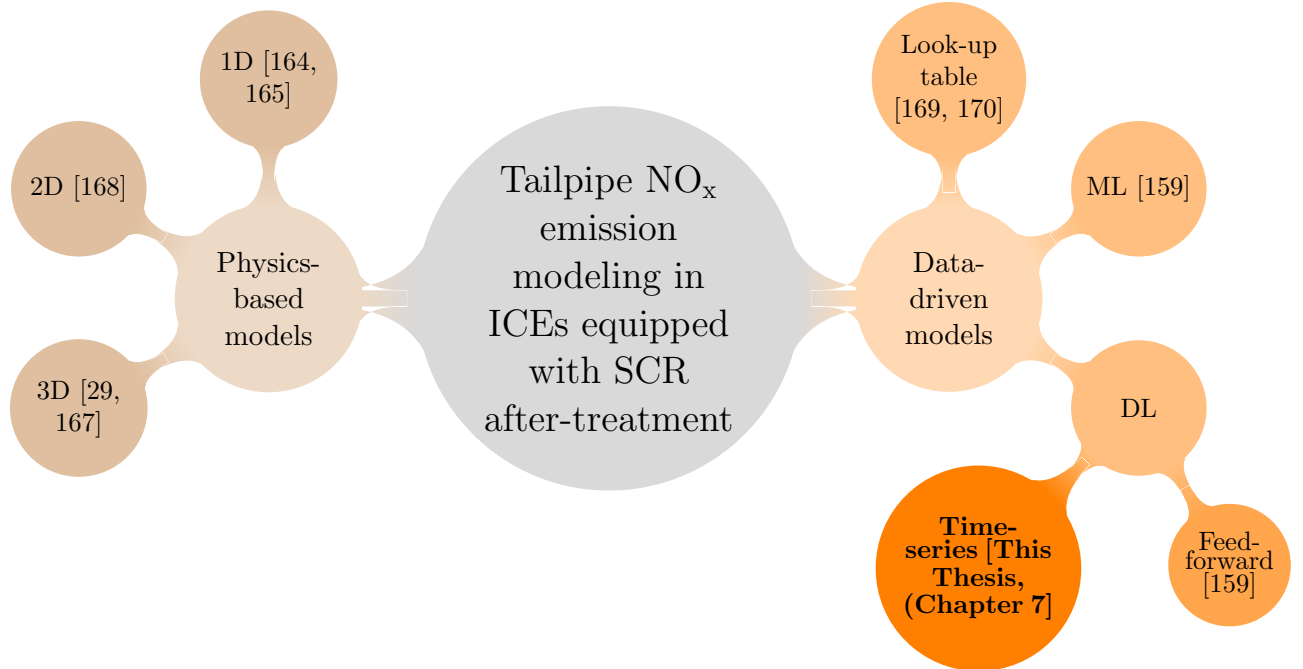
Figure 1.7: Tailpipe NO_x emission modeling studies for internal combustion engines (ICEs) with SCR in after-treatment system, ML stands for machine learning, DL stands for deep learning).The research gaps addressed by this thesis is highlighted by "This thesis (Chapter 7)" in the diagram.

To decrease the tailpipe carbon footprint in ICEs, one approach is to modify existing engines to burn alternative zero-carbon fuels like hydrogen. This method requires minimal changes to the current infrastructure and can be implemented by retrofitting already built trucks to operate on dual-fuel diesel-hydrogen systems. This approach significantly reduces the carbon footprint, providing a transitional pathway to zero-emission vehicles while the necessary infrastructure is being developed.

Fast and accurate steady-state and transient emission models are essential for these new ICEs that utilize alternative fuels such as hydrogen or a combination of alternative and fossil fuels, like hydrogen-diesel blends, in order to optimize, calibrate, and achieve optimal engine emissions control. Research gaps in the field of ICE emission and combustion modeling that this thesis is trying to address are grouped in three parts:

- Laminar flame speed modeling for alternative, hydrogen-fueled ICEs;

- Steady-state emission modeling for fossil-fueled and hydrogen-fueled ICEs;

- Transient emission modeling for fossil-fueled and hydrogen-fueled ICEs;

1.4.1 Laminar flame speed modeling

In the literature, one of the primary research gaps in the field of physics-based combustion modeling for ICEs utilizing alternative fuels is the lack of fast and accurate LFS models. Chapter 3 of this thesis addresses these research gaps in this field by developing ML LFS models for low-carbon fuels. The main parts of this work are summarized as:

- Laminar flame speed modeling has mainly been investigated at low temperature and pressure in the literature. To represent ICE conditions, these models require extrapolation, which may result in inaccurate predictions. In Chapter 3 of this thesis, thermo-chemical combustion mechanisms are used to calculate the LFS using design of experiments (DOE) to cover temperature and pressure ranges that closely resemble actual engine operating conditions. Consequently, the developed models do not require extrapolation for determining LFS in ICE operating conditions.

- To train an ML method for accurate LFS prediction, a large amount of data is required. This is because LFS has a complex and non-linear behavior. Many previous LFS studies have relied on small DOEs for training ML models to predict LFS. In contrast, in Chapter 3 of this thesis the LFS is estimated for large DOE sets with over 150,000 cases in total, exceeding previous studies with a maximum of 50,000 data points [64].

- As the emphasis on low-carbon fuels grows, a diverse range of such fuels for ICEs is anticipated. Future engines may be designed to operate on various low-carbon fuels or a combination of these fuels, depending on their availability in specific geographical locations. Although NH_3 is a zero-carbon fuel, no

study has explored the application of ML methods for modeling LFS for NH_3. Moreover, no study has investigated the development of ML methods capable of predicting LFS for a blends of low-carbon fuels. The complex combustion mechanism of NH_3 renders LFS calculation computationally expensive for use in 0D and 1D engine models. This highlights the importance of employing fast and accurate ML methods for calculating LFS for NH_3 and its combination with other low-carbon fuels. In Chapter 3 of this thesis, ANN and SVM ML models are developed to estimate LFS values for any combination of the three most prevalent low-carbon fuels: H_2, CH_3OH, and NH_3.

1.4.2 Steady-state emission modeling

Current research gaps in the literature in the field of steady-state emission modeling can be divided into two main categories: Fossil-fueled ICEs and hydrogen-fueled ICEs. Part III of this thesis focuses on developing WB, GB, BB steady-state emission models for medium-duty and heavy-duty engines powered by fossil fuels and hydrogen. Chapter 4 and Chapter 5 of this thesis address the following gaps in emission modeling for diesel ICEs and hydrogen-diesel ICEs:

Fossil-fueled ICEs

The main research gaps in the study of emission modeling for medium-duty and heavy-duty fossil-fueled ICEs, which are addressed in Chapter 4 of this thesis, include:

- Although some papers have investigated the effects of various parameters on diesel engine emission production, such as fuel properties [171], there is limited published soot emissions data for complete speed-load maps from medium-duty diesel compression ignition engines. This is due to the difficulty and cost of accurately measuring soot emissions and the extensive calibration efforts required for emission analyzers. In Chapter 4 of this thesis, soot emissions data for a full speed-load map of a 4.5 L 4-cylinder diesel engine is measured, providing a

benchmark to test different modeling methods in Section 4.1 of Chapter 4.

- The performance of ML methods in emission modeling is heavily dependent on the input feature set. It is common to primarily use physical knowledge for selecting input features, but this risks missing crucial features due to unknown or misunderstood physical relationships. This is particularly important in GB emission modeling, as the physics-based model generates numerous features, making it difficult to choose a subset based on physical knowledge. In Chapter 4 of this thesis, various input feature sets based on ML feature selection and physical knowledge are investigated to determine the optimal input features.

- Previous studies have used conventional ML methods such as SVM, ANN, and GPR with fixed input feature sets for soot emissions modeling. However, comprehensive studies investigating different ML methods and feature sets for soot emissions modeling are still lacking. In Chapter 4 of this thesis, eight different ML methods with five different input feature sets (40 models in total) are employed for soot emissions modeling and then evaluated.

- Post-processing methods for model selection and analyzing results have not been utilized in previous emissions modeling studies. In Chapter 4 of this thesis, a systematic unsupervised ML method is employed for analyzing and comparing different engine emissions models. Two K-means clustering algorithms that function as filters are used to select the best emissions models. This approach should be applicable to other engine modeling studies.

Hydrogen-fueled ICEs

In Chapter 5 of this thesis, the steady-state emissions of a dual-fuel hydrogen-diesel engine are modeled using WB, GB, and BB emission models, addressing the following research gaps in the current literature:

- While GB emission modeling has proven superior to BB emission modeling for traditional ICEs burning fossil fuels, there has been no study of GB emission modeling for hydrogen engines. In Chapter 5, BB and GB soot and NO_x emission models for a dual-fuel hydrogen-diesel CI engine are developed. The BB models offer the best computational efficiency useful for real-time combustion control implementation in an ECU. The GB models provide greater accuracy with higher computational expense, making them more suitable for an HIL setup in calibrating engine combustion controllers.

- ML-based LFS models have not been incorporated as a module in physics-based combustion engine modeling. These models can calculate LFS more rapidly than combustion kinetics models, reducing the overall computational cost of physics-based engine models. In Chapter 5 of this thesis, the hydrogen ML LFS models from Chapter 3 are embedded in physics-based models of hydrogen engines. The ML LFS model is validated using in-cylinder pressure traces for both an SI hydrogen engine and a CI dual-fuel hydrogen-diesel engine.

- All of the previous studies about emission modeling of hydrogen-fueled engines [87, 108] are done for only single type engine. In Chapter 5 combustion models are developed for both SI and CI and both single-fuel and dual-fuel hydrogen engines. The experimental setup for both engine types are described. The proposed models are tested against experimental data for predicting in-cylinder pressure trace, indicated mean effective pressure (IMEP), 50% burned fuel crank angle (CA50), and peak pressure for both SI and CI hydrogen engines.

- The input feature-set selection and hyperparameter optimization are two critical factors affecting ML model performance. In Chapter 5 of this thesis different input feature sets and ML methods are applied for GB and BB models. Furthermore, a systematic method is used to optimize the hyperparameters of ML methods, ensuring the high accuracy is achieved. This distinguishes the study

in Chapter 5 from previous researches [74, 94–96, 108, 130, 131], which uti-lized ML methods for emission prediction without systematically optimizing ML methods and input feature set.

1.4.3 Transient emission modeling

Transient emission modeling studies can be categorized into engine-out and tailpipe emission modeling. Engine-out emissions represent the engine exhaust emissions be-fore any after-treatment, while tailpipe emissions represent the final emissions after passing through all of the after-treatment systems. Due to the complexity of after-treatment systems, tailpipe emission modeling can be more challenging to model. Furthermore, tailpipe emission experimental data can be obtained in a laboratory set-ting or from real on-road driving conditions, with the latter providing a more realistic representation of environmental factors. In this thesis, Chapters 6 and 7 investigate engine-out and tailpipe transient emission modeling using both lab-generated and real on-road driving data. Due to the difficulty of transient soot emission measurements particularly on-road, Part IV focuses on NO_x emissions.

Hydrogen-diesel engine-out transient emission modeling

Chapter 6 of this thesis utilizes laboratory-generated engine-out emission data from a dual-fuel hydrogen-diesel engine to develop emission models. This chapter addresses the following gaps in the current literature:

- The current literature predominantly focuses on transient emission studies for traditional SI and CI ICEs fueled by fossil fuels. However, there is a significant lack of research on transient emission modeling for engines utilizing alterna-tive fuels, particularly hydrogen. These engines are well-suited for medium and heavy-duty tasks, which are more challenging to electrify compared to light ve-hicles [17]. Hydrogen addition can increase combustion temperatures and NO_x emissions, making accurate transient NO_x emission models crucial for effective

model-based control of dual-fuel hydrogen-diesel engines. Chapter 6 of this thesis presents a comprehensive investigation into the development of various NO_x transient emission models for a dual-fuel hydrogen-diesel engine.

- Data-driven modeling of transient emissions can be accomplished using three main methodologies: SSM, QSSM, and TSM. While some studies have compared the performance of two of these methods, there is a lack of research investigating and comparing the performance of all three models for the same engine and dataset. Chapter 6 compares the performance of SSM, QSSM, and TSM methodologies on both steady-state and transient NO_x emission data from a hydrogen-diesel CI engine, providing insights into the strengths and limitations of each methodology.

- GB emission modeling has been shown to enhance steady-state emission modeling [67, 68]. However, the application of GB modeling for transient emission modeling remains unexplored in the literature. Chapter 6 of this thesis investigates the use of GB modeling techniques in the form of SSM, QSSM, and TSM for modeling transient NO_x emissions.

- For model-based engine control, it is crucial to have a computationally efficient and accurate emission model. To address this, Chapter 6 investigates a range of different architectures and algorithms for time-series TSM modeling and compares their performance in terms of both accuracy and computational cost. Chapter 6 provides guidance on choosing the most appropriate TSM model based on the desired trade-off between accuracy and computational cost, taking into consideration the available computational resources. The results can help researchers and practitioners make informed decisions about which TSM model is best suited for their particular application, ensuring that the model is both accurate and computationally efficient.

Heavy-duty truck transient emission modeling

Chapter 7 of this thesis utilizes an extensive dataset of real on-road driving NO_x emissions from a class 8 heavy-duty diesel truck to develop tailpipe transient emission models and address the following gaps in the literature:

- Existing literature on DL models for tailpipe NO_x emissions predominantly relies on lab-generated data, which may not fully capture the system behavior in real on-road driving situations due to the data not fully covering all on-road simulations. In Chapter 7, real-driving data from a heavy-duty truck is used to train a time-series DL algorithm. The dataset used in Chapter 7 comprises over 4 million data points, measured at 10Hz sampling frequency, making it nearly ten times larger than the most extensive tailpipe NO_x emissions dataset previously reported in the literature. This data was collected from 37 highway trips with varied weather, truck weights, road conditions and temperature. This provides the most comprehensive dataset compared to similar studies [34, 170, 172], which collected on-road emission data over a few trips with consistent ambient conditions. Additionally, in Chapter 7, the impact of dataset size by four different datasets is examined, providing insight into the importance of dataset size.

- A prior study on DL modeling for tailpipe NO_x emissions [159] has primarily concentrated on feed-forward DL models. These models lack the ability to capture the transient (sequential) nature of NO_x emissions when modeling SCR system output NO_x emissions. In Chapter 7, four different time-series LSTM networks with different levels of complexity are examined to model the tailpipe NO_x emissions of a heavy-duty truck equipped with an SCR after-treatment system.

- Tailpipe NO_x emissions modeling studies [157, 159, 170] have been limited to

using a single input feature set. However, various applications often require models where the input feature set depends on the available data and the specific application. In Chapter 7, three models utilizing three different input feature sets are developed, each requiring different levels of information, making them suitable for a wide range of applications. In addition, this approach provides insight into the impact of input features on the tailpipe NO_x emissions model accuracy.

- Instantaneous and cumulative performance metrics that are used for evaluating the transient emission models in previous studies [157, 159, 170] are unrealistic in predicting if the emission is below or above the regulation. This is especially important in the automotive industry, as exceeding emission limit may result in non-compliance with emission regulations. In Chapter 7, model predictions are compared to the Tier 3 standard, and the F1 score metric is utilized to evaluate how well the models can predict whether the tailpipe NO_x emissions exceed or comply with the standard.

1.5 Contributions and Thesis outline

1.5.1 Thesis outline

This thesis is organized into five main parts that are described in eight chapters. The five parts and chapters within each part are schematically shown in Figure 1.8. The main parts and chapters of this thesis are as follows:

- **PART I: Introduction and Experimental Setups**

    - **Chapter 1** provides background, motivation, and main contributions of this thesis.

    - **Chapter 2** presents the details of the experimental setups used in this study, including CI diesel engine, SI hydrogen engine, CI hydrogen-diesel
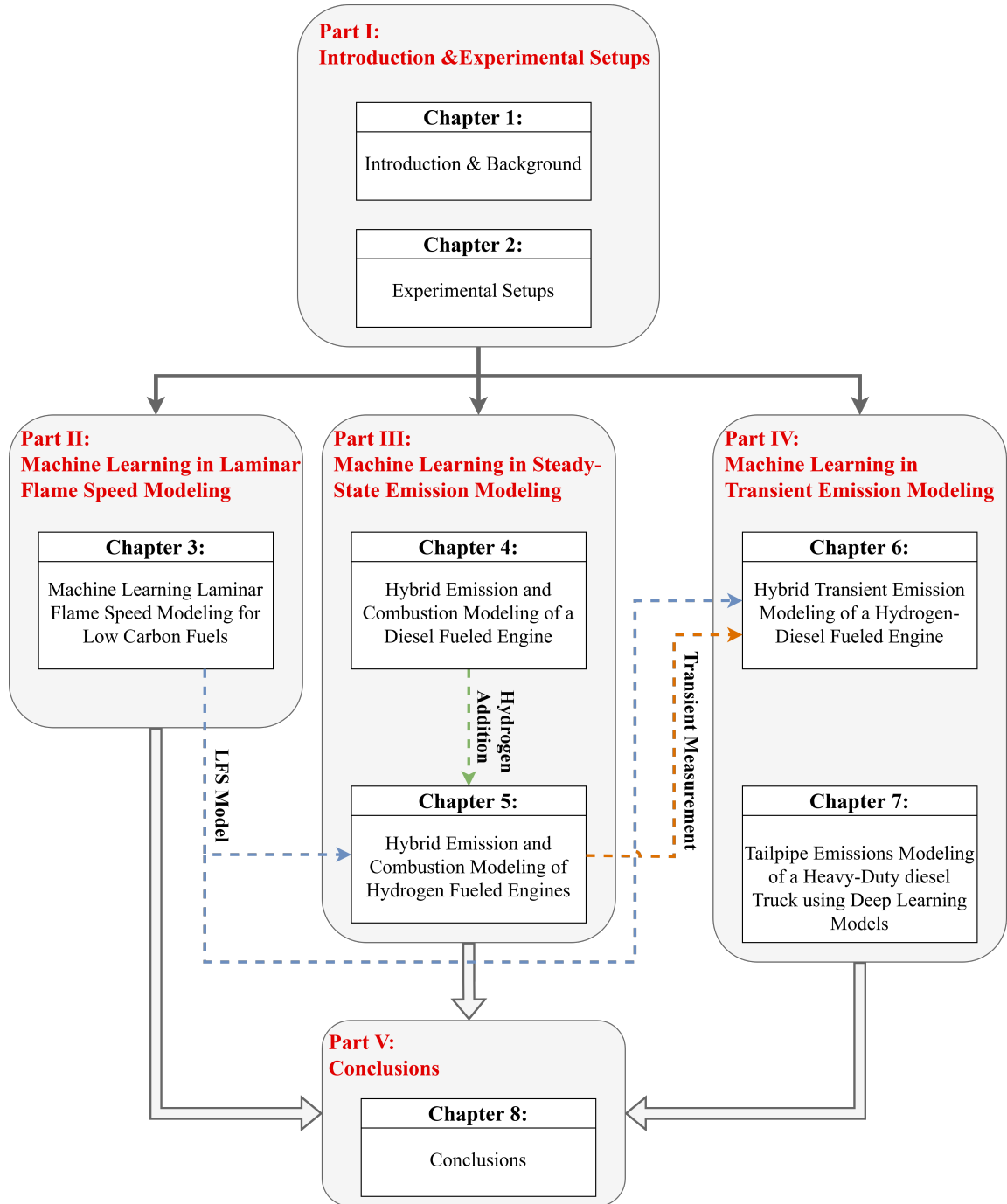
Figure 1.8: Schematic of the thesis organization. The dashed lines show the results from the early phases is being used in the successive phases.

engine, and tailpipe heavy-duty diesel truck emission measurement system.

- **PART II: Machine Learning in Laminar Flame Speed Modeling**

– **Chapter 3** describes developed ML-based LFS models for low-carbon fuels including hydrogen, methanol, and ammonia.

- **PART III: Machine Learning in Steady-State Emission Modeling**

  – **Chapter 4** describes developed steady-state WB, GB and BB soot emission models for a medium-duty CI diesel engine.

  – **Chapter 5** describes developed steady-state WB, GB and BB soot and NO_x emissions models for a medium-duty CI diesel-hydrogen engine as well as combustion models for a SI hydrogen engine.

- **PART IV: Machine Learning in Transient Emission Modeling**

  – **Chapter 6** provides developed DL transient GB and BB NO_x emissions models for a medium-duty CI diesel-hydrogen engine.

  – **Chapter 7** provides developed DL transient BB models for tailpipe NO_x emissions of a heavy-duty diesel truck using real-driving data.

- **PART V: Conclusions**

  – **Chapter 8** provides conclusions of this thesis.

1.5.2 Contributions

A summary of the main contributions of this thesis are:

- **PART I: Introduction and Experimental Setups**

  – Synthesis of exciting literature in the area of steady-state and transient engine-out and tailpipe emission modeling using physical, data-driven and hybrid methods.

  – Identified major research gaps that needs to be addressed for successful engine combustion and tailpipe emission control.

– Exploratory analysis of engine-out steady-state and transient emission data for soot and NO_x emissions from a diesel engine and hydrogen-diesel engine.

– Exploratory analysis and pre-processing of real-driving transient tailpipe emission data for a heavy-duty diesel truck.

- **PART II: Machine Learning in Laminar Flame Speed Modeling**

  – Created extensive LFS datasets for low carbon fuels including hydrogen, methanol, and ammonia using selected thermo-kinetic combustion mechanisms.

  – Developed fast and accurate ML-based LFS models for low carbon fuels including hydrogen, methanol, and ammonia.

  – Developed a fast and accurate ML-based model that can predict LFS for combinations of low carbon fuels including hydrogen, methanol, and ammonia.

- **PART III: Machine Learning in Steady-State Emission Modeling**

  – Developed WB, BB and GB for steady-state soot emission prediction of a medium-duty diesel engine using different ML methods.

  – Provided a systematic way of input feature set selection using combination of expert knowledge and an ML-based method.

  – Provided a systematic way of post-processing and model selection using a clustering ML-based method.

  – Developed WB, BB and GB for steady-state soot and NO_x emission prediction of a medium-duty hydrogen-diesel engine using different ML methods.

  – Provided a novel approach for physics-based combustion modeling by using ML-based LFS models inside combustion model and testing and validating

this approach by modeling a hydrogen SI engine and a hydrogen-diesel CI engine.

– Provided a systemic way of input feature-selection, ML model selection and hyperparameter optimization for emission modeling in hydrogen-fueled ICEs.

- **PART IV: Machine Learning in Transient Emission Modeling**

  – Comprehensive study of different methodologies for transient emission modeling in ICEs including SMM, QSSM, and TSM methodologies.

  – Developed transient BB and GB emission models for a hydrogen-diesel CI engine.

  – Introduced a method for systematic input feature-set selection using five different ML-based FS algorithms in combination with expert knowledge for transient emission modeling.

  – Presented a range of transient deep-learning emission models, each with varying degrees of complexity and computational requirements, to match the requirements of different applications with specific needs in terms of computational power and accuracy.

  – Developed BB deep-learning time-series emission models for tailpipe emission modeling using extensive real-driving dataset.

  – systematic study of the effects of dataset size and model complexity on the performance of the tailpipe emissions models.

  – Developed DL models for tailpipe emission prediction using different feature sets that can be used for a range of applications with different available input data from low to high level.

Chapter 2

Experimental Setups [1]

2.1 Compression Ignition Diesel Engine

To develop soot emission models for a CI diesel engine, a 4.5-L medium-duty Cummins diesel engine is used to collect soot emissions data. The engine specifications are listed in Table 2.1. This engine is located and tested in the University of Alberta internal combustion engine lab. Pictures and the schematics of the experimental setup for soot emissions data collection are shown in Figure 2.1. Intake air pressure, engine speed, load, injected fuel amount, and fuel rail pressure are recorded from the engine ECU. To record these data, the Cummins INLINE6 interface is used to connect ECU to the computer, and INSITE Pro Cummins is used to record and monitor data. A Kistler piezoelectric pressure sensor and Pico current clamp are used to measure the in-cylinder pressure and the injector command signal to one cylinder.

To measure soot emissions, a Pegasor Particle Sensor (PPS-M) is used. The schematic of the soot measurement setup is also shown in Figure 2.1b where engine-out exhaust gas flows through an inlet heater line to the pre-charger. The pre-charger is used to avoid any charge-related problem in soot measurement [173]. The pre-charger is essential to the accuracy of soot measurement as in recent emission technology, microscopic particles in the exhaust may be strongly charged. The Pegasor Pre-Charger is a self-heated, non-radioactive, negative diffusion charger. Using an integrated ion

---

[1] This chapter is partially based on [1–6]

40

Table 2.1: Diesel Engine specifications.

Parameter	Value
Engine name	Cummins QSB4.5
Engine type	In-Line, 4-Cylinder
Displacement	4.5 L
Bore × Stroke	102 mm × 120 mm
Peak torque	624 N.m @ 1500 rpm
Peak power	123 kW @ 2000 rpm
Aspiration	Turbocharged and Charge Air Cooled
Certification Level	Tier 3/Stage IIIA

trap, Pegasor can eliminate ions and small charged particles from the sample line gas and it charges larger particles into a known negative charge state. The sampling rate of PPS-M is 100 Hz with 100 dB Sensor to Noise Ratio (SNR). This sensor detects particle sizes in the range of $[0.001, 290]$ [mg/m^3]. The main PPS-M sensor's specifications are listed in Table 2.2.
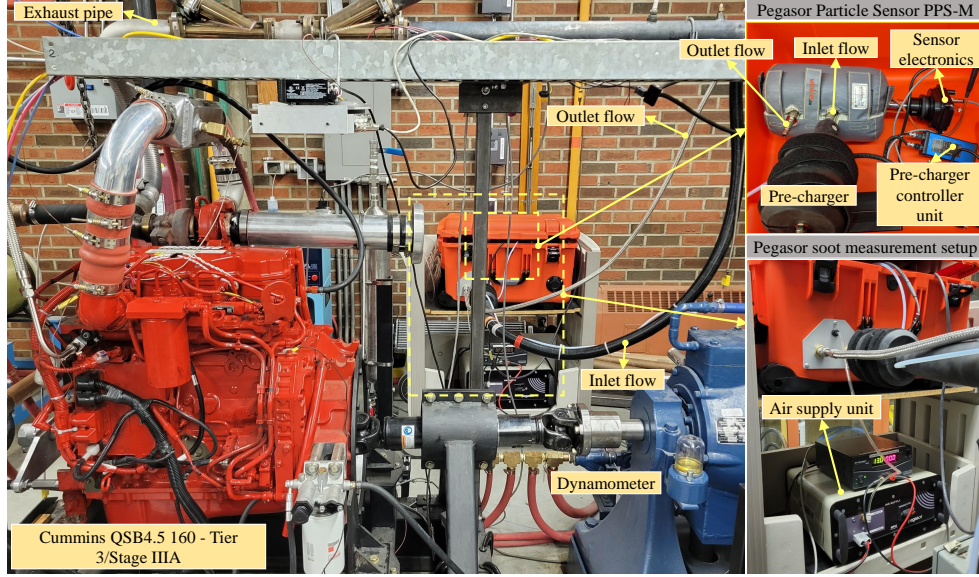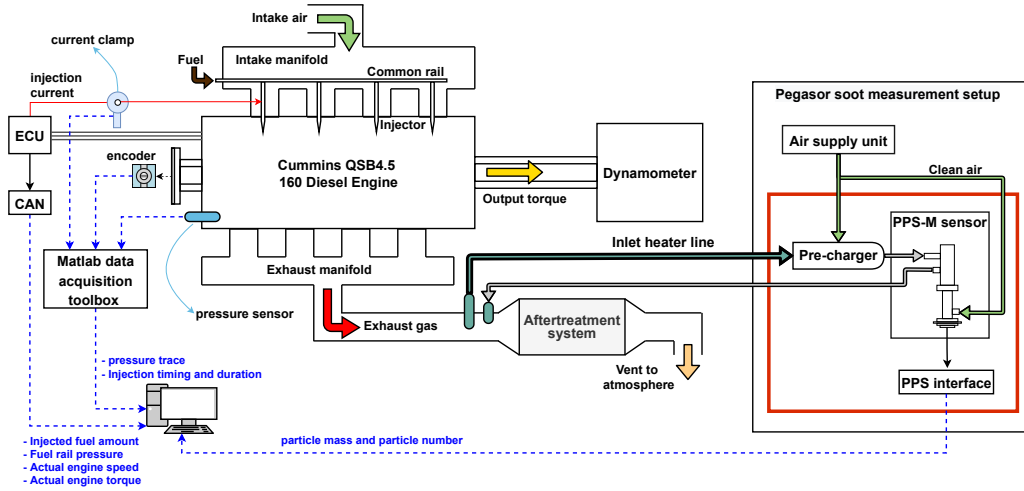
Figure 2.1: Diesel engine with soot measurement experimental setup. a: Experimental setup, b: Schematic of experimental setup. Full load is 624 N.m at 1500 rpm.

Table 2.2: The PPS-M sensor specifications.

Parameter	Value
Sensor temperature	200 °C
Extracted sample temperature	-40 up to 850 °C
Dilution	No need
Time response	0.2 s
Measured particle size range	10 nm and up
Trap voltage	60 V (10 nm lower cut) 400 V (23 nm lower cut , default) 2 kV (90 nm lower cut)
Particle number range	300 up to 10^9 1/cm^3
Particle mass range	10^{-3} up to 300 mg/m^3
Sample pressure	-20 kPa to $+100$ kPa
Clean air/Nitrogen supply	10 LPM @ 0.15 MPa
Operating voltage	24 V
Power consumption	6 W

2.2 Spark Ignition Hydrogen Engine

Table 2.3 shows the main characteristics of the SI hydrogen engine. The SI hydrogen engine is based on a 2 liter single-cylinder diesel engine, which was modified to burn hydrogen, by installing 6 hydrogen injectors, a spark plug and reducing the compression ratio. The hydrogen is injected into the intake manifold using 6 ring-shaped injectors with an injection pressure of 9 bar. These injectors are originally designed for natural gas injection. Also, a flame arrester system is installed between the hydrogen injectors and the combustion chamber to prevent mixture backfire from the combustion chamber to the intake manifold. Figure 2.2 shows the schematic of the experimental setup and pictures of different components of the SI hydrogen engine. More information about this engine and the experimental setup can be found in [174].

Table 2.3: Hydrogen spark ignition engine characteristics.

Characteristic	Spark Ignition
Fuel	Hydrogen
Number of cylinders	1
Displacement volume	2 Liter
Stroke	142 mm
Bore	128 mm
Compression ratio	8.5
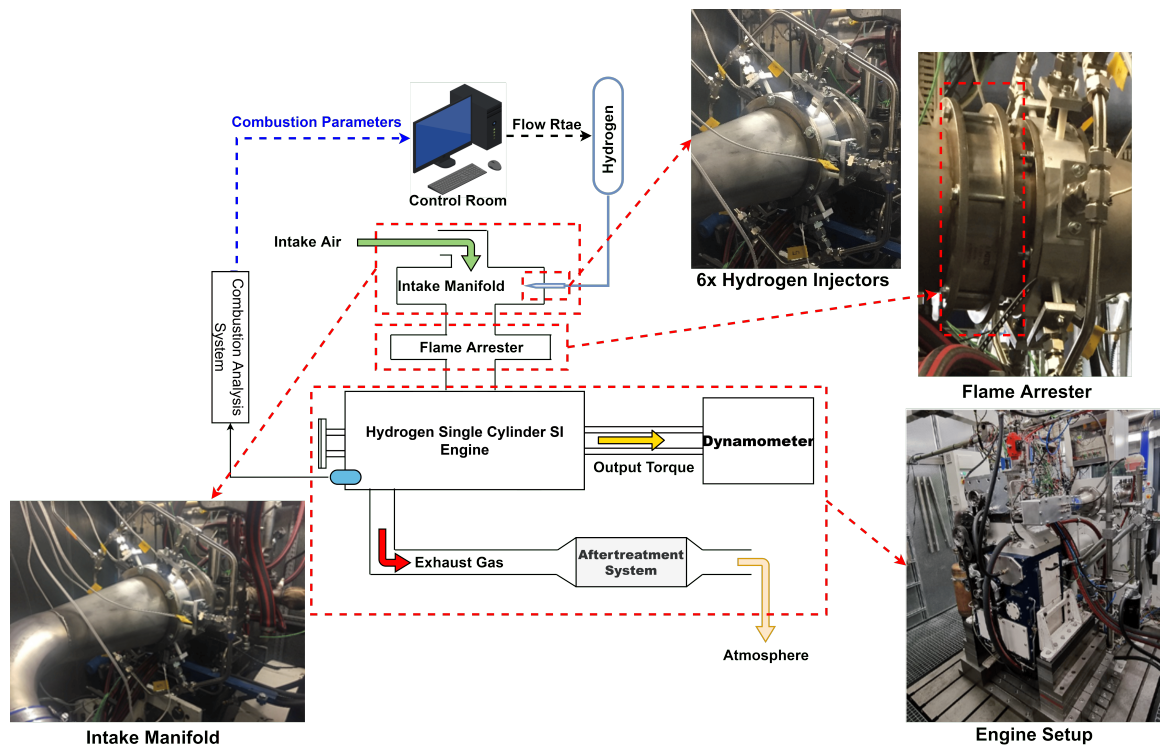
Figure 2.2: Hydrogen spark ignition engine experimental setup [174].

2.3 Compression Ignition Hydrogen-Diesel Engine

The CI diesel engine discussed in Section 2.1 was modified by adding a hydrogen injector to the intake port of one cylinder, transforming that cylinder into a dual-fuel hydrogen-diesel combustion. To accurately measure the emissions from the dual-fuel operation, sensors have been installed on a separated exhaust of the dual-fuel cylinder, while the other cylinders continue to operate on diesel fuel only. The injection timing of the hydrogen is precisely coordinated with the valve timing of the target cylinder to ensure all of the injected hydrogen goes to the target cylinder. Figure 2.3 shows the schematic and pictures of different components of the dual-fuel hydrogen-diesel engine experimental setup. The properties and specifications of the NOx sensor used for measuring NOx emissions are provided in Table 2.4 with more details on the sensor is available in [175–178]. The soot sensor is similar to the one introduced in the diesel-hydrogen compression ignition section. To control combustion, this diesel engine employs two diesel injection pulses - a short pilot injection and a longer main diesel injection. Figure 2.4 shows the adjusted injection setting for this engine. The control injection parameters in the experimental tests are: i) the crank angle at the start of injection for pulse 1 (SOI_{D1}), ii) the crank angle at the start of injection for pulse 2 (SOI_{D2}), iii) the duration of injection for pulse 2 (DOI_{D2}) which affects the diesel injection amount, and iv) the duration of hydrogen injection (DOI_{H2}) which affects the hydrogen injection amount. While the duration of diesel injection pulse 1 was kept constant (DOI_{D1}), the input ranges for SOI_{D1} and SOI_{D2} were adjusted to ensure that the diesel injection pulses did not overlap. This experimental setup was used for measuring steady-state and transient emission data.
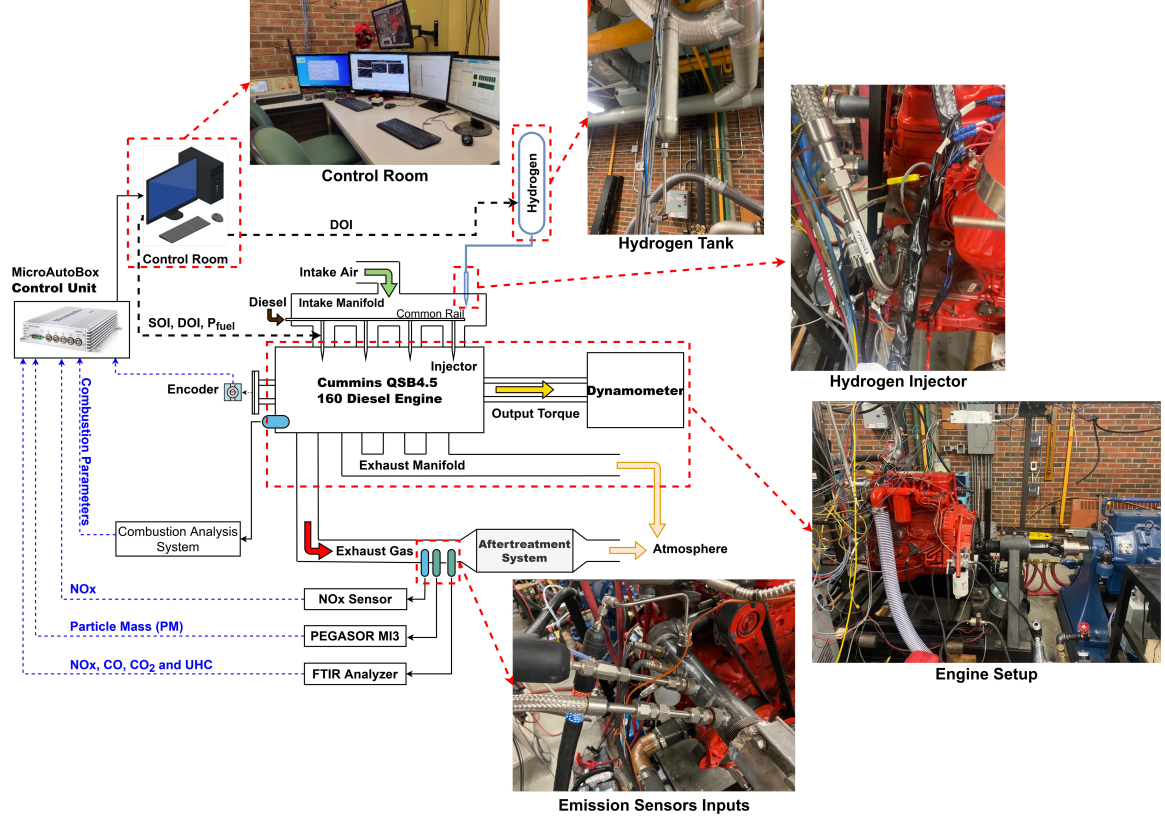
Figure 2.3: Dual-fuel compression ignition hydrogen-diesel engine experimental setup. SOI, DOI and P_{fuel} stands for start of injection, duration of injection, and fuel pressure, respectively. Full load is 624 N.m at 1500 rpm.
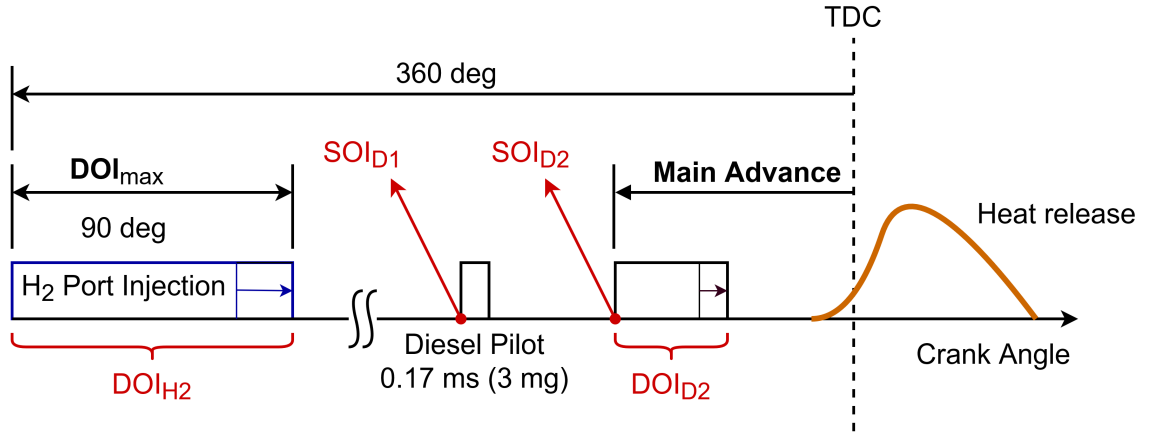
Figure 2.4: Hydrogen and diesel injection setting for hydrogen-diesel engine. Injection control parameters are shown in red. SOI_{D1} is the crank angle at the start of injection for diesel pulse 1, SOI_{D2} is the crank angle at the start of injection for diesel pulse 2, DOI_{D2} is the duration of injection for diesel pulse 2, and DOI_{H2} is the duration of hydrogen injection.

Table 2.4: ECM NO$_x$ sensor specifications

Sensor name	ECM-06-05
Range	NO$_x$: 0 to 5000 (ppm), λ (Lambda): 0.40 to 25, AFR: 6.0 to 364, O$_2$: 0 to 25 (%)
Accuracy	NO$_x$: $\pm$ 5 ppm (for 0 to 200 ppm), $\pm$ 20 ppm (for 200 to 1000 ppm), and $\pm$ 2.0 % (elsewhere)
Response Time	Less than 100 ms
Fuel Type	Programmable H:C, O:C, N:C ratios, and H$_2$
CAN	High Speed according to ISO 11898
Environment	-55 to +125 C for the module, 950 C (maximum continuous) for the NOx NO$_x$

2.4 Tailpipe Heavy-Duty Diesel Truck

The vehicle utilized in this study is a 2019 Peterbilt 579 trailer tractor, classified as a Class 8 truck. It features an Eaton automated 12-speed transmission, a 13,200 lbs. Meritor steering axle, and a 40,000 lbs. Meritor (forward and rear) rear axle. Figure 2.5 displays the truck's dimensions, consisting of a tractor and a 53-ft trailer. The shape and dimensions of the truck influence the truck air drag and fuel consumption.

The truck is equipped with a Cummins X15-Efficiency, 14.9 liter engine, which is certified as compliant to the US EPA Tier III emission regulations. Table 2.5 presents the primary characteristics of the truck engine used in this study.

Furthermore, a Single-Module™ after-treatment system was attached to the engine to reduce harmful exhaust emissions in order to ensure that emission regulations are met. The after-treatment system consists of 3 components: Diesel Oxidation Catalyst (DOC), Diesel Particulate Filter (DPF), and SCR. The DOC is the first device in the after-treatment system. It aids in the oxidization of the carbon monoxide and carbon oxides and the reduction of the Particulate Matter (PM). The DPF is placed behind the DOC to capture PM. The SCR converts the NOx and urea mixture into harmless nitrogen gas (N_2) and water vapor. Table 2.6 displays the operating temperature of three components in the after-treatment system.

Figure 2.6 presents the schematic and images of the truck, experimental measurement setup, and its various components, including the engine, after-treatment system, sensors, and Data Acquisition (DAQ) system. The custom-designed DAQ system was built to collect, save, and time-synchronize data from various subsystems. It includes safeguarding data, remote live monitoring of the system, and multiple data recording capabilities.

Table 2.5: Cummins ISX15 heavy-duty Engines' characteristics. hp stands for horse power, bhp stands for break horse power

Item	Description
Turbocharger	VGT Turbocharger
Fuel	Diesel
Number of cylinders	6
Displacement volume	14.9 Liter
Rated power	336 kW
Rated torque	2373 N·M
Governed speed	1800 rpm
Emission standard	US EPA Tier III emission regulations of 2017 (0.2 g/bhp-hr)

Table 2.6: Operating temperature of three components in the after-treatment system

Component	Operating temperature
DOC	260 to 399 °C
DPF	482 to 649 °C
SCR	Over 150 °C

(a) (b)
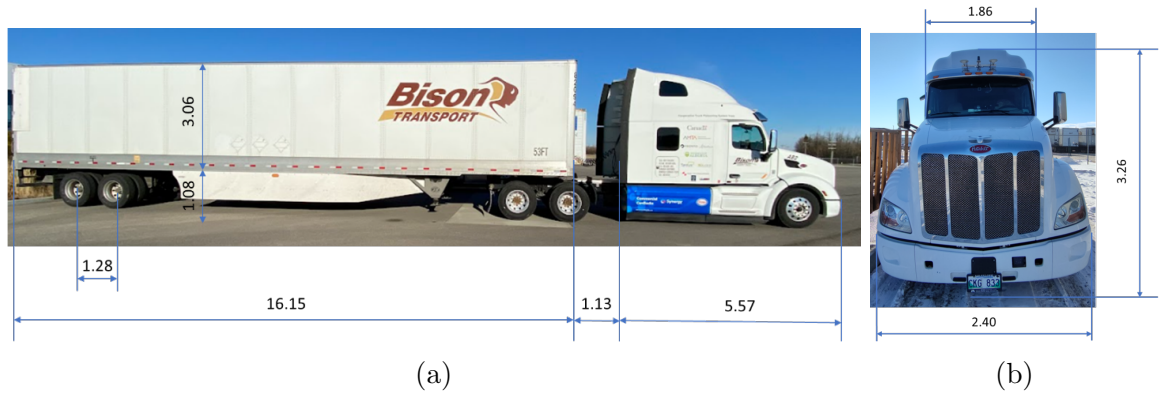
Figure 2.5: The tractor and trailer dimensions in meter
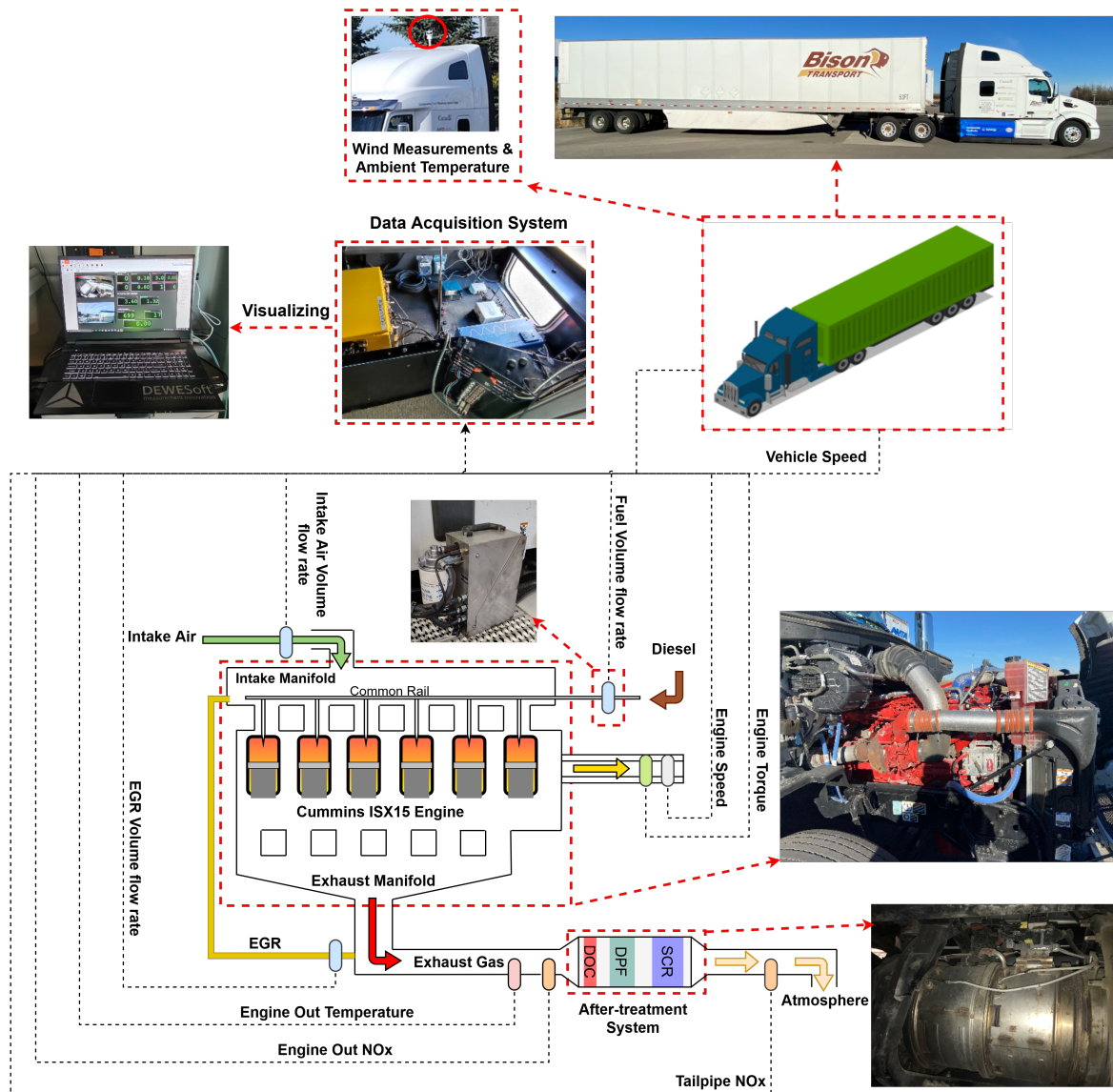
Figure 2.6: Schematic of the truck and experimental measurement setup of the heavy-duty diesel truck

2.5 Summary of chapter

This chapter provided the details of the experimental setups including CI diesel engine, SI hydrogen engine, CI hydrogen-diesel engine, and the tailpipe emission measurement setup for the heavy-duty truck. The first three setups are stationary setups located in the engine laboratories and were used to measure engine-out emissions, whereas the truck experimental setup is tested on the road to assess real-world tailpipe emissions. In the subsequent sections, data gathered from these setups will be employed to develop steady-state and transient emission models.

PART II: Machine Learning in Laminar Flame Speed Modeling

Chapter 3

Machine Learning Laminar Flame Speed Modeling for Low Carbon Fuels [1]

Artificial Neural Network (ANN) and Support Vector Machine (SVM) methods are designed to accurately predict Laminar Flame Speed (LFS) over the entire engine operating range for Ammonia (NH_3), Hydrogen (H_2), and Methanol (CH_3OH) fuels. These are promising zero-carbon or low-carbon alternative fuels for the transportation sector but require combustion models to optimize and control the engine performance. The developed Machine Learning (ML) methods provide an LFS prediction that requires several orders of magnitude less computation time than the original thermo-kinetic combustion mechanisms but has similar accuracy. Then an SVM and an ANN LFS model for blends of the three fuels are developed by combining LFS datasets of different fuels. Results show that for single fuels, ANN has better performance than SVM and can predict the LFS with a correlation coefficient R^2_{test} higher than 0.999. For fuel blends, SVM has better performance with R^2_{test} close to 0.999. These predictive ML LFS models can be integrated into 0D and 1D engine models and their low computation time makes them useful for engine development and for future model-based combustion control applications.

---

[1] This chapter is based on [1]

3.1 Methodology

This Chapter consists of two main parts. First, appropriate combustion mechanisms are selected [55, 62, 63] and validated using the available experimental data. Then, LFS is calculated using these combustion mechanisms for different fuels and combinations of fuels under varying physical conditions (temperature, pressure), and for different fuel-air equivalence ratio and EGR ratios. Two ML models (ANN and SVM) are trained and optimized using the created LFS simulation dataset. With the procedure shown in Figure 3.1, GT Power software is used in two steps. First, it provides an initial domain size by estimating flame thickness. Then, the advanced combustion toolset (ACT) of GT Power software calculates LFS based on the inputs.
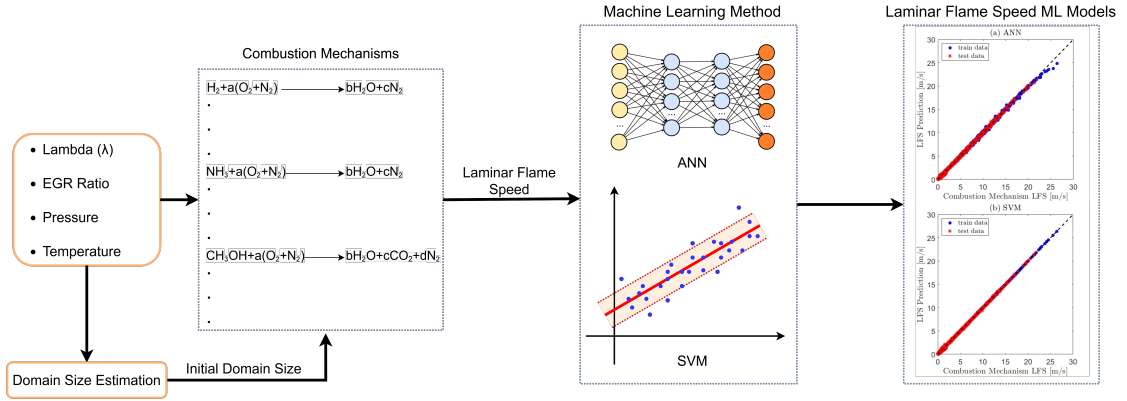
Figure 3.1: Laminar flame speed modeling process (Lambda=1/Equivalence Ratio)

3.1.1 Laminar flame speed calculation using combustion mechanisms

For LFS simulations, the first step is selecting fast and accurate thermo-kinetic combustion mechanisms. Different combustion mechanisms for the three fuels of H_2, CH_3OH and NH_3 were tested to select the best one because of the trade off between accuracy and computation time. Since it is not experimentally possible to measure LFS for high temperatures and pressures that represent the complete range of engine in-cylinder gas conditions, the combustion mechanisms are validated with the avail-

able experimental data which only includes part of engine in-cylinder gas conditions. The Mean Relative Error (MRE) for each mechanism is shown in Table 3.1 and shows that for a given fuel the MRE is within 1%. Thus, the mechanism with the lowest computation time for each fuel was chosen. Computation time is an important factor because of the high number of simulated cases in this study.

Table 3.1: Combustion mechanism for H_2, CH_3OH and NH_3 fuels. "Other fuel" column shows whether the combustion mechanism is able to predict LFS for other fuels. The selected combustion mechanism for each fuel in this study is shown with "*". MRE stands for mean relative error.

Fuel	Combustion Mechanism	Number of Species	Number of Reactions	Other Fuels	Run Time (s)	MRE (%)	Experimental Data for Validation
H_2	A. Keromnes, et al. [55]*	15	48	-	4	9.5	[54]
	RuiLi, et al. [179]	28	213	NH_3	480	9	
	San Diego mechanism [180]	58	270	CH_3OH	660	8.8	
CH_3OH	Christoffer Pichler, et al. [181]*	18	55	H_2	8	3.5	[59, 60]
	San Diego mechanism [180]	58	270	H_2	660	3.4	
	J. Beeckmann, et al. [60]	107	374	H_2	1200	3.2	
NH_3	Junichiro Otomo, et al. [63]*	32	212	H_2	600	9	[56, 58]
	KP Shrestha, et al. [182]	125	1094	H_2 and CH_3OH	3900	8.1	
	KP Shrestha, et al. [56]	125	1094	H_2 and CH_3OH	3900	8.1	

All the combustion mechanisms in Table 3.1 are tested for P=1 atm, T= 300 K, EGR=0, and Lambda=1 for the related fuels. These simulations were processed with Intel® Xeon® CPU E3-1245 V2 @ 3.40 GHz processor and 32 GB RAM and the run times for each of the combustion mechanisms are listed in Table 3.1. There is a direct

relationship between computation time and the number of species and the number of reactions, while the number of reactions has a higher impact on the computation time, compared to the number of species. Generally, NH_3 combustion mechanisms are much more detailed and require higher computational time than CH_3OH, and H_2. For this reason, a smaller DOE size is selected for NH_3 compared to H_2 and CH_3OH. This is explained in more detail in the next section. As seen in Table 3.1, all of the combustion mechanisms are able to predict LFS for H_2. Combustion mechanisms [56, 182] are able to predict the LFS for each of the three fuels and their blends, but they have the largest number of species and reaction among all of the combustion mechanisms which results in the highest computation time. Figures 3.2 to 3.4 show the validation of the combustion mechanisms of H_2, CH_3OH and NH_3 with experimental data.
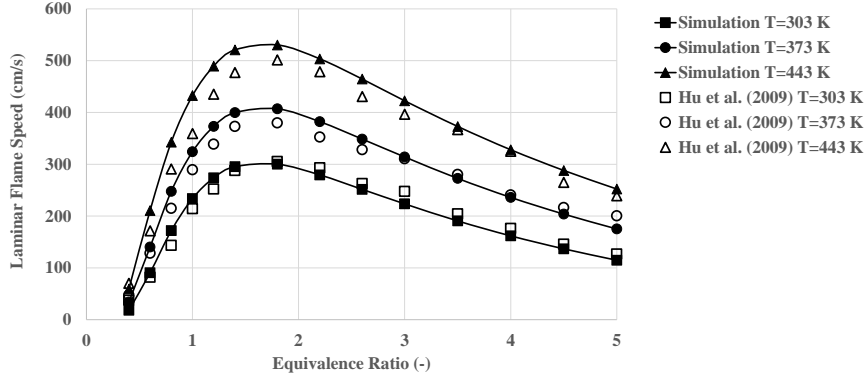
Figure 3.2: Hydrogen laminar flame speed validation for P=1 bar and EGR=0. The combustion mechanism is from [55], and the experimental data is from [54]. Mean relative error=9.5%.

Figure 3.4 also includes validation for blends of H_2 and NH_3. As seen in Figure 3.2-3.4, all of the selected combustion mechanisms have acceptable accuracy for LFS prediction with MRE less than 10%, which is appropriate for the purpose of LFS modeling for engine 0D or 1D simulations. After creating LFS datasets using the selected combustion mechanism, 80% of the LFS dataset for each fuel was selected randomly and used as the training data to develop and optimize the ML model.
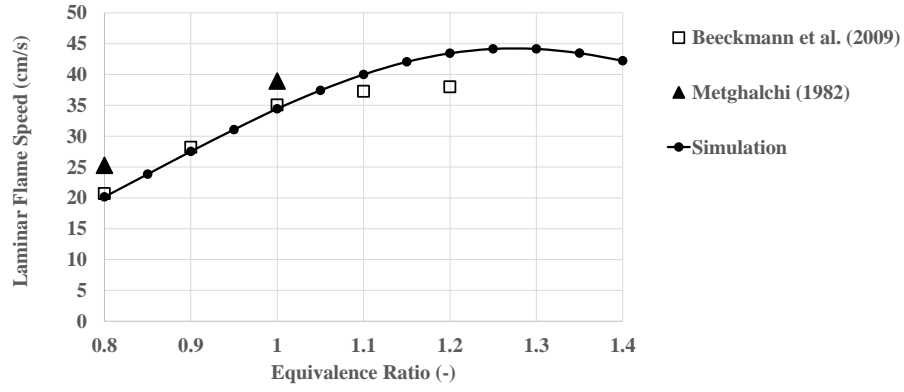
Figure 3.3: Methanol laminar flame speed validation for P=10 bar, T=373K and EGR=0. The combustion mechanism is from [181], and the experimental data is from [59, 60]. Mean relative error=3.5%.

The remaining 20% of the dataset was used as the test data to evaluate the model performance.
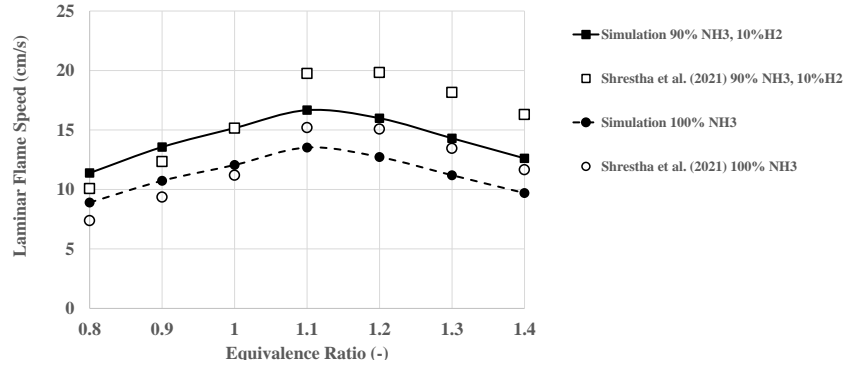
(a)
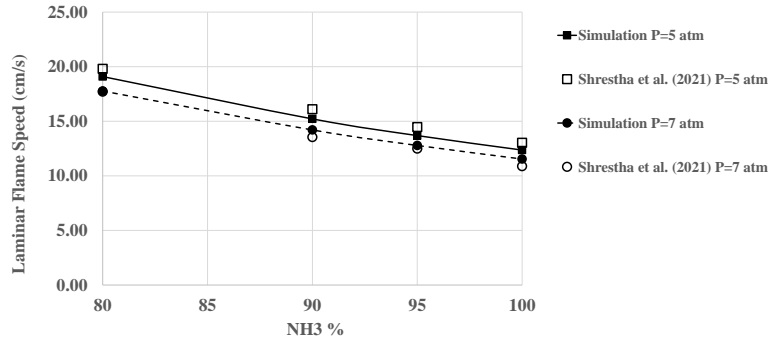
(b)

Figure 3.4: Ammonia and blends of ammonia and hydrogen laminar flame speed validation for EGR=0. a) Pressure =3 bar, b) Equivalence ratio=1. The combustion mechanism is from [63], and the experimental data is from [56]. Mean relative error=9%

.

3.2 Machine Learning Methods

The Machine learning methods that are used in this chapter are briefly described here. A regression model is a function in the form of, $\hat{y} = h_\theta(x_i)$, is fitted to given training set $\mathcal{D}_{train} = (x_i, y_i)$ in a way that $\hat{y}$ converges to y_i subject to given constrains. Here, x_i is the input feature set, y_i is the output set [2], and θ is the parameter set. The parameter set can be calculated by solving the cost function optimization problem

$$\min_\theta J(\theta) \quad \text{subjected to} \quad \phi(\theta) \tag{3.1}$$

where $J(\theta)$ is the cost function and $\phi(\theta)$ is the constraint function. The constraint function depends on the ML method. The cost function here is:

$$J(\theta) = \bar{J}(\theta) + \lambda L(\theta) \tag{3.2}$$

Where λ is the regulatory parameter used to control the bias-variance trade off [3]. The regularization term $L(\theta)$ is defined as

$$L(\theta) = \sum_{i=1}^{m} (\theta)^2 \tag{3.3}$$

3.2.1 Hyperparameter Optimization

Hyperparameters of an ML method should be optimized in order to achieve the highest level of accuracy. Different ML methods have different hyperparameters. The optimum hyperparameters values for a ML algorithm A_Λ which has N hyperparameters of $\Lambda = H_1, H_2, ..., H_N$, can be calculated by solving an optimization problem in the form of [183]

$$\Lambda^* = \arg\min_\Lambda V(h_\theta(x_i), \mathcal{D}_{train}, \mathcal{D}_{valid}) \tag{3.4}$$

where $V(h_\theta(x_i), \mathcal{D}_{train}, \mathcal{D}_{valid})$ estimates model performance using A_Λ for the training set $\mathcal{D}_{train}$ and the validation set $\mathcal{D}_{valid}$ for x_i as the input.

Bayesian optimization [184] is used for the optimization of the hyperparameters of the designed SVM and ANN models. This algorithm aims to minimize a scalar objective which here is minimum square error. There are three primary elements in this minimization: i) Gaussian process model $f(x)$, ii) A Bayesian update process to modify the Gaussian process model on each subsequent evaluation of $f(x)$ and iii) Acquisition function $a(x)$ which should be based on the Gaussian process model of $f(x)$. The next point x for evaluation is determined by maximizing $a(x)$. The algorithm optimization process starts with evaluating $y_i = f(x_i)$ for the number of seed points (x_i), randomly selected within the variable bounds. Then, at each iteration, the Bayesian algorithm updates the model with new hyperparamters values to obtain a posterior distribution over functions $Q(f|x_i, y \; for \; i = 1, ..., N)$. Here, N is the number of hyperparameters. Then new point x is found in a way that maximizes the acquisition function $a(x)$. Here, expected improvement (EI) is used as the acquisition function which is defined as:

$$\text{EI}(x, Q) = E_Q[max(0, \mu_Q(x_{best}) - f(x))] \tag{3.5}$$

where x_{best} and $\mu_Q(x_{best})$ are the location and the lowest value of the posterior mean, respectively. Q and x are posterior distribution over function $f(x)$ and x is the new point.

SVM method

SVM is a widely used ML methods that solves a convex quadratic programming problem in order to determine a correlation between inputs and outputs [185]. Due to the reliance on a kernel functions, SVM regression is a non-parametric technique. In SVM method, the cost function is defined as

$$J(\theta) = \frac{1}{2} \sum_{i=1}^{m} \theta_i^2 + C \sum_{i=1}^{m} (\zeta_i^+ + \zeta_i^-) \quad \text{subject to} \quad \phi(\theta) \tag{3.6}$$

where ζ_i^- and ζ_i^+, are slack variables that act as a penalty term which is weighted by parameter C which is called the box constraint. Large values of C result in stricter separation. For the SVM method, the constraint function $\phi(\theta)$ is:

$$\phi(\theta) = \begin{cases} y_i - h_\theta(x_i) \leq \epsilon + \zeta_i^+ \\ h_\theta(x_i) - y_i \leq \epsilon + \zeta_i^- \\ \zeta_i^-, \zeta_i^+ \geq 0 \end{cases} \tag{3.7}$$

where ϵ is the maximum absolute error across all of the training data [3]. In SVM, instead of using training data directly for the trainig of the model, a kernel function $K(x_i)$ is used, so the general form will be $\hat{y} = h_\theta(K(x_i))$ instead of $\hat{y} = h_\theta(x_i)$. Using a kernel function increases the feature set dimension and does not change the cost function. Different kernels including linear, polynomial, and Gaussian RBF kernels are often used in the SVM method. These kernels functions are defined as

$$K(x_i, x_j) = \begin{cases} x_i^T x_j & \text{Linear} \\ (x_i^T x_j + c)^n & \text{Polynomial} \\ exp(-\gamma ||x_i - x_j||_2^2) & \text{Gaussian RBF} \end{cases} \tag{3.8}$$

For the polynomial function, n is the degree of polynomial while γ is the scale of RBF kernel for Gaussian RBF kernel function [186]. In this study, the optimal kernel type, and optimal values for λ, ϵ and C (box constraint) parameters are found using the Bayesian optimization method for each of the three fuels, H_2, CH_3OH, and NH_3.

ANN method

ANN includes a set of algorithms that consist of nodes or neurons which are connected to each other with different weights. These algorithms are meant to resemble the neurons in a biological brain. In the simplest form, an ANN consists of these three layers; an input layer, a hidden layer and an output layer network. The complexity of an ANN model depends on the number of hidden layers and hidden neurons. Following Equations (3.2) and (3.3), the cost function of an ANN method is:

$$J(\theta) = \sum_{i=1}^{m} (h_\theta(x_i) - y_i) + \frac{\lambda}{2} \sum_{N=1}^{K-1} \sum_{i=1}^{s_k} \sum_{j=1}^{s_{k+1}} (\theta_{j,i}^{(k)})^2 \tag{3.9}$$

where N is the number of total layers (input + output + hidden layer), s_k is the number of neurons in k^{th} layer, and m is the training set size [3]. The first term of the equation minimizes absolute error while the second term (loss function) is used to regularize the prediction. Input and output parameters represent the number of neurons in the first and last layers, respectively. The function that connects different layers together is called the activation function $a(x)$ and the typical activation functions are:

$$a(x) = \begin{cases} \max(0,\text{x}) & \text{ReLU} \\ \tanh(\text{x}) & \text{Tanh} \\ \frac{1}{1+e^{-x}} & \text{sigmoid} \end{cases} \qquad (3.10)$$

where ReLU stands for Rectified linear unit. The activation function (ReLU, tanh, sigmoid), the optimal number of hidden layers, the optimal number of hidden neurons in each hidden layer, and optimal values for λ that are hyperparameters of the model are found using Bayesian optimization for each fuel.

The developed models, along with hyperparameters of each ML method are summarized in Table 3.2.

3.3   Results and Discussion

The developed ML models for LFS prediction have four inputs: mixture temperature T_m, mixture pressure P_m, EGR ratio, and Lambda λ (Lambda=1/fuel-air equivalence ratio). A DOE was developed for each fuel by selecting the ranges and the intervals for inputs. Table 3.3 summarizes the ranges, intervals, and the total number of simulated operating points for each fuel. The ranges are selected based on actual working conditions for engines burning H_2, CH_3OH and NH_3 fuels. Hydrogen has a very high flame speed and burning rate and consequently burning rich mixture of hydrogen can cause engine backfire, pre-ignition, knocking and damage [37]. For methanol [187] and ammonia [188], rich combustion is rare in practice so lean combustion is the focus of this study. For selecting the interval (increment) of operating conditions, physical understanding of LFS and the expected dynamics is used. The complexity

Table 3.2: Optimization hyperparameters of ML-based laminar flame speed models. In this table λ is the regularization parameter, ϵ is the maximum tolerable deviation, and c is the box constraint. Values for all hyperparameters were found using the Bayesian optimization method

Fuel	Model	Opt. Method	Opt. Hyperparameters
H_2	ANN	Bayesian	Number of hidden layers=1
			Layers Sizes=201,
			Activation Function =ReLU,
			λ= 1.493e-07
	SVM	Bayesian	Kernel function= Gaussian,
			ϵ=0.0013,
			λ=1.2278,
			c= 2.6874
CH_3OH	ANN	Bayesian	Number of hidden layers=2
			Layers Sizes=67, 266,
			Activation Function =ReLU,
			λ= 2.48e-08
	SVM	Bayesian	Kernel function= Gaussian,
			ϵ=0.0052,
			λ=0.5604,
			c= 3.1292
NH_3	ANN	Bayesian	Number of hidden layers=3
			Layers Sizes=7, 2, 229,
			Activation Function =ReLU,
			λ= 1.168e-05
	SVM	Bayesian	Kernel function= Polynomial,
			ϵ=0.0081,
			λ=1,
			c= 0.001
H_2+CH_3OH+NH_3	ANN	Bayesian	Number of hidden layers=3
			Layers Sizes=33, 17, 299,
			Activation Function =ReLU,
			λ= 2.973e-07
	SVM	Bayesian	Kernel function= Gaussian,
			ϵ=0.0056,
			λ=0.7850,
			c= 792.7372

of the NH_3 combustion mechanism results in longer simulation computation time compared to CH_3OH and H_2, so larger intervals are chosen to reduce the number of

simulations. The solver did not converge or returned an LFS of zero (no-combustion) for less than 10% of the data points. These points were removed in a pre-processing step to remove bias in the training dataset due to zero LFS values and improve the ML model accuracy.

Table 3.3: Design of experiment for laminar flame speed of different fuels including total number of simulations. Lambda=1/Equivalence ratio. The thermo-kinetic combustion mechanisms are: H_2 [55], CH_3OH [181], and NH_3 [63].

Fuel	Parameters	Min	Max	Intervals	Number of Points
H_2	Lambda	1	4	0.1	79,794
	EGR Ratio	0	0.5	0.05	
	Pressure (bar)	30	200	10	
	Temperature (K)	600	1200	50	
CH_3OH	Lambda	1	4	0.1	67,518
	EGR Ratio	0	0.5	0.05	
	Pressure (bar)	30	200	10	
	Temperature (K)	600	1100	50	
NH_3	Lambda	1	4	0.2	3,456
	EGR Ratio	0	0.5	0.1	
	Pressure (bar)	30	190	20	
	Temperature (K)	600	900	100	

LFS comparisons of ML prediction versus combustion mechanism simulation results for H_2 (Figure 3.5), CH_3OH (Figure 3.6) and NH_3 (Figure 3.7), are shown. It can be seen that for the input ranges in Table 3.3, the LFS values for H_2, CH_3OH and NH_3 are less than 30 m/s, 3 m/s, and 0.3 m/s, respectively. This indicates that using H_2 as a fuel in ICE could lead to an LFS that is 10 times greater than that of CH_3OH and 100 times greater than LFS of NH_3 fuel. The much smaller range of LFS for NH_3 made it possible to achieve good model accuracy despite using a smaller

data set. The large difference in LFS values for these fuels explains their different combustion characteristics and should be considered in engine design, especially in dual fuel engines. The accuracy, error and timing for the three fuels and the two ML methods are summarized in Table 3.4, which shows that ANN outperform SVM for H_2, CH_3OH and NH_3. The LFS of these fuels can be predicted by either of the two ML methods (ANN or SVM) with a high level of accuracy ($R^2_{test} > 0.96$). A comparison of the maximum error values for test data in Table 3.4 indicates that the maximum error for ANNs is much lower than SVMs. For LFS prediction, this is very important as it is a measure of the reliability of the model by indicating the maximum error that could be obtained with the model. For H_2 LFS prediction, the maximum error for ANN is around 0.5 m/s, which means that in the worst case, the LFS prediction is 0.5 m/s off from the actual value, whereas for SVM, there is a worst case prediction error of 2.5 m/s. The ANN method for H_2 has a high run time because it has a high number of hidden neurons and SVM method for NH_3 has low run time because it was developed using a smaller dataset compared to other fuels. Comparing run times in Table 3.1 and Table 3.4, ML methods are much faster in LFS calculations than thermo-kinetic combustion mechanisms. For instance, using the same hardware, the ANN model predicts LFS for H_2 4,160,000 times faster than the fastest combustion mechanism [55], and for NH_3, the ANN model is 689,000,000 times faster than the fastest thermo-kinetic combustion mechanism [63] listed in Table 3.1.

When fueling an engine only with H_2, issues such as engine knocking tendency, safety, storage, and energy density must be overcome. Using a combination of H_2 with another fuel is an alternative. To maintain low CO_2, the second fuel should be an LCF (e.g. NH_3 and CH_3OH) depending on availability. Combining different fuels can affect the LFS value depending on the percentage of each fuel in the blended mixture. For blends of fuels, LFS calculations require a combined combustion mechanisms that include both the combustion mechanisms and cross-terms. This increases the computation time for the LFS calculation and provides further motivations to use ML
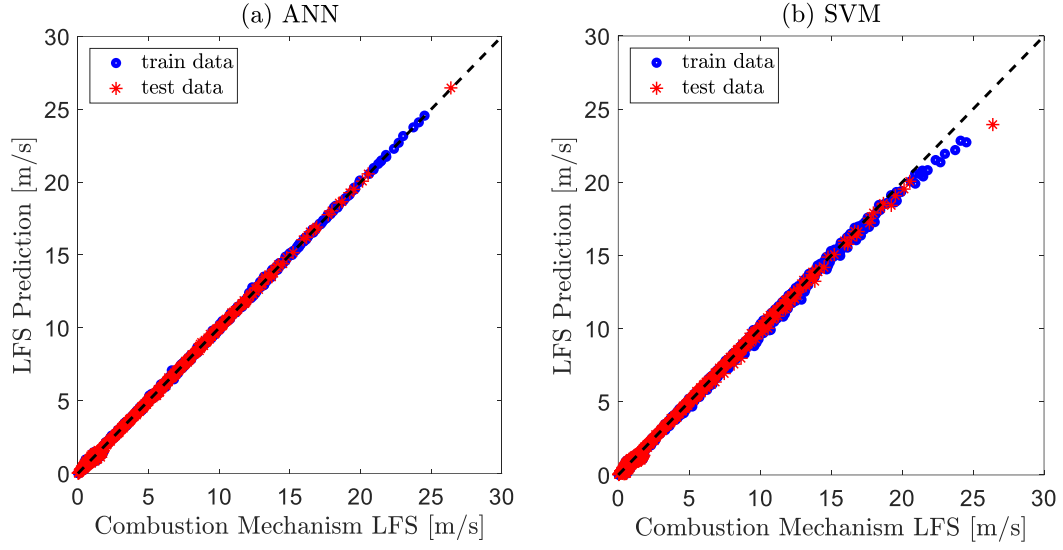
Figure 3.5: ANN and SVM models predictions versus simulations from combustion mechanisms for training and test data for $\underline{H_2 \text{ laminar flame speed}}$. $R^2_{\text{test, ANN}}$=0.9997, $R^2_{\text{test, SVM}}$=0.9986
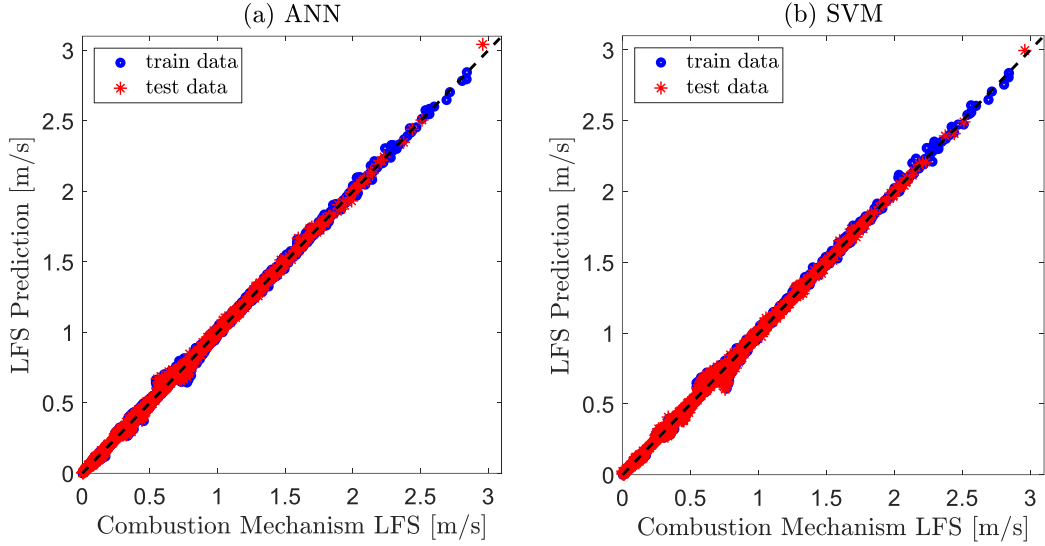
Figure 3.6: ANN and SVM models predictions versus simulations from combustion mechanisms for training and test data for $\underline{CH_3OH \text{ laminar flame speed}}$. $R^2_{\text{test, ANN}}$=0.9997, $R^2_{\text{test, SVM}}$=0.9995

methods when fast LFS prediction is needed. To predict LFS for a blend of fuels with a single ML method, the LFS model should be able to predict the LFS value for any combination of H_2, CH_3OH, and NH_3 with an acceptable accuracy. To do this the

67
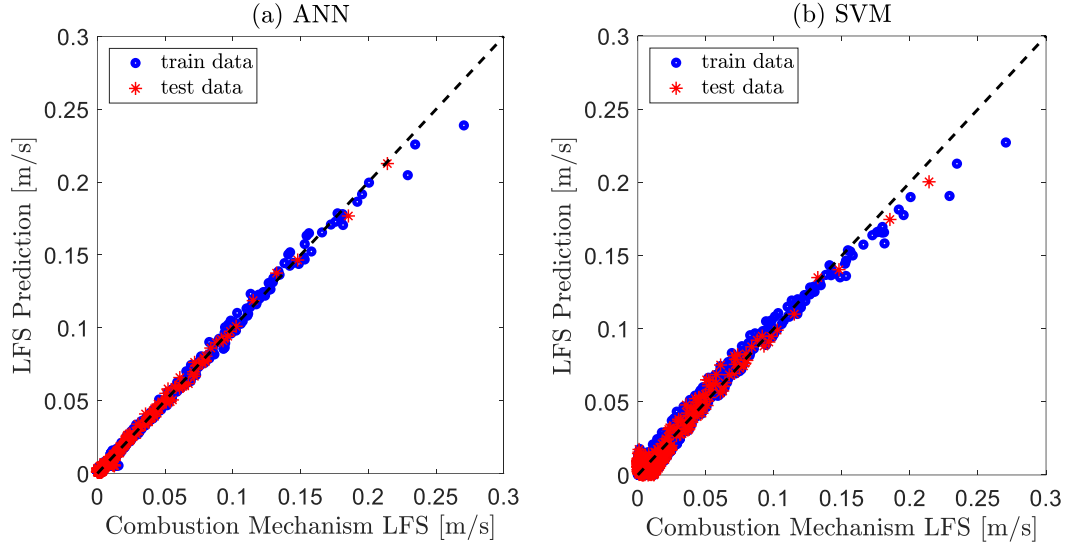
Figure 3.7: ANN and SVM models predictions versus simulations from combustion mechanisms for training and test data for $\underline{NH_3\ \text{laminar flame speed}}$. $R^2_{\text{test, ANN}}=0.9979$, $R^2_{\text{test, SVM}}=0.9658$

mass fraction of each fuel is added as an input to the model. This results in additional three inputs (hydrogen mass fraction M_{H2}, methanol mass fraction M_{CH_3OH}, and ammonia mass fraction M_{NH_3}) to the four existing inputs (temperature T_m, pressure P_m, Lambda λ, and EGR), making 7 inputs in total. A new simulation dataset is created by first combining H_2, CH_3OH, and NH_3 datasets and the ML model is made more accurate by augmenting data points that include blended fuels. Table 3.5 shows the DOE of the dual fuel datasets that are added to the single fuel datasets to train the ML algorithm. The developed ML algorithm could predict LFS for any combinations of these three fuels, but this algorithm was not trained with blends of CH_3OH, and NH_3 LFS data due to very high computation time (Table 3.1). So, the LFS prediction of this ML algorithm is only valid for LFS prediction of H_2, CH_3OH, and NH_3 as single fuels, and blends of H_2 with CH_3OH or NH_3 as dual fuels. The model prediction accuracy for blends of CH_3OH and NH_3 is not known.

The ML prediction versus combustion mechanism simulation results for LFS for the combination of H_2, CH_3OH and NH_3 as fuels are shown in Figure 3.8. Both ANN

and SVM models produce an accurate LFS prediction, but in contrast to Figure 3.5-3.7, it appears that SVM is slightly more accurate than ANN which is reflected in Table 3.4. The increased SVM accuracy is attributed to SVM method properties. Since the SVM method works by breaking data into separate categories [186], it can distinguish between the various fuels with greater precision. Datasets and ML codes for LFS prediction for combination of H_2, CH_3OH and NH_3 fuels are publically available via the link in the appendix.
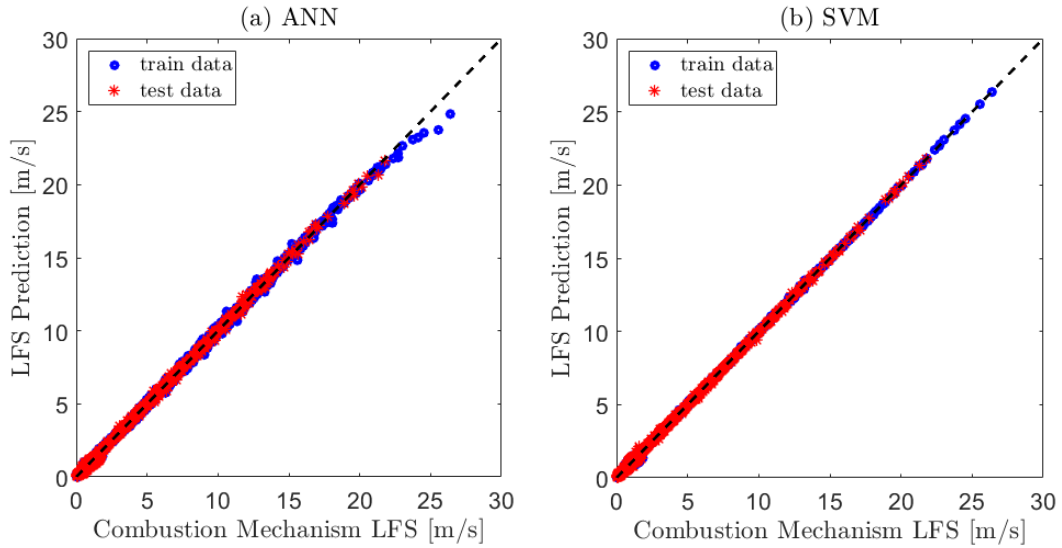
Figure 3.8: ANN and SVM models predictions versus simulations from combustion mechanisms for training and test data for H$_2$+CH$_3$OH+NH$_3$ laminar flame speed. $R^2_{\text{test, ANN}}$=0.9986, $R^2_{\text{test, SVM}}$=0.9989

The ML predictions versus combustion mechanism simulations for two dual fuels, 50% H$_2$-50% NH$_3$ and 50% H$_2$-50% CH$_3$OH for different values of pressure, temperature, EGR ratio and Lambda are shown in Figure 3.9. The results show that the LFS value has a reverse relationship with pressure, EGR ratio and it has a direct relationship with temperature and equivalence ratio value (reverse relationship with Lambda), which match the expected LFS physics. In addition, the ML and combustion mechanism LFS estimation follow the same trend in all subplots in Figure 3.9 and the deviation between them is less than 10% for more than 90% of the points.
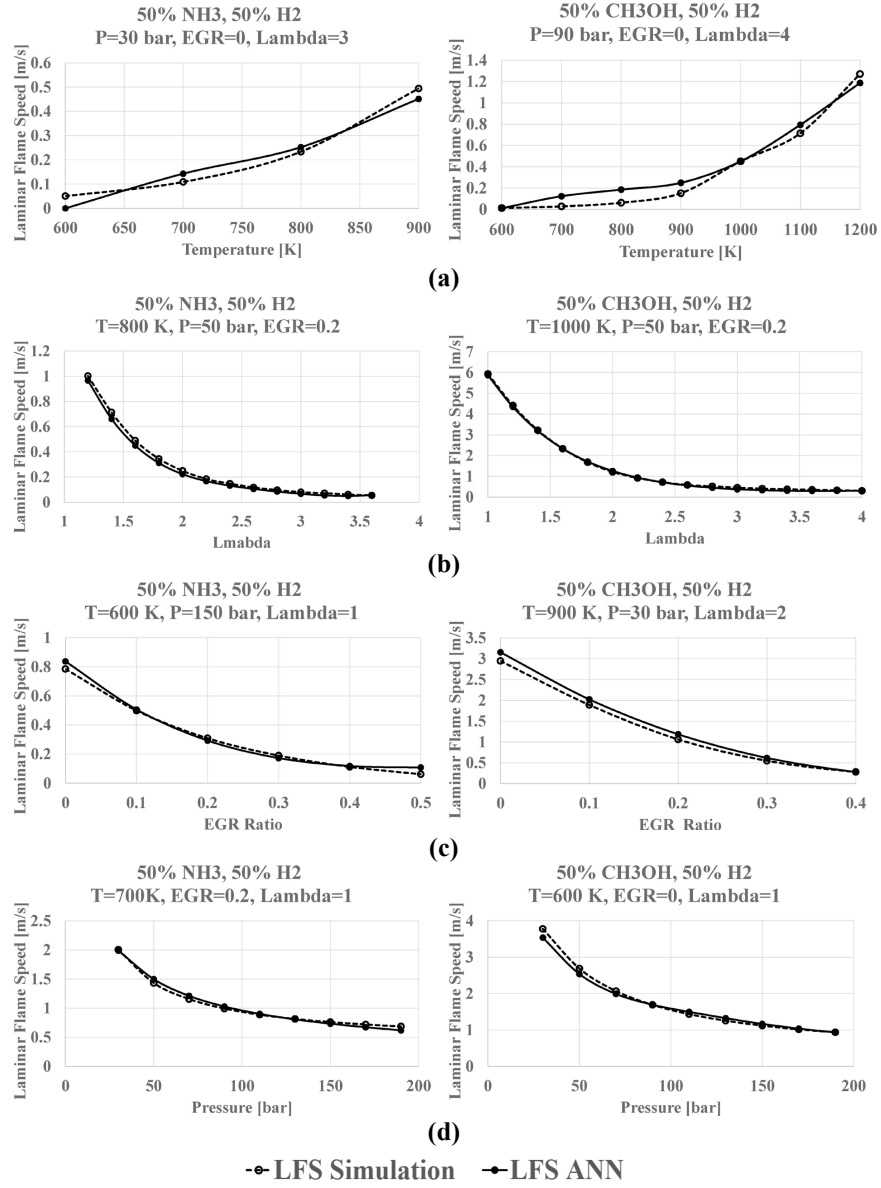
Figure 3.9: ANN model laminar flame speed validation over different parameters: (a) LFS as a function of temperature at constant pressure, EGR ratio and Lambda, (b) LFS as a function of Lambda at constant temperature, pressure and EGR ratio,(c) LFS as a function of EGR ratio at constant temperature, pressure and Lambda, (d) LFS as a function of pressure at constant temperature, EGR ratio and Lambda. Left column: 50% H_2 and 50% NH_3 as the fuel, right column: 50% H_2 and 50% CH_3OH as the fuel.

Table 3.4: ANN and SVM laminar flame speed models accuracy and error for different fuels

Fuel	Number of data points	Criteria	ANN	SVM
H$_2$	79,794	R$^2_{\text{train}}$	0.9997	0.9986
		R$^2_{\text{test}}$	0.9997	0.9986
		RMSE$_{\text{train}}$[m/s]	0.0400	0.0833
		RMSE$_{\text{test}}$[m/s]	0.0414	0.0848
		|E$_{\text{test,max}}$|[m/s]	0.5020	2.4459
		t$_{\text{run}}$[μs]	0.96	100.38
CH$_3$OH	67,518	R$^2_{\text{train}}$	0.9997	0.9997
		R$^2_{\text{test}}$	0.9997	0.9995
		RMSE$_{\text{train}}$[m/s]	0.0081	0.0076
		RMSE$_{\text{test}}$[m/s]	0.0081	0.0094
		|E$_{\text{test,max}}$|[m/s]	0.1301	0.1509
		t$_{\text{run}}$[μs]	1.57	31.91
NH$_3$	3,456	R$^2_{\text{train}}$	0.9978	0.9756
		R$^2_{\text{test}}$	0.9979	0.9658
		RMSE$_{\text{train}}$[m/s]	0.0019	0.0067
		RMSE$_{\text{test}}$[m/s]	0.0016	0.0067
		|E$_{\text{test,max}}$|[m/s]	0.0085	0.0165
		t$_{\text{run}}$[μs]	1.11	0.19
H$_2$+CH$_3$OH+NH$_3$	160,272	R$^2_{\text{train}}$	0.9987	0.9991
		R$^2_{\text{test}}$	0.9986	0.9989
		RMSE$_{\text{train}}$[m/s]	0.0634	0.0537
		RMSE$_{\text{test}}$[m/s]	0.0632	0.0568
		|E$_{\text{test,max}}$|[m/s]	0.6178	0.5977
		t$_{\text{run}}$[μs]	0.87	96.25

Table 3.5: Design of experiment ranges for H_2+NH_3 and H_2+CH_3OH combustion

Fuel	Parameters	Min	Max	Intervals	Number of Points
H_2+NH_3	Lambda	1	4	0.2	
	EGR Ratio	0	0.5	0.1	3,456
	Pressure (Bar)	30	190	20	
	Temperature (K)	600	900	100	
H_2+CH_3OH	Lambda	1	4	0.2	
	EGR Ratio	0	0.5	0.1	6,048
	Pressure (Bar)	30	190	20	
	Temperature (K)	600	1200	100	

3.4 Summary of chapter

The Laminar Flame Speed (LFS) is an important characteristics of the fuel-air mixture that is required for engine combustion models so it is essential that LFS estimation is accurate. Machine Learning (ML) methods, that require a fraction of the computation time compared with the original thermo-kinetic combustion mechanisms, were used to develop accurate models for predicting LFS of these three Low Carbon Fuels (LCFs): Hydrogen (H_2), Methanol (CH_3OH), Ammonia (NH_3), and for blends of these fuels.

To develop the ML model, an appropriate combustion mechanism for each of these three fuels were selected from the literature based on an accuracy-computation cost trade-off. Available experimental data was then used to validate LFS prediction for each combustion mechanism. Then the LFS model was integrated into the ACT package from GT Power software as the solver and the LFS was simulated by systematically varying the temperature, pressure, exhaust gas recirculation (EGR) ratio, and Lambda. Input ranges were chosen to cover a large range of engine in-cylinder gases at the end of compression and early combustion (temperature range 600-1300 K, pressure range 30-200 bar, EGR range 0-0.5, and Lambda range 1-4) resulting in 79794, 67518, and 3456 simulated data points for H_2, CH_3OH and NH_3 respectively. For these input ranges, LFS values for H_2, CH_3OH and NH_3 are found to be less than 30 m/s, 3 m/s, and 0.3 m/s, respectively. These datasets were used to train and optimize two ML methods, Artificial Neural Network (ANN) and Support Vector Machine (SVM), for each fuel. Results show that the two ML methods have accurate performance for all fuels, achieving $R^2_{\text{test}} > 0.96$ in all cases.

To get an LFS model for blends of these three single fuels the same process was followed but new dataset containing approximately 10,000 data points of blended fuels was augmented to the datasets from these three fuels. Using the combined new dataset, ANN and SVM algorithms were trained and optimized to create ML models

that could predict LFS for blends of fuels with varying mass fractions. For all the fuels tested, LFS showed an inverse relationship with pressure, EGR ratio and Lambda, but a direct relationship with temperature. It was found that ANNs perform better in predicting LFS for single fuels, while SVMs achieved a better result for predicting LFS for the fuel blends.

Very low computational time of the created LFS models in this Chapter allow their investigation into 0D and 1D engine models for engine development and for future model-based combustion control applications.

PART III: Machine Learning in Steady-State Emission Modeling

Chapter 4

Hybrid Emission and Combustion Modeling of Diesel Fueled Engines [1]

Development and analysis of diesel engine soot emissions modeling for control applications are presented in this chapter. Physical (white-box WB), black-box (BB), and gray-box (GB) models are developed for soot emissions prediction. Additionally, different feature sets based on the least absolute shrinkage and selection operator (LASSO) feature selection method and physical knowledge are combined to develop computationally efficient soot models with good precision. The physical model is a virtual engine modeled in GT-Power software that is parameterized using relevant experimental data. Different machine learning (ML) methods, including Regression Tree (RT), Ensemble of Regression Trees (ERT), Support Vector Machines (SVM), Gaussian Process Regression (GPR), Artificial Neural Network (ANN), and Bayesian Neural Network (BNN) are used to develop the BB models. The GB models include a combination of the physical and BB models. A total of five feature sets and eight different ML methods are tested. An analysis of the accuracy, training time and test time of the models is performed using the K-means clustering algorithm. It provides a systematic way for categorizing the feature sets and methods based on their performance and selecting the best method for a specific application.

---

[1] This chapter is based on [3]

4.1 Methodology

4.1.1 Experimental data

The experimental diesel engine shown in Figure 2.1 was tested for 219 engine steady state operating conditions over the full range of engine speeds and loads. Figure 4.1 shows a color map of raw soot emissions data with respect to engine speed (x-axis) and load (y-axis), where black dots represent experimental points. Since this engine is designed for stationary applications typically at 1800 rpm, it has limited operating conditions. Therefore, 219 data points in Figure 4.1 covers most of the desired operating conditions. For highway truck application due to various driving cycles, higher number of data-points is required [68].
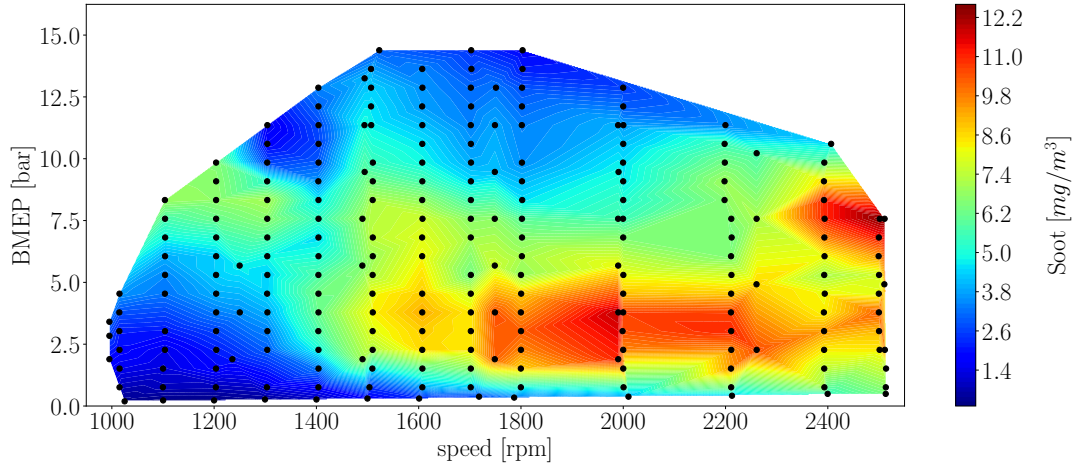
Figure 4.1: Engine-out soot measurements over speed and break mean effective pressure (BMEP) for the diesel engine.

The diesel engine used in this study has three injection pulses, and the third injection is active in 39% of the experimentally collected data. Another main fuel path feature that affects soot emissions is fuel rail pressure that used as a feature in soot emissions modeling. The majority of data are collected in fuel rail pressure from 700 to 1100 bar. The data collected from experiments in this study (219 points) broadly covers most of the operating conditions of the engine.

4.1.2 Gray-box and black-box models

The physics-based model (WB), BB, and GB are described in this section. The first step toward developing physics-based and GB models was developing and parameterizing the GT-Power physics-based model. GT power is a commercial software for modeling combustion engines. Physics-based modeling of the diesel engine is carried out using the GT power software, which contains several chemical and physical sub-models that simulate the complex engine combustion processes. DIpulse is a GT Power model that is used as the combustion model since it can be applied to multi-injection diesel combustion engine.

The Hiroyasu model [189] is used as the physics-based soot model. The model is calibrated by using 8% of the experimental data. The calibration process uses Genetic Algorithm (GA) NSGA-III [190] for multi-objective Pareto optimization as the search algorithm. The multipliers for combustion model are: Enterainment Rate Multiplier, Ignition Delay Multiplier, Premixed Combustion Rate Multiplier, and Diffusion Combustion Rate Multiplier. There are also these two multipliers in the soot model: the soot formation multiplier and the soot burn-up multiplier. The GAs minimize the deviation between the experimental and simulation in-cylinder pressure trace and soot emissions values to calculate the optimal multipliers. GA is the optimal choice for problems with different levels of complexity, because of its ability to explore a broad design space [190]. The two key inputs for GA are the population size and the number of generations. Here, two different GAs are used for combustion model calibration and soot model calibration. The population size is 16 for both algorithms but the number of generations for combustion model calibration and soot model calibration are 16 and 10, respectively, due to combustion model complexity and including more factors compared to the soot model. Figure 4.3 schematically shows how the soot model and combustion model multipliers are calculated using the GA-based algorithm. The GAs, based on the results obtained,

took into account experimental results of soot emissions and in-cylinder pressure traces for some optimization points. In this case, the calibration process for soot emissions and in-cylinder pressure trace was done separately using two different GAs.

The number of injection pulses and injection timing are important control inputs that affect soot emissions production in diesel engines [191]. There are three main pulses in the Cummins diesel engine injection system: Pulse I is pre-injection, Pulse II is the main injection, and Pulse III is post-injection which only occurs over a limited load range. Post injection plays a crucial rule in lowering soot emissions production by increasing the soot emissions burn rate [192].

The in-cylinder pressure trace for different load and speed conditions are shown as a function of crank angle (CAD) in Figure 4.2. Case I (136 [N.m] in 1200 [rpm]), case IV (271 [N.m] in 1800 [rpm]) and case VI (353 [N.m] in 2400 [rpm]) are selected from optimization points for model calibration (refer to Figure 4.3) while other cases are not used for calibration. The validation result for crank angle position where 50% of the heat is released (CA50), NOx, intake manifold pressure and maximum in-cylinder pressure are shown in Figure 4.4. The average error for CA50 and maximum in-cylinder pressure are up to approximately 2 CAD and 6% respectively, demonstrating that the physics-based model's matches the experiment.

To use ML for BB or GB models, input features should be selected. The process of selecting important features out of feature set is called feature selection (FS). FS reduces the size of input feature set which results in improving ML method performance. FS process is depicted schematically in Figure 4.3. A total of five feature sets are used in this study to simulate soot emissions. For FS in this work, a combination of physical insight and LASSO feature selection technique is used. For physics-based insight feature selection, the most significant features are selected based on an expert prior knowledge while LASSO feature selection offers a systematic way for feature selection regardless of prior knowledge of system.

Figure 4.2: Diesel engine physics-based model validation for six operating points.(Case I: 136 [N.m] in 1200 [rpm], Case II: 271 [N.m] in 1600 [rpm], Case III: 271 [N.m] in 1400 [rpm], Case IV: 271 [N.m] in 1800 [rpm], Case V: 271 [N.m] in 2000 [rpm], and Case VI: 353 [N.m] in 2400 [rpm]).

Figure 4.3: physics-based model calibration and feature selection process.

Two BB feature sets (that contain only experimental data) are: i) without any feature selection method (BB), and ii) BB + LASSO (BB + L). The GB features sets are: GB + PHYS, GB + L and GB + PHYS + L. In GB + PHYS, data-driven features are chosen solely based on physical insight into soot oxidation and

formation processes. With GB + L, the LASSO feature selection method selects the parameters. Finally, GB + PHYS + L first uses physical insight to select the most important features, then the LASSO feature selection method is applied to select the final features. The number of features for the five different methods and steps are summarised in Figure 4.3.

(a)   (b)   (c)   (d)
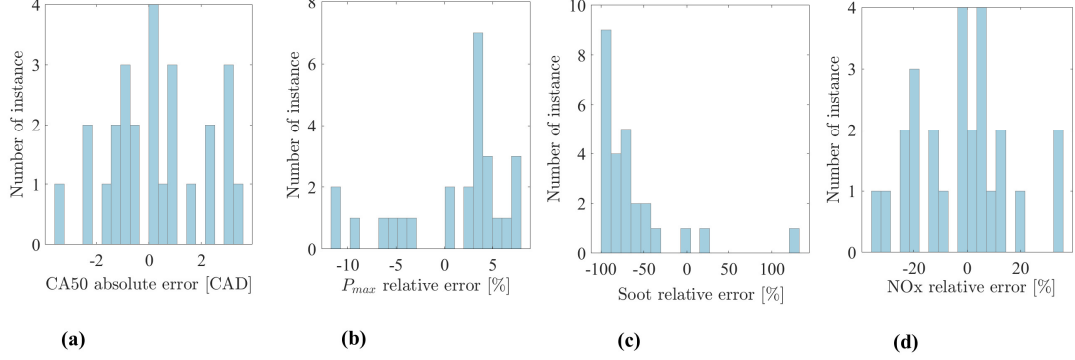
Figure 4.4: Histogram of error between physics-based model and experimental data for diesel engine. (**a**) CA50 absolute error [CAD], bin=0.36, (**b**) Maximum In-cylinder pressure (P_{max}) relative error [%], bin=1.25, (**c**) Soot emission relative error [%], bin=11.75 (**d**) NOx emission relative error [%], bin=3.64.

A schematic representation of BB and GB soot modeling is shown in Figure 4.5. The measured injection timing is used for the virtual engine. The GB and BB model inputs are similar to those shown in Figure 4.3, including injection properties (total mass of injected fuel, start of injection (SOI), fuel rail pressure), intake manifold pressure, BMEP, and engine speed. The K-means clustering algorithm is used for selecting the most suitable models and feature sets based on errors and timing (testing and training times). Two K-means clustering algorithms are applied (the first filter and the second filter). The first filter eliminates feature sets and models with low accuracy and slow training time and prediction time, whereas the second filter selects the best ML method along with feature sets in terms of accuracy and training and prediction cost for different applications. Finally, 12 soot models are chosen in total, which will be described in detail in section 4.3.
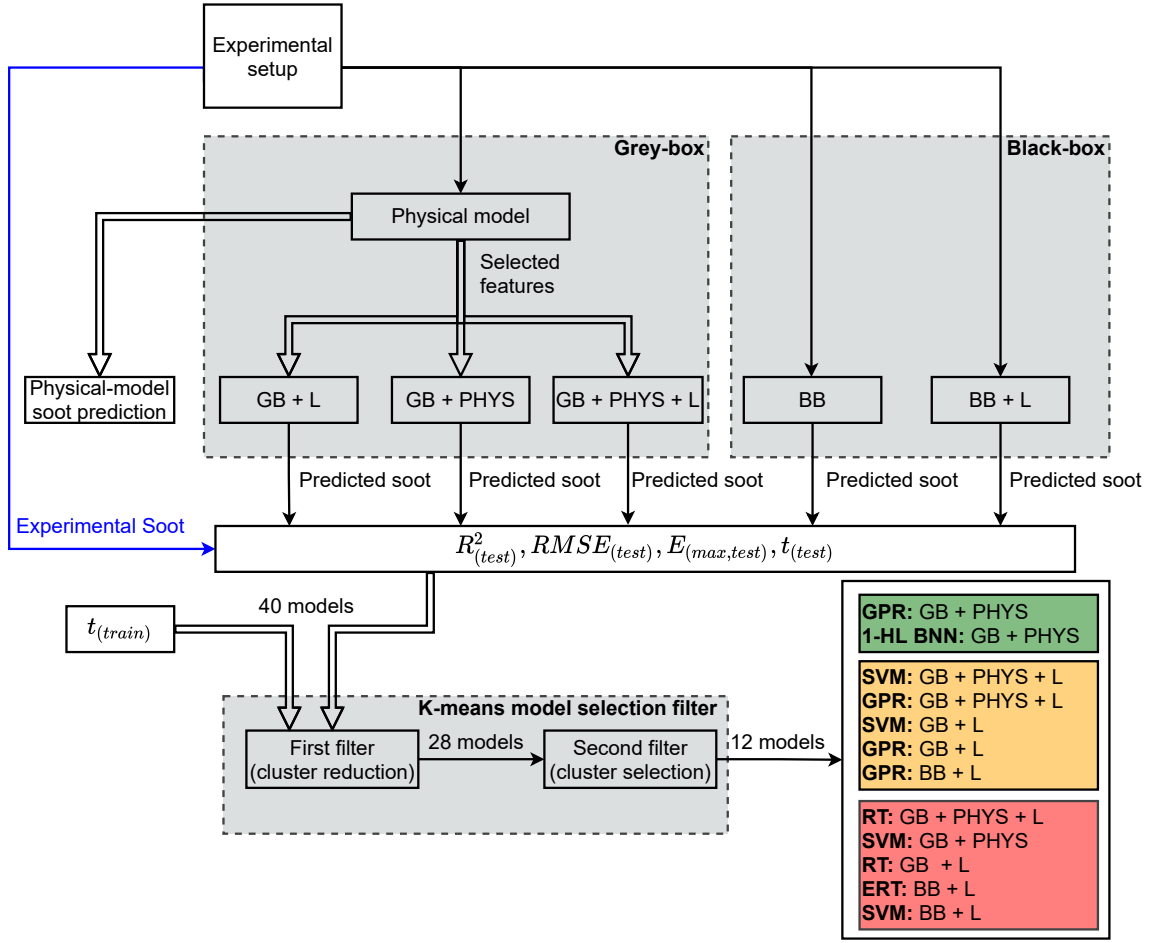
Figure 4.5: Overview of the gray-box (GB) and black-box (BB) soot emissions model selection process by K-means clustering algorithm. RT stands for regression tree, ERT stands for ensemble of regression tree, SVM stands for support vector machine, GPR stands for Gaussian process regression, BNN stands for Bayesian neural network

4.2 Machine Learning Methods

ML algorithms are used in all three of pre-processing, modeling, and post-processing.

4.2.1 Pre-Processing: feature selection

For finding the most effective soot prediction parameters, least absolute shrinkage and selection operator (LASSO) feature selection algorithm is employed for both BB and GB models. LASSO is a regression method that performs feature selection and regularization to improve the model's prediction accuracy. In LASSO regression, the

predicted output is $\hat{y}_i = \theta^T x_i$ where θ is model's coefficient that is calculated by minimizing the following cost function

$$J(\theta) = \frac{1}{m}\sum_{i=1}^{m}(y_i - \hat{y}_i)^2 + \lambda \sum_{i=1}^{m}|\theta_i| \tag{4.1}$$

where m is the number of training data points, $\sum_{i=1}^{m}|\theta_i|$ is the L_1 regularization and λ is regularization variable. Adding L_1 regularization leads to driving the weights down to exactly zero (produces sparsity in the solution) and results in performing a systematic feature selection [193]. This sparsity depends on λ, which is calculated in the cross-validation process in the current study.

4.2.2 Regression models

These five well-known supervised learning regression algorithms are employed: RT, ERT, GPR, SVM, and ANN. These are used to train both the BB and GB soot models.

A data-driven regression model can be generalized to fitting a parameterized model, $\hat{y} = h_\theta(x_i)$, for given training set $\mathcal{D}_{train} = (x_i, y_i)$ such that $\hat{y}$ converges to y_i subject to given constrains. In this problem, x_i is input feature, y_i is the measured output, and θ is the parameters set. The parameters set can be calculated by solving following optimization problem

$$\begin{aligned} \min_{\theta} \quad & J(\theta) \\ \text{s.t.} \quad & \phi(\theta) \end{aligned} \tag{4.2}$$

where $\phi(\theta)$ is constraints function and $J(\Theta)$ is a cost function which is defined as

$$J(\Theta) = \bar{J}(\Theta) + \lambda L(\Theta) \tag{4.3}$$

where $\bar{J}(\Theta)$ is defined based on error $e_i(\Theta) = h_\theta(x_i) - y_i$ to minimize prediction error while regularization term, $L(\Theta)$, is added to regulate parameters, Θ. In general, $L(\Theta)$ is L_1 or L_2 loss function for regularization purpose. For LASSO regression, L_1 loss function is used while in other regression methods such as Ridge, SVM, and ANN L_2 loss function is used. The L_2 loss function is defined as

$$L_2(\Theta) = \sum_{i=1}^{m} (\theta)^2 \tag{4.4}$$

The regulatory parameter or penalized variable, λ, produces a trade-off between the smoothness of the model and the training error tolerance minimization [193].

K-Fold cross validation

K-fold cross-validation algorithm is used to avoid overfitting of models during training. K-fold cross-validation first rearranges the dataset randomly and then divides the dataset into k groups. In this study, 5-fold validation is used for all ML methods. In each iteration, the K-fold algorithm chooses one group as a fold, trains a model on the rest of the groups (out of the fold), and assess it on the fold set [194].

Regression tree (RT)

RT is a modeling method with an iterative process of splitting the data into branches where the main algorithm to train RT is Classification and Regression Trees (CART) [195]. In a regression tree, the data are divided into different classes similar to classification problem with only difference is that each class is assigned to a specific value. RT divides data to k classes based on threshold, t_k, based on following cost function

$$J(\theta) = \frac{m_{left}}{m} \text{MSE}_{left} + \frac{m_{right}}{m} \text{MSE}_{right} \tag{4.5}$$

where Mean Squared Error (MSE) is defined as

$$\text{MSE}(\theta) = \frac{1}{m} \sum_{i=1}^{m} (y_i - \hat{y}_i)^2 \tag{4.6}$$

where $\hat{y} = \frac{1}{m_{node}} \sum_{i \in \text{node}} y(i)$ and m_{left} and m_{right} are left and right branches of the tree. In this method, both k and t_k are considered as model weights and integrated in θ. To avoid overfitting, a minimum number of samples required at a leaf node (Minimum Samples Leaf (MSL)) is added to the CART algorithm as a regularization

parameter. The maximum depth of tree that integrated in $\phi(\theta)$ is another regularisation parameter [193].

Ensemble of regression trees (ERT)

ERT is constructed using several decision trees. Three primary hyperparameters to tune ERT are aggregation methods, number of learners, and MSL. In ensemble learning, Bootstrap aggregation (Bagging) and hypothesis boosting (Boosting) are two standard aggregation methods. In bagging, the training algorithm is the same for every predictor, while the training set is a random subset of the training set, i.e., several RT are trained based on different random subsets of the training set. The well-known example of using bagging method is Random Forest. In boosting, a sequential architecture of several weak learners is aggregated, i.e., series of RTs are trained based on the same training data and layers of RT connected through a series architecture [193]. In this study, Bayesian optimization is used to tune the ERT hyperparameters including number of learners (number of RT in ERT), MSL, and aggregating method (boosting/bagging).

Support vector machine (SVM)

SVM is an ML method to find a correlation between input-output by solving a convex quadratic programming problem. The cost function of SVM can be defined as

$$J(\theta) = \frac{1}{2} \sum_{i=1}^{m} \theta_i^2 + C \sum_{i=1}^{m} (\zeta_i^+ + \zeta_i^-) \tag{4.7}$$

where ζ_i^- and ζ_i^+, are so-called slack variables and perform as penalty variables to tackle a possible infeasibility of an optimization problem. C includes regulatory parameters. Equation (4.7) follows the original cost function defined in [196] and equals to $1/\lambda$ [193]. Thus, SVM optimization equation can be rewritten as

$$J(\theta) = \frac{\lambda}{2} \sum_{i=1}^{m} \theta_i^2 + \sum_{i=1}^{m} (\zeta_i^+ + \zeta_i^-) \tag{4.8}$$

The constraint function, $\phi(\theta)$, of SVM in Equation (4.2) is

$$\phi(\theta) = \begin{cases} y_i - h_\theta(x_i) \leq \epsilon + \zeta_i^+ \\ h_\theta(x_i) - y_i \leq \epsilon + \zeta_i^- \\ \zeta_i^-, \zeta_i^+ \geq 0 \end{cases} \tag{4.9}$$

where ϵ is the maximum tolerable deviation for all training data [39, 185, 197]. In SVM, instead of training data in $\hat{y} = h_\theta(x_i)$, a function of training data, so-called kernel function can be replaced, $\hat{y} = h_\theta(\Gamma(x_i))$. This method is called SVM kernels trick and adding the kernel does not affect the cost function other than using higher dimension feature set instead of x_i in $\hat{y}$. Different kernels such as linear, polynomial, and Gaussian RBF kernels can be considered in optimization. These kernels are defined as

$$K(x_i, x_j) = \begin{cases} x_i^T x_j & \text{Linear} \\ (x_i^T x_j + c)^n & \text{Polynomial} \\ exp(-\gamma||x_i - x_j||_2^2) & \text{Gaussian RBF} \end{cases} \tag{4.10}$$

where n and γ are degree of polynomial and scale of RBF kernel, respectively, [186]. In this study, optimal kernel type including kernel parameters, i.e., scale and degree of freedom, as well as λ and ϵ are found using Bayesian optimization.

Gaussian process regression (GPR)

GPR is a nonparametric and Bayesian-based approach that has superior performance with small data sets and can provide an uncertainty measure on the predictions [198]. The main advantage of GPR is probabilistic prediction. Unlike other supervised ML methods, GPR infers a probability distribution over all possible ML model parameter values. The GPR cost function is defined based on negative log marginal likelihood as

$$J(\theta) = -log(p(\theta|y, X)) \tag{4.11}$$

where $p(\theta|y, X)$ is posterior distribution (i.e., a likelihood function of θ given X and y) that is defined based on Bayes' Rule as

$$p(\theta|y, X) = \frac{p(y|X, \theta)p(\theta)}{p(y|X)} \tag{4.12}$$

$p(y|X, \theta)$ is a likelihood function of y given X and θ, and $P(y|X)$ is marginal likelihood function of y given X [198]. Different covariance kernel functions are considered in this study, such as Exponential Kernel, Matern, and Quadratic Kernel with different options. Here, two standard kernels for GPR method including Rational Quadratic kernel function and Matérn kernel function are used. Rational Quadratic kernel function defines as

$$K(x_i, x_j|\theta) = \sigma_l^2 (1 + \frac{r^2}{2\alpha\sigma_l^2})^{-\alpha} \tag{4.13}$$

and general Matérn kernel function defines as

$$K_{p+1/2}(x_i, x_j) = \sigma_f^2 \exp\left(-\frac{\sqrt{2p+1}r}{\sigma_l}\right) \frac{p!}{(2p)!} \sum_{i=1}^{p} \frac{(p+i)!}{i!(p-i)!} \left(\frac{2\sqrt{2p+1}r}{\sigma_l}\right)^{p-i} \tag{4.14}$$

where r is the Euclidean distance between x_i and x_j ($r = \sqrt{(x_i - x_j)^T(x_i - x_j)}$), σ_l is characteristic length scale, σ_f is signal standard deviation, and α is a positive-valued scale-mixture parameter [198]. In Equation (4.15), usual value for p is $p = 0$ (Matérn 1/2 $K_{1/2}(x_i, x_j)$), $p = 1$ (Matérn 3/2 $K_{3/2}(x_i, x_j)$), and $p = 2$ (Matérn 5/2 $K_{5/2}(x_i, x_j)$). The Beysian optimization method in this study results using Matérn 5/2 function as a optimum choice for GB + L, GB + PHYS, and GB + PHYS + L which defines as

$$K_{5/2}(x_i, x_j) = \sigma_f^2 (1 + \frac{\sqrt{5}r}{\sigma_l} + \frac{5r^2}{3\sigma_l^2}) \exp(-\frac{\sqrt{5}r}{\sigma_l}) \tag{4.15}$$

Artificial neural network (ANN)

As the steady-state soot emission dataset used in this Chapter is relatively small, only shallow ANNs with only 1 or 2 hidden layers are used here. Similar to previous ML methods, the cost function of an ANN method can be written following Equation (4.2) notation as

$$J(\theta) = \sum_{i=1}^{m} (h_\theta(x_i) - y_i) + \frac{\lambda}{2} \sum_{k=1}^{K-1} \sum_{i=1}^{s_k} \sum_{j=1}^{s_{k+1}} (\theta_{j,i}^{(k)})^2 \tag{4.16}$$

where K and s_k, and m are number of total layers (input + output + hidden layer), number of neurons in k^{th} layer, and size of the training set, respectively. The first term in this equation is used to minimize modeling error while L_2 loss function is used for regulization. As input neurons and output neurons are set by input and output layers, only hidden layer number and neuron size are found by using grid search, i.e., $(L_{HL} = K - 2)$ and the number of neurons (s_2 and s_3) in the HL.

Bayesian-based ANN, denoted as BNN, is referring to extending ANN with Bayesian inference. Unlike ANN which model's weights are assigned as a single value, in BNN, weights are considered a probability distribution. These probability distributions of network weights are used to estimate the uncertainty in weights and predictions [199]. All ANN and BNN configuration combinations are evaluated in this optimization method, and the best model is obtained based on cross-validation data.

4.2.3 Hyperparameters optimization

Hyperparameters of ML methods such as tolerated error (defined inside constrain function $\phi(\theta)$), regularization parameter (λ), optimization iteration stop criteria in optimization problem of Equation (4.2) play an important role to decrease modeling error and to increase model reliability. If an ML algorithm such as A_Λ has N hyperparameters such as $\Lambda = \lambda_1, \lambda_2, ..., \lambda_N$, the optimum hyperparameters can be found by solving following optimization problem [183]

$$\Lambda^* = \arg \min_\Lambda V(h_\theta(x_i), \mathcal{D}_{train}, \mathcal{D}_{valid}) \tag{4.17}$$

where $V(h_\theta(x_i), \mathcal{D}_{train}, \mathcal{D}_{valid})$ measures performance of a model for given training and validation set, $\mathcal{D}_{training}$ and $\mathcal{D}_{valid}$ based on algorithm A_Λ.

In this work, Bayesian optimization [184] is used for RT, SVM, and ERT models hyperparameters optimization while grid search [193] method is used for ANN models.

For the Bayesian optimization to tune hyperparameters, the evaluation used in

Equation (4.17) is

$$V(\lambda) = \frac{1}{n}\sum_{i=1}^{m}(\hat{y}_i - y_i)^2 \qquad (4.18)$$

where $A_\Lambda \in \{RT, ERT, SVM\}$ and m is size of training set. The model is trained based on training $\mathcal{D}_{train}$ and cross-validated on $\mathcal{D}_{valid}$ in the inner loop of this optimization. Then, $V(\lambda)$ is calculated using both training and cross-validation sets.

To evaluate all possible hyperparameter combinations in ANN methods, grid search is often used [68]. A search along the space of hyperparameters learning with high probability is tried in Bayesian optimization while in grid search, all the possible hyperparameters combinations within a given range are tried. In this study, all combination of layer $L \in \{1, 2\}$ (shallow network) and neurons $s_l \in (1, 40)$ are considered where L and s_l are number of layers and number of neurons in l^{th} layer. The layers and neuron's upper limit are set to 2 and 40, respectively, since the limited number of training data means a deeper network should be avoided.

4.2.4   Post-processing: model selection

The K-means clustering algorithm, an unsupervised ML method, is used for analysing the results and selecting the best feature sets and methods for different applications. K-means algorithm divides data into n clusters with equal variance. To do this the K-means algorithm tries to divide this data into M disjoint clusters, then minimizes the within-cluster sum-of-squares or inertia, which is the sum of squared Euclidean distance between cluster members and cluster center

$$E(m_1, ..., m_M) = \sum_{i=1}^{N}\sum_{k=1}^{M} I(x_i \in C_k)||x_i - m_k||^2 \qquad (4.19)$$

where m_k is the center of cluster k. If $x_i \in C_k$, $I(x_i \in C_k)=1$; otherwise, $I(x_i \in C_k)=0$. The algorithm starts with random centers and updates the centers in each iteration until the centers remain unchanged, which is a local optimum point. In order to find out the optimum number of clusters for a data set, the elbow method could be used. In this method, inertia is plotted as a function of the number of clusters. The elbow

of this curve shows the optimum number of clusters. All these models are evaluated for the test set in the following section.

4.3 Results and Discussion

The engine experimental data including 80% (175 points) of the data points are used for training $\mathcal{D}_{train}$, and 20% of the data points are used for testing $\mathcal{D}_{test}$ (44 points). Figure 4.6 shows the distribution of the test and training data. The K-fold validation method with five folds ($k = 5$) is also included in training $\mathcal{D}_{valid}$. Testing data $\mathcal{D}_{test}$ is used only for the final evaluation of the model.
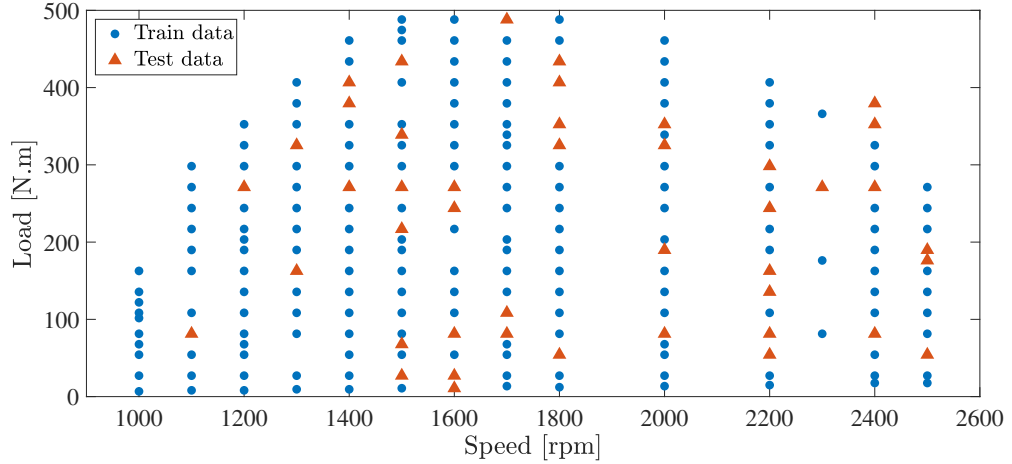
Figure 4.6: Training and test data for ML approaches, 175 data points are used as the training dataset (80%) and 44 data points are used as the testing dataset (20%).

Tables 4.1 and 4.2 show details about the data-driven methods that are used in this study and their performance for different feature sets. A total of 40 models are defined by five different feature sets and eight ML methods. Model performance is evaluated by considering the following criteria:

1. The coefficient of determination of test data R^2_{test};

2. Root Mean Square of Error of test data $RMSE_{\text{test}}$ [mg/m^3];

3. Maximum of absolute prediction error of test data $|E_{\text{test,max}}|$ [mg/m^3];

90

4. Training time t_{train} [s];

5. Prediction time t_{test} [ms].

The accuracy of the model is based on the first three criteria. The third criterion is particularly useful to assess the model reliability since outliers cause high maximum errors. High maximum error means that model will be inaccurate in some instances. A low maximum error is associated with less severe outliers and a more robust model. There is a direct relationship between the complexity of the model and the training time. Overfitting is more likely to occur in complex models, so typically less complex models are more likely to show the same performance for different applications [200]. The K-means clustering algorithm is employed to choose the most appropriate models and feature sets for a variety of applications including calibration, real-time control, and to study the effect of changes in different engine components. The above five separate parameters are used as the input feature set for the K-means algorithm. The appropriate number of clusters must be first determined before using the K-means algorithm. This is accomplished with the elbow method, and the optimum number of clusters of 6 was found.

Figure 4.7 shows the result of clustering of the models. The same colour is assigned to models that are part of the same cluster. The first filter (the first K-means algorithm) aims to exclude data sets and methods with low accuracy and high training and testing times. The red and black clusters (the clusters where the members are shown in red and black in Figure 4.7) have a very low accuracy compared to other clusters members (low R^2, high RMSE and high $|E_{max}|$ in Figure 4.7a–c). Higher t_{test} is the main characteristic of the green cluster members in comparison to other clusters based on Figure 4.7d. Additionally, pink clusters have a considerably larger t_{training} than the others based on Figure 4.7e. This analysis leads to the removal of red, black, green, and pink clusters due to their low accuracy and long training and prediction (testing) times. As a result, 12 of the 40 models are removed by the first

filter, leaving 28 models for the second K-means based filter.
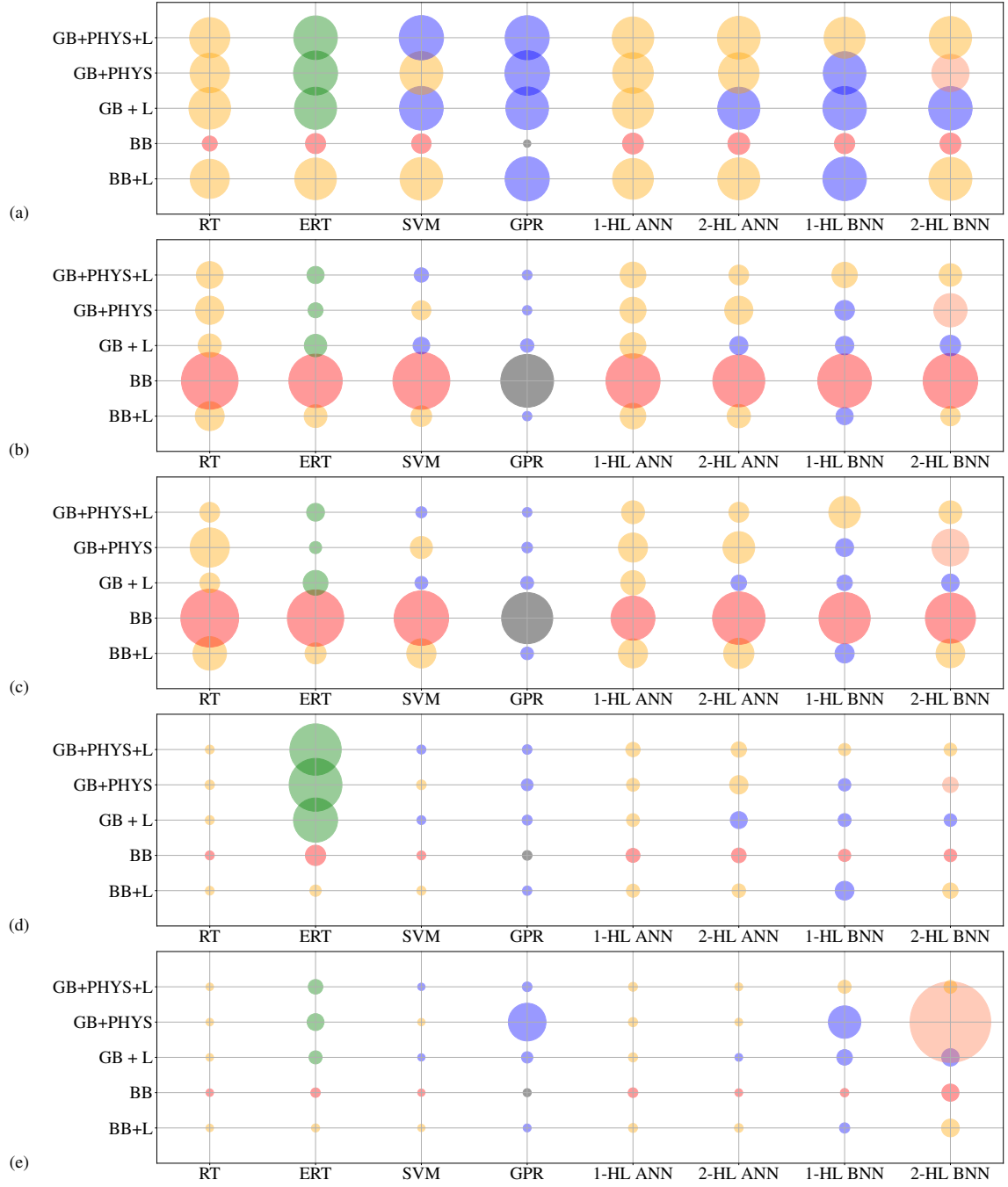
Figure 4.7: First filter clustering of models using K-means algorithm: 40 models divided to 6 clusters and sorted based on (**a**) R^2_{test}, (**b**) $\text{RMSE}_{\text{test}}$ [mg/m^3], (**c**) $|E_{\text{test,max}}|$[mg/m^3], (**d**) t_{test} [ms] (test time), and (**e**) t_{train} [ms] (training time).

A second K-means filter is applied to choose the best models out of the remaining models for the varied applications including real-time control and calibration. Fig-

ure 4.8 shows the result of the clustering by means of the second filter. Each cluster is assigned a number to simplify the subsequent discussion. The error values, training time, and test time for members of different clusters are shown in Figure 4.9. Members of clusters 1, 4 and 2 have higher accuracy than other clusters. Members of cluster 0 have the largest maximum error, lowest R^2 and highest RMSE based on Figure 4.9a–c. As a result, this cluster can be removed as it is low in accuracy. Using the remaining models, which feature sets and methods were best suited to the different applications could be determined. Table 4.3 shows the selected ML methods and feature sets for different applications.

For accuracy, R^2, RMSE and $|E_{max}|$ are important parameters. Reliability of a model depends heavily on its $|E_{max}|$. A high value of $|E_{max}|$ indicates severe outliers. As a result, there is a possibility of high error rates for some predictions in the model, making it unreliable. Training time is a deciding factor in choosing a model with a low degree of complexity. The selection of models is limited to experimental feature sets for real-time control and adaptive learning because only measurable features could be used as input in real-time control. Therefore, the experimental feature sets (BB and BB + L) are acceptable. Unlike real-time control, virtual tests are based on feature sets generated by the engine model (GB, GB + L, and GB + PHYS + L). Clustering is used to choose the models with the highest possible accuracy for different applications. Based on Figure 4.9a–c clusters 2 and 4 have the highest accuracy and reliability, so the majority of their members were selected for these factors. Based on Figure 4.9e, cluster 2 is characterized by the high training time. Therefore, its members are not selected based on lower complexity criterion. Cluster 1 has acceptable accuracy for most of its cases, despite not being as accurate as cluster 4 and has a low training time. As a result, some of the members of cluster 1 are rated as less complex.

Table 4.3 shows the remaining 12 models selected for different applications. Figure 4.10 shows the prediction vs. experiment diagrams for the physical model. Figure 4.11 shows the prediction vs. experiment diagrams for the test data for 12 selected

models. By comparing the results in Figures 4.10 and 4.11, the physical soot model has much lower accuracy than the proposed model. This is attributed to the complexity of soot formation and oxidation processes [12] making it difficult for soot emissions formation and oxidation process to be adequately represented by 1D physical models [12]. Model-based studies for soot emissions prediction show the same trend [28], and have motivated the data-driven methods of soot emissions prediction.
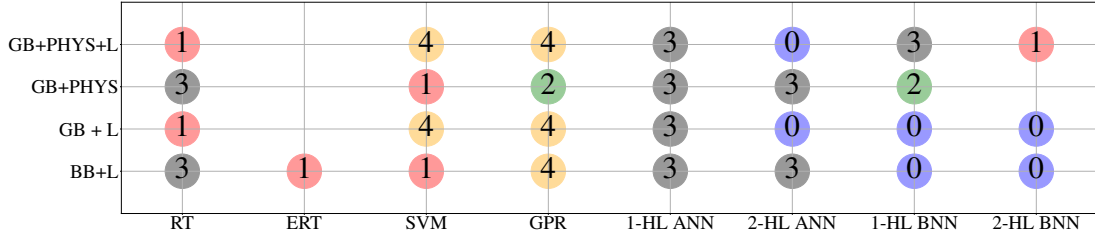
Figure 4.8: Assigned colours for the second clustering filter of models using K-means algorithm.

GPR and SVM are the most accurate methods for this data set as shown in Table 4.3. The virtual engine model enhances the model's accuracy since 4 out of 5 models that are selected for high accuracy have used some forms of gray-box feature set. In general, SVM: GB + PHYS + L and GPR: BB + L are found as the best models among gray-box and black-box models, respectively. Figure 4.12 shows the accuracy of soot prediction for these two models for the training and the test data. For most of the engine's load and speed ranges, both models are quite accurate in soot prediction. In comparison to GPR: BB + L model (black-box), the SVM: GB + PHYS + L model (gray-box) have less outliers. The reason for this is attributed to using the physical model in the gray-box model, which assists in reducing outliers in soot emissions prediction.

A comparison of soot emission model accuracy of this study and studies in the literature is given in Table 4.4. As seen, the developed model in this study outperform the developed models in the previous studies in terms of accuracy.

As seen, the best gray-box model developed in this study (SVM: GB + PHYS +
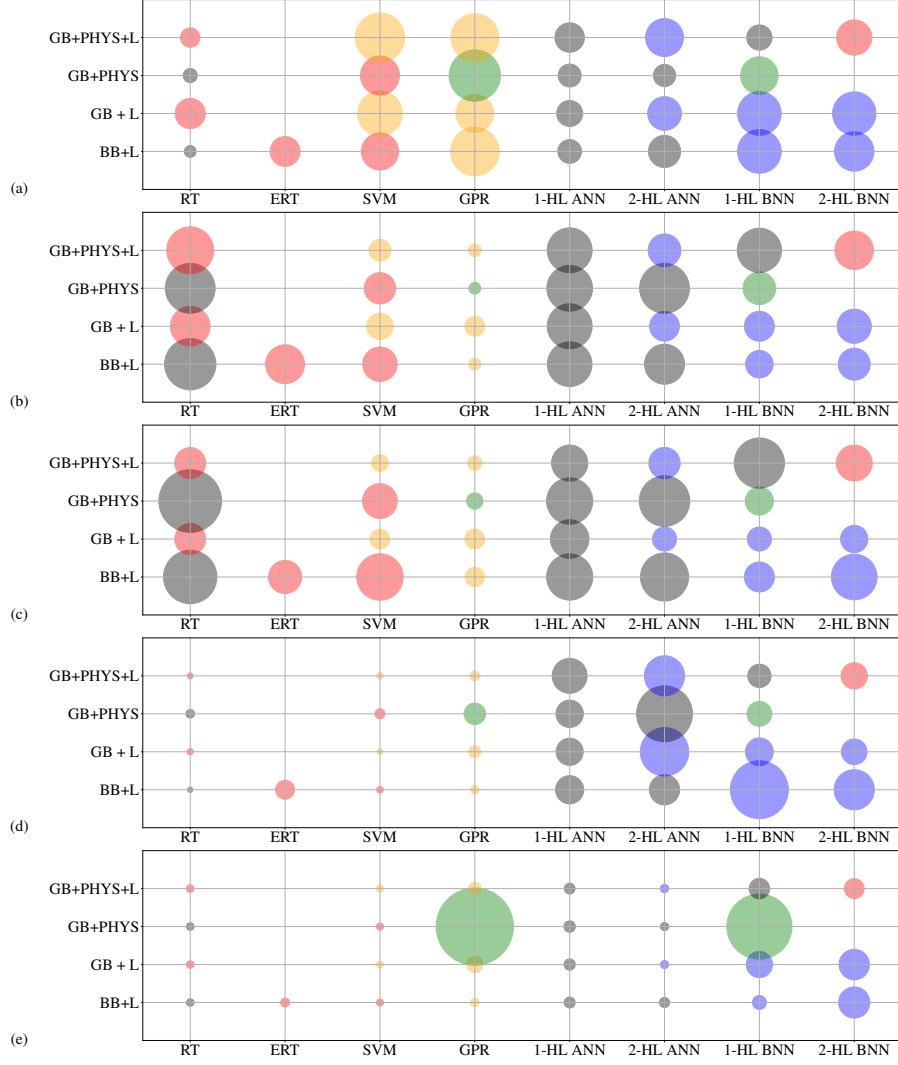
Figure 4.9: Second filter for clustering of Models using K-means algorithm: 28 models divided to 5 clusters where three clusters including 12 models have been chosen as final selection. (**a**) R^2_{test}, (**b**) $RMSE_{test}$ [mg/m^3], (**c**) $|E_{test,max}|$[mg/m^3], (**d**) t_{test} [ms] (test time), and (**e**) t_{train} [ms] (training time).
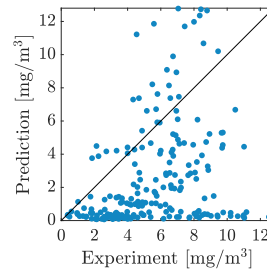
Figure 4.10: Comparison of the Physics-based GT-power model prediction against experimental data (good accuracy is when the data follows the diagonal line).
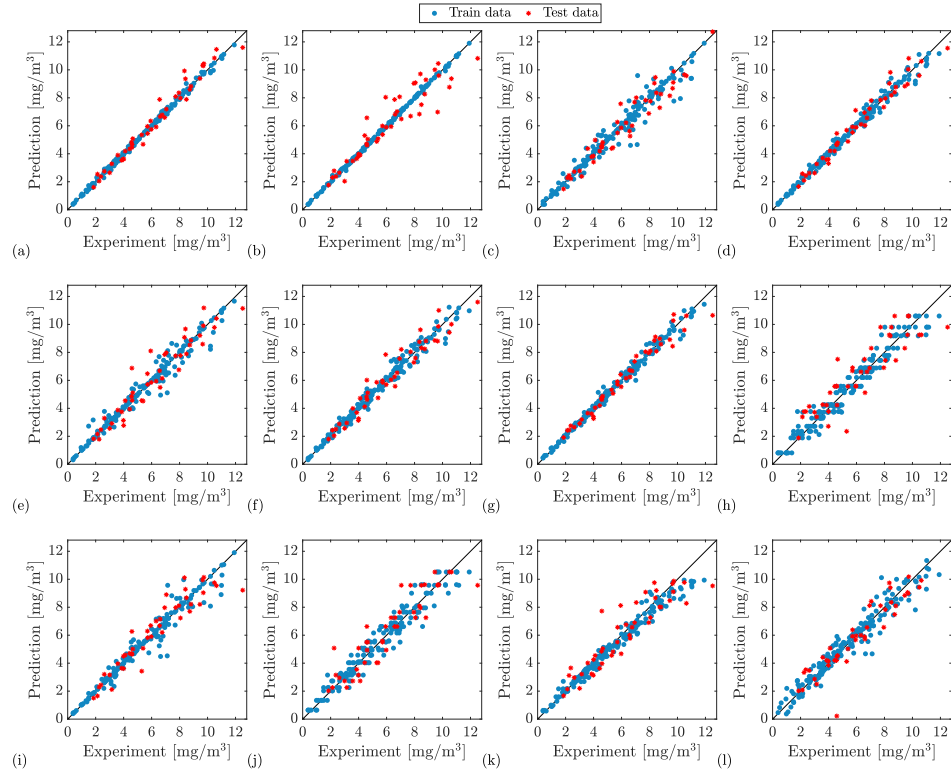
Figure 4.11: Comparison of model prediction against experimental data for different models including (**a**) **GPR:** GB + PHYS, (**b**) **1-HL BNN:** GB + PHYS, (**c**) **SVM:** GB + PHYS + L, (**d**) **GPR:** GB + PHYS + L, (**e**) **SVM:** GB, (**f**) **GPR:** GB, (**g**) **GPR:** BB + L, (**h**) **RT:** GB + PHYS + L, (**i**) **SVM:** GB + PHYS, (**j**) **RT:** GB, (**k**) **ERT:** BB + L, (**l**) **SVM:** BB + L (good accuracy is when the data follows the diagonal line).

L) outperforms the best models presented in the previous studies.
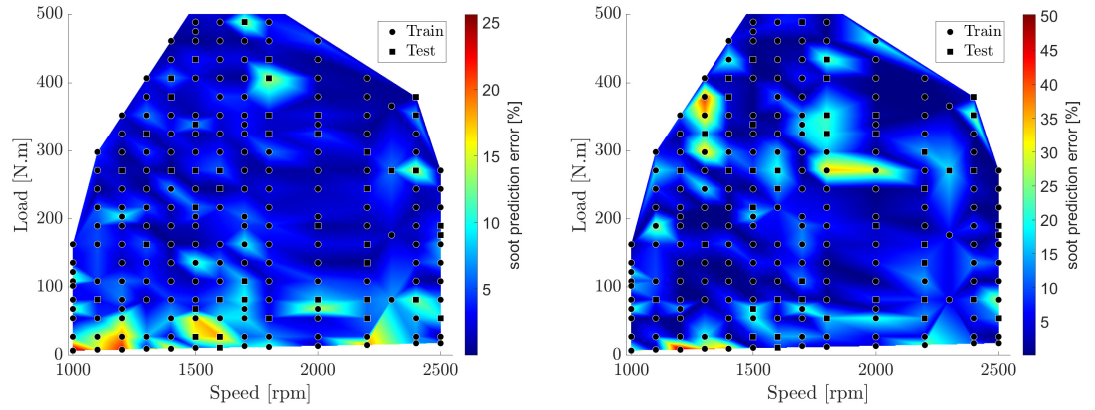
Figure 4.12: Prediction error [%] over engine speed and load for two models: (**a**) **GPR:** BB + L, (**b**) **SVM:** GB + PHYS + L.

Table 4.1: Training and optimization of ML-based model hyperparameters. MSL is minimum samples leaf for regression tree and ensembles trees methods, λ is the regularization parameter and ϵ is the maximum tolerable deviation for support vector machione method, and σ_l is the length scale of Gaussian process regression method.

Method	Opt. Method	Opt. Hyper-parameters	Model Type	Opt. Model Configuration
RT	Bayesian	Min samples leaf (MSL)	BB	MSL = 13
			BB + L	MSL = 1
			GB + L	MSL = 5
			GB + PHYS	MSL = 5
			GB + PHYS + L	MSL = 5
ERT	Bayesian	Ensemble method, min samples leaf, and number of learners	BB	Boosting, 75 Learners, and MSL = 2
			BB + L	Boosting, 28 Learners, and MSL = 4
			GB + L	Boosting, 35 Learners, and MSL = 5
			GB + PHYS	Boosting, 488 Learners, and MSL = 47
			GB + PHYS + L	Boosting, 487 Learners, and MSL = 2
SVM	Bayesian	Kernel function λ and ϵ	BB	Cubic, $\lambda = 0.96$, $\epsilon = 0.010$
			BB + L	Quadratic, $\lambda = 0.77$, $\epsilon = 0.330$
			GB + L	Gaussian, $\lambda = 9.59$, $\epsilon = 0.004$
			GB + PHYS	Quadratic, $\lambda = 3.49$, $\epsilon = 0.003$
			GB + PHYS + L	Cube, $\lambda = 5.79$, $\epsilon = 0.009$
GPR	Bayesian	Kernel function, initial value for the noise standard deviation (σ)	BB	Rational quadratic, $\sigma = 12.68$
			BB + L	Rational quadratic, $\sigma = 0.0005$
			GB + L	Matérn 5/2, $\sigma = 0.0001$
			GB + PHYS	Matérn 5/2, $\sigma = 0.0001$
			GB + PHYS + L	Matérn 5/2, $\sigma = 2.996$
1-HL ANN	Grid search	Number of neurons in each layer	BB	Network conf.: [25]
			BB + L	Network conf.: [19]
			GB + L	Network conf.: [4]
			GB + PHYS	Network conf.: [4]
			GB + PHYS + L	Network conf.: [19]
2-HL ANN	Grid search	Number of neurons in each layer	BB	Network conf.: [7,25]
			BB + L	Network conf.: [25, 31]
			GB + L	Network conf.: [4, 13]
			GB + PHYS	Network conf.: [7,13]
			GB + PHYS + L	Network conf.: [16, 19]
1-HL BNN	Grid search	Number of neurons in each layer	BB	Network conf.: [7]
			BB + L	Network conf.: [31]
			GB + L	Network conf.: [31]
			GB + PHYS	Network conf.: [13]
			GB + PHYS + L	Network conf.: [25]
2-HL BNN	Grid search	Number of neurons in each layer	BB	Network conf.: [7,28]
			BB + L	Network conf.: [16, 13]
			GB + L	Network conf.: [10, 22]
			GB + PHYS	Network conf.: [22, 22]
			GB + PHYS + L	Network conf.: [10, 19]

Table 4.2: ML-based data-driven soot models comparison– BB, L, GB, and PHYS stand for black-box, LASSO, gray-box, and physical insight, respectively

Model	Criteria	RT	ERT	SVM	GPR	1-HL NN	2-HL NN	1-HL BNN	2-HL BNN
BB	R^2_{train}	0.85	0.95	0.86	0.87	0.86	0.86	0.88	0.90
	R^2_{test}	0.41	0.51	0.50	0.27	0.52	0.54	0.51	0.52
	$RMSE_{train}[mg/m^3]$	1.41	0.90	1.39	1.35	1.44	1.38	1.27	1.21
	$RMSE_{test}[mg/m^3]$	2.52	2.38	2.53	2.35	2.41	2.32	2.39	2.43
	$|E_{test,max}|[mg/m^3]$	8.7	8.5	8.2	7.7	6.6	7.9	7.7	7.5
	$t_{test}[ms]$	2.23	16.73	2.08	3.11	8.66	9.53	6.47	6.93
	$t_{train}[s]$	0.74	3.50	0.40	1.56	3.77	1.11	2.07	14.31
BB + L	R^2_{train}	0.98	0.99	0.97	1	0.97	0.98	0.99	0.99
	R^2_{test}	0.87	0.91	0.93	0.96	0.90	0.92	0.95	0.94
	$RMSE_{train}[mg/m^3]$	0.48	0.52	0.66	0.28	0.66	0.63	0.22	0.20
	$RMSE_{test}[mg/m^3]$	1.33	1.07	0.98	0.51	1.19	1.10	0.83	0.93
	$|E_{test,max}|[mg/m^3]$	5.02	3.14	4.37	1.87	4.35	4.53	2.85	4.3
	$t_{test}[ms]$	1.94	5.26	2.27	2.73	7.49	8	14.7	10.4
	$t_{train}[s]$	0.75	1.57	0.44	1.32	2.80	2.33	4.57	15.13
GB + L	R^2_{train}	0.97	0.99	0.98	0.99	0.96	0.96	0.99	0.99
	R^2_{test}	0.92	0.93	0.95	0.94	0.90	0.92	0.95	0.95
	$RMSE_{train}[mg/m^3]$	0.62	0.06	0.48	0.38	0.73	0.72	0.34	0.09
	$RMSE_{test}[mg/m^3]$	1.09	1.00	0.81	0.67	1.2	0.88	0.88	0.97
	$|E_{test,max}|[mg/m^3]$	2.9	3.7	1.9	1.9	3.6	2.3	2.3	2.6
	$t_{test}[ms]$	2.21	47.16	2.05	3.59	7.24	12.42	7.39	6.86
	$t_{train}[s]$	0.79	8.57	0.37	6.1	2.97	1.04	12.10	14.66
GB + PHYS	R^2_{train}	0.98	0.99	0.98	0.99	0.97	0.98	0.99	0.99
	R^2_{test}	0.87	0.96	0.94	0.97	0.90	0.89	0.93	0.83
	$RMSE_{train}[mg/m^3]$	0.54	0.01	0.57	0.13	0.70	0.6	0.07	0.01
	$RMSE_{test}[mg/m^3]$	1.3	0.74	0.91	0.5	1.2	0.94	1.2	1.06
	$|E_{test,max}|[mg/m^3]$	5.88	1.8	3.3	1.58	4.35	4.76	2.67	5.52
	$t_{test}[ms]$	2.74	58.19	3.1	5.87	7.3	14.22	6.69	10.63
	$t_{train}[s]$	0.75	13.90	0.46	43.24	3.09	1.11	35.87	103.90
GB + PHYS + L	R^2_{train}	0.98	0.99	0.98	0.99	0.95	0.98	0.99	0.99
	R^2_{test}	0.89	0.95	0.97	0.96	0.91	0.94	0.90	0.93
	$RMSE_{train}[mg/m^3]$	0.60	0.01	0.57	0.31	0.87	0.49	0.13	0.08
	$RMSE_{test}[mg/m^3]$	1.24	0.83	0.71	0.52	1.2	0.94	1.19	1.06
	$|E_{test,max}|[mg/m^3]$	2.94	2.65	1.64	1.41	3.42	2.97	4.73	3.4
	$t_{test}[ms]$	2.06	56.31	2.28	3.08	9.13	10.4	6.32	7.06
	$t_{train}[s]$	0.79	10.65	0.52	3.77	2.70	1.22	8.59	8.22

Table 4.3: Selected models based on K-means filters

Cluster	Model	Accuracy	Reliability	Less complexity	Real-time control	Virtual test
2	**GPR:** GB + PHYS	×	×			×
2	**1-HL BNN:** GB + PHYS		×			
4	**SVM:** GB + PHYS + L	×	×	×		×
4	**GPR:** GB + PHYS + L	×	×	×		×
4	**SVM:** GB + L	×	×	×		×
4	**GPR:** GB + L		×	×		×
4	**GPR:** BB + L	×	×	×	×	
1	**RT:** GB + PHYS + L			×		
1	**SVM:** GB + PHYS			×		
1	**RT:** GB + L			×		
1	**ERT:** BB + L					
1	**SVM:** BB + L			×	×	

Table 4.4: Comparison between studies about soot emissions modeling using gray-box models

Study	Machine learning method	Soot modeling R^2_{test}
Lang et al. [81]	GPR	0.83
Mohammad et al. [68]	ANN	0.95
Current study	SVM/GPR	0.97

4.4 Summary of chapter

To predict soot emissions for a compression ignition engine, physical, black-box (BB), and gray-box (GB) modeling were used. GB and BB soot emissions models were developed using eight different machine learning methods. Based on the LASSO feature selection method and physical insight, five different feature sets were tested for BB and GB models. To analyze the results, the K-means clustering algorithm was applied in two steps to categorize the models according to their performance. Different methods and feature sets were chosen for various applications. Real-time control is only feasible with BB methods since the physics-based model is too computationally expensive for use in the current ECUs. Based on the results, the GPR method with LASSO as the feature selection method is the most reliable ML method/feature set with $R^2_{\text{test}} = 0.96$, $\text{RMSE}_{\text{test}}$ $[\text{mg/m}^3] = 0.51$, $|E_{\text{test,max}}|[\text{mg/m}^3] = 1.87$ and t_{test} $[\text{ms}] = 2.73$. GB models can be used as a virtual engine to conduct simulation tests for development and calibration purposes, reducing the need for costly experiments. Among GB models, SVM-based ML method along with using LASSO and physical insight for feature selection provides the best performance with $R^2_{\text{test}} = 0.97$, $\text{RMSE}_{\text{test}}$ $[\text{mg/m}^3]$ $= 0.71$, $|E_{\text{test,max}}|[\text{mg/m}^3] = 1.64$ and t_{test} $[\text{ms}] = 2.28$. In most cases, GB models outperform their BB counterparts in terms of accuracy.

Chapter 5

Hybrid Emission and Combustion Modeling of Hydrogen Fueled Engines [1]

Hydrogen is an important zero-carbon fuel that can be used as the primary fuel for spark ignition (SI) engines or in dual-fuel operation in compression ignition (CI) engines. The combustion properties of hydrogen often result in high combustion temperature which produces harmful nitrogen oxides (NO_x) emissions. To reduce NO_x and soot emissions from hydrogen fueled engines, an engine can be optimized using a hardware-in-the-loop (HIL) setup to reduce calibration efforts for the engine. In addition, optimal model based combustion control (MCC) can reduce engine-out emissions. Both of HIL and MCC techniques require fast and accurate NO_x and soot emission models. The accuracy of a fast physics-based engine model with pre-mixed combustion is dependent on predicting the laminar flame speed (LFS). In this chapter, LFS is predicted using an artificial neural network (ANN) machine learning (ML) method. Then the LFS model and engine combustion model are validated for both an SI hydrogen engine and for a CI hydrogen-diesel engine. Next, black-box (BB) and gray-box (GB) soot and NO_x emission models are developed for the hydrogen-diesel engine using ANN, support vector machine (SVM) and Gaussian process regression (GPR) methods with different feature-sets and compared with a

---

[1] This chapter is based on [4]

common one-dimensional physics-based NO_x model. The developed GB and BB emission models can be used for engine hardware-in-the-loop (HIL) setups where accuracy is essential and model-based real time hydrogen combustion control where computational cost is essential.

5.1   Methodology

In this chapter, the developed ML LFS model from chapter 3, [1] is embedded into physics-based combustion models in GT-Power software to create engine models for a dual-fuel hydrogen-diesel CI engine and a single-fuel hydrogen SI engine. The use of ML LFS models is integrated in the physics-based models developed is a novel approach. These models are physics-based models with machine learning laminar flame speed (PMLS) because ML algorithm is used as part of the physics-based model. The developed PMLS are then validated using engine experimental data to match in-cylinder pressure. The model validation shows PMLS is valid for both SI and CI engines and also for both single-fuel and dual-fuel modes. After model validation for both engines, emission models for the dual-fuel hydrogen-diesel engine are developed. For this purpose, first, the PMLS for dual-fuel diesel-engine is calibrated for a wide operating range. Then, BB and GB emission models are developed using the PMLS and experimental data from the engine. The PMLS, BB and GB emission models, and ML methods are described in Sections 5.1 and 5.2.

5.1.1   Physics-based model with machine learning laminar flame speed (PMLS)

The hydrogen SI engine and the dual-fuel hydrogen-diesel engine are both modeled in GT-Power software using the embedded ANN LFS model from [1]. The ML LFS model gets the temperature, pressure, and fuel-air equivalence ratio at each crank angle from the physics-based engine model and calculates the LFS value. The calculated LFS value is then used by the physics-based combustion model to estimate the

engine parameters for the following crank angle. The SI turbulent flame model and the dual-fuel combustion model in GT-Power software are used as the physics-based models for the hydrogen SI engine and the hydrogen-diesel CI engine, respectively. The SI turbulent flame model is developed based on studies in references [201–203]. This model is able to predict the burn rate for homogeneous charge SI engines and considers the effects of cylinder's geometry, spark location and timing, air motion, and fuel properties.

For the hydrogen-diesel CI engine, the dual-fuel combustion model in GT-Power software is used. This model combines a direct-injection diesel multi-pulse model with the SI turbulent flame model to simulate the CI combustion process. By utilizing this model, the combustion rate for a dual-fuel engine can be predicted, where a pilot injection is used to ignite the fuel-air mixture. The model divides the cylinder contents into three thermodynamic zones, including the main unburned zone, the spray zone with injected fuel and entrained gas, and the spray burned zone with combustion products [204, 205]. As the diesel spray enters the premixed mixture of hydrogen-air, it decelerates due to the entrainment of unburned and burned gases into the pulse. The intermixing of pulses occurs through entrainment, which can be controlled by the entrainment rate multiplier. The Arrhenius expression is used to model the ignition delay of the mixture in each pulse, which can be adjusted by the ignition delay multiplier. Upon ignition of a pulse, the mixture is set aside for premixed combustion. The combustion rate of this process is assumed to be kinetically-limited and can be modified by the premixed combustion rate multiplier. The model also assumes that the unburned fuel-air mixture is entrained into the flame front at a rate proportional to the sum of the turbulent flame speed and LFS, and the burn rate depends on the remaining amount of unburned mixture ahead of the flame front as below:

$$\frac{dM_e}{dt} = \rho_u A_e (S_T + S_L) \tag{5.1}$$

$$\frac{dM_b}{dt} = \frac{M_e - M_b}{\tau} \qquad (5.2)$$

$$\tau = \frac{\lambda}{S_L} \qquad (5.3)$$

Where M_e is the entrained mass, ρ_u is the unburned mixture density, A_e is the surface area at flame front, S_L is the LFS which is calculated by the ANN model for each crank angle using temperature, pressure and equivalence ratio at that crank angle, S_T is the turbulent flame speed, M_b is the burned mass, t is time, τ is the time constant and λ is the Taylor microscale length. There are three calibration parameters that control the burn rates: turbulent flame speed multiplier, Taylor length scale multiplier and flame Kernel growth multiplier. These three calibration parameters are utilized to calculate λ and S_T using the provided LFS by the ANN model. Finally, the remaining unmixed fuel and entrained gases in the pulse mix and continue to burn primarily in a diffusion-limited phase. The rate of this combustion can be adjusted by the diffusion combustion rate multiplier. So, there are 7 calibration parameters in total that are used to tune the dual-fuel hydrogen-diesel CI engine model.

The SI turbulent model that is used for modeling hydrogen SI engine models premixed combustion initiated by spark ignition. Therefore, the model requires only flame propagation combustion multipliers including the turbulent flame speed multiplier, Taylor length scale multiplier, and flame kernel growth multiplier.

A genetic algorithm similar to [2, 3] is used for in-cylinder pressure traces calibration for both engine models. In total, 79 experimental data points from the dual-fuel hydrogen-diesel engine and three experimental data points from the hydrogen SI engine are measured. For the hydrogen SI engine, one case (33% of the available experimental data) is used for model calibration, and two cases (66% of the available experimental data) are used for model validation. For the hydrogen-diesel CI engine, 8 cases (10% of the available experimental data) are used in the calibration process and 71 cases (90% of the available experimental data) are used for model validation. Table 5.1 shows the ranges of the experimental data for hydrogen SI and hydrogen-

diesel CI engines. The schematic of the calibration process for hydrogen SI engine is shown in Figure 5.1. The same approach is also followed for the hydrogen-diesel engine. For the hydrogen SI engine, the input variables are the duration of hydrogen injection and spark timing. For the hydrogen-diesel CI engine, the input variables include the duration of hydrogen injection, diesel pulse 1 start of injection, diesel pulse 2 start of injection, and diesel pulse 2 duration of injection (diesel pulse 1 duration of injection is constant for all cases).

Figure 5.2 shows the experimental and simulation in-cylinder pressure trace for three of the non-calibration (validation) cases for the CI hydrogen-diesel engine and shows close agreement to experiment. Figure 5.3 presents the LFS and burned fuel fractions for case 77 of the dual-fuel hydrogen diesel engine, where the hydrogen energy fuel fraction is the highest, accounting for 75% of the total energy. The LFS value, calculated using ANN ML method, ranges from 0 to 3 as depicted in Figure 5.3. The results indicate that approximately 75% of the fuel is burning through premixed combustion, while the remaining 25% is being burned through non-premixed combustion. Upon further analysis of both the hydrogen SI engine and the hydrogen-diesel CI engine, it has been found that the LFS value consistently falls within the range of 0 to 3m/s across all cases. Additionally, the premixed combustion burn rate typically ranges between 0 to 75% for the CI hydrogen diesel engine, and this value is directly correlated with the hydrogen energy fraction. Specifically, as the hydrogen energy fraction increases, the premixed combustion burn rate tends to increase as well.

Finally, Figure 5.4 shows the experimental and simulation values for IMEP, CA50, peak pressure and net indicated thermal efficiency for both hydrogen SI engine and hydrogen-diesel CI engine. As seen in Figures 5.2 and 5.4, the experimental and simulation results match closely, which confirms the validation of the PMLS for both engines.

The emission measurements were only available from the dual-fuel CI engine, emis-

sion modeling of the dual-fuel diesel engine using BB and GB emission models are described in the nest section.

Table 5.1: Hydrogen-fueled engine operating conditions for the experimental data.

Engine Type	Number of cases	Engine Speed (rpm)	IMEP (bar)	Hydrogen Energy Ratio (%)	Fuel Energy kJ/cycle	Lambda (-)	Emission Measurement
Compression ignition hydrogen-diesel engine	79	1500	6.5-8.9	0-75	1.8-2.4	1.2-2.2	NO_x and Soot
Spark ignition hydrogen engine	3	1080	4.5-4.9	100	2.3-2.5	2.4-3	-
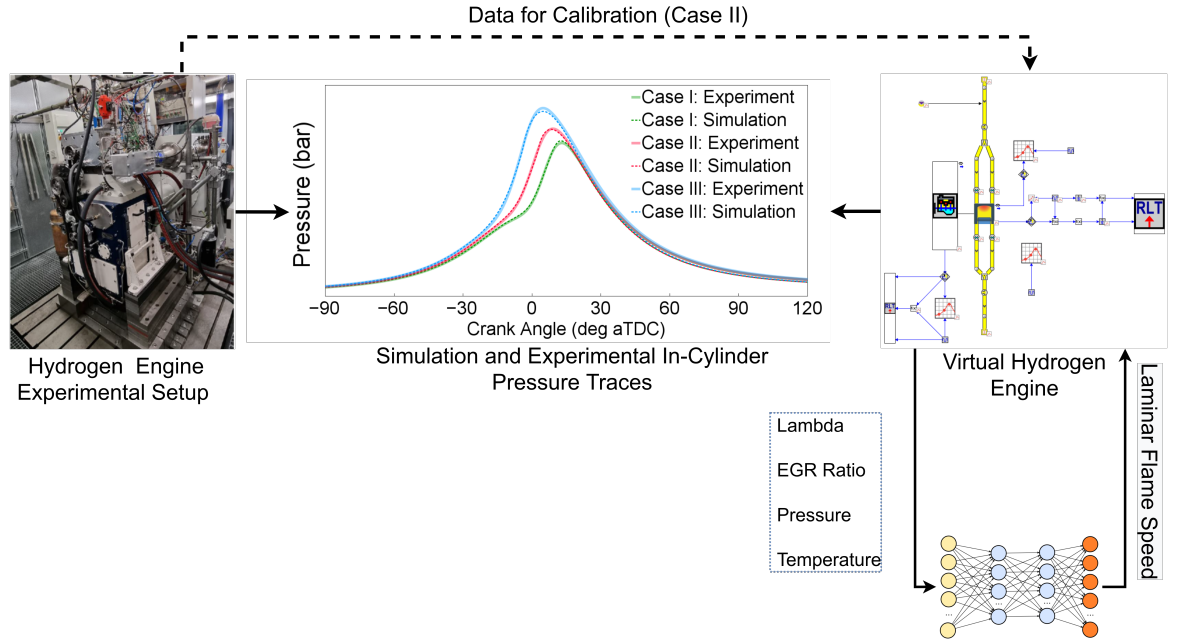
Figure 5.1: The calibration process of the physics-based model with machine learning laminar flame speed for the spark ignition hydrogen engine. Pressure trace validation for calibration case (II) and validation cases (I and III) are also shown.

5.1.2 Gray-box and black-box emission models

After developing the PMLS, the next step toward GB emission modeling is feature selection using the outputs from the PMLS. For this purpose, 36 important features, in terms of their effect on the emissions production, are selected using expert knowledge
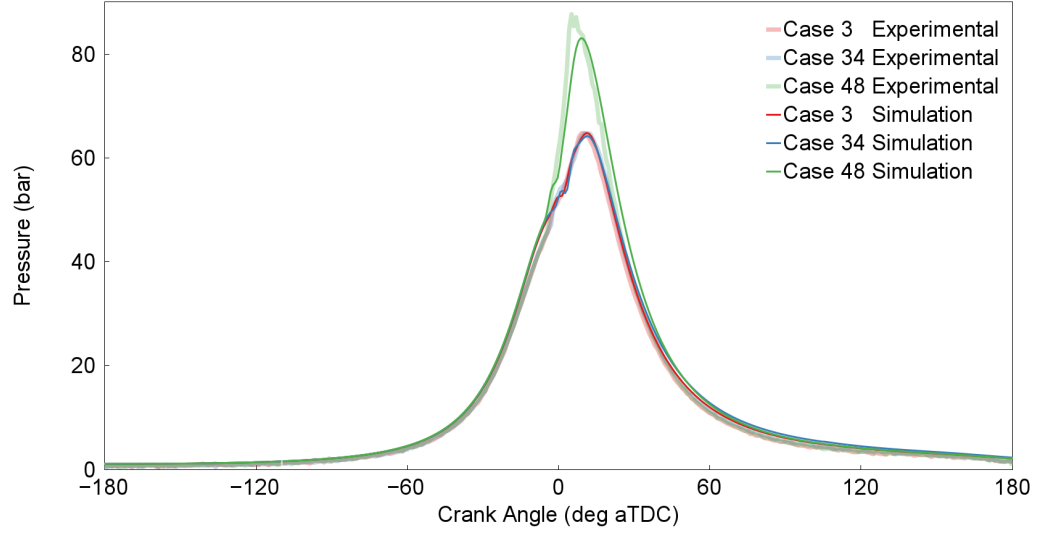
Figure 5.2: In-cylinder pressure trace validation for physics-based model with machine learning laminar flame speed for hydrogen-diesel compression ignition engine for 3 validation cases. Case 3: lambda=2 and hydrogen energy ratio (HER)= 3%, Case 34: lambda=1.7 and HER= 22%, Case 48: lambda=1.5 and HER= 36%. Mean absolute error below 2% (average covariance of the experimental data=2%).
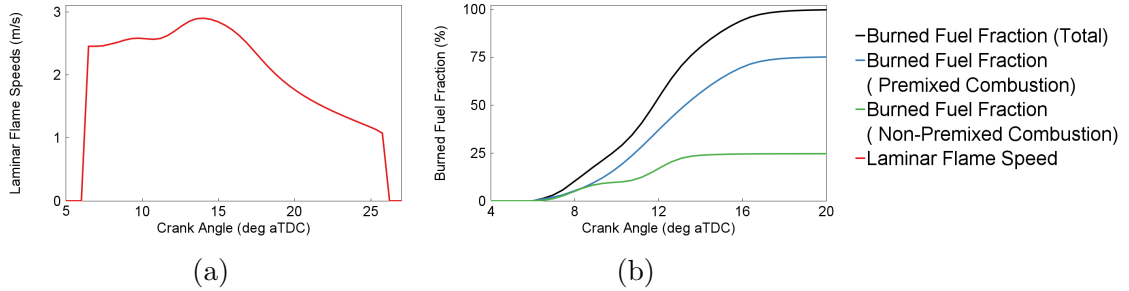
Figure 5.3: Laminar flame speed and burned fuel fraction for case 77 (hydrogen energy fraction=75%).

about the combustion process. Then, these features are used as the input of the SVM, ANN and GPR ML methods. Figure 5.5 shows the methodology that is used for developing and comparing PMLS (clear-box) BB and GB emission models for the dual-fuel hydrogen-diesel engine. As seen in Figure 5.5, two types of GB models are developed in this study. The first GB model (GB) uses all of the selected features by expert knowledge as the input, whereas the second gray box model (GB+FS) utilizes a second feature selection process using ML least absolute shrinkage and selection operator (LASSO) to select input features.
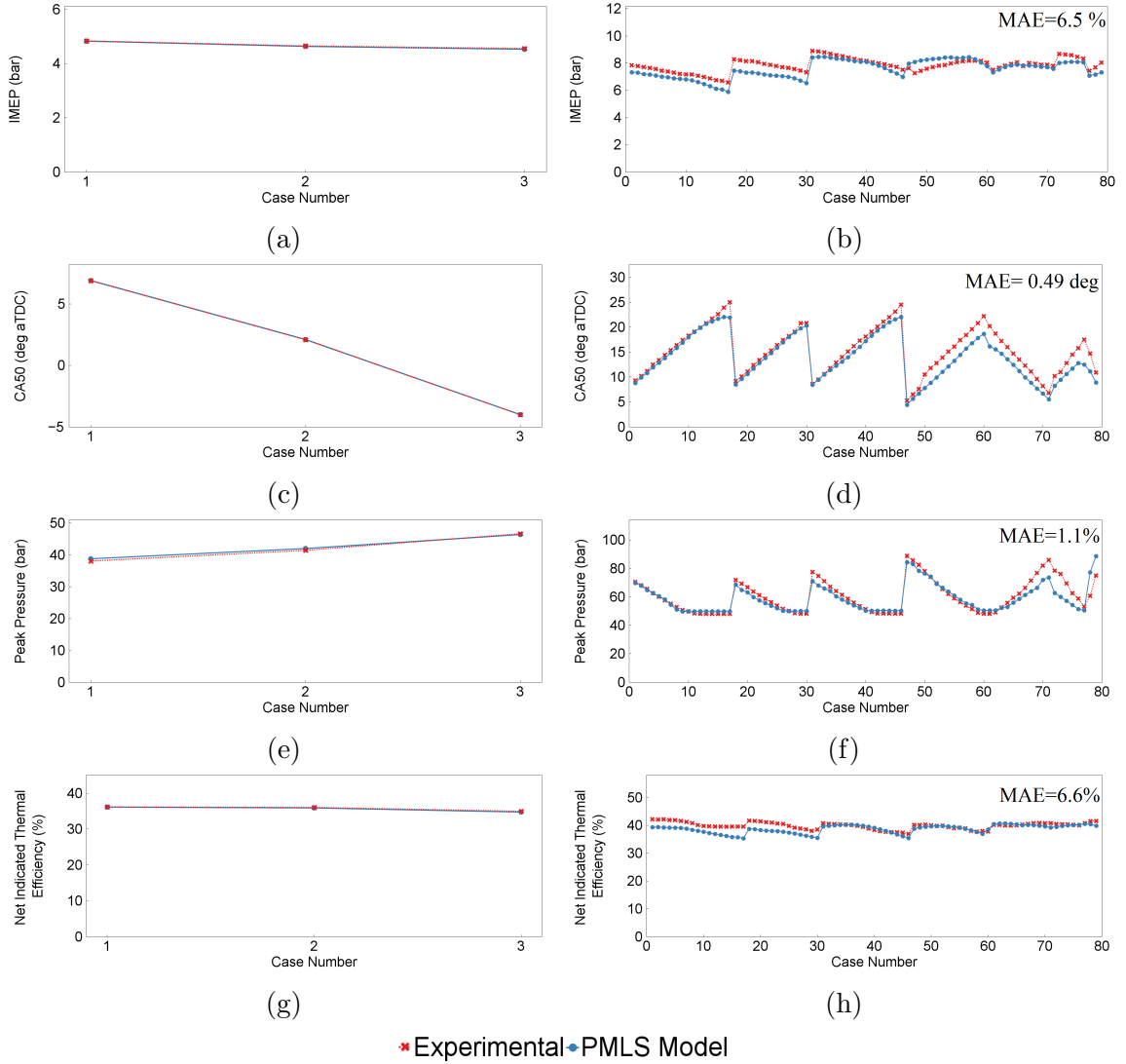
Figure 5.4: Experimental validation of the PMLS for predicting IMEP, CA50, Peak pressure, and Net indicated thermal efficiency. Left plots are for the spark ignition hydrogen engine and right plots are for the compression ignition hydrogen-diesel engine. PMLS stands for physics-based model with machine learning laminar flame speed, IMEP stands for indicated mean effective pressure, CA50 stands for 50% burned fuel crank angle, and MAE stands for mean absolute error.

5.2   Machine Learning Methods

Three ML methods of ANN, SVM, and GPR were used for black-box and gray-box emission modeling.
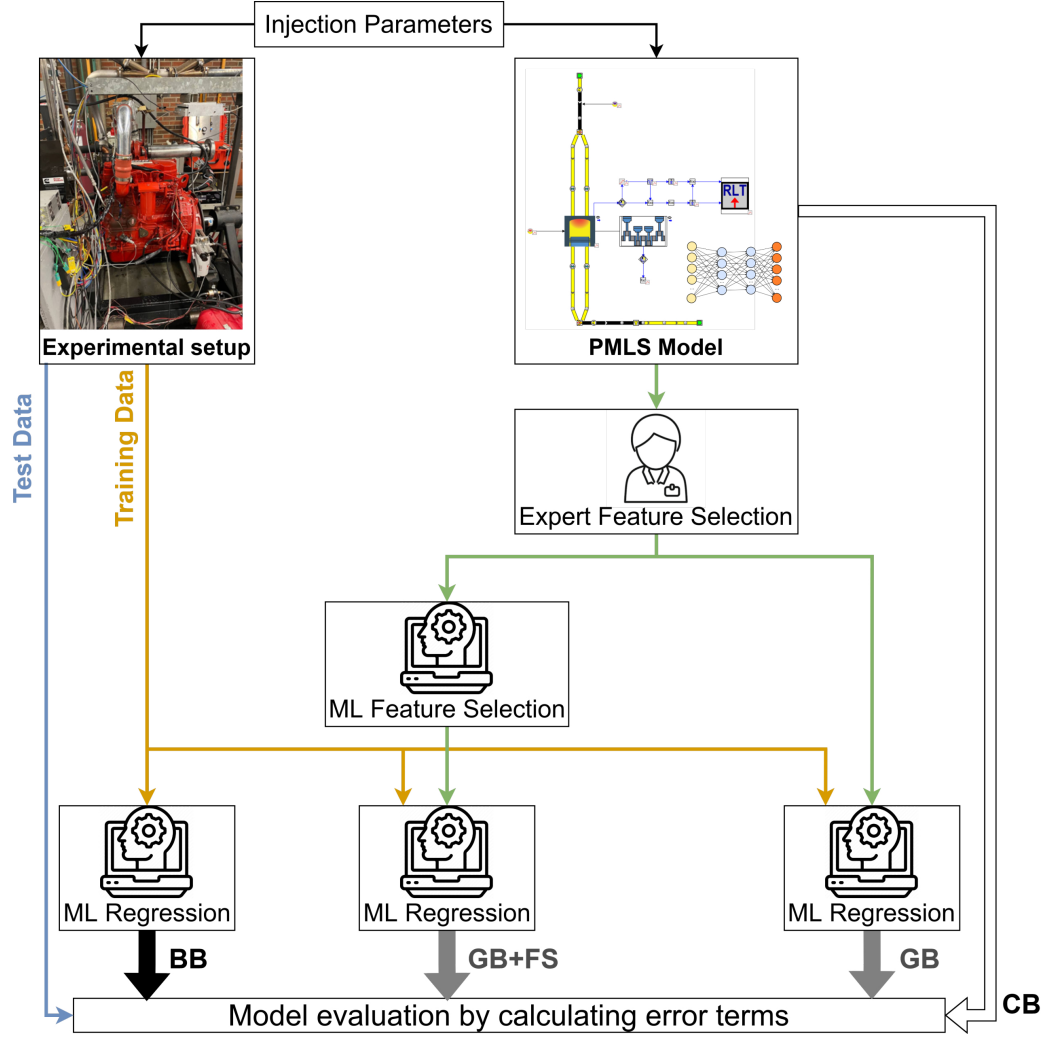
Figure 5.5: Overview of the physics-based model with machine learning laminar flame speed (clear-box (CB)), gray-box (GB), gray-box+ LASSO feature selection (GB+FS), gray-box (GB) and black-box (BB) emission models. The hollow arrow shows CB model, gray arrows show GB models, and black arrow shows BB model. In addition, the training data is shown with orange colour, the test data is shown with blue colour, and the output data from physics-based model is shown with green colour.

5.2.1 Regression models

Artificial neural network (ANN) method

Here, ReLU activation function is used for ANN models. λ is the ridge (L2) regularization penalty term that controls the so called bias-variance trade off. Higher λ values generally reduce variance and increases model bias. Higher numbers of hidden

layers and neurons will result in a more complex model and generally reduces model bias and increases model variance but overfitting should be avoided.

Gaussian process regression (GPR) method

GPR is a non-parametric kernel-based probabilistic ML method in which a probability distribution over a space of functions is used to predict the response. In the GPR method, the form of the former mean function of the model is determined by a basis function. In this chapter, the optimized form of basis function is selected among zero, constant and linear functions. The kernel function determines the correlation in the response based on the distance between the predictor values and the response. Here, the optimized kernel function is selected from rational quadratic, squared exponential, matern 5/2, matern 3/2, and exponential rational quadratic kernel functions for each GPR model [206]. For further model performance improvement, both isotropic and non-isotropic kernels have been tested. The isotropic kernel uses the same correlation length scales for all of the predictors, whereas in non-isotropic kernels, each predictor variable has its own separate correlation length scale. Using a non-isotropic kernel can enhance model performance, but it increases the training time [206]. Kernel scale is the correlation length scale that is used for all predictors. Lower values of kernel scale generally increase the variance and decrease the model bias. Finally, σ is the estimated noise standard deviation. Higher σ values generally result in variance reduction and increased bias [206].

Support vector machine (SVM) method

SVM regression is a non-parametric method, in which a kernel function is used for training instead of using the data directly for training (more details in Chapter 4. Kernel function increases the dimension of the training data [8]. In this chapter, the optimized kernel function is selected from Gaussian, linear, quadratic and cubic functions. The box constraint parameter (ϵ) determines the penalty applied to ob-

servations with large residuals. Higher box constraint values generally increase the variance and decrease the model bias. The kernel scale hyperparameter controls the scale of the predictors, which highly influences the kernel's variation. Higher kernel scale value generally reduce the variance and increase the model bias. Finally, prediction errors smaller than ϵ are neglected and treated as zero. Higher ϵ values generally reduce the variance and increase the model bias.

To achieve the best performance using ML models it is necessary to avoid over fitting while achieving the highest possible accuracy. In this study, 80% of the data was used for training of the ML methods and 20% of the data was used as the test data. The k-fold cross validation technique with 5 folds is used to avoid overfitting in the training process. This cross-validation algorithm rearranges and divides the training dataset randomly into k groups. During each iteration of the algorithm, a fold is selected, a model is trained on the remainder of the groups (excluding the fold), then the developed model is assessed based on the selected fold.

5.2.2 Hyperparameter optimization

To achieve the high levels of accuracy, the hyperparameters of each ML method are optimized using Bayesian optimization algorithm [207]. This algorithm is minimizing a scalar objective, which in this study is the minimum square error. Three important factors are involved in this process: i) Gaussian model $f(x)$, ii) Bayesian update process of $f(x)$ and iii) Acquisition function $a(x)$. Different functions can be used as the acquisition function $a(x)$. In this study, the expected improvement (EI) is used as the acquisition function:

$$\text{EI}(x, Q) = E_Q[max(0, \mu_Q(x_{best}) - f(x))] \tag{5.4}$$

where x_{best} is the location of the posterior mean, $\mu_Q(x_{best})$ is the lowest value of the posterior mean, Q is the posterior distribution over function $f(x)$ and x is the new point.

In the optimization process, first, the algorithm evaluates $y_i = f(x_i)$ for the randomly selected seed points (x_i). At each iteration, the algorithm updates the hyperparameter values and obtain a posterior distribution over functions $Q(f|x_i, y \ for \ i = 1, ..., N)$, where N is the number of hyperparameters. Finally, the algorithm finds the new point x based on maximizing the acquisition function $a(x)$. The developed models, along with hyperparameters of each ML method are summarized in Table 5.2.

Table 5.2: Optimization hyperparameters of the ML-based emission models. In this table λ is the regularization parameter, σ is the estimated noise standard deviation, and ϵ is the maximum tolerable deviation.

ML Method	Optimization Method	Optimization Hyperparameters
ANN	Bayesian	Number of hidden layers (1-3)
		Number of neurons in each layer (1-300)
		λ
GPR	Bayesian	Basis function
		Kernel function
		Kernel scale
		σ
SVM	Bayesian	Kernel function
		Box constraint
		Kernel scale
		ϵ

5.3 Results and Discussion

Two important aspects in BB and GB emission modeling are the input feature-set and ML method. In this section, the effects of these two factors on the emission model performance are investigated using three input feature sets and three ML methods. The three input feature sets in this study are: BB feature set (only injection param-

eters including timing and injection mass for hydrogen and diesel fuels), GB feature set (including all of the selected features from the PMLS by means of expert knowledge) and GB + LASSO feature set which uses LASSO feature selection algorithm in addition to the expert knowledge to select the input feature set. Figure 5.6 shows the prediction versus experiment for training and test data for NO_x and soot emissions using these feature sets. In addition, Table 5.3 shows the accuracy and error terms for NO_x and soot emissions using different input feature sets as well as NO_x prediction by the PMLS (Zeldovich mechanism). ML based models (BB and GB models) are much more accurate than PMLS which justifies the use of ML methods for emission modeling. As seen in Figure 5.6 and Table 5.3, for both NO_x and soot emissions, GB models outperform BB models. Figure 5.7 shows the improvement in RMSE and the maximum error by using GB models and feature selection compared to the BB models. Based on Figure 5.7, both NO_x and soot GB models have at least 40% lower maximum error and RMSE compared to the BB versions of these models. In addition, as seen in Figure 5.7, using ML feature selection in GB models leads to further reduction in these error terms (around 10% for soot emissions and around 20% for NO_x emissions). The improved performance of the GB model is attributed to the use of a physical model which provides the ML model more information compared to the BB model. LASSO feature selection further improved the performance of the GB models for both NO_x and soot emissions, although it had a large improvement for the NO_x model compared to the soot model. This improvement is attributed to the fact that feature selection prevents using unnecessary data in the training process which results in less model bias and better model performance on the test data. As seen in Figure 5.7, feature selection reduced RMSE and maximum error 13% and 27% for NO_x emissions, and 13% and 7% for soot emissions compared to the GB models without feature selection. The GB model with feature selection for NO_x emissions achieved around 70% lower maximum error and RMSE compared to the BB model, whereas the GB model with feature selection for soot emissions achieved around 50%

lower maximum error and RMSE compared to the BB model. In summary, the GB models are shown to be accurate for predicting NO_x and soot emissions, while adding ML feature selection to the GB models makes them more reliable and accurate by reducing the maximum error in the prediction.

All of the developed ML models have similar prediction computation times. The computation time for each case of the PMLS is 7.13 seconds. Because the GB models need to run the PMLS for each case, the overall computation time for the GB models are 7.13 seconds higher than the BB models as it can be seen in Table 5.3. All of the simulations in this study has been carried out using Intel^R Xeon^R CPU E3-1245 V2 @ 3.40 GHz processor and 32 GB RAM. Based on [1], using a thermo-kinetic combustion mechanism instead of ML LFS model will increase the prediction time for each case of the model from 7.13 s to more than 2 hours. This makes the thermo-kinetic model impractical for GB emission modeling purposes. Even by using ML LFS, GB models are still impractical for model-based control due to their computational time. However, high accuracy of the GB models compared to the BB models makes them better suited for use as a virtual engine for HIL setups where higher computational power is available and model accuracy is more important. The HIL setup can be used for engine control calibration, and assessment of combustion control strategies.

NO_x emission predicted by PMLS is among the selected features by LASSO feature selection for both NO_x and soot emissions prediction. This shows although emission prediction by 1D physics-based models might not be accurate enough for direct emission prediction, these models can improve the GB model prediction when their emission prediction is used as an ML model input. Figure 5.8 shows the experimental value, as well as different model prediction values for NO_x and soot emissions for 79 different cases. The developed PLMS model in this study can predict NO_x emission using Zeldovich mechanism but it can not predict soot, since it is recognized that physical 1D soot models do not have the capability to predict soot emissions accurately [3]. Figure 5.8a shows that PMLS NO_x emission prediction is not as ac-

curate as other models, but it follows the experimental trend which explains why it has been selected by LASSO feature selection algorithm as an important feature. Comparing the BB model and the GB model prediction with the experimental values clearly shows that GB model outperforms the BB model for NO_x and soot emission predictions. This can be attributed to the extra information provided by the PMLS including NO_x prediction using Zeldovich mechanism. This highlights the importance of using a combination of PMLS and data-driven ML models in the form of GB method for emission prediction to achieve higher accuracy.

To investigate the performance of other ML methods, GPR and SVM, with the best performance for emission prediction, are compared to the other ML methods in [3], and are also tested to predict NO_x and soot emissions using the best feature set (GB+LASSO). Similar to the ANN method, the hyperparameters of the GPR and SVM models were optimized using the methodology that was explained in Section 5.2 and Chapter 4. Figure 5.9 shows the prediction versus experiment for training and test data for NO_x and soot emissions using GB+LASSO feature set and by means of ANN, GPR and SVM ML methods. In addition, Table 5.4 shows the accuracy and error terms for NO_x and soot emissions prediction for these models. GPR and ANN have almost the same performance and they are very accurate for emission prediction ($R^2_{\text{test}} > 0.99$). The SVM models are less accurate, especially for NO_x emissions. Based on these results, soot and NO_x emissions of the dual-fuel hydrogen-diesel engine can be predicted with R^2_{test} higher than 0.99 when using an optimized ANN or GPR with GB+LASSO feature set. The run time is very similar among the three methods since the main processing time was attributed to getting values of features from the GT-Power model.
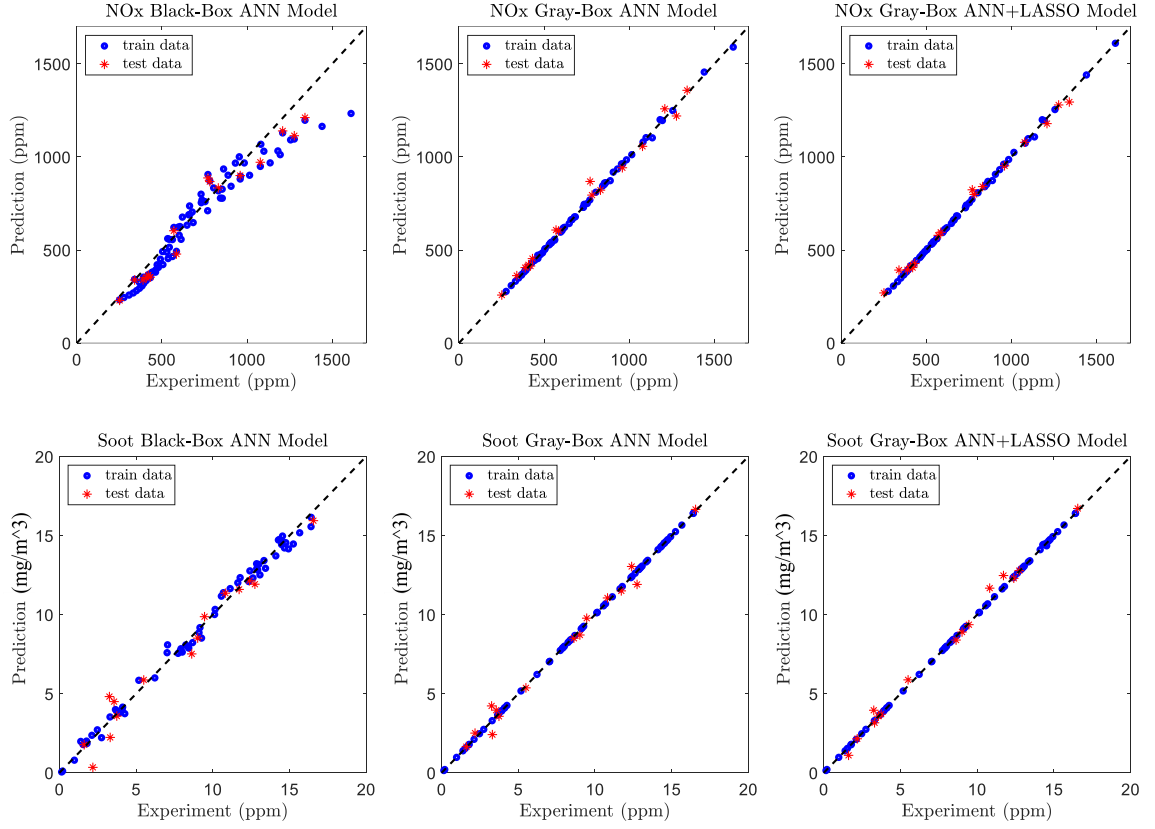
Figure 5.6: Prediction versus experiment for the developed ANN models using Black-box, gray-box and gray-box+LASSO feature sets for NO_x and soot emissions.

Table 5.3: Accuracy and run time of ANN NO_x and soot emission models with different input feature sets. PMLS stands for physical model with machine learning laminar flame speed. t_{run} is the simulation time for each case.

Emission	Criteria	PMLS	ANN-Black-Box	ANN-Gray-box	ANN-Gray-Box+LASSO
NO_x	R^2_{test}	0.751	0.957	0.991	0.996
	$RMSE_{test}$ (ppm)	185.51	83.54	35.27	24.65
	$|E_{test,max}|$ (ppm)	471.33	163.25	98.16	53.40
	t_{run} (s)	7.13	0.002	7.132	7.132
Soot	R^2_{test}	-	0.97	0.99	0.995
	$RMSE_{test}$ (mg/m³)	-	0.848	0.499	0.385
	$|E_{test,max}|$ (mg/m³)	-	1.83	0.97	0.86
	t_{run} (s)	-	0.002	7.132	7.132
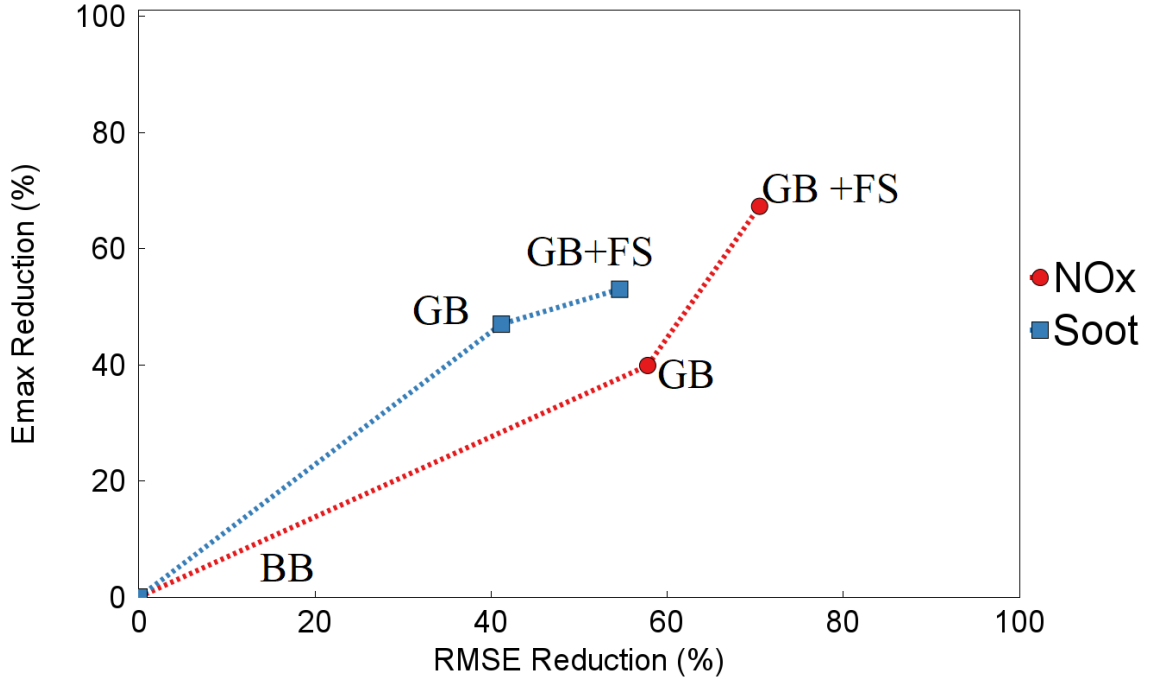
Figure 5.7: Maximum error and RMSE reduction of the gray-box models (GB) and the gray-box + LASSO feature selection models (GB+FS) compared to the black-box models for NO_x and soot emissions.

Table 5.4: Error terms of ANN, SVM and GPR for NO_x and soot emission models using gray-box + LASSO feature set. t_{run} is the simulation time for each case.

Emission	Model	Criteria	ANN	GPR	SVM
NO_x	Gray-box+LASSO	R^2_{test}	0.996	0.998	0.95
		$RMSE_{test}$ (ppm)	24.65	13.16	111.84
		$|E_{test,max}|$ (ppm)	53.40	31.40	292.39
		t_{run} (s)	7.132	7.132	7.132
Soot	Gray-box+LASSO	R^2_{test}	0.995	0.995	0.98
		$RMSE_{test}$ (mg/m^3)	0.385	0.337	0.529
		$|E_{test,max}|$ (mg/m^3)	0.86	0.62	1.49
		t_{run} (s)	7.133	7.132	7.133

(a)

(b)
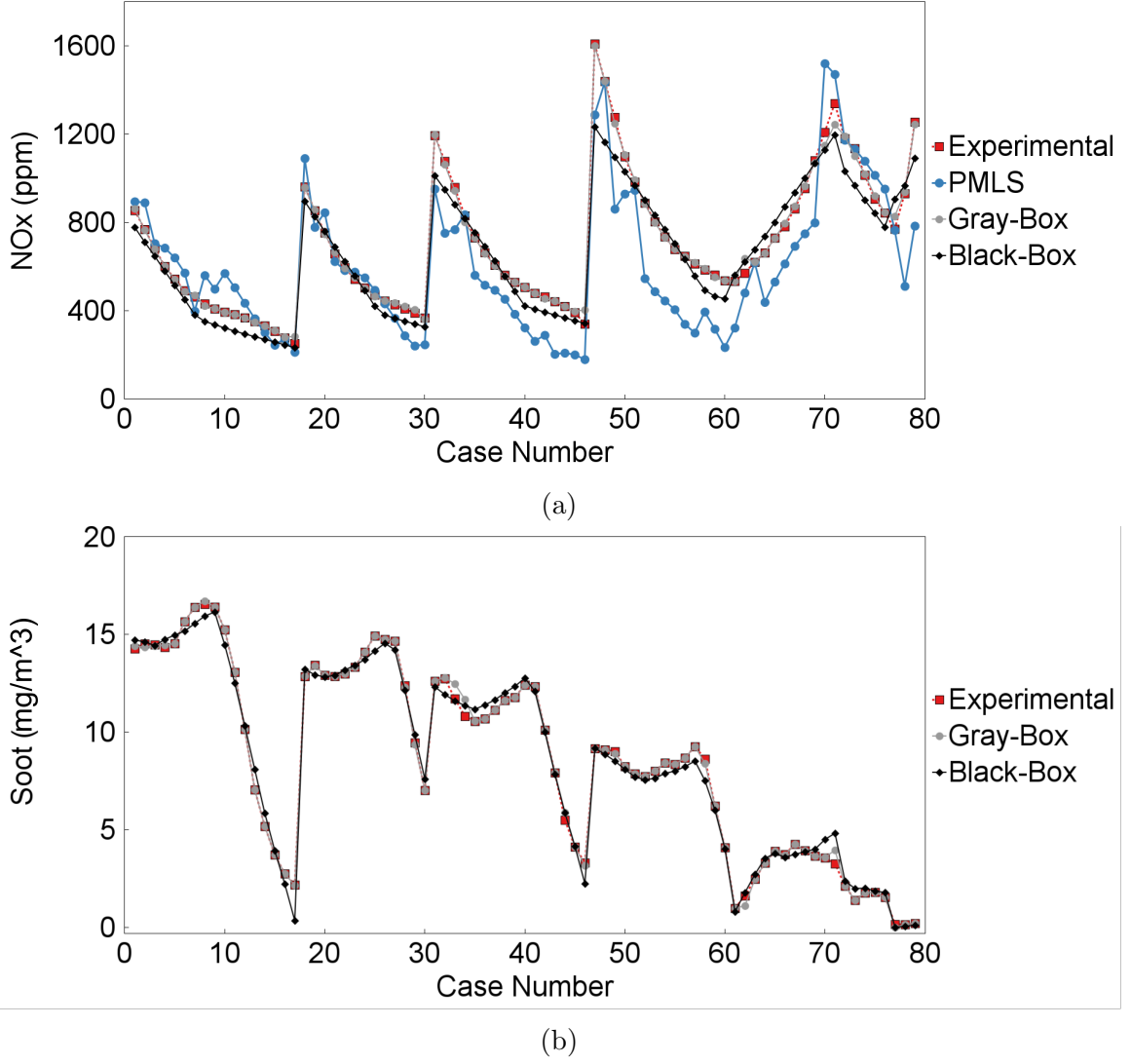
Figure 5.8: Experimental and predicted NO$_x$ and soot emissions. PMLS stands for physical model with machine learning laminar flame speed. Average covariance of the experimental measurement for NO$_x$ and soot emissions are 2.1 and 5.7, respectively.
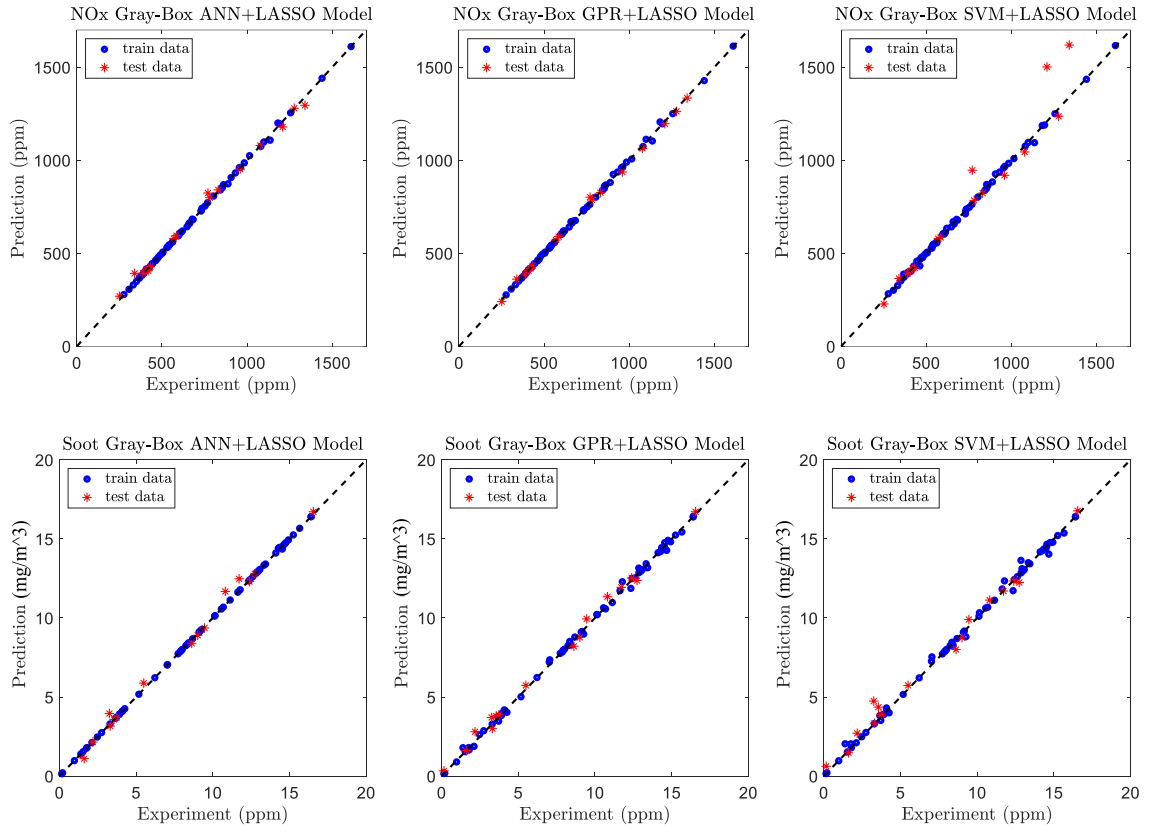
Figure 5.9: Prediction versus experiment for the developed ANN, GPR, and SVM models using gray-box+LASSO feature set for NO_x and soot emissions.

5.4   Summary of chapter

The development of computationally-efficient accurate emission models for hydrogen fueled engines was described. In particular, methods to expedite physical modeling along with black-box (BB) and gray-box (GB) methods were studied. Laminar flame speed (LFS) which is an input of the physical combustion model was calculated using artificial neural network (ANN) machine learning (ML) method from Chpater 3 to speed up simulation for the physics-based engine emission model. Embedding ML LFS model in the physics-based engine model formed a physical model with machine learning laminar flame speed (PMLS) which is computationally much faster than the similar physical models. Combustion and LFS models were validated by experimental data from a spark ignition hydrogen engine and a compression ignition dual-fuel hydrogen-diesel engine. Then, a physics-based, BB and GB emission models were created for the dual-fuel hydrogen-diesel engine. BB emission models were developed by training and optimizing ML methods using experimental data from the test bench, whereas both measured data from the experimental setup and outputs of the PMLS were used for training and optimizing ML methods in GB emission modeling. The main findings of this chapter are as follows:

- Using embedded ML LFS model instead of thermo-kinetic combustion mechanisms in the physics-based model led to the PMLS which is more than a thousand time faster than the traditional physical models that use thermo-kinetic combustion mechanism. Fast engine simulation enables the development of GB emission models using PMLS for NO_x and soot emissions in an expeditious way.

- The developed GB emission models are suitable for use as a virtual engine for a hardware-in-the-loop (HIL) setup where more computational time is less critical compared to a production electronic control unit (ECU) for combustion control. Thus the HIL can benefit from high fidelity, fast emission models.

- The developed BB models are approximately thousand times faster than the GB models, making them suitable for model-based control applications where computation time is crucial. The developed BB models in this chapter can predict NO_x and soot emissions in 0.002 s for each case using Intel® Xeon® CPU E3-1245 V2 @ 3.40 GHz processor and 32 GB RAM.

- GB emission models showed better performance compared to the BB emission models. Since the PMLS is part of the GB model and provides extra information, this enables the GB model to predict emissions more accurately. For example, although physically predicted NO_x was not of sufficient accuracy, it followed the experimental trend for all of the cases, making it a useful additional feature for emission prediction. NO_x emissions predicted by the Zeldovich mechanism in PMLS was among the selected features by ML feature selection algorithm for both NO_x and soot GB models. This demonstrates that a 1D physics-based model emission prediction can be used as an important input to the ML methods to improve ML model performance. Compared to the BB models, the developed GB emission models have approximately 70% lower maximum error and RMSE for NO_x emissions and around 50% lower RMSE and maximum error for soot emissions on test data.

- The PMLS provides many output parameters for use in feature selection with the selection of important features difficult using expert knowledge. Feature selection using ML prevents unnecessary data entering training process of ML method which results in less bias and better prediction on the test data. ML feature selection helped GB models to reduce RMSE and maximum error around 13% and 27% for predicting NO_x emissions and 13% and 7% for predicting soot emissions on test data, respectively.

PART IV: Machine Learning in Transient Emission Modeling

Chapter 6

Hybrid Transient Emission Modeling of a Hydrogen-Diesel Fueled Engine [1]

Development of transient NO_x emission models of hydrogen-diesel engine as a tool for future engines to minimize NO_x emissions is the focus of this chapter. The reduction of emissions from internal combustion engines (ICEs) is an urgent research priority due to environmental crises and global warming and the relevant regulations. One promising approach is to use alternative fuels like hydrogen to significantly decrease ICEs' carbon footprint. Converting medium and heavy-duty diesel engines to dual-fuel hydrogen-diesel engines is the focus as these engines are hard to electrifies. However, adding hydrogen can increase the combustion temperature and result in elevated NOx emissions, which highlights the need for accurate and fast NOx emissions models. To minimize NOx, these emission models are essential for engine model-based control and for engine calibration and optimization using hardware-in-the-loop (HIL) setups. In this chapter, a fast-response NOx emissions sensor is used to measure the transient NOx emissions from a dual-fuel hydrogen-diesel engine. Subsequently, steady-state models (SSMs), quasi steady-state models (QSSMs), and transient sequential models (TSMs) in the form of black-box (BB) and gray-box (GB) models are developed for transient NOx emissions prediction. GB models utilize both infor-

---

[1] This chapter is based on [5]

mation from a 1D physical engine model and experimental data for training, while BB models only use experimental data. SSMs are optimized artificial neural networks (ANNs) trained using steady-state data, QSSMs are optimized ANNs trained using transient data, and TSMs are time-series networks trained using transient data. Long short-term memory (LSTM) and gated recurrent unit (GRU) networks are used for the time-series networks. The results showed that the 1D physical model has the worst performance and model performance improves successively from SSM to QSSM and from QSSM to TSM. The BB TSM models are the most suitable for engine model-based control, as they are fast and accurate and can predict transient NOx emissions with an R^2 value greater than 0.96 at 89,000 predictions per second. The GB TSM models are the most accurate among all the developed models that can predict transient NOx emissions with an R^2 value greater than 0.97 and more accurate steady-state performance than BB. The extra accuracy of the GB TSM models makes them the best choice for HIL setups where more computational power delivers the required high accuracy.

6.1 Methodology

6.1.1 Engine transient experimental data

The engine experimental setup from Section 2.3 (Figure 2.3) was utilized to measure NOx emissions over 82300 engine cycles at constant engine speed of 1500 RPM which is a duration of over 6500 seconds. To control combustion, this diesel engine employs two diesel injection pulses - a short pilot injection and a longer main diesel injection as shown in Figure 2.4. The control injection parameters in the experimental tests are: i) the crank angle at the start of injection for pulse 1 (SOI_{D1}), ii) the crank angle at the start of injection for pulse 2 (SOI_{D2}), iii) the duration of injection for pulse 2 (DOI_{D2}) which affects the diesel injection amount, and iv) the duration of hydrogen injection (DOI_{H2}) which affects the hydrogen injection amount. While the duration of diesel

injection pulse 1 was kept constant (DOI_{D1}), the input ranges for SOI_{D1} and SOI_{D2} were adjusted to ensure that the diesel injection pulses did not overlap. The inputs and outputs of these experimental measurements are shown in Figure 6.1. As it seen the testing conditions were highly transient, with the hydrogen energy ratio varying from 0 to 80%. The same experimental setup setup was also used for NOx emissions measurement of 79 steady-state cases, which are used for calibrating WB model and developing SSM models. The steady-state data are also used for investigating the performance of QSSMs and TSMs in steady-state conditions.
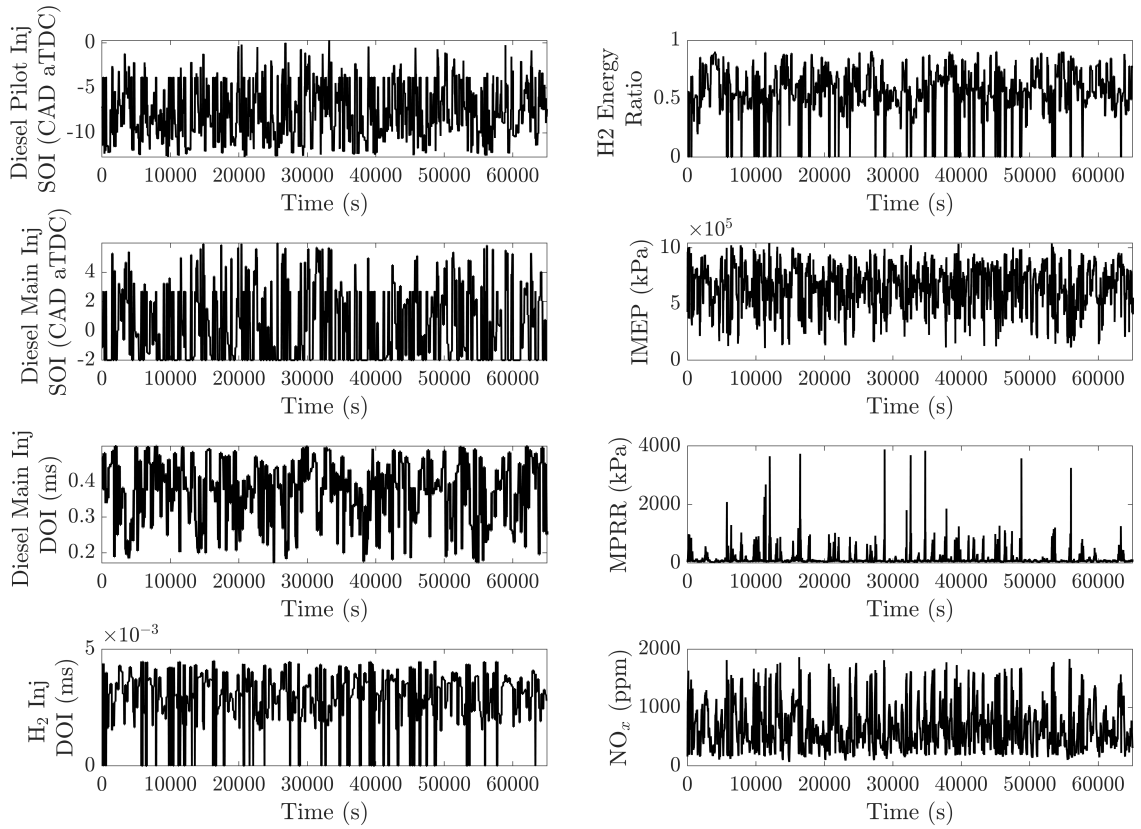
Figure 6.1: Dual-fuel compression ignition hydrogen-diesel engine experimental data over 82300 engine cycles at constant engine speed of 1500 rpm and without EGR. MPRR stands for maximum pressure raise rate. NOx emissions experimental range is 0-1860 ppm.

6.1.2 Physical model

The physical model or WB model for the dual-fuel hydrogen-diesel was created using the dual-fuel combustion model in the GT-Power software. This model is a combination of direct-injection diesel multi-pulse and SI combustion model that designed for dual-fuel SI-CI combustion. The cylinder contents in the model are divided into three thermodynamic zones with distinct compositions and temperatures. That includes an unburned zone, a spray zone with injected fuel and entrained gas, and a spray burned zone with combustion products. The combustion rate is predicted based on the amount of unburned mixture behind the flame front, which is influenced by the sum of the turbulent flame speed (TFS) and the flame area. The ML-based LFS model from Chapter 3 is used for LFS calculation which is then used to calculate TFS. The developed PMLS model in Chapter 5 is used as the physics-based in this chapter.

The PMLS model is used for GB modeling similar to the methodology in Chapter 5. To do this, the physical model produces physical outputs for each engine case. The physical outputs are then selected through a combination of expert knowledge and FS algorithms. These selected outputs form the training data for the ML algorithm results in a GB model that is trained using a wider range of input parameters compared to BB models which are only trained using four main inputs (SOI_{D1}, SOI_{D2}, DOI_{D2} and DOI_{H2}).

6.2 Machine Learning and Deep Learning Methods

ML models are now employed for predicting NOx emissions through three methodologies: SSM, QSSM, and TSM.

6.2.1 SSM and QSSM emissions models

A fully connected ANN was selected as the classical ML approach for SSM and QSSM, since it was found in Chapters 4-5 that optimized ANNs can outperform other classical ML algorithms such as SVM, RF, GPR, and ERT. The hyperparameters of the ANN model, including the number of hidden layers, the number of hidden neurons per layer, and the regularization parameter (λ), were optimized using Bayesian optimization method. This optimization involves three main components: i) Gaussian model $f(x)$, ii) Bayesian update of $f(x)$, and iii) the Acquisition function $a(x)$. The algorithm updates the hyperparameter values at each iteration and obtains a posterior distribution over the functions $Q(f|x_i, y)$ for $i = 1, ..., N$, where N represents the number of hyperparameters. The algorithm then identifies the new point x by maximizing the acquisition function $a(x)$ similar to the methodology used in Chapters 3, 5.

The SSM models were trained and validated using 79 steady-state cases of dual-fuel hydrogen-diesel engine. For the QSSMs, over 82300 transient cycles were used (Figure 6.1), with 70% of the data designated for training, 15% for validation, and 15% for testing. The QSSMs were trained using the training data and the best models were selected based on their performance on the validation set. Finally, the models were tested using the test data which was not used for training or validation.

6.2.2 TSM emissions models

TSM models use time series sequential ML algorithms, such as LSTM and GRU networks, which are RNN algorithms that use gates to overcome the vanishing gradient problem. A GRU network [208] has two gates, a relevance gate, and an update gate, along with one memory cell $c^{<t>}$. The memory cell retains information about previous time steps, and the relevance gate determines how much influence the memory cell should have on the current prediction. The update gate determines whether the memory cell information needs to be updated using a cell candidate $\tilde{c}^{<t>}$. In this

algorithm, the activation at each time step $a^{<t>}$ is equal to $c^{<t>}$. On the other hand, an LSTM network [209] is a more complex RNN algorithm with three gates: the update gate, forget gate, and output gate. In this algorithm, $a^{<t>}$ is different from $c^{<t>}$, and the output gate's job is to determine $a^{<t>}$ based on $c^{<t>}$. In an LSTM network, $c^{<t>}$ first enters the forget gate to drop unnecessary information. Then, the update gate adds new information to $c^{<t>}$ using $\tilde{c}^{<t>}$. The key difference between LSTM and GRU is that LSTM can drop and add information to $c^{<t>}$ separately. This capability gives the LSTM algorithm more predictive power for time series, but it also makes it more complex and time-consuming to train since it has more trainable parameters than GRU. In addition, in an LSTM network, $a^{<t>}$ is not similar to $c^{<t>}$, and the output gate calculates $a^{<t>}$ from $c^{<t>}$ at each time step. Table 6.1 shows the summary of equations for LSTM and GRU networks.

Time-series deep learning algorithms

LSTM and GRU networks are employed to construct TSM models for BB and GB NOx emissions. Figure 6.2 shows the schematic of the BB LSTM and GB GRU TSMs. Similar architectures are also used for the GB LSTM and BB GRU TSMs. As it seen, the ESM acts as an extra layer in the network for the GB models. The TSM network architecture comprises three fully connected layers at the beginning, followed by a time series layer (either LSTM or GRU), a drop-off layer, and an output layer at the end. The drop-off layer randomly deactivates half of the network during each training iteration, thereby reducing overfitting and training computational expenses. This architecture was determined through trial and error and trade-off between complexity and minimizing error. To train these models, MATLAB Deep Learning Toolbox© with the Adam algorithm with mini batch size of 1024 has been used. The training, validation, and test data were similar to those used in QSSMs, and the training process continued until the validation loss consistently started to increase. At that point, the training was halted and the model with the lowest validation loss was chosen
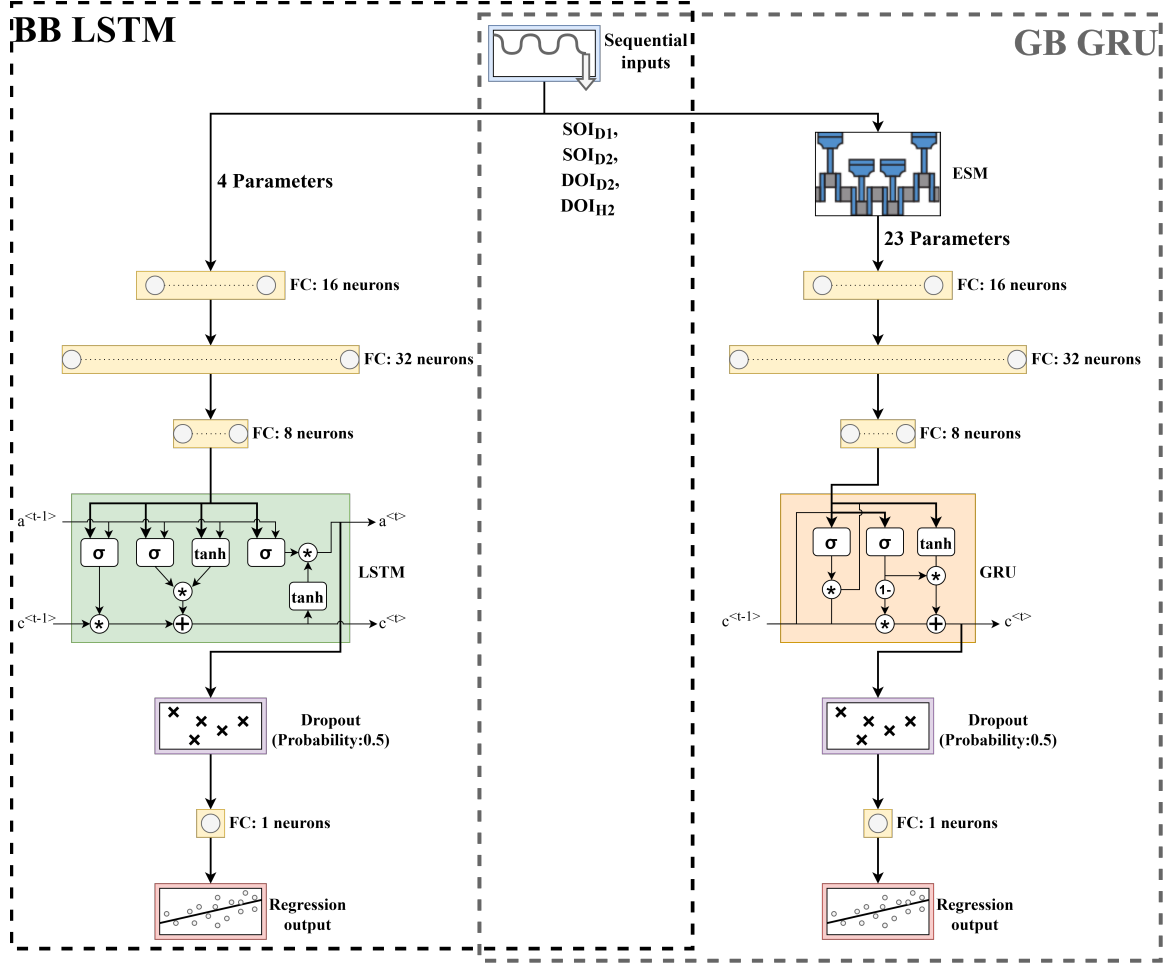
Figure 6.2: Transient sequential models architecture. Left: BB LSTM model, right: GB GRU model. SOI_{D1} is the crank angle at the start of injection for diesel pulse 1, SOI_{D2} is the crank angle at the start of injection for diesel pulse 2, DOI_{D2} is the duration of injection for diesel pulse 2, and DOI_{H2} is the duration of hydrogen injection, ESM stands for engine simulation model.

6.2.3   Feature Selection

The choice of the input feature set is a crucial factor in the performance of the emission modeling GB algorithm as it was shown in Chapter 4. It is highlighted in Chapters 4 and 5 that relying solely on expert physical knowledge may not be sufficient for selecting the most important physical features for emission modeling. Incorporating ML algorithms for FS in conjunction with expert knowledge has been shown to improve the performance of the GB model. To this end, four FS algorithms (F-test, minimum redundancy maximum relevance (MRMR), RReliefF, and least

Table 6.1: Equations of LSTM and GRU Sequential models. In the equations, $G_{u,f,o,r}$ shows gates, $b_{u,f,o,r,c}$ shows biases matrices, $W_{u,f,o,r,c}$ shows weight matrices, σ shows the sigmoid activation function, and $*$ shows element-wise multiplication.

Criteria	LSTM	GRU
Number of gates/states	3/2	2/1
Gate 1	(Update gate) $G_u = \sigma\left(W_u[a^{<t-1>}, x^{<t>}] + b_u\right)$	(Update gate) $G_u = \sigma\left(W_u[a^{<t-1>}, x^{<t>}] + b_u\right)$
Gate 2	(Forget gate) $G_f = \sigma\left(W_f[a^{<t-1>}, x^{<t>}] + b_f\right)$	(Relevance gate) $G_r = \sigma\left(W_r[a^{<t-1>}, x^{<t>}] + b_r\right)$
Gate 3	(Output gate) $G_o = \sigma\left(W_o[a^{<t-1>}, x^{<t>}] + b_o\right)$	-
Cell candidate	$\tilde{c}^{<t>} = \tanh\left(W_c[a^{<t-1>}, x^{<t>}] + b_c\right)$	$\tilde{c}^{<t>} = \tanh\left(W_c[G_r * a^{<t-1>}, x^{<t>}] + b_c\right)$
Memory cell	$c^{<t>} = G_u * \tilde{c}^{<t>} + G_f * c^{<t-1>}$	$c^{<t>} = G_u * \tilde{c}^{<t>} + (1 - G_u) * c^{<t-1>}$
Activation	$a^{<t>} = G_o * c^{<t>}$	$a^{<t>} = c^{<t>}$

absolute shrinkage and selection operator (LASSO)) were employed, and their effect on the GB model's performance was evaluated in comparison to the BB model. Here, each of the FS algorithms that are used in this study are briefly described.

F-test algorithm

F-test algorithm [210] evaluates the significance of each predictor, which involves comparing the means of response values across different predictor variable values. The p-values derived from these F-test statistics can then be used to rank the features, with higher scores corresponding to lower p-values. Essentially, an F-test examines whether the response values for different predictor variable values are drawn from populations with the same mean or not, and the resulting scores reflect the negative logarithm of the p-values.

MRMR algorithm

The MRMR algorithm [211] aims to identify the most effective set of features that can accurately represent the response variable, while ensuring that the features are both mutually and maximally dissimilar. To achieve this, the algorithm works towards minimizing the redundancy of the selected feature set, while simultaneously maximizing its relevance to the response variable. This is done by quantifying both the redundancy and relevance of the features using mutual information measures, which consider the pairwise mutual information of features as well as the mutual information of a feature with the response variable. The MRMR algorithm [211] is specifically designed for regression problems, and its objective is to identify an optimal feature set S that maximizes the relevance (V_S) of S with respect to the response variable y, while minimizing its redundancy (W_S), as defined through mutual information I.

RReliefF algorithm

RReliefF [212] is a weight-based algorithm that determines the importance of predictors when the response variable y is a multiclass categorical variable. The algorithm aims to penalize the predictors that generate different values for observations belonging to the same class while rewarding those that generate different values for observations belonging to different classes. Initially, RReliefF sets all the weights for predictors, denoted as W_j, to zero. The algorithm then proceeds iteratively by selecting a random observation x_r, finding the k-nearest observations for each class, and updating the weights for the predictors F_j based on the values of the nearest neighbors x_q. Specifically, the weights of the predictors are updated by decreasing the value of W_j if the predictor F_j generates different values for observations belonging to the same class, and increasing the value of W_j if F_j generates different values for observations belonging to different classes. This algorithm works for categorical and continuous features.

LASSO algorithm

As it was explained in Chapters 4 and 5, LASSO is a type of regression analysis that combines variable selection and regularization to improve the model's predictive accuracy. Specifically, the LASSO regression incorporates a penalty term, represented by the variable λ, in the cost function to penalize the l_1 norm. This approach tends to drive the weights of certain features down to exactly zero, resulting in a sparse solution that automatically selects the most relevant features for the prediction task. Here, the degree of sparsity is controlled by the value of λ, which is tuned using a cross-validation approach.

6.3   Results and Discussion

The input feature set for all BB models was comprised of four features: SOI_{D1}, SOI_{D2}, DOI_{D2}, and DOI_{H2}. To construct GB models, expert physical knowledge of NOx emissions formation was used to initially identify the most important physical features, which are outputs of the physical model. Then, four FS algorithms (F-test, MRMR, RReliefF, and LASSO) were employed on the transient training dataset to further narrow down the selected features. Table 6.2 shows the performance of ANN QSSMs that were trained and optimized using the selected features from each FS algorithm, and Figure 6.3 provides a comparison of the performance of each FS algorithm with the BB model in terms of maximum error improvement, root-mean-square-error (RMSE) improvement, mean absolute percentage error (MAPE) improvement, and R^2 improvement.

The expert selection (ES) of features, which involves using all features selected based on physical knowledge alone, resulted in a weaker performance compared to most other FS algorithms that combined expert knowledge with ML algorithms. The F-test algorithm outperformed the other FS algorithms, with the highest improvement of RMSE, maximum error, and R^2 values compared to the BB model. It also has a

very similar MAPE value to RRelief, which has the lowest MAPE. Furthermore, it can be seen that the use of GB modeling significantly improves emission prediction for QSSMs compared to BB models. The GB QSSM, which uses the F-test FS algorithm, outperformed the BB model in terms of MAPE and RSME by over 30% and 40% respectively. This indicates that the GB model is significantly more accurate than BB model. The improved accuracy can be attributed to the physical model being integrated into the GB model, which provides additional information for the ML method and captures the transient nature of the emission. The physical model's output is dependent on previous states and is fed into the classical ML method, resulting in improved performance on transient data. In contrast, the BB QSSM relies solely on injection inputs from the current time step for prediction and cannot utilize information from previous steps. Furthermore, the NOx emissions prediction by the physical model is among the selected features by all of the algorithms. This shows that although 1D physics-based models may not be sufficiently accurate for direct transient emission prediction, they can still enhance the performance of GB models when used as inputs for ML models.

The F-test algorithm selected almost all of the features chosen by other FS algorithms, and the 23 features it identified were used for QSSMs and TSMs. For SSM, a similar approach was followed, and seven features were selected using the F-test algorithm, as the training dataset for SSM comprised steady-state data.

Table 6.2: NOx emissions prediction of Grey-box quasi steady-state models using different feature sets selected by different feature selection methods. NOx emissions experimental range is 0-1860 ppm.

Metric	BB	GB-ES	GB-F-test	GB-RReiliefF	GB-LASSO	GB-MRMR
Number of features	4	42	23	10	7	7
R^2_{test} (%)	68.4	78.9	87	83	81.4	69.4
$RMSE_{test}$ (ppm)	216.8	180.4	140.5	159.5	166.7	216.6
$|MAPE_{test}|$ (%)	60.7	20.4	15.5	15.2	18.1	21.5
$|E_{test,max}|$ (ppm)	1374	1156	1051	1211	1395	1646
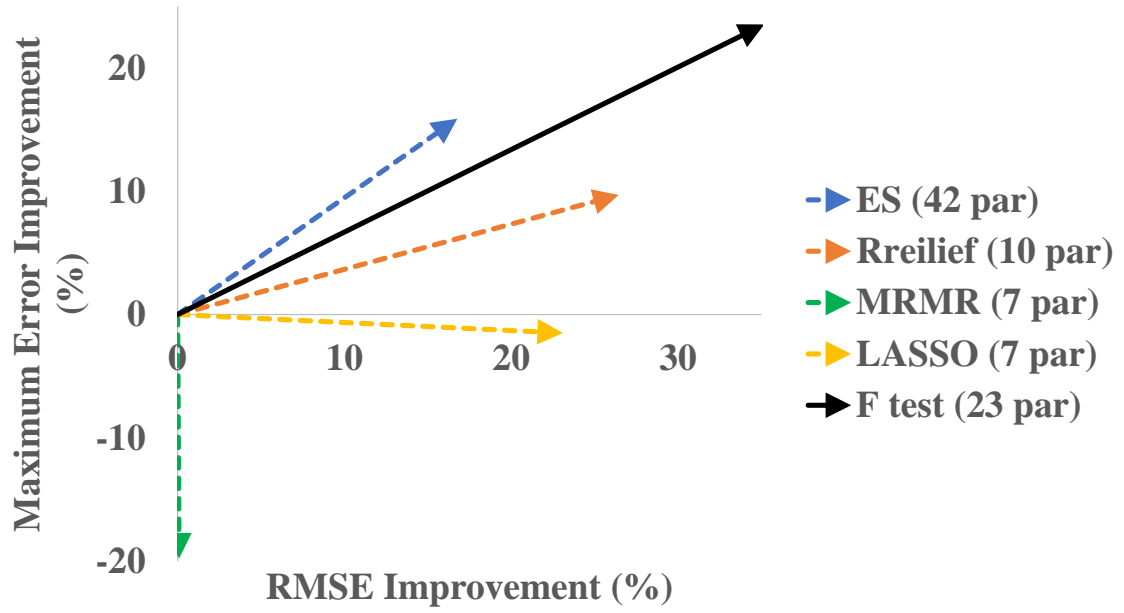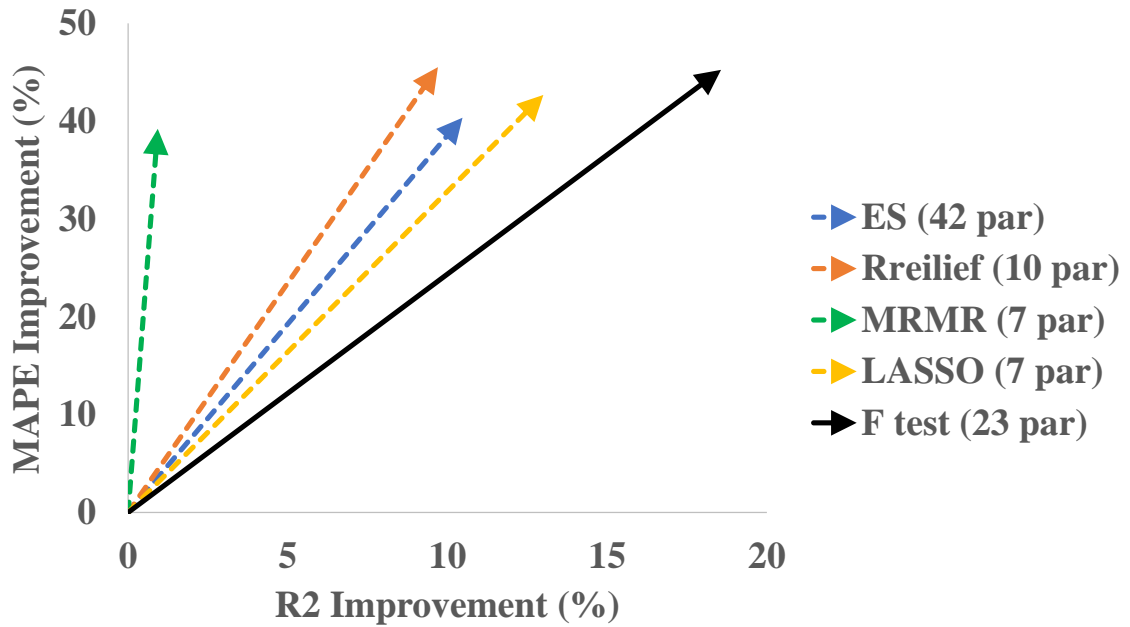
Figure 6.3: Comparison of black-box and grey-box quasi steady-state models with feature selection using different algorithms. a) Maximum error and RMSE improvement compared to black-box model, b) MAPE and R^2 improvement compared to black-box model

The number of hidden units in the time series layer is a critical factor that significantly affects the ability of TSMs to capture the sequential nature of the transient emission data. However, a very high number of hidden units can lead to a more complex model that is unsuitable for engine model-based control and might also result in overfitting. To determine the optimal number of hidden units in the time series layer, the BB LSTM architecture (shown in Figure 6.2) with different numbers of hidden units within the LSTM layer were developed. The training and validation transient NOx emissions dataset were used for this purpose. The modeling was carried out using a system equipped with an Intel^R Xeon^R CPU E3-1245 V2 @ 3.40 GHz processor and 32 GB of RAM.

As shown in Table 6.3, increasing the number of hidden units results in a higher number of trainable parameters in the model, which can increase training and prediction time. An increase in the number of hidden units initially leads to a significant improvement in model performance. However, this trend eventually slows down, and after a certain point, increasing the number of hidden units has little to no effect on model performance and may even degrade it.

The analysis shows that increasing the number of hidden units up to 16 (as shown in Figure 6.4) improves model accuracy without significantly affecting computational speed. Increasing the number of hidden units from 16 to 64 slightly improves model accuracy but makes the model slower. Increasing the number of hidden units past 64 only results in a slower model without a corresponding increase in accuracy. Considering the trade-off between accuracy and computation cost, a range of 16 to 64 hidden units appears to be the best choice.

Based on this analysis, if accuracy is the most critical factor in the accuracy-computational cost trade-off, the recommended choice would be the LSTM network with 64 hidden units. To investigate the performance of other popular time series network (GRU) and the effects of GB modeling on time series networks, GB LSTM model, BB GRU model and GB GRU model (shown in Figure 6.2) were modeled with

Table 6.3: Effect of hidden unit number on LSTM model performance in NOx emissions prediction.

Dataset	Metric	LSTM1	LSTM2	LSTM3	LSTM4	LSTM5	LSTM6
	Number of hidden units	4	8	16	32	64	128
	Number of model parameters	1100	1400	2500	6100	19600	71100
	Prediction per second	82000	75000	69000	59000	46000	20000
Transient (83000 cycles)	R^2_{test} (%)	95.7	95.7	96.7	96.7	96.7	96.7
	$RMSE_{test}$ (ppm)	127	93.7	77.4	76.1	72.3	71.9
	$MAPE_{test}$ (%)	16.8	12.1	9.1	8	7.8	7.5
	$|E_{test,max}|$ (ppm)	590	439	408	479	397	585
Steady-state (79 cases)	RMSE (ppm)	200.7	200.7	217	170	168	162
	|MAPE| (%)	24	24	26	20	20	18
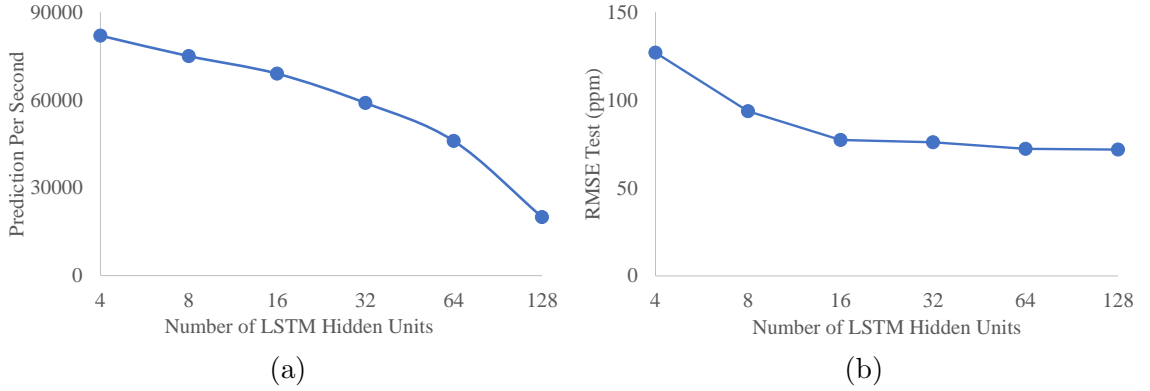
Figure 6.4: Effect of hidden unit number on LSTM model's RMSE and prediction rate.

64 hidden units within the time series layer. Table 6.4 compares the performance of these four models in terms of model complexity, computational cost, and accuracy.

The GRU model has fewer trainable parameters for the same number of units than the LSTM model because it has a simpler structure than the LSTM network. This makes the GRU model faster than the LSTM model. However, GB models are much slower in prediction than BB models because the physical model inside the GB models needs to simulate each case and feed the network with its output, making the model considerably slower.

In terms of accuracy, GB LSTM and GB GRU are more accurate than the cor-

responding BB models. This demonstrates that GB modeling can improve TSMs. However, compared to QSSMs, the difference in accuracy between GB and BB models for time series networks is much smaller. This is because time series networks are DL algorithms that effectively capture the sequential nature of the transient emission, leaving little room for improvement by using additional information provided by physical models in the form of GB models.

The GB LSTM model has the best steady-state and transient performance among the four models. It has the highest R^2, and the lowest RMSE, MAPE, and maximum error for the transient tests although all other three models are also very accurate. GB LSTM model also has the best steady-state performance (lowest RMSE and MAPE). The steady-state performance of the other three models are almost similar. The higher accuracy of GB LSTM network makes it the best option for applications where accuracy is more important than computational cost such as using the model as the virtual engine in hardware-in-the-loop (HIL) setup. For model-based engine control where computational cost is crucial, BB LSTM or GRU network with 64 units can be used. The BB GRU model is slightly less accurate than the LSTM version, but it is almost twice as fast for the same number of hidden units, making it an excellent choice for model-based control purposes.

In summary, selecting the appropriate TSM depends on the specific application's requirements. Here for NOx emissions modeling, the GB LSTM model that can predict transient NOx emissions with $R^2 > 0.97$ and MAPE=7.4% at 3 prediction per second is the best option for high accuracy applications like HIL setup. The BB GRU or LSTM networks are more than 10000 time faster than the GB LSTM model which makes them more appropriate for the applications where computational cost is crucial such as model based engine control. These models can predict transient NOx emissions with $R^2 > 0.96$ and MAPE=8% which is slightly less accurate than the GB LSTM model.

To assess the effectiveness of various modeling methodologies for NOx emissions,

Table 6.4: Comparison of time-series networks' performance for transient and steady-state NOx emission modeling.

Dataset	Metric	BB-LSTM	GB-LSTM	BB-GRU	GB-GRU
	Number of hidden units	64	64	64	64
	Number of ML model parameters	19600	20000	14900	15200
	Prediction per second	46000	3	89000	3
Transient (83000 cycles)	R^2_{test} (%)	96.7	97.1	96.6	96.7
	$RMSE_{test}$ (ppm)	72.3	67.8	72.5	71.9
	$MAPE_{test}$ (%)	7.9	7.4	8	7.9
	$|E_{test,max}|$ (ppm)	397	370	459	399
Steady-state (79 cases)	RMSE (ppm)	168	155	175	206
	MAPE (%)	20	14	21	21

Table 6.5 presents a comparison of ESM, SSMs, OSSMs and TSMs in terms of their computational cost and performance on both steady-state and transient data. Additionally, Figure 6.5 illustrates the improvement achieved by BB and GB SSMs, QSSMs, and TSMs compared to the ESM in terms of maximum error, RMSE, R^2, and MAPE. In both Table 6.5 and Figure 6.5, the BB and GB TSMs are LSTM networks with 64 units. To provide a visual representation, Figure 6.6 presents the BB and GB predictions for SSM, QSSM, and TSM, as well as the experimental NOx emissions values on the test dataset.

Comparing the performance of these models gives a better understanding of the improvement level achieved between methodologies. The results show that, overall, the performance of the models improves as we move from left to right in Table 6.5 and Figure 6.5, and from top to bottom in Figure 6.6. The GB models perform better than their BB counterparts on both steady-state and transient data which can visually be seen in Figure 6.6. In terms of transient performance, all of the ML models outperform the ESM, with BB models being considerably faster.

Overall, the ESM has the poorest transient performance compared to all models, while BB models offer improved transient performance and faster computational speed compared to traditional physical models, making them a better choice for model-based

control applications. SSMs demonstrate the best steady-state performance since these models are trained on steady-state data. Nevertheless, it is not recommended to use models trained on steady-state data for predicting transient data since SSMs perform poorly in transient situations compared to other ML methods.

In both Table 6.5 and Figure 6.5, a significant difference exists between the performance of TSMs and QSSMs, which is more pronounced than in previous studies that investigated both BB QSSMs and TSMs [138, 139]. The significant performance difference observed between TSMs and QSSMs in this study (Figure 6.5) can be attributed to the highly transient nature of the data used for modeling, as shown in Figure 6.1. The transient dataset used in this study involves four varying injection parameters, which contributes to the complexity of the data and highlights the need for appropriate TSM approaches to achieve accurate results. Figure 6.6 shows that QSSMs exhibit poorer performance in highly transient regions, where the experimental NOx emissions demonstrate more fluctuations and variations. This supports the conclusion that using time series models is essential when dealing with highly transient data, which includes high gradients of changes in engine parameters over time such as load, injection parameters, and hydrogen energy ratio. In this situation, TSMs perform much better than QSSMs. In less transient situations where changes in engine parameters over time is more gradual, QSSMs (specifically GB QSSMs) can be as accurate as TSMs.

Table 6.5: Comparison of grey-box (GB) and black-box (BB) models, including steady-state models (SSMs), quasi steady-state models (QSSMs), and transient sequential models (TSMs) for transient and steady-state emission modeling.

Dataset	Metric	ESM	SSM		QSM		TSM	
			BB	GB	BB	GB	BB	GB
	Prediction per second	3	400000	3	280000	3	46000	3
Transient (83000 cycles)	R^2_{test} (%)	16	52	63	68.4	87	96.7	97.1
	$RMSE_{test}$ (ppm)	631	279.2	228.9	216.8	140.5	72.3	67.8
	$MAPE_{test}$ (%)	83.4	30.6	27.3	28.5	15.5	7.9	7.4
	$|E_{test,max}|$ (ppm)	1630	1495	1468	1388	1051	397	370
Steady-state (79 cases)	RMSE (ppm)	292	10	1	652	548	168	155
	MAPE (%)	35	2	1	50	35	20	14
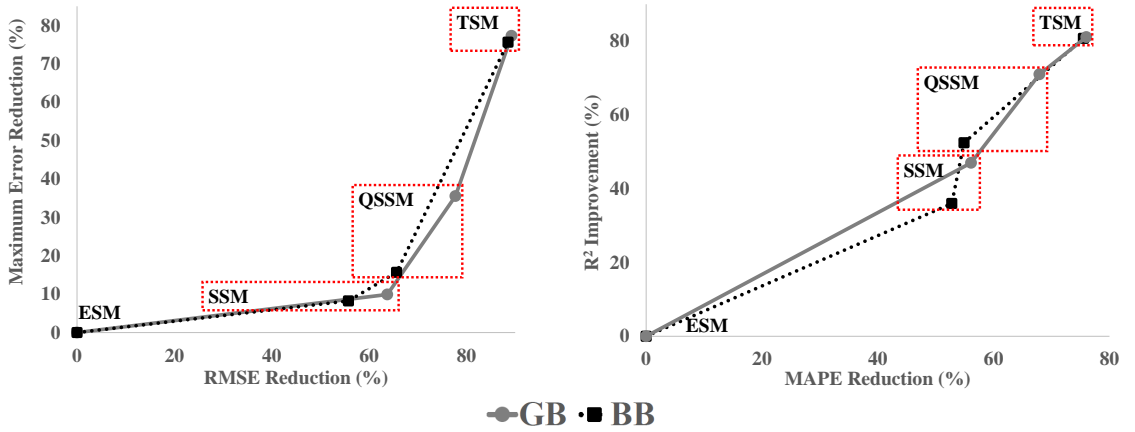
Figure 6.5: Comparison of the improvement in performance of steady-state models (SSMs), quasi steady-state models (QSSMs), and transient sequential models (TSMs) compared to engine simulation model (ESM). a) Improvement in maximum error and RMSE compared to ESM, b) Improvement in MAPE and R^2 compared to ESM.
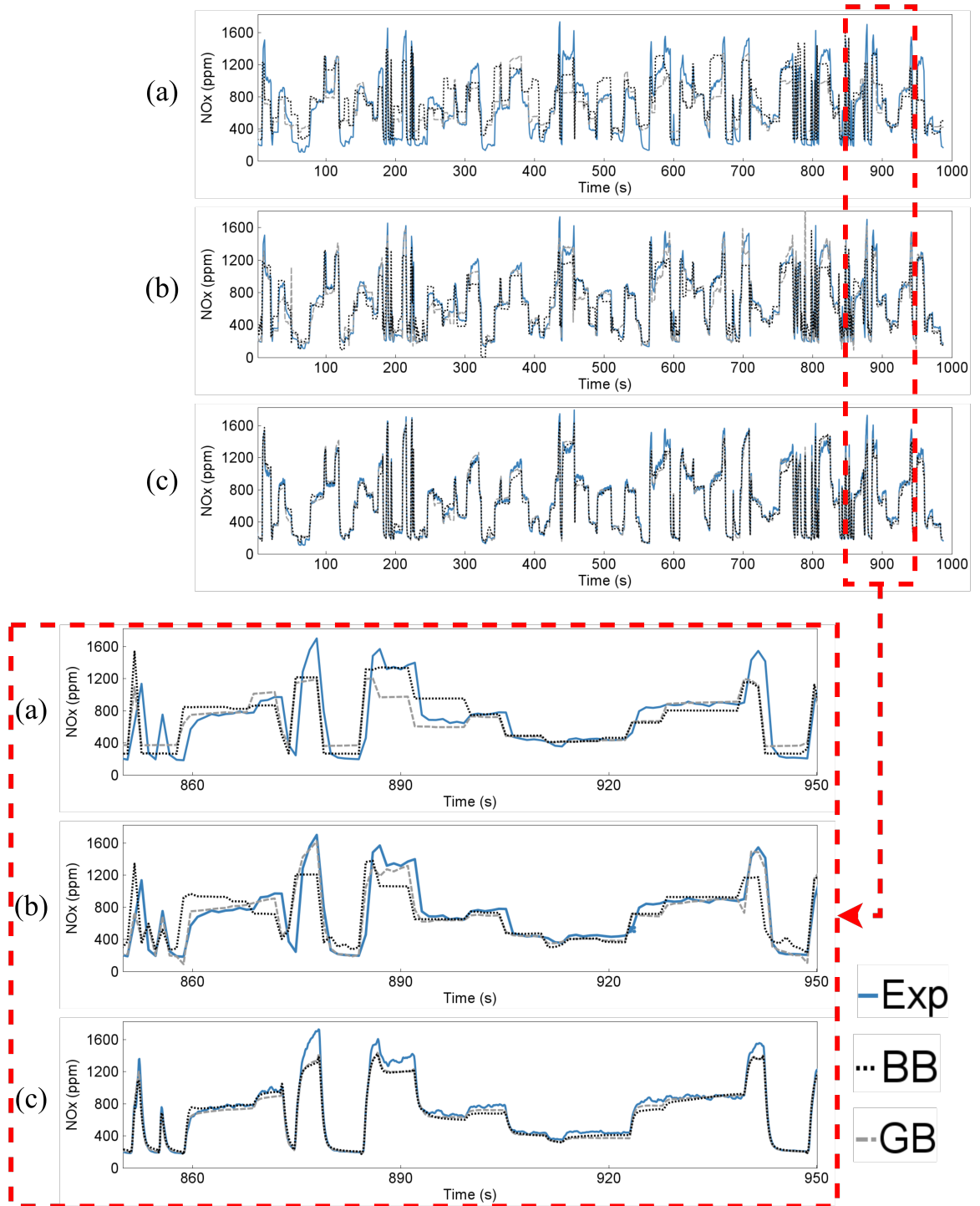
Figure 6.6: Comparison of experimental NOx emissions and predictions by black-box and grey-box models over the test data. a) steady-state models, b)quasi steady-state models, c) transient sequential model (LSTM with 64 hidden neurons). The figure on bottom shows the zoomed in region enclosed within the red box in the above figure.

6.4   Summary of chapter

In this chapter, predictive models for transient NOx emissions from a dual-fuel hydrogen-diesel engine using various modeling techniques and methodologies were developed. Specifically, steady-state models (SSMs), quasi steady-state models (QSSMs), and transient sequential models (TSMs) using black-box (BB) and gray-box (GB) approaches were developed. For the BB models, the machine learning (ML) model is trained solely on experimental data, with diesel and hydrogen injection timing as the inputs. For the GB models, outputs from a 1D engine physical model were augmented to the experimental data to train the ML model. This helped to capture the complexity of the engine's behavior. To identify the most informative features for the GB models, two steps were performed. First, expert knowledge on NOx emissions formation in internal combustion engines (ICEs) was used to identify the most important physical model outputs. Second, the four feature selection (FS) algorithms of F-test, minimum redundancy maximum relevance (MRMR), RReliefF, and least absolute shrinkage and selection operator (LASSO) were applied to further narrow down the selected features. Results showed that all of the FS algorithms perform better than the expert knowledge, with the F-test algorithm yielding the best results. Using the selected features from the F-test algorithm, GB SSMs, QSSMs, and TSMs NOx models were developed. The main findings of this chapter are as follows:

- The data-driven models, including SSMs, QSSMs, and TSMs, outperform the 1D physical engine simulation model (ESM) in transient NOx emission modeling. Furthermore, the QSSMs outperformed SSMs, and TSMs were the most accurate among the three data-driven model types.

- GB models outperformed BB models across all methodologies (SSMs, QSSMs, and TSMs), with notable enhancements in SSMs and QSSMs. This can be attributed to the fact that classical ANNs in SSMs and QSSMs do not consider the impact of prior states on the current state, while GB models effectively

143

account for such effects. However, the performance difference between GB and BB TSM models is minimal, as the time series network already considers the effect of previous states on the current state. Thus, the extra information from GB modeling may not significantly improve TSMs.

- Optimum number of hidden neurons in the time series layer for NOx emissions modeling using the suggested architecture is found to be between 16 and 64.

- The performance difference between QSSMs and TSMs depends on the level of transience in the dataset. For highly transient datasets (for instance the hydrogen energy ratio varies between 0 and 80% and there are high gradients of changes in engine parameters over time), TSMs significantly outperform QSSMs. However, for datasets with lower levels of transience, the performance gap between the two methodologies is narrower.

- Both GRU and LSTM networks demonstrated strong performance in transient NOx emission modeling. Although LSTM is generally more accurate, it is also more computationally expensive. Therefore, for model-based control purposes where computational speed is important, GRU may be the optimal choice since it is almost twice as fast as LSTM with the same number of hidden units. The BB GRU model with 64 hidden neurons, can predict transient NOx emissions with an R^2 value greater than 0.96. For applications such as hardware-in-the-loop, where accuracy is critical and computational cost is less important, GB LSTM models, which were the most accurate models developed in this chapter, can be used. The GB LSTM model with 64 hidden neurons can predict transient NOx emissions with an R^2 value greater than 0.97 and better steady-state performance compared to other models. Using Intel® Xeon® CPU E3-1245 V2 @ 3.40 GHz processor and 32 GB RAM, the BB GRU model and GB LSTM model with 64 hidden units can predict NOx emissions at the speed of 89000 and 3 cases, per second.

Chapter 7

Tailpipe Emissions modeling of a heavy duty diesel truck using deep learning models [1]

Selective Catalytic Reduction (SCR) is a critical technology for enabling heavy-duty trucks, to meet increasingly stringent emission standards. Reliable tailpipe NO_x emission models for vehicles with SCR systems have a number of applications, including engine and after-treatment system model-based control, diagnostics, and vehicle system-level simulations, all contributing to keeping emission levels as low as possible. This chapter employs real-driving on-road emission data from a heavy-duty Class 8 truck, consisting of over 4 million data points collected across more than 10,000 km of driving in various conditions, to develop deep learning long short-term memory (LSTM) networks to predict tailpipe NO_x emissions. The effects of dataset size and model complexity on model performance are explored, with the largest training dataset in this chapter containing around 3.5 million data-points and the most complex model consisting of over 0.5 million parameters. Furthermore, three distinct feature sets, consisting of 9, 7, and 5 features, are employed in the model development process. These models can be used for a variety of applications based on the amount and type of available input data. The models' performance in predicting cumulative and instantaneous NO_x emissions, as well as their ability to determine

---

whether the emission level is below or above the emission standard, is assessed. It is found that achieving satisfactory performance in instantaneous and cumulative tailpipe NO_x emissions requires a comprehensive training dataset. Increasing model complexity only enhances model performance to a certain extent, dependent on the size of the training dataset. The best model developed in this chapter can predict tailpipe NO_x emissions with an R^2 higher than 0.9 for instantaneous NO_x emissions and less than a 2% error for cumulative NO_x emissions on the test data. Furthermore, the high-level model, which only requires vehicle driving cycle data, can predict cumulative NO_x emissions with less than a 5% error. This makes this model suitable for system-level vehicle simulation tasks where limited input information is available.

7.1   Methodology

7.1.1   Collecting on-road emission data

On-road tests were conducted on Highway 2 between Calgary and Edmonton, Alberta, Canada using the experimental setup displayed in Figure 2.6. The designated route is primarily a 4-lane divided highway featuring relatively low grades ($< 6\%$) and long straight sections. Figure 7.1 shows the testing route on Highway 2 between Edmonton and Calgary in Central Alberta. Edmonton's elevation is 670 m, while Calgary's is 1,048 m, resulting in a difference of 378 m. The average slope along the road is 1.3 m per km. The truck data was collected in both directions via round trips, as uphill and downhill road grades affect vehicle tractive power. A weather station sensor was installed on the truck to measure apparent wind speed [2] and ambient temperature. Table 7.1 displays the range of truck weights and weather conditions during the tests. It should be noted that the maximum allowable weight for a five-axle tractor/trailer combination (the vehicle used in this study) is 40,000 kg in Alberta, Canada [213].

Based on the understanding of parameters affecting tailpipe NOx emissions, 9

---

[2] Apparent wind speed is the wind experienced by the truck in motion and is the relative velocity of the wind in relation to an observer in the truck.

effective variables were measured for predicting NOx emissions. These parameters as well as their range and their average value are shown in Table 7.2. All variables were measured at a sampling frequency of 10Hz. The wide ranges of the selected input parameters in Table 7.2 highlights the requirement for a comprehensive dataset that covers different driving conditions. Based on Table 7.2, the SCR after-treatment system effectively reduced exhaust NOx emissions by over 90% on average. This highlights the significant effectiveness of SCR technology in reducing exhaust NOx emissions in heavy-duty diesel trucks.

The truck traveled Highway 2 between Edmonton and Calgary 20 times back and forth over the course of 1 month (January 2022) under commercial operation, transporting goods with varying weights. Out of these trips, data from 37 trips (over 10,000 km and 4 million data-points) were used in this study to develop tailpipe NOx emissions models. From these 37 trips, 31 trips were used as the training data set, 3 trips as the validation data set, and 3 trips as the test data set. The validation and test sets remain the same for all models developed in this study, while different subsets of the training data are used for model training depending on the model. The extensive dataset used in this study, that covers various test conditions, is almost 10 times larger than the largest dataset previously used for this purpose in the literature [159]. The large dataset used in this study enables the developed models to cover wider range of transient operation and model complex dynamic of transient tailpipe NOx emissions better. The dataset developed in this study, including the first five features listed in Table 7.10, along with tailpipe NOx emissions values for 37 trips (covering over 10,000 km of driving and 4 million data points), has been made publicly available online. This dataset serves as a valuable resource for researchers interested in studying tailpipe NOx emissions.

(a) Driving map [Google Maps]

(b) Satellite view[Google Maps]

(c) Topography and elevation [topographic-map]
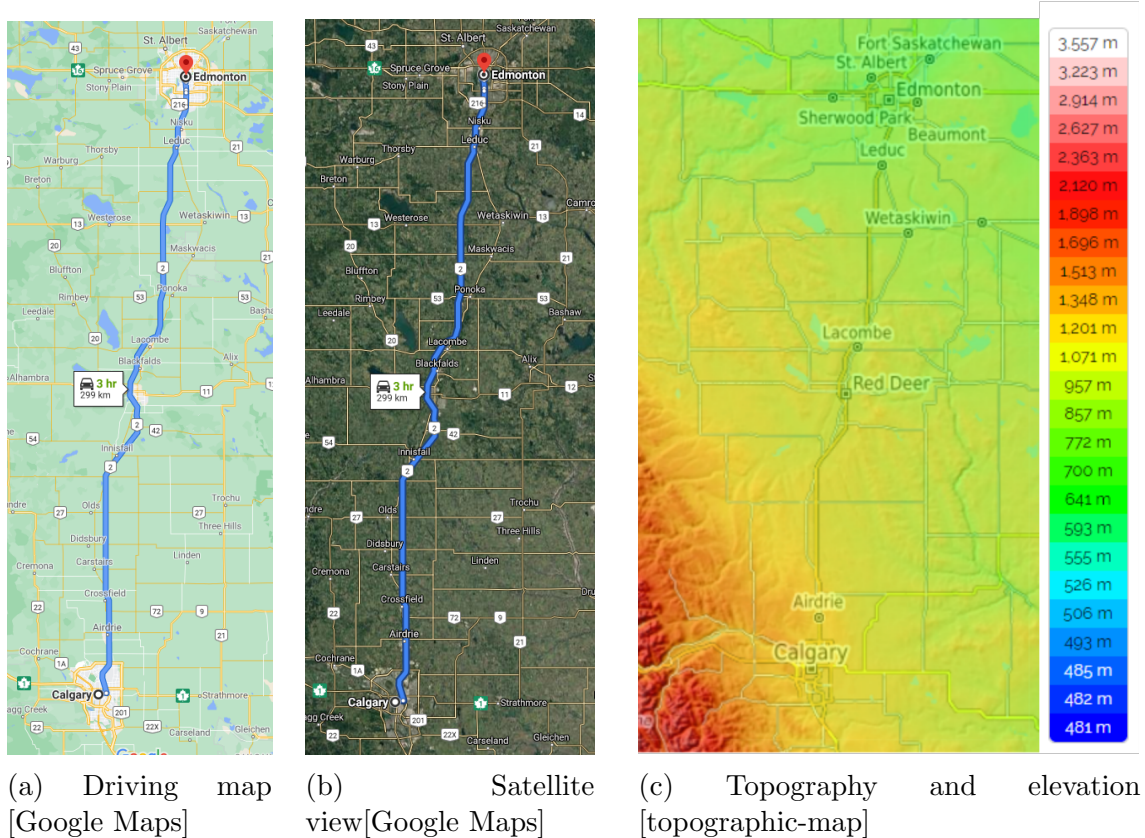
Figure 7.1: Highway 2 Edmonton-Calgary, Central Alberta, Canada

Table 7.1: Test conditions for 11,700 km of testing the truck.

Parameter	Value
Gross truck mass	15,963 to 39,342 kg
Ambient temperature	-24 to 12 °C
Apparent wind speed	33.0 to 152.9 km/h

7.2 Deep Learning Method

In this study, a DL LSTM network architecture is utilized for predicting tailpipe NOx emissions. As it was explained earlier in Chapter 7, the LSTM model employs a special form of time series sequential ML algorithms, which are a category of recurrent neural network (RNN) algorithms that utilize gates to address the vanishing gradient issue.

Table 7.2: Measured parameters on the truck (at 10 Hz) and model inputs and outputs

Function	Variables	Range	Average
	Ambient Temperature	-24 to 12 (°C)	-0.4 (°C)
	Vehicle Speed	1 to 115.5 (km/h)	87.5 (km/h)
	Engine Speed	486.9 to 2036.8 (rpm)	1103.3 (rpm)
	Engine torque	0 to 2601.1 (N.m)	1081.7 (N.m)
Model inputs-predictors	Fuel consumption	0 to 71.4 (L/h)	27 (L/h)
feature set 1 (FS1)	EGR flow rate (kg/h)	0 to 570 (kg/h)	171.2 (kg/h)
	Intake air mass flow rate	83.9 to 2101.6 (kg/h)	669.7 (kg/h)
	SCR intake temperature	79 to 374.69 (°C)	266.3 (°C)
	SCR intake NOx emissions	0.2 to 3012 (ppm)	0.005 (kg/km)
Model output (response)	Tailpipe NOx emissions	0 to 2693.4 (ppm)	0.00048 (kg/km)

An LSTM network as it was explained in Chapter 6, comprises three gates: an update gate G_u, a forget gate G_f, and an output gate G_o, along with a memory cell $c^{<t>}$ and an activation $a^{<t>}$ (see [209] for details). The memory cell is referred to as the long-term state, while the activation is known as the short-term state. The update gate evaluates whether the memory cell's information needs updating using a cell candidate $\tilde{c}^{<t>}$. The output gate determines $a^{<t>}$ based on $c^{<t>}$. Within an LSTM network, $c^{<t>}$ initially passes through the forget gate to discard irrelevant information. Subsequently, the update gate incorporates new information into $c^{<t>}$ using $\tilde{c}^{<t>}$. Finally, the output gate calculates $a^{<t>}$ from $c^{<t>}$ at each time step. A distinguishing feature of LSTM compared to other RNN algorithms like Gated Recurrent Networks (GRUs) is its ability to independently remove and add information to $c^{<t>}$, which enhances the algorithm's predictive capacity for time series. However, this increased capability also leads to a more time-intensive training process due to a greater number of trainable parameters compared to other RNN algorithms. Table 7.3 presents a summary of equations for the designed LSTM network.

Here, four distinct LSTM network configurations, each featuring varying numbers of fully connected layers and hidden units in the LSTM layer, were implemented to predict tailpipe NOx emissions. Details of these four models can be found in Table 7.4 and their schematics are shown in Figure 7.2. The LSTM network architecture begins with several fully connected layers where the number of hidden neurons increases as the network goes deeper, followed by an LSTM time series layer. The LSTM output is connected to a series of fully connected layers where the number of hidden neurons decreases for each subsequent layer after the LSTM layer. Finally, a dropout layer and an output layer are present. The dropout layer randomly deactivates half of the network during each training iteration, thus reducing overfitting and training computational costs. These architectures were established through a trial-and-error process, taking into account the trade-off between complexity and error minimization. To train these models, the MATLAB Deep Learning Toolbox[c], in conjunction with the Adam algorithm and a mini-batch size of 1024, were employed. The stopping point for training is determined by the validation loss. Training continues for decreasing validation loss. Once the validation loss consistently begins to rise, the training stops, and the model with the lowest validation loss is selected. This method ensures a balance in the so-called variance-bias trade-off.

The performance metrics that were used for instantaneous and cumulative tailpipe NOx emissions are listed in Table 7.5. In this table, true positive (T_P) is the number of cases where the model correctly predicted that the NOx emissions value is above the emission standard, such that both the actual and predicted values indicate that the NOx emissions exceeds the standard. False positive (F_P) is the number of cases where the model incorrectly predicted that the NO_x emission value is above the emission standard. This is a type I error, since the model predicted a violation when there was none. False negative (F_N) is the number of cases where the model incorrectly predicted that the NOx emissions value is below the emission standard. This is a Type II error, as the model failed to identify a violation when one was present. In

Table 7.3: Equations of LSTM Sequential model. In the equations; $G_{u,f,o}$ shows gates; $b_{u,f,o,c}$ shows biases matrices; $W_{u,f,o,c}$ shows weight matrices; σ shows the sigmoid activation function, and $*$ shows element-wise multiplication.

Criteria	LSTM Model
Number of gates	3
Number of states	2
Update gate	$G_u = \sigma\left(W_u[a^{<t-1>}, x^{<t>}] + b_u\right)$
Forget gate	$G_f = \sigma\left(W_f[a^{<t-1>}, x^{<t>}] + b_f\right)$
Output gate	$G_o = \sigma\left(W_o[a^{<t-1>}, x^{<t>}] + b_o\right)$
Cell candidate	$\tilde{c}^{<t>} = \tanh\left(W_c[a^{<t-1>}, x^{<t>}] + b_c\right)$
Memory cell (long-term state)	$c^{<t>} = G_u * \tilde{c}^{<t>} + G_f * c^{<t-1>}$
Activation (short-term state)	$a^{<t>} = G_o * c^{<t>}$

Table 7.4: Details of four deep learning LSTM architectures utilized in this study.

Criteria	Complexity level 1 **(CL1)**	Complexity level 2 **(CL2)**	Complexity level 3 **(CL3)**	Complexity level 4 **(CL4)**
Number of hidden layers	9	11	13	15
Number of LSTM layer units	8	16	32	64
Number of model parameters	8.3k	33.4k	133.3k	531.8k

this study, an F1 score (see Table 7.5) is employed to represent the model's ability to predict if tailpipe NOx emissions are below or above the standard level.
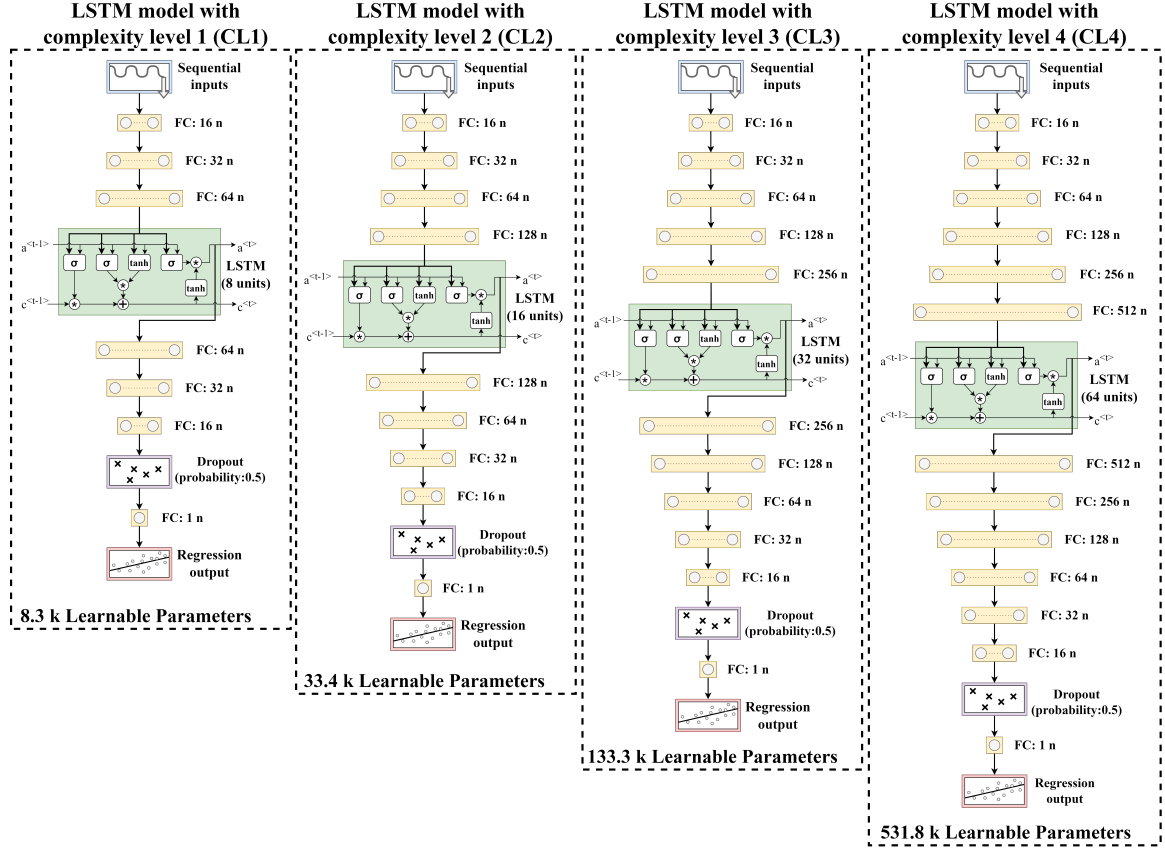
Figure 7.2: Four architectures of deep learning LSTM models structures utilized in this study, ranging from left to right ranging the simplest to the most complex. FC stands for fully connected layer.

7.3 Results and Discussion

Three critical factors influencing the performance of a DL model are the training dataset size, model complexity, and input feature set. The study in this chapter investigates the effects of these factors on the performance of tailpipe NOx emissions models for a heavy-duty truck using real-driving on-road data. Similar to Chapters 3, 5 and 6, all modeling in this study was conducted on a system featuring an Intel® Xeon® CPU E3-1245 V2 @ 3.40 GHz processor and 32 GB of RAM.

7.3.1 Training dataset size effects

The training dataset consists of 31 trips on Highway 2 between Edmonton and Calgary, totaling over 8,000 km- approximately 100 hours of driving measured with 10

Table 7.5: Performance metrics equations, n is the total number of samples, $NOx_{exp,i}$ is the experimental value at time i, $NOx_{pred,i}$ is the predicted value at time i, $\overline{NOx}_{exp}$ represents the mean of the experimental values, "end" represents the last value in the dataset, T_P is true positive, F_P is false positive and F_N is false negative.

Metrics type	Performance metrics	Equation
Instantaneous	R^2	$1 - \dfrac{\sum_{i=1}^{n}(NOx_{exp,i}-NOx_{pred,i})^2}{\sum_{i=1}^{n}(NOx_{exp,i}-\overline{NOx}_{exp})^2}$
	$RMSE$ [ppm]	$\sqrt{\dfrac{\sum_{i=1}^{n}(NOx_{exp,i}-NOx_{pred,i})^2}{n}}$
	MAE [ppm]	$\dfrac{\sum_{i=1}^{n}|NOx_{exp,i}-NOx_{pred,i}|}{n}$
Cumulative	$Error$ [%]	$\dfrac{\sum_{i=1}^{end} NOx_{pred,i}-\sum_{i=1}^{end} NOx_{exp,i}}{\sum_{i=1}^{end} NOx_{exp,i}} \times 100\%$
	$MAPE$ [%]	$\dfrac{100\%}{n}\sum_{i=1}^{n}\left|\dfrac{\sum_{j=1}^{i} NOx_{exp,j}-\sum_{j=1}^{i} NOx_{pred,j}}{\sum_{j=1}^{i} NOx_{exp,j}}\right|$
	$F_1\ score$	$2 \cdot \dfrac{\text{precision}\cdot\text{recall}}{\text{precision}+\text{recall}}$ where $\quad$ precision $= \frac{T_P}{T_P+F_P}$, recall $= \frac{T_P}{T_P+F_N}$

Hz frequency. This results in a dataset of approximately 3.5 million data points. In order to study the influence of training dataset size on model performance, four subsets of the training dataset, presented in Table 7.6, are used.

The LSTM model CL1 from Figure 7.2 using feature set 1 (FS1) from Table 7.2 was trained on these four training datasets (DS1-DS4). The CL1 model was selected for the training dataset size study due to its relatively lower computational cost, as training other models with a 3.5M data-point dataset (DS4) would be too compu-

Table 7.6: Details of four training datasets used for developing deep learning LSTM tailpipe NOx emissions models

Criteria	Dataset 1 (DS1)	Dataset 2 (DS2)	Dataset 3 (DS3)	Dataset 4 (DS4)
Training dataset trips	1	3	9	31
Training dataset samples	117261	324485	1048567	3465331

tationally expensive. The performance metrics for the developed models are listed in Table 7.7. The performance metrics for instantaneous NOx emissions and timing for these models are displayed in Figure 7.3. Increasing the dataset size improves the model performance for predicting instantaneous NOx emissions. This trend is also observed in Figure 7.4, which presents experimental and predicted instantaneous NOx emissions for different models for a portion of the test dataset. There is a linear relationship between dataset size and training time, but prediction time remains constant for different models, as shown in Table 7.7 and Figure 7.3.

The cumulative NOx emissions diagram for different models, as well as the experimental value for the test dataset and cumulative performance metrics diagrams is shown in Figure 7.5. As expected, larger training dataset sizes lead to better performance in terms of cumulative NOx emissions prediction. Both Figures 7.3 and 7.5 demonstrate limited performance improvement from dataset 1 (DS1) to DS2, highlighting the importance of using a large dataset for developing tailpipe NOx emissions models. DS1 and DS2 contain only a few trips for model training and do not yield an accurate model.

Figure 7.5 also presents the cumulative NOx emissions value based on the Tier 3 standard. Comparing the experimental NOx emissions value with this standard reveals that in the measured tailpipe emissions initially exceeded the standard before remaining below the required limit for the rest of the trip. It is essential for a model to predict when tailpipe emissions surpass the required standard. Based on

Table 7.7, the developed model using DS4 has the highest F1 score, indicating that this model is highly capable of correctly predicting whether the cumulative tailpipe emission is below or above the standard level. The same observation can be made from Figure 7.5c. It seems that increasing the size of the dataset can improve the model's F1 score. The only exception is the developed model using DS3, which has a low F1 score value, despite that this model has high accuracy in cumulative and instantaneous performance metrics. This demonstrates that relying solely on these metrics is insufficient for evaluating a model, as they do not adequately represent the model's capacity to determine if the emissions produced are below or above standard levels. This highlights the importance of the F1 score metric, introduced in this study, for evaluating the model's capability to accurately predict if the emission levels fall below or above the required standard limits.

Next, the DS3 dataset is used to investigate the effect of DL model complexity on performance to determine whether increasing model complexity can improve the F1 score.

7.3.2   Deep learning model complexity effects

In this section, the four models (CL1-CL4) showed in Figure 7.2 are each trained using the DS3 training dataset from Table 7.6. Details of these models are listed in Table 7.4. The performance metrics for the developed CL1-CL4 models are presented in Table 7.8. For reference, the model CL1 in Table 7.8 is the same as model DS3 in Table 7.7. The performance metrics for instantaneous NOx emissions and timing for these models are displayed in Figure 7.6. Model performance in predicting instantaneous NOx emissions improves as model complexity increases from CL1 to CL3. However, model performance declines when complexity increases from CL3 to CL4 which is attributed to overfitting. This can be better understood in Figure 7.7, which compares the R^2 values for training, validation, and test sets. As seen, the training R^2 consistently increases from model CL1 to CL4, while the validation and

Table 7.7: Effect of training dataset size (DS1-DS4) on the performance metrics.

	Training dataset	DS1	DS2	DS3	DS4
Model Properties	Model	CL1	CL1	CL1	CL1
	Input feature set	FS1	FS1	FS1	FS1
	Training time (per epoch [s])	9	17.1	48.5	157.5
	Prediction time (per case [μs])	4.5	4.5	4.5	4.5
Instantaneous Error Terms	R^2_{test}	0.78	0.8	0.87	0.91
	$RMSE_{test}$ (ppm)	11.2	10.7	8.8	7.2
	MAE_{test} (ppm)	9.4	9.1	7.5	6.1
Cumulative Error Terms	Error (%)	22.1	21.6	14.5	1.7
	MAPE (%)	24.2	21.6	16	6.9
	F1 Score	0.21	0.81	0.25	0.92

test R^2 values increase from model CL1 to CL3 but decrease from model CL3 to CL4. This indicates that increasing the model complexity from CL3 to CL4 is causing the model to overfit the training data, leading to decreased performance on unseen test and validation sets. The same trend is also observed in Figure 7.8, which presents experimental and predicted instantaneous NOx emissions for different models for a portion of the test dataset. Increasing the model complexity also increases both the training and prediction times of the model, as shown in Table 7.8 and Figure 7.6.

Figure 7.9 presents the cumulative NOx emissions and cumulative performance metrics diagrams for different models. A similar trend to that observed in Figure 7.6 is also observed here, where increasing model complexity from CL1 to CL3 enhances model performance in terms of cumulative NOx emissions prediction but then degrades it going from CL3 to CL4.

The increase in model complexity significantly enhances the F1 score, addressing the limitation of model DS3 from the previous section. When comparing the

Figure 7.3: Effect of training dataset size (DS1-DS4) on performance metrics for instantaneous tailpipe NOx emissions prediction and the associated model training and prediction times. Model architecture and input feature set are CL1 and FS1, respectively.

performance metrics of the best models in Table 7.8 (CL3) and Table 7.7 (DS4), it becomes apparent that model CL3 trained using DS3 performs almost as well as model CL1 trained using DS4, which was the top-performing model in the previous section. This suggests that higher model complexity might be able to compensate for smaller datasets. However, model CL1 trained using DS4 still exhibits slightly better performance in all metrics, highlighting the limited potential for improvement through increased complexity alone. A comparison of the computational cost for these two models reveals that they have approximately similar training time, but the prediction time for model CL1 trained using DS4 is less than half that of model CL3 trained using DS3. In conclusion, a simpler model trained on a larger dataset (CL1 trained using DS4) is a more favorable choice than a more complex model trained on a smaller dataset (CL3 trained using DS3) due to its higher accuracy and lower prediction time. This finding implies that increasing the dataset size, if feasible, could
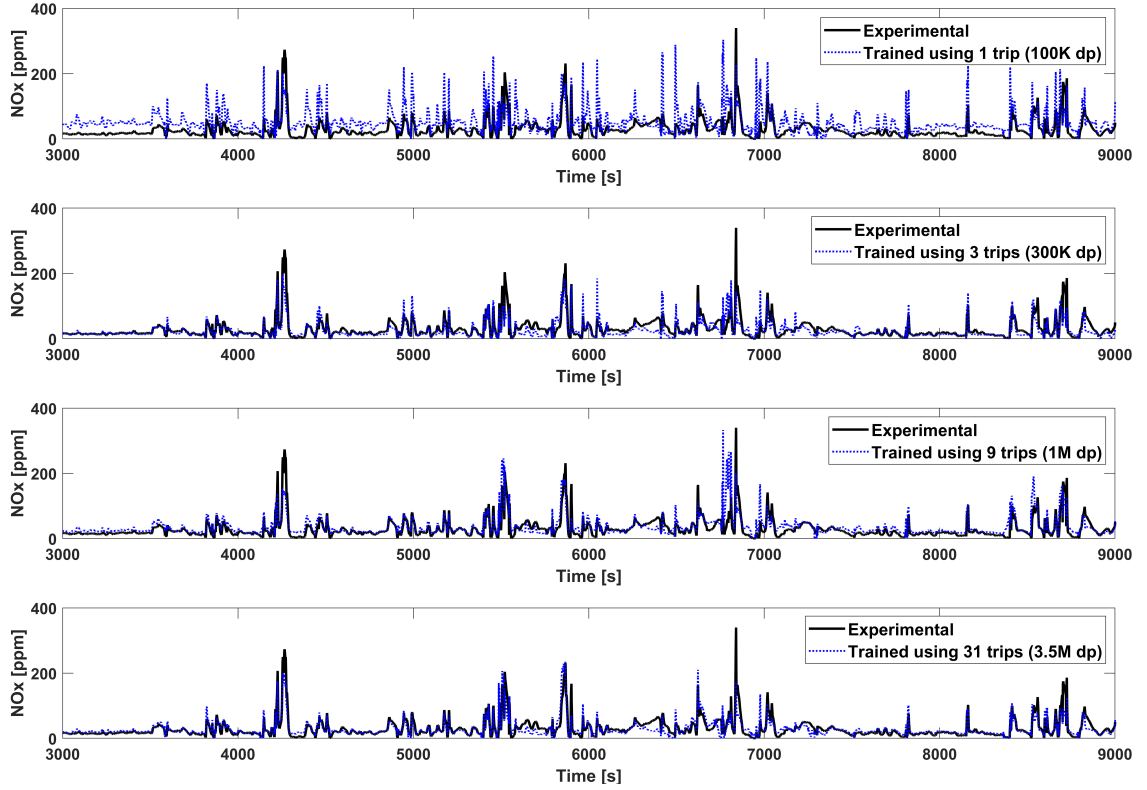
Figure 7.4: Comparison of experimental and predicted instantaneous tailpipe NOx emissions for models developed using different training dataset sizes (DS1-DS4), focusing on a portion of the test dataset. Model architecture and input feature set are CL1 and FS1, respectively.

be a more effective strategy than increasing model complexity.

7.3.3 Input feature set effects

The input feature set is a critical factor in ML models for predicting emissions performance [3, 4]. Furthermore, the input feature set can only be chosen from available measurements, which varies among different applications. The FS1 has 9 features which are listed in Table 7.2 and requires engine and after-treatment system information. This means, the requirement for engine and after-treatment models or measurements of the 9 features that may not always be available. In this section, models are trained with two additional feature sets, feature set 2 (FS2) and FS3 with 7 and 5 input features, which are listed in Table 7.9. DS4 from Table 7.6 and
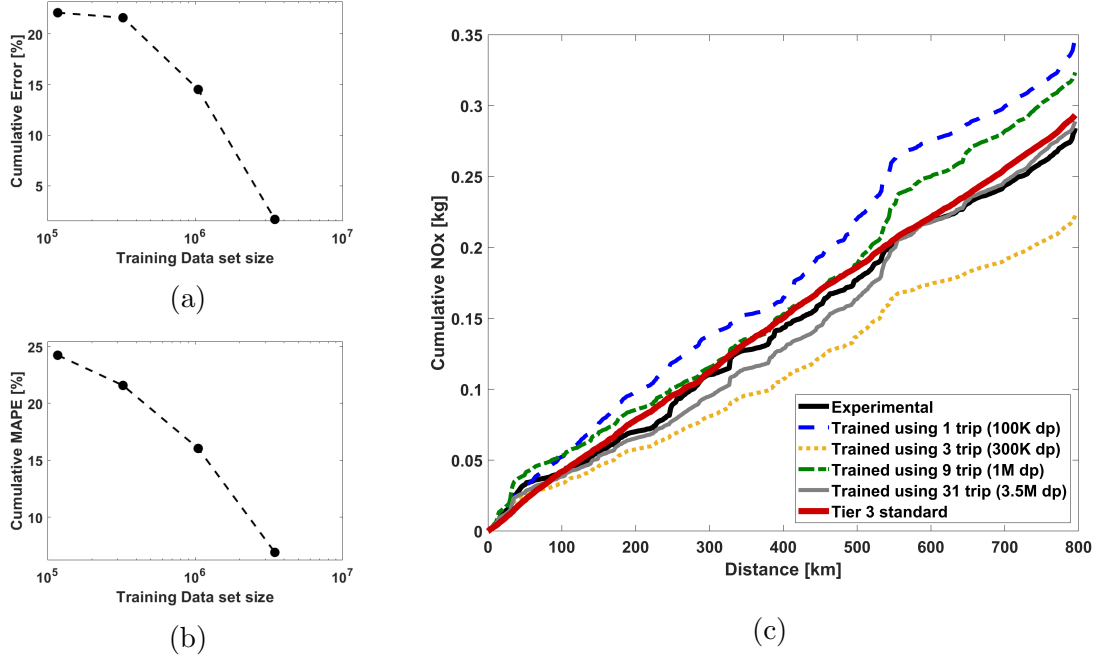
Figure 7.5: Cumulative tailpipe NOx emissions for models developed using different training dataset sizes: (a) and (b) show cumulative performance metrics, while (c) compares experimental results, model predictions, and Tier 3 standard value for cumulative tailpipe NOx emissions across the test dataset. Model architecture and input feature set are CL1 and FS1, respectively.

CL1 from Figure 7.2 are used as the training dataset and LSTM model architecture, respectively.

The FS2 only needs engine information as inputs, which can be provided by the engine model or sensors. The FS3, has the lowest number of input features, only requires engine and vehicle speed, engine torque, fuel consumption and ambient temperature. These data can be provided using a high-level vehicle simulation model (e.g. from Autonomy software) or using data from a Vehicle Control Unit (VCU).

The performance metrics for the developed models using FS1-FS3 are presented in Table 7.10. The developed model using FS1 in Table 7.10 is identical to the developed model using DS4 in Table 7.7. The performance metrics for instantaneous NOx emissions and timing for these models are illustrated in Figure 7.10. Model performance in predicting instantaneous NOx emissions is directly related to the

Table 7.8: Effects of model complexity (CL1-CL4) on performance metrics.

	Model	CL1	CL2	CL3	CL4
Model Properties	Training dataset	DS3	DS3	DS3	DS3
	Input feature set	FS1	FS1	FS1	FS1
	Training time (per epoch [s])	48.5	93.8	177.4	284.9
	Prediction time (per case [μs])	4.5	5.6	10.45	16.05
Instantaneous Error Terms	R^2_{train}	0.89	0.90	0.92	0.95
	$R^2_{validation}$	0.88	0.89	0.90	0.88
	R^2_{test}	0.87	0.87	0.89	0.86
	$RMSE_{test}$ (ppm)	8.8	8.3	7.3	8.6
	MAE_{test} (ppm)	7.5	7	6.2	7.2
Cumulative Error Terms	Error (%)	14.5	8.1	2.8	6.4
	MAPE (%)	16	8.8	4.6	6.1
	F1 Score	0.25	0.33	0.9	0.72

available information in the input feature set. A similar trend is also evident in Figure 7.11.

A comparison of Figure 7.10 and Figure 7.12 reveals that enhancing the input feature set by adding more features has a greater impact on instantaneous performance metrics compared to cumulative performance metrics. All of the developed models using FS1, FS2, and FS3 can predict cumulative NOx at the end of the trip with an error lower than 5% and relatively high F1 scores for the test dataset. This is particularly significant for the model developed using FS3, as its primary application is in system-level vehicle on-road emissions simulation where detailed information about the engine and after-treatment system is generally not available. In such applications, the focus is on the cumulative amount of tailpipe NOx emissions produced during trips, rather than instantaneous NOx emissions prediction. The solid perfor-
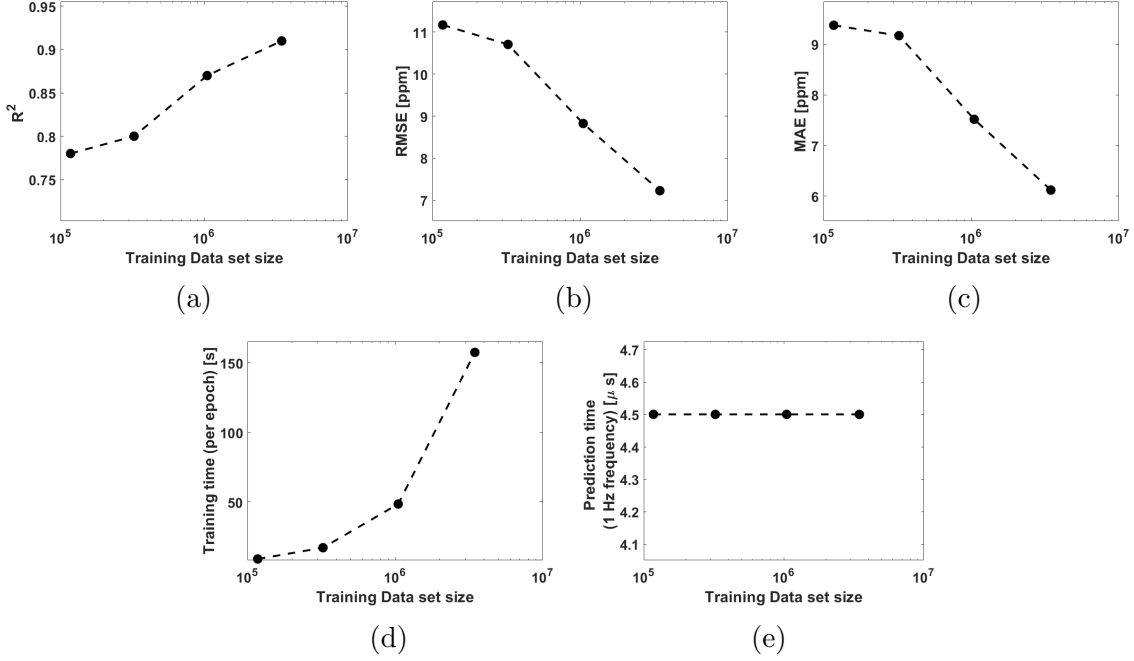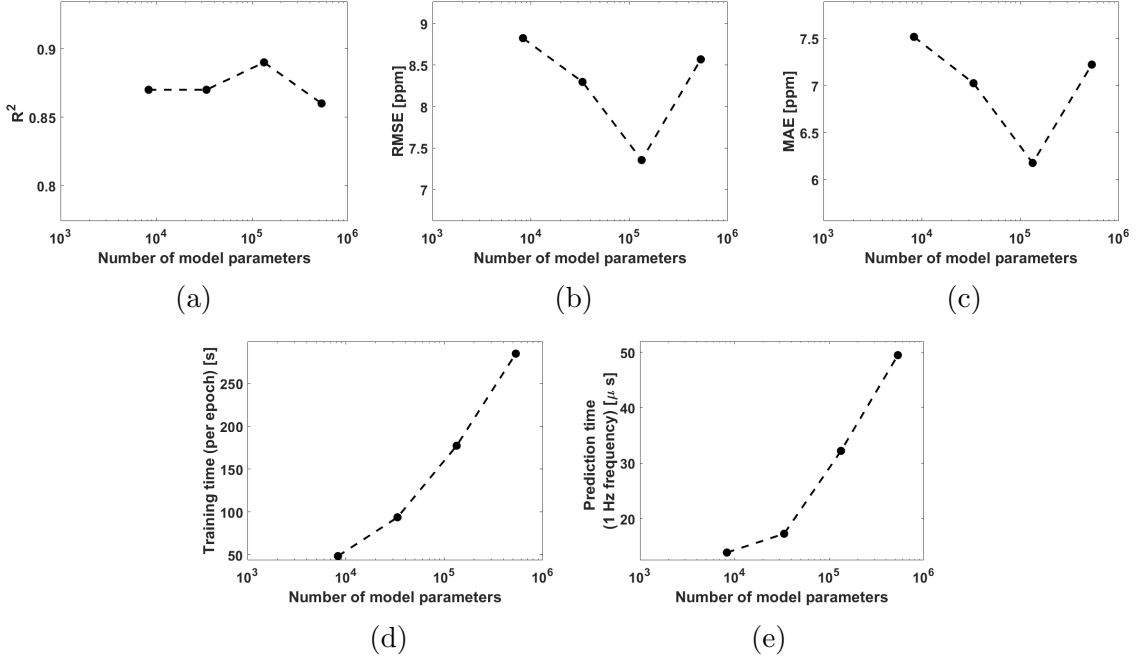
Figure 7.6: Effect of LSTM model complexity on performance metrics for instantaneous tailpipe NOx emissions prediction and the associated model training and prediction times. Training dataset and input feature set are DS3 and FS1, respectively.

(a) Training set   (b) Validation set   (c) Test set
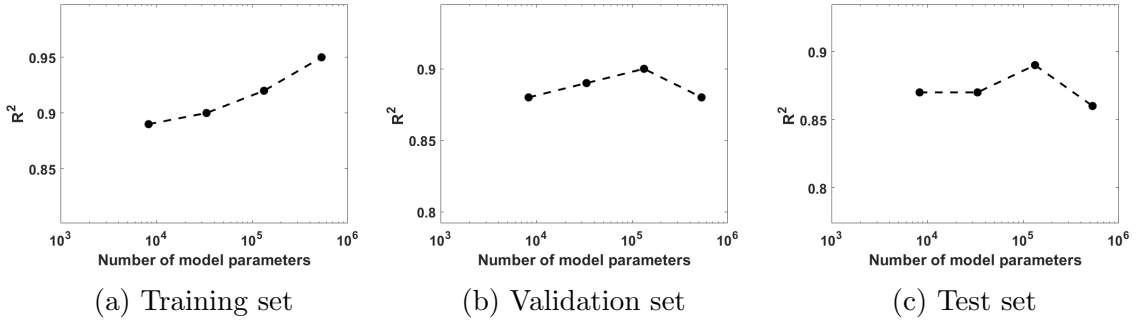
Figure 7.7: Effect of model complexity on prediction R^2 for training, validation, and test sets. Training dataset and input feature set are DS3 and FS1, respectively.

mance of the developed model using FS3 in cumulative performance metrics makes it a suitable for system-level vehicle simulation applications. The main difference between models developed using FS2 and FS1 is that the FS1 model also requires after-treatment information. These models have similar applications and can be used for engine and after-treatment system model-based control, diagnostics, and studying the effects of various parameters on tailpipe NOx emissions. Because of their high
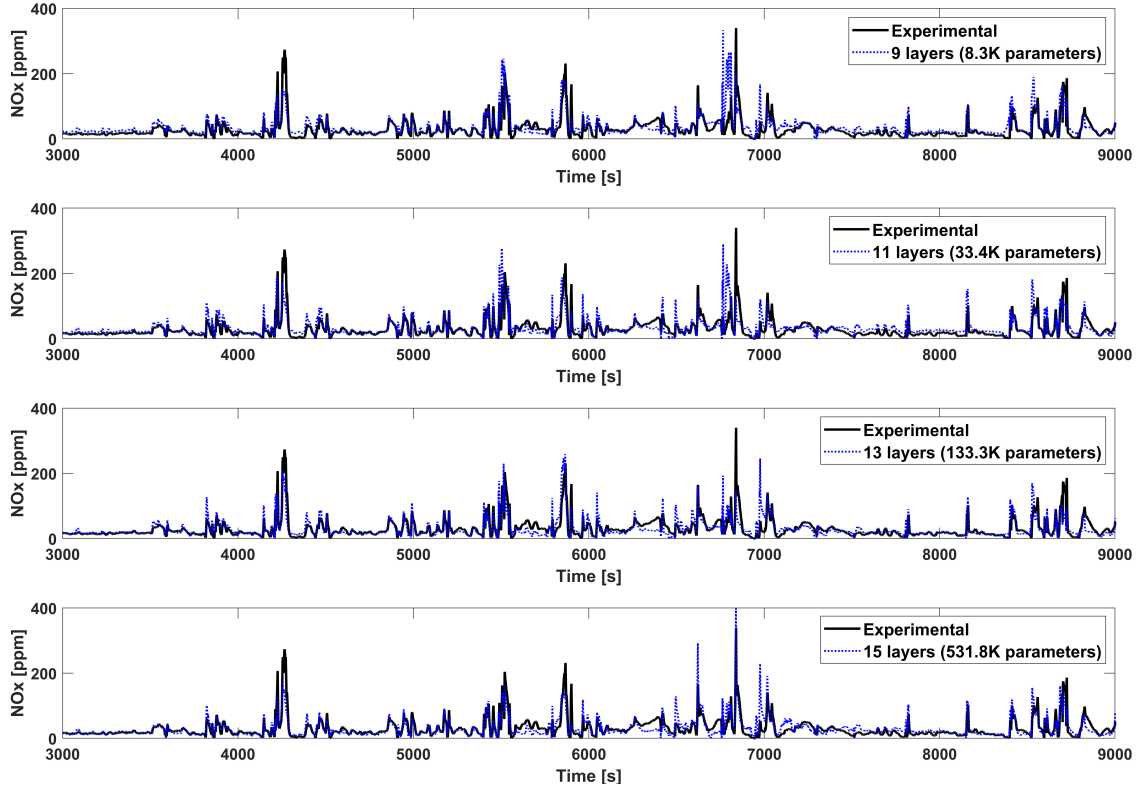
Figure 7.8: Comparison of experimental and predicted instantaneous tailpipe NOx emissions for models with varying complexity levels, focusing on a portion of the test dataset. Training dataset and input feature set are DS3 and FS1, respectively.

accuracy in both cumulative and instantaneous metrics, both of these models can be used for tailpipe NOx emissions diagnosis. Although the developed model using FS1 has superior performance, as it is more accurate in both cumulative and instantaneous performance, its usability depends on the availability of the after-treatment system model or sensors to obtain the necessary information.
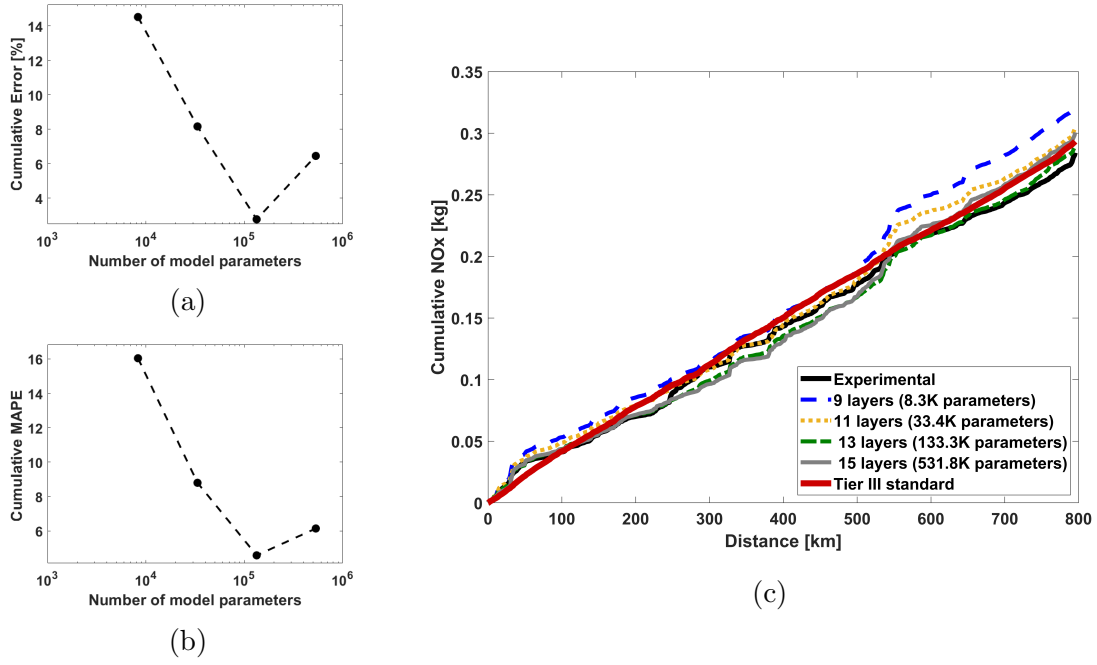
Figure 7.9: Cumulative tailpipe NOx emissions for LSTM models with varying complexity levels: (a) and (b) show cumulative performance metrics, while (c) compares experimental results, model predictions, and Tier 3 standard value for cumulative tailpipe NOx emissions across the test dataset. Training dataset and input feature set are DS3 and FS1, respectively.

Table 7.9: Three input feature sets used for testing the model performance dependency on applications and available data from an actual vehicle or vehicle model.

	Feature set 1 (FS1)	Feature set 2 (FS2)	Feature set 3 (FS3)
Input Features	Ambient temperature	Ambient temperature	Ambient temperature
	Vehicle speed	Vehicle speed	Vehicle speed
	Engine speed	Engine speed	Engine speed
	Engine torque	Engine torque	Engine torque
	Fuel consumption	Fuel consumption	Fuel consumption
	Intake air mass flow rate	Intake air mass flow rate	
	EGR flow rate	EGR flow rate	
	SCR intake temperature		
	SCR intake NOx		
Requirements	Engine and after-treatment models/sensors	Engine model/sensors	Vehicle drive cycle
Application	Engine/after-treatment control and diagnostic, sensor diagnostic	Engine/after-treatment control and diagnostic, sensor diagnostic	Vehicle simulation in real-driving cycles

Table 7.10: Effects of different input feature sets in Table 7.9 including FS1 to FS3 on performance metrics.

|	Input feature set	FS1	FS2	FS3
Model Properties	Model	CL1	CL1	CL1
	Training dataset	DS4	DS4	DS4
	Training time (per epoch [s])	157.5	156.4	156
	Prediction time (per case [μs])	4.5	4.45	4.4
Instantaneous Error Terms	R^2_{test}	0.91	0.85	0.80
	$RMSE_{\text{test}}$ (ppm)	7.2	8.6	10.2
	MAE_{test} (ppm)	6.1	7.2	8.8
Cumulative Error Terms	Error (%)	1.7	4.4	4.8
	MAPE (%)	6.9	7.2	12.7
	F1 Score	0.92	0.87	0.75
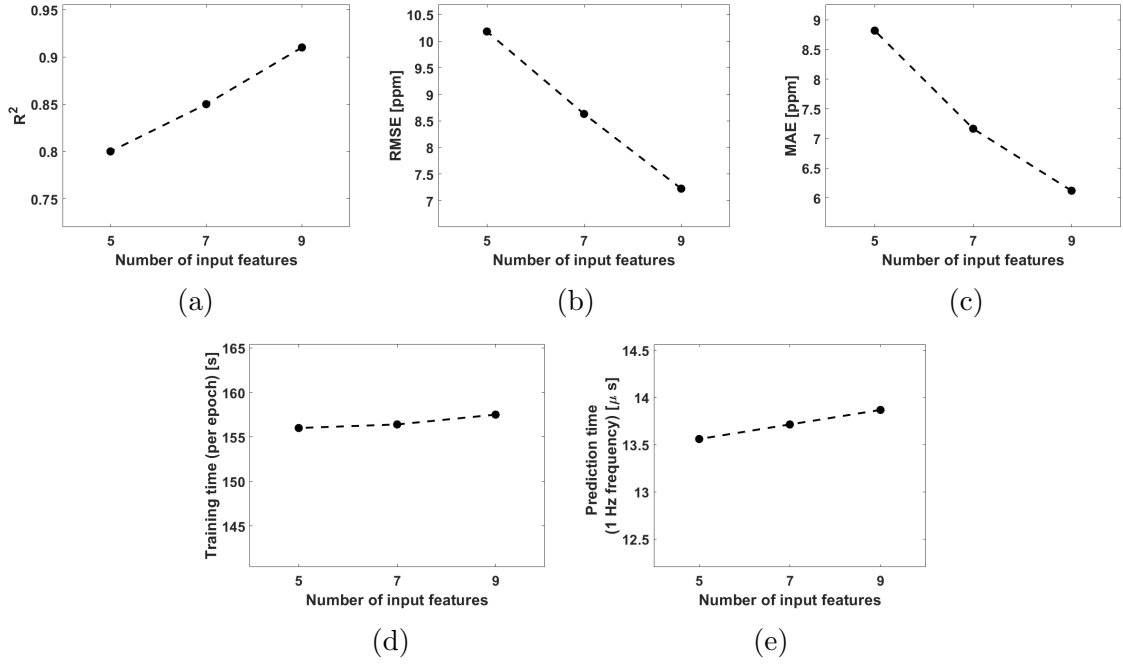
Figure 7.10: Effect of LSTM model input feature set on performance metrics for instantaneous tailpipe NOx emissions prediction and the associated model training and prediction times. Training dataset and model architecture are DS4 and CL1, respectively.
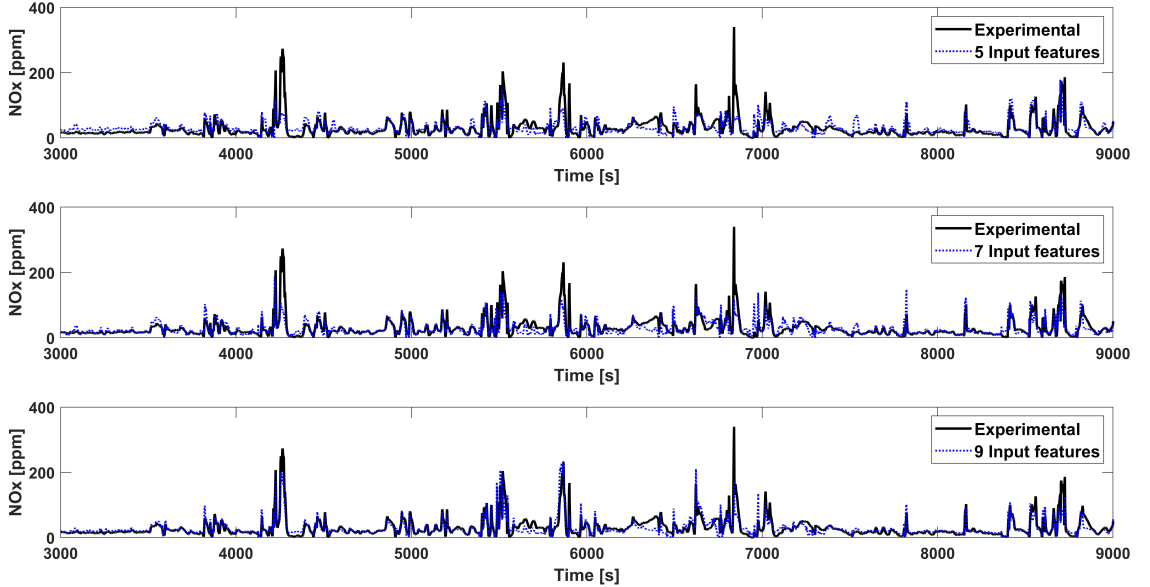
Figure 7.11: Comparison of experimental and predicted instantaneous tailpipe NOx emissions for models with different input feature sets (FS1-FS3), focusing on a portion of the test dataset. Training dataset and model architecture are DS4 and CL1, respectively.
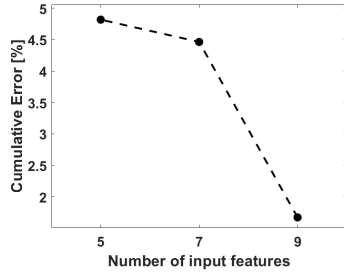
(a)
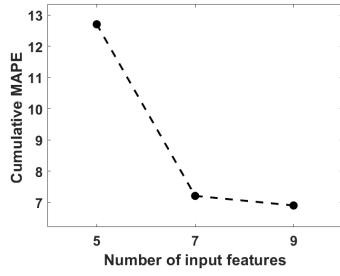
(b)
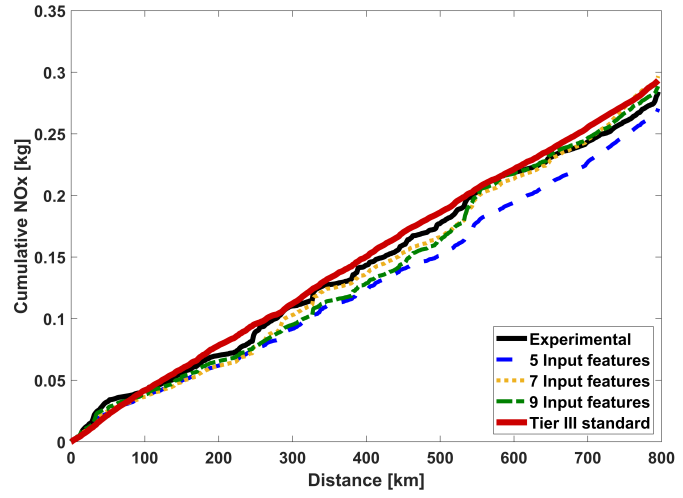
(c)

Figure 7.12: Cumulative tailpipe NOx emissions for LSTM models with different input feature sets (FS1-FS3): (a) and (b) show cumulative performance metrics, while (c) compares experimental results, model predictions, and Tier 3 standard value for cumulative tailpipe NOx emissions across the test dataset. Training dataset and model architecture are DS4 and CL1, respectively.

7.4   Summary of chapter

Tailpipe NO_x emissions models were developed using an extensive dataset of on-road real-driving data from a heavy-duty Class 8 truck. The dataset consists of over 10,000 km of driving, collected at a 10Hz frequency, resulting in more than 4 million data-points. Over 8,000 km, equivalent to around 3.5 million data-points, of this data was used as training dataset, with the remaining data being divided between validation and test sets. The effects of i)training dataset size, ii) model complexity, and iii) input feature set on the performance of models in predicting both instantaneous and cumulative tailpipe NOx emissions were investigated. In addition, this study explored the model's capability to determine compliance with the Tier 3 standard for truck tailpipe emissions.

The main findings of Chapter 7 include:

- Developing accurate tailpipe NO_x emissions models for vehicles with an SCR systems requires extensive datasets covering various driving conditions. Models with training dataset sizes below 1 million data points did not perform well in this study. This is attributed to the complex process inside SCR system and dynamics of tailpipe NOx emissions, as well as the diverse range of input variables that cannot be fully represented by only a few trips. Consequently, an extensive dataset covering various operating conditions is necessary to capture the complexity and variability of tailpipe NO_x emissions accurately.

- While increasing model complexity can improve performance to a certain extent, provided overfitting is avoided, it cannot compensate for smaller dataset sizes. Generally, the training dataset size has a stronger effect on model performance than model complexity for predicting tailpipe NO_x emissions.

- Three distinct input feature sets, comprising 9 (FS1), 7 (FS2), and 5 (FS3) features, were utilized in the development of the models. The most accurate

model, FS1 uses 9 input features, requires both engine and after-treatment data obtainable through models or sensors. The FS2 model relies solely on engine information, while the FS3 model only needs the vehicle drive cycle information as the input data. Models FS1 and FS2 are well-suited for applications that require high levels of accuracy in predicting both instantaneous and cumulative NO_x emissions, such as model-based engine and exhaust after-treatment control, and diagnostics. But, the selection of the model depends on the available input data. In contrast, FS3 is better suited for system-level vehicle simulations when cumulative NOx emissions value is to be predicted, and limited data is accessible to assess vehicle compliance with emission standards. All three models demonstrate the ability to predict cumulative NOx emissions at the end of test trips with an error lower than 5%.

- Instantaneous and cumulative performance metrics can not adequately represent the model's capacity to determine if the tailpipe emissions meet the required standard levels. The F1 score metric was employed to evaluate model performance in this task, with the highest-performing models achieving an F1 score of over 0.9.

- The best developed model can predict tailpipe NO_x emissions for the heavy-duty truck with an R^2 higher than 0.9 for instantaneous NO_x, and cumulative NO_x emissions with lower than 2% error at the end of test trips.

- On average, during 10000 km of real-world driving, the engine-out and tailpipe NOx emissions are 0.005 kg/km and 0.00048 kg/km, respectively. This indicates that the SCR after-treatment system successfully reduced exhaust NOx emissions by over 90%. These findings clearly demonstrate the effectiveness of SCR technology in reducing exhaust NO_x emissions from heavy-duty diesel trucks.

PART V: Conclusions

Chapter 8

Conclusions

The application of machine learning (ML) and deep learning (DL) techniques in combustion, engine, and both steady-state and transient emission modeling was the focus of this thesis.

8.1 Machine Learning in Laminar Flame Speed Modeling

In Part II (Chapter 3) of the thesis, the focus was on developing ML-based laminar flame speed (LFS) models, an essential characteristic for engine combustion models. This resulted in ML methods for predicting LFS of three low carbon fuels (LCFs) - hydrogen, methanol, and ammonia, and their blends, using artificial neural network (ANN) and support vector machine (SVM) algorithms. These ML-based models can predict LFS over ranges of inputs including air-fuel mixture temperature, pressure, exhaust gas reticulation (EGR) and air-fuel ratio that represent internal combustion engines (ICEs) working conditions. Both ANN and SVM algorithms demonstrated accurate performance for all fuels, achieving $R^2_{\text{test}} > 0.96$ in all cases. The low computational time of these LFS models which is hundreds of thousands of times faster than traditional thermo-kinetic combustion mechanisms enables their use in engine development and model-based combustion control applications. The datasets and ML models from this thesis were made available online for future studies [1]. This work

171

was published in [1].

8.2 Machine Learning in Steady-State Emission Modeling

Part III (Chapters 4 and 5) of this thesis focused on developing steady-state white-box (WB), black-box (BB), and gray-box (GB) emission models for fossil-fueled and hydrogen-fueled engines. Modeling of soot emissions from ICEs is difficult but essential for engine compliance with future emissions regulation. First, WB, BB, and GB modeling techniques were used to predict soot emissions for a compression ignition engine in Chapter 4. WB model was found to be very inaccurate, but BB models were found suitable for real-time combustion control as they are fast and accurate, while GB models were useful as a virtual engine for development and calibration purposes as they are more accurate but require more computational power. The BB models are over a thousands times faster than the GB models.

In Chapter 5, the diesel engine from Chapter 4 was converted to a dual-fuel diesel-hydrogen engine by adding port hydrogen injection. The ML LFS model was embedded in to the physics-based model resulting in a much faster physical model with machine learning laminar flame speed (PMLS). BB and GB emission models were created for the dual-fuel hydrogen-diesel engine using experimental data and outputs of the PMLS. It was found that expert input feature selection is not sufficiently accurate so ML-based feature selection is used to reduce bias and improves predictions on test data, leading to better emission model performance. Similar to the fossil-fueled engine, it was found that BB models are much faster than GB models, making them suitable for model-based control applications with $R^2 > 0.95$ for both NO_x and soot emissions. On the other hand, GB emission models are more accurate with $R^2 > 0.99$ for both NO_x and soot emissions but require higher computational power. This makes GB models suitable for hardware-in-the-loop (HIL) setups where more computational power is available and accuracy is crucial.

The finding from part III (Chapters 4 and 5) of this thesis are published in [2–4].

8.3 Machine Learning in Transient Emission Modeling

Transient engine-out and tailpipe NO_x emissions from ICEs were investigated in this phase. Predictive models for engine-out transient NO_x emissions from the dual-fuel hydrogen-diesel engine were developed in the first part. Gated recurrent unit (GRU) and long short term memory (LSTM) networks were compared for transient NO_x emission modeling. While LSTM was more accurate, GRU was faster and more suitable for model-based control purposes. The GB LSTM model achieved the highest accuracy with an R^2 >0.97 for transient NO_x emissions. The fast and highly accurate transient emission models developed in Chapter 6 can serve as a tool for hydrogen-diesel engine model-based control, diagnostic, optimization and calibration.

Next, tailpipe NO_x emissions models using an extensive real-driving dataset consist of over 10000 km of driving (over 4 million data-points) from a heavy-duty Class 8 truck were developed. The study investigated the effects of training dataset size, model complexity, and input feature set on model performance. The results showed the training dataset size had the strongest effect on the prediction accuracy. The best model achieved R^2 >0.91 for instantaneous NO_x emission prediction and an error lower than 2% for cumulative NO_x emission prediction. The designed LSTM deep learning (DL) models have different input feature set that allows these models to serve different applications. The developed model with the smallest input feature set only requires ambient temperature, vehicle speed, engine speed, engine torque and fuel consumption data which makes this model ideal for on-road vehicle system-level simulation. The two other models which require engine and after-treatment data as input data, provide better accuracy which makes them suitable for engine and after-treatment model-based control, diagnostics, calibration, and optimization. The results from Chapters 6 and 7 were submitted for publication [5, 6].

Finally, the results and conclusion of the emission models from this thesis are visually demonstrated in Figure 8.1.
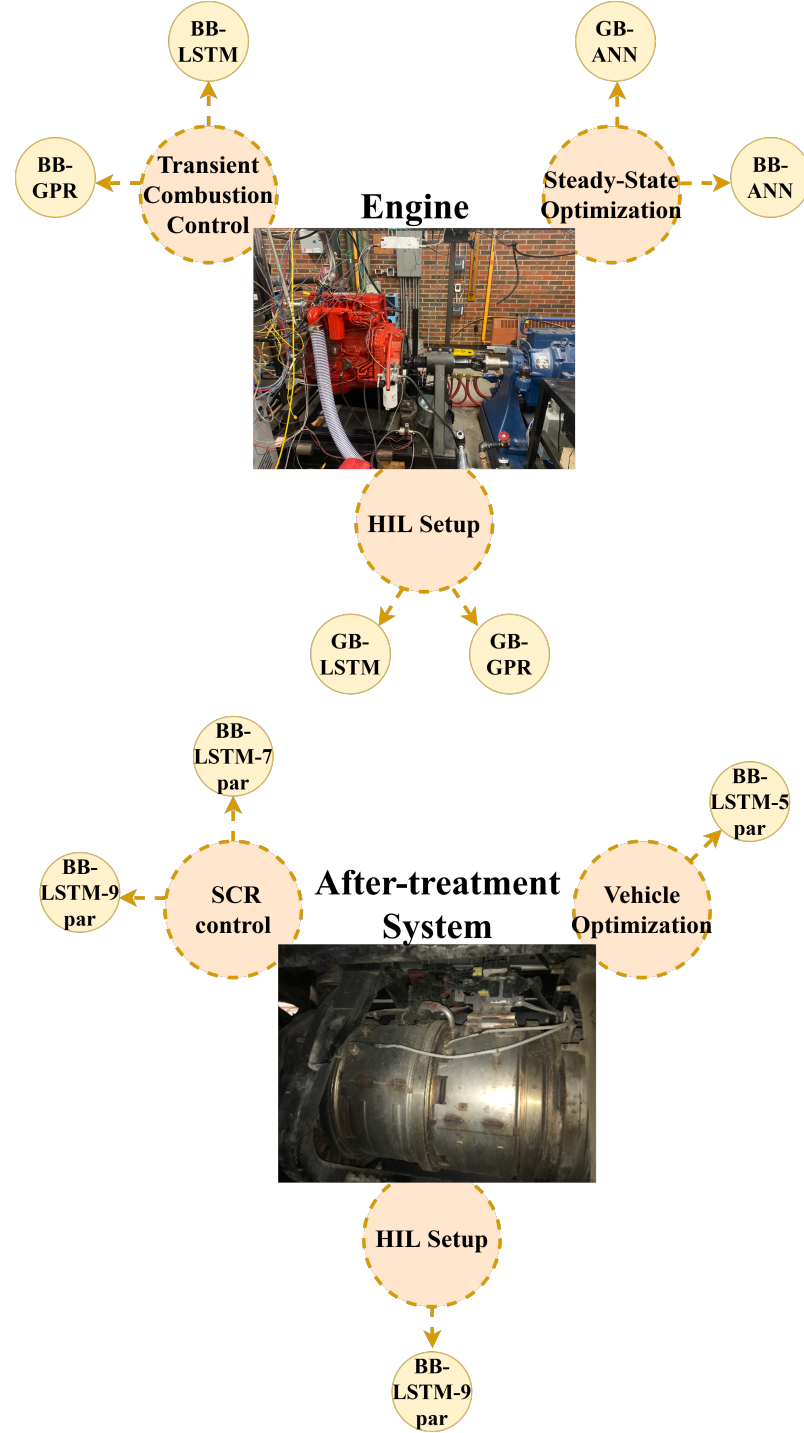
Figure 8.1: Best developed engine and after-treatment emission models for different applications. GB stands for gray-box, BB stands for black-box, HIL stands for hardware-in-the-loop, and par shows the number of input features of the model.

8.4   Future Work

Potential avenues for extending this work in the future include:

- The models developed in this thesis can be implemented for engine model-based control on the engine setup, and the performance of model-based controllers utilizing these models can be compared against conventional controllers.

- Collect on-road real-driving emissions from hydrogen-diesel trucks and develop real world driving (RDE) tailpipe emission models specific to hydrogen-diesel vehicles, building upon the tailpipe emission models from Chapter 7 of this thesis.

- Adding a variable geometric turbine (VGT) supercharger and EGR system to the current hydrogen-diesel dual-fuel engine and develop fast and accurate emission models using the methodology developed in this thesis, along with methods of transfer learning.

- The GB models from this thesis can be utilized in engine HIL setups to provide the benefits of reducing costly experimental tests for engine calibration /optimization.

Bibliography

[1] S. Shahpouri *et al.*, "Laminar flame speed modeling for low carbon fuels using methods of machine learning," *Fuel*, vol. 333, p. 126 187, 2023.

[2] S. Shahpouri, A. Norouzi, C. Hayduk, R. Rezaei, M. Shahbakhti, and C. R. Koch, "Soot emission modeling of a compression ignition engine using machine learning," *IFAC-PapersOnLine*, vol. 54, no. 20, pp. 826–833, 2021.

[3] S. Shahpouri, A. Norouzi, C. Hayduk, R. Rezaei, M. Shahbakhti, and C. R. Koch, "Hybrid machine learning approaches and a systematic model selection process for predicting soot emissions in compression ignition engines," *Energies*, vol. 14, no. 23, p. 7865, 2021.

[4] S. Shahpouri, D. Gordon, C. Hayduk, R. Rezaei, C. R. Koch, and M. Shahbakhti, "Hybrid emission and combustion modeling of hydrogen fueled engines," *International Journal of Hydrogen Energy*, 2023.

[5] S. Shahpouri, D. Gordon, C. R. Koch, and M. Shahbakhti, "Transient emission modeling of a hydrogen-diesel engine using hybrid and machine learning methods," *Submitted to International Journal of Engine Research*, Submission data: 7 June 2023.

[6] S. Shahpouri, D. Gordon, C. R. Koch, and M. Shahbakhti, "Tailpipe NO_x emissions modeling of a heavy duty diesel truck using deep learning models," *Submitted to Applied Energy*, Submission data: 2 June 2023.

[7] EPA, "US transportation sector greenhouse gas emissions: 1990–2019," *Office of Transportation and Air Quality EPA-420-F-21-049*, 2019.

[8] A. Norouzi, H. Heidarifar, M. Shahbakhti, C. R. Koch, and H. Borhan, "Model predictive control of internal combustion engines: A review and future directions," *Energies*, vol. 14, no. 19, p. 6251, 2021.

[9] W. H. Organization *et al.*, *WHO (2005) air quality guidelines for particulate matter, ozone, nitrogen dioxide and sulfur dioxide, global update 2005, summary of risk assessment*, 2006.

[10] R. W. Atkinson *et al.*, "Long-term exposure to ambient ozone and mortality: A quantitative systematic review and meta-analysis of evidence from cohort studies," *BMJ open*, vol. 6, no. 2, e009493, 2016.

[11] Environment and Climate Change Canada, *Canada's air pollutant emissions inventory report 2023. Available at: Https://publications.gc.ca/site/eng/9.869731/publication.html*, 2023.

[12] H. Omidvarborna, A. Kumar, and D.-S. Kim, "Recent studies on soot modeling for diesel combustion," *Renewable and Sustainable Energy Reviews*, vol. 48, pp. 635–647, 2015.

[13] A. Norouzi, H. Heidarifar, M. Shahbakhti, C. R. Koch, and H. Borhan, "Model predictive control of internal combustion engines: A review and future directions," *Energies*, vol. 14, no. 19, 2021.

[14] Z. Zheng, L. Yue, H. Liu, Y. Zhu, X. Zhong, and M. Yao, "Effect of two-stage injection on combustion and emissions under high EGR rate on a diesel engine by fueling blends of diesel/gasoline, diesel/n-butanol, diesel/gasoline/n-butanol and pure diesel," *Energy Conversion and Management*, vol. 90, pp. 1–11, 2015.

[15] W. Yi *et al.*, "Multiple optical diagnostics on effects of fuel properties on spray flames under oxygen-enriched conditions," *Fuel*, vol. 291, p. 120 129, 2021.

[16] Environment and Climate Change Canada, *National inventory report 1990–2020: Greenhouse gas sources and sinks in canada: Executive summary*, 2022.

[17] J. Archsmith, E. Muehlegger, and D. S. Rapson, "Future paths of electric vehicle adoption in the united states: Predictable determinants, obstacles, and opportunities," *Environmental and Energy Policy and the Economy*, vol. 3, no. 1, pp. 71–110, 2022.

[18] J. Merkisz, P. Bielaczyc, J. Pielecha, and J. Woodburn, "RDE testing of passenger cars: The effect of the cold start on the emissions results," *SAE Technical Paper*, no. No. 2019-01-0747, 2019.

[19] "History of heavy duty emissions standards. [online] available at: Https://www.aecc.eu/legislation/heavy-duty-vehicles/ [Accessed on June 5, 2022]."

[20] J Thangaraja and C Kannan, "Effect of exhaust gas recirculation on advanced diesel combustion and alternate fuels-a review," *Applied Energy*, vol. 180, pp. 169–184, 2016.

[21] P. Chen and J. Wang, "Air-fraction modeling for simultaneous diesel engine NOx and PM emissions control during active DPF regenerations," *Applied Energy*, vol. 122, pp. 310–320, 2014.

[22] S. Shahpouri and E. Houshfar, "Nitrogen oxides reduction and performance enhancement of combustor with direct water injection and humidification of inlet air," *Clean Technologies and Environmental Policy*, vol. 21, no. 3, pp. 667–683, 2019.

[23] E Amani, M. Akbari, and S Shahpouri, "Multi-objective CFD optimizations of water spray injection in gas-turbine combustors," *Fuel*, vol. 227, pp. 267–278, 2018.

[24] J. Hunicz, M. Mikulski, M. S. Geca, and A. Rybak, "An applicable approach to mitigate pressure rise rate in an HCCI engine with negative valve overlap," *Applied Energy*, vol. 257, p. 114 018, 2020.

[25] Y. Qian, Z. Wu, J. Guo, Z. Li, C. Jiang, and X. Lu, "Experimental studies on the key parameters controlling the combustion and emission in premixed charge compression ignition concept based on diesel surrogates," *Applied Energy*, vol. 235, pp. 233–246, 2019.

[26] A. Norouzi, S. Shahpouri, D. Gordon, M. Shahbakhti, and C. R. Koch, "Safe deep reinforcement learning in diesel engine emission control," *Proceedings of the Institution of Mechanical Engineers, Part I: Journal of Systems and Control Engineering*, p. 09 596 518 231 153 445, 2023.

[27] A. Norouzi *et al.*, "Deep learning based model predictive control for compression ignition engines," *Control Engineering Practice*, vol. 127, p. 105 299, 2022.

[28] R. Rezaei, C. Hayduk, E. Alkan, T. Kemski, T. Delebinski, and C. Bertram, "Hybrid phenomenological and mathematical-based modeling approach for diesel emission prediction,"

[29] B. Kaźmierski and Ł. J. Kapusta, "The importance of individual spray properties in performance improvement of a urea-SCR system employing flash-boiling injection," *Applied Energy*, vol. 329, p. 120 217, 2023.

[30] B. Choi, K. Lee, and G. Son, "Review of recent after-treatment technologies for de-NOx process in diesel engines," *International Journal of Automotive Technology*, vol. 21, pp. 1597–1618, 2020.

[31] V Praveena and M. L. J. Martin, "A review on various after treatment techniques to reduce NOx emissions in a CI engine," *Journal of the Energy Institute*, vol. 91, no. 5, pp. 704–720, 2018.

[32] J. Ko, D. Jin, W. Jang, C.-L. Myung, S. Kwon, and S. Park, "Comparative investigation of NOx emission characteristics from a Euro 6-compliant diesel passenger car over the NEDC and WLTC at various ambient temperatures," *Applied energy*, vol. 187, pp. 652–662, 2017.

[33] J. Guo, Y. Ge, L. Hao, J. Tan, Z. Peng, and C. Zhang, "Comparison of real-world fuel economy and emissions from parallel hybrid and conventional diesel buses fitted with selective catalytic reduction systems," *Applied energy*, vol. 159, pp. 433–441, 2015.

[34] Z. Mera, N. Fonseca, J.-M. López, and J. Casanova, "Analysis of the high instantaneous NOx emissions from Euro 6 diesel passenger cars under real driving conditions," *Applied energy*, vol. 242, pp. 1074–1089, 2019.

[35] B. Shadidi, G. Najafi, and T. Yusaf, "A review of hydrogen as a fuel in internal combustion engines," *Energies*, vol. 14, no. 19, p. 6209, 2021.

[36] D. Akal, S. Öztuna, and M. K. Büyükakın, "A review of hydrogen usage in internal combustion engines (gasoline-LPG-diesel) from combustion performance aspect," *International Journal of Hydrogen Energy*, vol. 45, no. 60, pp. 35 257–35 268, 2020.

[37] P. Dimitriou and T. Tsujimura, "A review of hydrogen as a compression ignition engine fuel," *International Journal of Hydrogen Energy*, vol. 42, no. 38, pp. 24 470–24 486, 2017.

[38] EuroVI, "commission regulation (EU) 2016/646 of 20 April 2016 amending regulation (EC) NO692/2008 as regards emissions from light passenger and commercial vehicles (Euro 6)," in *Euro 6 regulation*, 2016.

[39] A. Norouzi, D. Gordon, M. Aliramezani, and C. R. Koch, "Machine learning-based diesel engine-out NOx reduction using a plug-in pd-type iterative learning control," in *2020 IEEE Conference on Control Technology and Applications (CCTA)*, 2020, pp. 450–455.

[40] A. Norouzi, K. Ebrahimi, and C. R. Koch, "Integral discrete-time sliding mode control of homogeneous charge compression ignition (HCCI) engine load and combustion timing," *IFAC-PapersOnLine*, vol. 52, no. 5, pp. 153–158, 2019.

[41] D. Gordon *et al.*, "Support vector machine based emissions modeling using particle swarm optimization for homogeneous charge compression ignition engine," *International Journal of Engine Research*, p. 14 680 874 211 055 546, 2021.

[42] M. Aliramezani, C. R. Koch, and M. Shahbakhti, "Modeling, diagnostics, optimization, and control of internal combustion engines via modern machine learning techniques: A review and future directions," *Progress in Energy and Combustion Science*, vol. 88, p. 100 967, 2022.

[43] H. Liu, S. Ma, Z. Zhang, Z. Zheng, and M. Yao, "Study of the control strategies on soot reduction under early-injection conditions on a diesel engine," *Fuel*, vol. 139, pp. 472–481, 2015.

[44] B. Singalandapuram Mahadevan, J. H. Johnson, and M. Shahbakhti, "Development of a Kalman filter estimator for simulation and control of particulate matter distribution of a diesel catalyzed particulate filter," *International Journal of Engine Research*, vol. 21, no. 5, pp. 866–884, 2020.

[45] Z Gao and W Schreiber, "A phenomenologically based computer model to predict soot and NOx emission in a direct injection diesel engine," *International Journal of Engine Research*, vol. 2, no. 3, pp. 177–188, 2001.

[46] M Del Pecchia, V Pessina, F Berni, A d'Adamo, and S Fontanesi, "Gasoline-ethanol blend formulation to mimic laminar flame speed and auto-ignition quality in automotive engines," *Fuel*, vol. 264, p. 116 741, 2020.

[47] F. N. Egolfopoulos, N. Hansen, Y. Ju, K. Kohse-Höinghaus, C. K. Law, and F. Qi, "Advances and challenges in laminar flame experiments and implications for combustion chemistry," *Progress in Energy and Combustion Science*, vol. 43, pp. 36–67, 2014.

[48] N. F. Munajat, C. Erlich, R. Fakhrai, and T. H. Fransson, "Influence of water vapour and tar compound on laminar flame speed of gasified biomass gas," *Applied Energy*, vol. 98, pp. 114–121, 2012.

[49] "Chapter 4 - combustion performance of biojet fuels," in *Biojet Fuel in Aviation Applications*, C. T. Chong and J.-H. Ng, Eds., Elsevier, 2021, pp. 175–230.

[50] E. Mallard, "Recherches experimentales et theoriques sur la combustion des melanges gaseux explosifs," *Ann. Mines*, vol. 8, no. 4, pp. 274–568, 1883.

[51] X. Hu and H. Wei, "Experimental investigation of laminar flame speeds of propane in O2/CO2 atmosphere and kinetic simulation," *Fuel*, vol. 268, p. 117 347, 2020.

[52] Z. Wang, Z. Lu, S. C. Yelishala, H. Metghalchi, and Y. A. Levendis, "Laminar burning speeds and flame instabilities of isobutane carbon dioxide air mixtures at high pressures and temperatures," *Fuel*, vol. 268, p. 117 410, 2020.

[53] X. Li, E. Hu, X. Lu, S. Huang, and Z. Huang, "Experimental and kinetic study on laminar flame speeds of hexene isomers and n-hexane," *Fuel*, vol. 243, pp. 533–540, 2019.

[54] E. Hu, Z. Huang, J. He, and H. Miao, "Experimental and numerical study on laminar burning velocities and flame instabilities of hydrogen–air mixtures at elevated pressures and temperatures," *International Journal of Hydrogen Energy*, vol. 34, no. 20, pp. 8741–8755, 2009.

[55] A. Kéromnès *et al.*, "An experimental and detailed chemical kinetic modeling study of hydrogen and syngas mixture oxidation at elevated pressures," *Combustion and Flame*, vol. 160, no. 6, pp. 995–1011, 2013.

[56] K. P. Shrestha *et al.*, "An experimental and modeling study of ammonia with enriched oxygen content and ammonia/hydrogen laminar flame speed at elevated pressure and temperature," *Proceedings of the Combustion Institute*, vol. 38, no. 2, pp. 2163–2174, 2021.

[57] H. Lesmana, M. Zhu, Z. Zhang, J. Gao, J. Wu, and D. Zhang, "Experimental and kinetic modelling studies of laminar flame speed in mixtures of partially dissociated NH3 in air," *Fuel*, vol. 278, p. 118 428, 2020.

[58] C. Lhuillier, P. Brequigny, N. Lamoureux, F. Contino, and C. Mounaïm-Rousselle, "Experimental investigation on laminar burning velocities of ammonia/hydrogen/air mixtures at elevated temperatures," *Fuel*, vol. 263, p. 116 653, 2020.

[59] M. Metghalchi and J. C. Keck, "Burning velocities of mixtures of air with methanol, isooctane, and indolene at high pressure and temperature," *Combustion and Flame*, vol. 48, pp. 191–210, 1982.

[60] J Beeckmann, O Röhl, and N Peters, "Experimental and numerical investigation of iso-octane, methanol and ethanol regarding laminar burning velocity at elevated pressure and temperature," *SAE Technical Paper*, no. No. 2009-01-1774, 2009.

[61] D. Wang, C. Ji, S. Wang, J. Yang, and Z. Wang, "Effects of data point number on laminar flame speed extrapolation," *Fuel*, vol. 278, p. 118 265, 2020.

[62] C. Pichler and E. J. Nilsson, "Reduced kinetic mechanism for methanol combustion in spark-ignition engines," *Energy & Fuels*, vol. 32, no. 12, pp. 12 805–12 813, 2018.

[63] J. Otomo, M. Koshi, T. Mitsumori, H. Iwasaki, and K. Yamada, "Chemical kinetic modeling of ammonia oxidation with improved reaction mechanism for ammonia/air and ammonia/hydrogen/air combustion," *International Journal of Hydrogen Energy*, vol. 43, no. 5, pp. 3004–3014, 2018.

[64] L Pulga, G. Bianchi, S. Falfari, and C Forte, "A machine learning methodology for improving the accuracy of laminar flame simulations with reduced chemical kinetics mechanisms," *Combustion and Flame*, vol. 216, pp. 72–81, 2020.

[65] J. An, G. He, K. Luo, F. Qin, and B. Liu, "Artificial neural network based chemical mechanisms for computationally efficient modeling of hydrogen/carbon monoxide/kerosene combustion," *International Journal of Hydrogen Energy*, vol. 45, no. 53, pp. 29 594–29 605, 2020.

[66] R. Nakazawa, Y. Minamoto, N. Inoue, and M. Tanahashi, "Species reaction rate modelling based on physics-guided machine learning," *Combustion and Flame*, p. 111 696, 2021.

[67] A. Mohammad, R. Rezaei, C. Hayduk, T. Delebinski, S. Shahpouri, and M. Shahbakhti, "Physical-oriented and machine learning-based emission modeling in a diesel compression ignition engine: Dimensionality reduction and regression," *International Journal of Engine Research*, p. 14 680 874 211 070 736, 2022.

[68] A. Mohammad, R. Rezaei, C. Hayduk, T. O. Delebinski, S. Shahpouri, and M. Shahbakhti, "Hybrid physical and machine learning-oriented modeling approach to predict emissions in a diesel compression ignition engine," *SAE Technical Paper*, no. No. 2021-01-0496, 2009.

[69] F. vom Lehn, L. Cai, B. C. Cáceres, and H. Pitsch, "Exploring the fuel structure dependence of laminar burning velocity: A machine learning based group contribution approach," *Combustion and Flame*, vol. 232, p. 111 525, 2021.

[70] Y. Wang, Y. Ma, D. Xie, Z. Yu, and E Jiaqiang, "Numerical study on the influence of gasoline properties and thermodynamic conditions on premixed laminar flame velocity at multiple conditions," *Energy*, p. 121 049, 2021.

[71] K. Malik, M. Żbikowski, and A. Teodorczyk, "Laminar burning velocity model based on deep neural network for hydrogen and propane with air," *Energies*, p. 3381, 2020.

[72] R. J. Varghese and S. Kumar, "Machine learning model to predict the laminar burning velocities of H2/CO/CH4/CO2/N2/air mixtures at high pressure and temperature conditions," *International Journal of Hydrogen Energy*, vol. 45, no. 4, pp. 3216–3232, 2020.

[73] N. Shah, P. Zhao, D. DelVescovo, and H. Ge, "Prediction of autoignition and flame properties for multicomponent fuels using machine learning techniques," *SAE Technical Paper*, no. No. 2019-01-1049, 2019.

[74] S. Molina, R. Novella, J. Gomez-Soriano, and M. Olcina-Girona, "New combustion modelling approach for methane-hydrogen fueled engines using machine learning and engine virtualization," *Energies*, vol. 14, no. 20, p. 6732, 2021.

[75] K. S. Oppenauer and D. Alberer, "Soot formation and oxidation mechanisms during diesel combustion: Analysis and modeling impacts," *International Journal of Engine Research*, vol. 15, no. 8, pp. 954–964, 2014.

[76] J. Gao and T.-W. Kuo, "Toward the accurate prediction of soot in engine applications," *International Journal of Engine Research*, vol. 20, no. 7, pp. 706–717, 2019.

[77] S. Khurana, S. Saxena, S. Jain, and A. Dixit, "Predictive modeling of engine emissions using machine learning: A review," *Materials Today: Proceedings*, vol. 38, pp. 280–284, 2021.

[78] M. Grahn, K. Johansson, and T. McKelvey, "Data-driven emission model structures for diesel engine management system development," *International Journal of Engine Research*, vol. 15, no. 8, pp. 906–917, 2014.

[79] X. Niu, C. Yang, H. Wang, and Y. Wang, "Investigation of ann and svm based on limited samples for performance and emissions prediction of a crdi-assisted marine diesel engine," *Applied Thermal Engineering*, vol. 111, pp. 1353–1364, 2017.

[80] M Bidarvatan, V Thakkar, M Shahbakhti, B Bahri, and A. A. Aziz, "Grey-box modeling of HCCI engines," *Applied Thermal Engineering*, vol. 70, no. 1, pp. 397–409, 2014.

[81] M. Lang, P. Bloch, T. Koch, T. Eggert, and R. Schifferdecker, "Application of a combined physical and data-based model for improved numerical simulation of a medium-duty diesel engine," *Automotive and Engine Technology*, vol. 5, no. 1, pp. 1–20, 2020.

[82] C. M. Le Cornec, N. Molden, M. van Reeuwijk, and M. E. Stettler, "Modelling of instantaneous emissions from diesel vehicles with a special focus on NOx: Insights from machine learning techniques," *Science of The Total Environment*, vol. 737, p. 139 625, 2020.

[83] F. A. Shamsudheen, K. Yalamanchi, K. H. Yoo, A. Voice, A. Boehman, and M. Sarathy, "Machine Learning Techniques for Classification of Combustion Events under Homogeneous Charge Compression Ignition (HCCI) Conditions," 2020.

[84] H. Zhou, Y. C. Soh, and X. Wu, "Integrated analysis of CFD data with K-means clustering algorithm and extreme learning machine for localized HVAC control," *Applied Thermal Engineering*, vol. 76, pp. 98–104, 2015.

[85] Z. Sun *et al.*, "Hydrogen engine operation strategies: Recent progress, industrialization challenges, and perspectives," *International Journal of Hydrogen Energy*, 2022.

[86] S. S. Ravi and M. Aziz, "Clean hydrogen for mobility–quo vadis?" *International Journal of Hydrogen Energy*, 2022.

[87] T. Tsujimura and Y. Suzuki, "Development of a large-sized direct injection hydrogen engine for a stationary power generator," *International Journal of Hydrogen Energy*, vol. 44, no. 22, pp. 11 355–11 369, 2019.

[88] J. Lee, C. Park, J. Bae, Y. Kim, Y. Choi, and B. Lim, "Effect of different excess air ratio values and spark advance timing on combustion and emission characteristics of hydrogen-fueled spark ignition engine," *International Journal of Hydrogen Energy*, vol. 44, no. 45, pp. 25 021–25 030, 2019.

[89] Q.-h. Luo *et al.*, "Experimental investigation of combustion characteristics and NOx emission of a turbocharged hydrogen internal combustion engine," *International Journal of Hydrogen Energy*, vol. 44, no. 11, pp. 5573–5584, 2019.

[90] M. Dinesh, J. K. Pandey, and G. Kumar, "Study of performance, combustion, and NOx emission behavior of an SI engine fuelled with ammonia/hydrogen blends at various compression ratio," *International Journal of Hydrogen Energy*, 2022.

[91] J. Krishnanunni, D. Bhatia, and L. M. Das, "Experimental and modelling investigations on the performance and emission characteristics of a single cylinder hydrogen engine," *International Journal of Hydrogen Energy*, vol. 42, no. 49, pp. 29 574–29 584, 2017.

[92] Y. Karagöz, Ö. Balcı, and H. Köten, "Investigation of hydrogen usage on combustion characteristics and emissions of a spark ignition engine," *International Journal of Hydrogen Energy*, vol. 44, no. 27, pp. 14 243–14 256, 2019.

[93] H. Zhu and J. Duan, "Research on emission characteristics of hydrogen fuel internal combustion engine based on more detailed mechanism," *International Journal of Hydrogen Energy*, vol. 44, no. 11, pp. 5592–5598, 2019.

[94] S. Yıldırım, E. Tosun, A. Çalık, İ. Uluocak, and E. Avşar, "Artificial intelligence techniques for the vibration, noise, and emission characteristics of a hydrogen-enriched diesel engine," *Energy Sources, Part A: Recovery, Utilization, and Environmental Effects*, vol. 41, no. 18, pp. 2194–2206, 2019.

[95]   C. Ji, H. Wang, C. Shi, S. Wang, and J. Yang, "Multi-objective optimization of operating parameters for a gasoline wankel rotary engine by hydrogen enrichment," *Energy Conversion and Management*, vol. 229, p. 113 732, 2021.

[96]   C. Shi, C. Ji, H. Wang, S. Wang, J. Yang, and Y. Ge, "Comparative evaluation of intelligent regression algorithms for performance and emissions prediction of a hydrogen-enriched wankel engine," *Fuel*, vol. 290, p. 120 005, 2021.

[97]   X. Yu *et al.*, "A comparative study on effects of homogeneous or stratified hydrogen on combustion and emissions of a gasoline/hydrogen SI engine," *International Journal of Hydrogen Energy*, vol. 44, no. 47, pp. 25 974–25 984, 2019.

[98]   Y. Du, X. Yu, L. Liu, R. Li, X. Zuo, and Y. Sun, "Effect of addition of hydrogen and exhaust gas recirculation on characteristics of hydrogen gasoline engine," *International Journal of Hydrogen Energy*, vol. 42, no. 12, pp. 8288–8298, 2017.

[99]   S Manigandan, P Gunasekar, S Poorchilamban, S Nithya, J Devipriya, and G Vasanthkumar, "Effect of addition of hydrogen and tio2 in gasoline engine in various exhaust gas recirculation ratio," *International Journal of Hydrogen Energy*, vol. 44, no. 21, pp. 11 205–11 218, 2019.

[100]   Y. Karagöz, T. Sandalcı, and A. S. Dalkılıç, "Effects of hydrogen and oxygen enrichment on performance and emissions of an SI engine under idle operating condition," *International Journal of Hydrogen Energy*, vol. 40, no. 28, pp. 8607–8619, 2015.

[101]   X. Yu *et al.*, "Experimental study on lean-burn characteristics of an SI engine with hydrogen/gasoline combined injection and EGR," *International Journal of Hydrogen Energy*, vol. 44, no. 26, pp. 13 988–13 998, 2019.

[102]   F. Salek, M. Babaie, S. V. Hosseini, and O. A. Bég, "Multi-objective optimization of the engine performance and emissions for a hydrogen/gasoline dual-fuel engine equipped with the port water injection system," *International Journal of Hydrogen Energy*, vol. 46, no. 17, pp. 10 535–10 547, 2021.

[103]   J. Yang, C. Ji, S. Wang, Z. Zhang, D. Wang, and Z. Ma, "Numerical investigation of the effects of hydrogen enrichment on combustion and emissions formation processes in a gasoline rotary engine," *Energy Conversion and Management*, vol. 151, pp. 136–146, 2017.

[104]   X. Duan *et al.*, "Experimental study the effects of various compression ratios and spark timing on performance and emission of a lean-burn heavy-duty spark ignition engine fueled with methane gas and hydrogen blends," *Energy*, vol. 169, pp. 558–571, 2019.

[105]   C.-f. Lee, Y. Pang, H. Wu, J. J. Hernández, S. Zhang, and F. Liu, "The optical investigation of hydrogen enrichment effects on combustion and soot emission characteristics of CNG/diesel dual-fuel engine," *Fuel*, vol. 280, p. 118 639, 2020.

[106] X. Leng *et al.*, "Effects of hydrogen enrichment on the combustion and emission characteristics of a turbulent jet ignited medium speed natural gas engine: A numerical study," *Fuel*, vol. 290, p. 119 966, 2021.

[107] X. Sun *et al.*, "Effect of hydrogen enrichment on the flame propagation, emissions formation and energy balance of the natural gas spark ignition engine," *Fuel*, vol. 307, p. 121 843, 2022.

[108] Y. Huang and F. Ma, "Intelligent regression algorithm study based on performance and NOx emission experimental data of a hydrogen enriched natural gas engine," *International Journal of Hydrogen Energy*, vol. 41, no. 26, pp. 11 308–11 320, 2016.

[109] Y. Wang, X. Zhou, and L. Liu, "Theoretical investigation of the combustion performance of ammonia/hydrogen mixtures on a marine diesel engine," *International Journal of Hydrogen Energy*, vol. 46, no. 27, pp. 14 805–14 812, 2021.

[110] J. Vavra, I. Bortel, and M. Takats, "A dual fuel hydrogen-diesel compression ignition engine and its potential application in road transport," *SAE Technical Paper*, no. No. 2019-01-0564, 2019.

[111] S. Verma, A. Suman, L. Das, S. Kaushik, and S. Tyagi, "A renewable pathway towards increased utilization of hydrogen in diesel engines," *International Journal of Hydrogen Energy*, vol. 45, no. 8, pp. 5577–5587, 2020.

[112] N. Castro, M. Toledo, and G. Amador, "An experimental investigation of the performance and emissions of a hydrogen-diesel dual fuel compression ignition internal combustion engine," *Applied Thermal Engineering*, vol. 156, pp. 660–667, 2019.

[113] P. Dimitriou, M. Kumar, T. Tsujimura, and Y. Suzuki, "Combustion and emission characteristics of a hydrogen-diesel dual-fuel engine," *International Journal of Hydrogen Energy*, vol. 43, no. 29, pp. 13 605–13 617, 2018.

[114] P. Sharma and A. Dhar, "Effect of hydrogen supplementation on engine performance and emissions," *International Journal of Hydrogen Energy*, vol. 43, no. 15, pp. 7570–7580, 2018.

[115] B. Subramanian and V. Thangavel, "Experimental investigations on performance, emission and combustion characteristics of diesel-hydrogen and diesel-HHO gas in a dual fuel CI engine," *International Journal of Hydrogen Energy*, vol. 45, no. 46, pp. 25 479–25 492, 2020.

[116] S. Nag, P. Sharma, A. Gupta, and A. Dhar, "Experimental study of engine performance and emissions for hydrogen diesel dual fuel engine with exhaust gas recirculation," *International Journal of Hydrogen Energy*, vol. 44, no. 23, pp. 12 163–12 175, 2019.

[117] P. Dimitriou, T. Tsujimura, and Y. Suzuki, "Hydrogen-diesel dual-fuel engine optimization for CHP systems," *Energy*, vol. 160, pp. 740–752, 2018.

[118] M. Talibi, P. Hellier, R. Morgan, C. Lenartowicz, and N. Ladommatos, "Hydrogen-diesel fuel co-combustion strategies in light duty and heavy duty CI engines," *International Journal of Hydrogen Energy*, vol. 43, no. 18, pp. 9046–9058, 2018.

[119] P. Dimitriou, T. Tsujimura, and Y. Suzuki, "Low-load hydrogen-diesel dual-fuel engine operation–A combustion efficiency improvement approach," *International Journal of Hydrogen Energy*, vol. 44, no. 31, pp. 17 048–17 060, 2019.

[120] M. T. Chaichan, "Performance and emission characteristics of CIE using hydrogen, biodiesel, and massive EGR," *International Journal of Hydrogen Energy*, vol. 43, no. 10, pp. 5415–5435, 2018.

[121] X. Liu, A. Srna, H. L. Yip, S. Kook, Q. N. Chan, and E. R. Hawkes, "Performance and emissions of hydrogen-diesel dual direct injection (H2DDI) in a single-cylinder compression-ignition engine," *International Journal of Hydrogen Energy*, vol. 46, no. 1, pp. 1302–1314, 2021.

[122] R. Juknelevičius, A. Rimkus, S. Pukalskas, and J. Matijošius, "Research of performance and emission indicators of the compression-ignition engine powered by hydrogen-diesel mixtures," *International Journal of Hydrogen Energy*, vol. 44, no. 20, pp. 10 129–10 138, 2019.

[123] C. Yuan, C. Han, Y. Liu, Y. He, Y. Shao, and X. Jian, "Effect of hydrogen addition on the combustion and emission of a diesel free-piston engine," *International Journal of Hydrogen Energy*, vol. 43, no. 29, pp. 13 583–13 593, 2018.

[124] K. Bayramoğlu and S. Yılmaz, "Emission and performance estimation in hydrogen injection strategies on diesel engines," *International Journal of Hydrogen Energy*, vol. 46, no. 57, pp. 29 732–29 744, 2021.

[125] H. Koten, "Hydrogen effects on the diesel engine performance and emissions," *International Journal of Hydrogen Energy*, vol. 43, no. 22, pp. 10 511–10 519, 2018.

[126] A. I. Jabbr and U. O. Koylu, "Influence of operating parameters on performance and emissions for a compression-ignition engine fueled by hydrogen/diesel mixtures," *International Journal of Hydrogen Energy*, vol. 44, no. 26, pp. 13 964–13 973, 2019.

[127] A. I. Jabbr, H. Gaja, and U. O. Koylu, "Multi-objective optimization of operating parameters for a H2/diesel dual-fuel compression-ignition engine," *International Journal of Hydrogen Energy*, vol. 45, no. 38, pp. 19 965–19 975, 2020.

[128] M. Karimi, X. Wang, J. Hamilton, and M. Negnevitsky, "Numerical investigation on hydrogen-diesel dual-fuel engine improvements by oxygen enrichment," *International Journal of Hydrogen Energy*, 2022.

[129] H An, W. Yang, A Maghbouli, J Li, S. Chou, and K. Chua, "A numerical study on a hydrogen assisted diesel engine," *International Journal of Hydrogen Energy*, vol. 38, no. 6, pp. 2919–2928, 2013.

[130] K. sv and S. K. Masimalai, "Predicting the performance and emission characteristics of a Mahua oil-hydrogen dual fuel engine using artificial neural networks," *Energy Sources, Part A: Recovery, Utilization, and Environmental Effects*, vol. 42, no. 23, pp. 2891–2910, 2020.

[131] H. Duan, Y. Huang, R. K. Mehra, P. Song, and F. Ma, "Study on influencing factors of prediction accuracy of support vector machine (SVM) model for NOx emission of a hydrogen enriched compressed natural gas engine," *Fuel*, vol. 234, pp. 954–964, 2018.

[132] "Heavy-duty vehicle and engine greenhouse gas emission regulations.last amended on october 3, 2022. [online] available at: Http://laws-lois.justice.gc.ca [Accessed on November 5, 2022]."

[133] A. Norouzi, M. Aliramezani, and C. R. Koch, "A correlation-based model order reduction approach for a diesel engine NOx and brake mean effective pressure dynamic model using machine learning," *International Journal of Engine Research*, vol. 22, no. 8, pp. 2654–2672, 2021.

[134] M. Aliramezani, A. Norouzi, and C. R. Koch, "Support vector machine for a diesel engine performance and NOx emission control-oriented model," *IFAC-PapersOnLine*, vol. 53, no. 2, pp. 13 976–13 981, 2020.

[135] A. Jeyamoorthy *et al.*, "Development and comparison of virtual sensors constructed using AI techniques to estimate the performances of IC engines," *SAE Technical Paper*, no. No. 2022-01-1064, 2022.

[136] A. Brusa, E. Giovannardi, M. Barichello, and N. Cavina, "Comparative evaluation of data-driven approaches to develop an engine surrogate model for NOx engine-out emissions under steady-state and transient conditions," *Energies*, vol. 15, no. 21, p. 8088, 2022.

[137] V. Ahire, M. Shewale, and A. Razban, "A review of the state-of-the-art emission control strategies in modern diesel engines," *Archives of Computational Methods in Engineering*, pp. 1–19, 2021.

[138] M. H. Moradi, A. Heinz, U. Wagner, and T. Koch, "Modeling the emissions of a gasoline engine during high-transient operation using machine learning approaches," *International Journal of Engine Research*, vol. 23, no. 10, pp. 1708–1716, 2022.

[139] Y. Wang, Y. Yu, and J. Li, "Predicting the transient NOx emissions of the diesel vehicle based on LSTM neural networks," in *2020 IEEE Conference on Telecommunications, Optics and Computer Science (TOCS)*, IEEE, 2020, pp. 261–264.

[140] J. Li, Y. Yu, Y. Wang, L. Zhao, and C. He, "Prediction of transient NOx emission from diesel vehicles based on deep-learning differentiation model with double noise reduction," *Atmosphere*, vol. 12, no. 12, p. 1702, 2021.

[141] M. Mirzaeian and S. Langridge, "Creating a virtual test bed using a dynamic engine model with integrated controls to support in-the-loop hardware and software optimization and calibration," *Energies*, vol. 14, no. 3, p. 652, 2021.

[142] J. M. Luján, A. Garcia, J. Monsalve-Serrano, and S. Martínez-Boggio, "Effectiveness of hybrid powertrains to reduce the fuel consumption and NOx emissions of a Euro 6d-temp diesel engine under real-life driving conditions," *Energy Conversion and Management*, vol. 199, p. 111 987, 2019.

[143] R. Rezaei, D. Kovacs, C. Hayduk, M. Mennig, and T. Delebinski, "Euro VII and beyond with hydrogen combustion for commercial vehicle applications: From concept to series development," *SAE International Journal of Advances and Current Practices in Mobility*, vol. 4, no. 2021-01-1196, pp. 559–569, 2021.

[144] R. Finesso, G. Hardy, A. Mancarella, O. Marello, A. Mittica, and E. Spessa, "Real-time simulation of torque and nitrogen oxide emissions in an 11.0 l heavy-duty diesel engine for model-based combustion control," *Energies*, vol. 12, no. 3, p. 460, 2019.

[145] D. Neumann, L. Schäfers, P. Muthyala, J. Andert, and S. Pischinger, "Reduction of transient engine-out no x-emissions by advanced digital combustion rate shaping," *Automotive Innovation*, vol. 3, pp. 181–190, 2020.

[146] S.-Y. Lee *et al.*, "Scalable mean value modeling for real-time engine simulations with improved consistency and adaptability," *SAE Technical Paper*, no. No. 2019-01-0195, 2019.

[147] C. Xia *et al.*, "Simulation study on transient performance of a marine engine matched with high-pressure SCR system," *International Journal of Engine Research*, p. 14 680 874 221 084 052, 2022.

[148] A. M. Marinoni *et al.*, "RDE cycle simulation by 0d/1d models to investigate ic engine performance and cylinder-out emissions," *International Journal of Engine Research*, p. 14 680 874 221 141 936, 2022.

[149] P. Mentink, D. Escobar-Valdivieso, A. Forrai, X. Seykens, and F. Willems, "Experimental validation of a virtual engine-out NOx sensor for diesel emission control," *International Journal of Engine Research*, vol. 20, no. 10, pp. 1037–1046, 2019.

[150] J. Fu *et al.*, "Application of artificial neural network to forecast engine performance and emissions of a spark ignition engine," *Applied Thermal Engineering*, vol. 201, p. 117 749, 2022.

[151] X. Fang, F. Zhong, N. Papaioannou, M. H. Davy, and F. C. Leach, "Artificial neural network (ANN) assisted prediction of transient NOx emissions from a high-speed direct injection (HSDI) diesel engine," *International Journal of Engine Research*, vol. 23, no. 7, pp. 1201–1212, 2022.

[152] F. Rosero, N. Fonseca, J.-M. López, and J. Casanova, "Real-world fuel effi-
ciency and emissions from an urban diesel bus engine under transient operating
conditions," *Applied Energy*, vol. 261, p. 114 442, 2020.

[153] Y. Yu, Y. Wang, J. Li, M. Fu, A. N. Shah, and C. He, "A novel deep learning
approach to predict the instantaneous NOx emissions from diesel engine," *Ieee
Access*, vol. 9, pp. 11 002–11 013, 2021.

[154] H. Xie *et al.*, "Parallel attention-based LSTMfor building a prediction model of
vehicle emissions using PEMS and OBD," *Measurement*, vol. 185, p. 110 074,
2021.

[155] S. Shin, Y. Lee, J. Park, M. Kim, S. Lee, and K. Min, "Predicting transient
diesel engine NOx emissions using time-series data preprocessing with deep-
learning models," *Proceedings of the Institution of Mechanical Engineers, Part
D: Journal of Automobile Engineering*, vol. 235, no. 12, pp. 3170–3184, 2021.

[156] X. Du, G. Yang, Y. Chen, J. Ran, and L. Zhang, "The different poisoning
behaviors of various alkali metal containing compounds on SCR catalyst,"
Applied Surface Science, vol. 392, pp. 162–168, 2017.

[157] P. Xie, M. Gao, H. Zhang, Y. Niu, and X. Wang, "Dynamic modeling for
NOx emission sequence prediction of SCR system outlet based on sequence
to sequence long short-term memory network," *Energy*, vol. 190, p. 116 482,
2020.

[158] M. Aliramezani, A. Norouzi, and C. R. Koch, "A grey-box machine learn-
ing based model of an electrochemical gas sensor," *Sensors and Actuators B:
Chemical*, vol. 321, p. 128 414, 2020.

[159] R. Pillai *et al.*, "Modeling and predicting heavy-duty vehicle engine-out and
tailpipe nitrogen oxide (NOx) emissions using deep learning," *Frontiers in
Mechanical Engineering*, p. 11, 2022.

[160] P. M. Estrada, D. de Lima, P. H. Bauer, M. Mammetti, and J. C. Bruno, "Deep
learning in the development of energy management strategies of hybrid electric
vehicles: A hybrid modeling approach," *Applied Energy*, vol. 329, p. 120 231,
2023.

[161] W. Hu *et al.*, "Mechanistic assessment of NO oxidative activation on tungsten-
promoted ceria catalysts and its consequence for low-temperature NH3-SCR,"
Applied Energy, vol. 330, p. 120 306, 2023.

[162] M. Devarakonda, G. Parker, J. H. Johnson, V. Strots, and S. Santhanam,
"Adequacy of reduced order models for model-based control in a urea-SCR
aftertreatment system," *SAE Technical Paper*, no. No. 2008-01-0617, 2009.

[163] S. Duraiarasan, R. Salehi, F. Wang, A. Stefanopoulou, M. Allain, and S. Ma-
hesh, "Real-time embedded models for simulation and control of clean and
fuel-efficient heavy-duty diesel engines," *SAE Technical Paper*, no. No. 2020-
01-0257, 2020.

[164] T. M. Harris and T. Gardner, "Modeling of aftertreatment technologies to meet a future HD low-NOx standard," *SAE Technical Paper*, no. No. 2019-01-0043, 2019.

[165] Z. Gao, D. Deter, D. Smith, J. Pihl, C Daw, and J. Parks II, "Engine-aftertreatment in closed-loop modeling for heavy duty truck emissions control," Oak Ridge National Lab.(ORNL), Oak Ridge, TN (United States), Tech. Rep., 2019.

[166] X. Liang, B. Zhao, F. Zhang, and Q. Liu, "Compact research for maritime selective catalytic reduction reactor based on response surface methodology," *Applied Energy*, vol. 254, p. 113 702, 2019.

[167] M. K. A. Wardana and O. Lim, "Investigation of ammonia homogenization and NOx reduction quantity by remodeling urea injector shapes in heavy-duty diesel engines," *Applied Energy*, vol. 323, p. 119 586, 2022.

[168] M. K. Sampath and F. Lacin, "CFD study of sensitivity parameters in SCR NOx reduction modeling," *SAE Technical Paper*, no. No. 2014-01-2346, 2014.

[169] N. Singh, B. Adelman, S. Malagari, and K. Hickey, "Ultra-low NOx emission prediction for heavy duty diesel applications using a map-based approach," *SAE Technical Paper*, no. No. 2019-01-0987, 2019.

[170] F. Rosero, N. Fonseca, J.-M. López, and J. Casanova, "Effects of passenger load, road grade, and congestion level on real-world fuel consumption and emissions from compressed natural gas and diesel urban buses," *Applied Energy*, vol. 282, p. 116 195, 2021.

[171] H. Liu *et al.*, "Experimental investigation of the effects of diesel fuel properties on combustion and emissions on a multi-cylinder heavy-duty diesel engine," *Energy Conversion and Management*, vol. 171, pp. 1787–1800, 2018.

[172] H. Mei *et al.*, "Characterization of exhaust CO, HC and NOx emissions from light-duty vehicles under real driving conditions," *Atmosphere*, vol. 12, no. 9, p. 1125, 2021.

[173] L Tarabet, K. Loubar, M. Lounici, K Khiari, T Belmrabet, and M. Tazerout, "Experimental investigation of di diesel engine operating with eucalyptus biodiesel/natural gas under dual fuel mode," *Fuel*, vol. 133, pp. 129–138, 2014.

[174] R. Rezaei, C. Hayduk, A. Fandakov, M. Rieß, M. Sens, and T. O. Delebinski, "Numerical and experimental investigations of hydrogen combustion for heavy-duty applications," *SAE Technical Paper*, no. No. 2021-01-0522, 2021.

[175] M. Aliramezani, C. R. Koch, R. Hayes, and R. Patrick, "Amperometric solid electrolyte NOx sensors - the effect of temperature and diffusion mechanisms," *Solid State Ionics*, vol. 313, pp. 7 –13, 2017.

[176] M. Aliramezani, C. R. Koch, and R. Patrick, "Phenomenological model of a solid electrolyte NOx and O2 sensor using temperature perturbation for on-board diagnostics," *Solid State Ionics*, vol. 321, pp. 62 –68, 2018.

[177] M. Aliramezani, C. R. Koch, M. Secanell, R. E. Hayes, and R. Patrick, "An electrochemical model of an amperometric NOx sensor," *Sensors and Actuators B: Chemical*, vol. 290, pp. 302–311, Apr. 5, 2019.

[178] M. Aliramezani, A. Norouzi, and C. R. Koch, "A grey-box machine learning-based model of an electrochemical gas sensor," *Sensors and Actuators B: Chemical*, vol. 321, p. 128 414, 2020.

[179] R. Li, A. A. Konnov, G. He, F. Qin, and D. Zhang, "Chemical mechanism development and reduction for combustion of NH3/H2/CH4 mixtures," *Fuel*, vol. 257, p. 116 059, 2019.

[180] Combustion Research Group, "The San Diego mechanism: Chemical kinetic mechanisms for combustion applications," *Mechanical and Aerospace Engineering (Combustion Research), University of California at San Diego, CA, http://web. eng. ucsd. edu/mae/groups/combustion/mechanism. html (Accessed on September 1, 2021)*, 2014.

[181] Y. Wang *et al.*, "A new machine learning algorithm to optimize a reduced mechanism of 2-Butanone and the comparison with other algorithms," *ES Materials & Manufacturing*, vol. 6, no. 2, pp. 28–37, 2019.

[182] K. P. Shrestha, L. Seidel, T. Zeuch, and F. Mauss, "Detailed kinetic mechanism for the oxidation of ammonia including the formation and reduction of nitrogen oxides," *Energy & Fuels*, vol. 32, no. 10, pp. 10 202–10 217, 2018.

[183] *Automated machine learning: methods, systems, challenges: Chapter 3- Neural Architecture Search, author=Hutter, Frank and Kotthoff, Lars and Vanschoren, Joaquin, year=2019, 10.1007/978-3-030-05318-5, publisher=Springer Nature.*

[184] J. Snoek, H. Larochelle, and R. P. Adams, "Practical Bayesian optimization of machine learning algorithms," *Advances in Neural Information Processing Systems*, vol. 25,

[185] A. Norouzi, M. Aliramezani, and C. R. Koch, "A correlation-based model order reduction approach for a diesel engine NOx and brake mean effective pressure dynamic model using machine learning," *International Journal of Engine Research*, vol. 22, no. 8, pp. 2654–2672, 2021.

[186] "A grey-box machine learning based model of an electrochemical gas sensor," *Sensors and Actuators B: Chemical*, vol. 321, p. 128 414, 2020.

[187] S. Verhelst, J. W. Turner, L. Sileghem, and J. Vancoillie, "Methanol as a fuel for internal combustion engines," *Progress in Energy and Combustion Science*, vol. 70, pp. 43–88, 2019.

[188] P. Dimitriou and R. Javaid, "A review of ammonia as a compression ignition engine fuel," *International Journal of Hydrogen Energy*, vol. 45, no. 11, pp. 7098–7118, 2020.

[189] H. Hiroyasu, T. Kadota, and M. Arai, "Development and use of a spray combustion modeling to predict diesel engine efficiency and pollutant emissions: Part 1 combustion modeling," *Bulletin of JSME*, vol. 26, no. 214, pp. 569–575, 1983.

[190] K. Deb and H. Jain, "An evolutionary many-objective optimization algorithm using reference-point-based nondominated sorting approach, part I: solving problems with box constraints," *IEEE transactions on evolutionary computation*, vol. 18, no. 4, pp. 577–601, 2013.

[191] L. Rao, Y. Zhang, S. Kook, K. S. Kim, and C.-B. Kweon, "Understanding the soot reduction associated with injection timing variation in a small-bore diesel engine," *International Journal of Engine Research*, vol. 22, no. 3, pp. 1001–1015, 2021.

[192] S. M. Farhan, W. Pan, W. Yan, Y. Jing, and L. Lili, "Effect of post-injection strategies on regulated and unregulated harmful emissions from a heavy-duty diesel engine," *International Journal of Engine Research*, p. 1 468 087 420 980 917, 2020.

[193] A. Géron, *Hands-on machine learning with Scikit-Learn, Keras, and Tensor-Flow: Concepts, tools, and techniques to build intelligent systems.* 2019.

[194] J. D. Rodriguez, A. Perez, and J. A. Lozano, "Sensitivity analysis of k-fold cross validation in prediction error estimation," *IEEE Transactions on Pattern Analysis and Machine Intelligence*, vol. 32, no. 3, pp. 569–575, 2009.

[195] R. A. Berk, *Statistical learning from a regression perspective: Chapter 3- Classification and regression trees (CART).* 2008, vol. 14.

[196] C. Cortes and V. Vapnik, "Support-vector networks," *Machine learning*, vol. 20, no. 3, pp. 273–297, 1995.

[197] M. Aliramezani, A. Norouzi, and C. R. Koch, "Support vector machine for a diesel engine performance and NOx emission control-oriented model," *IFAC-PapersOnLine*, vol. 53, no. 2, pp. 13 976–13 981, 2020.

[198] M. Seeger, "Gaussian processes for machine learning," *International Journal of Neural Systems*, vol. 14, no. 02, pp. 69–106, 2004.

[199] F. D. Foresee and M. T. Hagan, "Gauss-Newton approximation to Bayesian learning," in *Proceedings of International Conference on Neural Networks (ICNN'97)*, vol. 3, 1997, pp. 1930–1935.

[200] J. H. Friedman, *The elements of statistical learning: Data mining, inference, and prediction.* springer open, 2017.

[201] S. Hires, R. Tabaczynski, and J. Novak, "The prediction of ignition delay and combustion intervals for a homogeneous charge, spark ignition engine," *SAE transactions*, pp. 1053–1067, 1978.

[202] N. C. Blizard and J. C. Keck, "Experimental and theoretical investigation of turbulent burning model for internal combustion engines," *SAE Transactions*, pp. 846–864, 1974.

[203] T. Morel, C. I. Rackmil, R. Keribar, and M. J. Jennings, "Model for heat transfer and combustion in spark ignited engines and its comparison with experiments," *SAE transactions*, pp. 348–362, 1988.

[204] H Hiroyasu, "Fuel spray penetration and spray angle in diesel engines," *Trans. JSME*, vol. 44, no. 385, pp. 3208–3220, 1980.

[205] D. Jung and D. N. Assanis, "Multi-zone DI diesel spray combustion model for cycle simulation studies of engine performance and emissions," *SAE Transactions*, pp. 1510–1532, 2001.

[206] W. C. KI *et al.*, "Gaussian processes for machine learning," *International Journal of Neural Systems*, vol. 14, 2006.

[207] J. Mockus, *Bayesian approach to global optimization: theory and applications.* 2012, vol. 37.

[208] J. Chung, C. Gulcehre, K. Cho, and Y. Bengio, "Empirical evaluation of gated recurrent neural networks on sequence modeling," *arXiv preprint arXiv:1412.3555*, 2014.

[209] S. Hochreiter and J. Schmidhuber, "Long short-term memory," *Neural computation*, vol. 9, no. 8, pp. 1735–1780, 1997.

[210] P. Dhal and C. Azad, "A comprehensive survey on feature selection in the various fields of machine learning," *Applied Intelligence*, pp. 1–39, 2022.

[211] C. Ding and H. Peng, "Minimum redundancy feature selection from microarray gene expression data," *Journal of Bioinformatics and Computational Biology*, vol. 3, no. 02, pp. 185–205, 2005.

[212] M. Robnik-Šikonja and I. Kononenko, "Theoretical and empirical analysis of relieff and rrelieff," *Machine learning*, vol. 53, pp. 23–69, 2003.

[213] Government of Alberta, *Alberta commercial vehicle – weight and dimension regulations. Available at: Https://www.alberta.ca/commercial-vehicle-weight-and-dimensions-regulations.aspx [Accessed on May 16, 2023]*, 2023.

[214] A. Norouzi *et al.*, "Machine learning integrated with model predictive control for imitative optimal control of compression ignition engines," *IFAC-PapersOnLine*, vol. 55, no. 24, pp. 19–26, 2022.

[215] S. Shahpouri, A. Norouzi, C. Hayduk, R. Rezaei, C. R. Koch, and M. Shahbakhti, "Modeling of a single fuel hydrogen spark ignition and a dual-fuel diesel-hydrogen engines.," *CICS, Ottawa*, 2022.

Appendix A: Ph.D. Publications

A.1 Peer Reviewed Journal Papers [1, 2, 4–6, 26, 27, 67]

A.1.1 Published Papers

1. **Shahpouri, S.**, Norouzi, A., Hayduk, C., Rezaei, R., Shahbakhti, M. and Koch, C.R., 2021. Hybrid machine learning approaches and a systematic model selection process for predicting soot emissions in compression ignition engines. Energies, 14(23), p.7865. DOI: https://doi.org/10.3390/en14237865

2. **Shahpouri, S.**, Norouzi, A., Hayduk, C., Fandakov, A., Rezaei, R., Koch, C.R. and Shahbakhti, M., 2023. Laminar Flame Speed modeling for Low Carbon Fuels using methods of Machine Learning. Fuel, 333, p.126187. DOI: https://doi.org/10.1016/j.fuel.2022.126187

3. **Shahpouri, S.**, Gordon, D., Hayduk, C., Rezaei, R., Koch, C.R. and Shahbakhti, M., 2023. Hybrid emission and combustion modeling of hydrogen fueled engines. International Journal of Hydrogen Energy, 0360-3199, DOI: https://doi.org/10.1016/j.ijhydene.2023.03.153

4. Norouzi, A., **Shahpouri, S.**, Gordon, D., Winkler, A., Nuss, E., Abel, D., Andert, J., Shahbakhti, M. and Koch, C.R., 2022. Deep learning based model predictive control for compression ignition engines. Control Engineering Practice, 127, p.105299. DOI: https://doi.org/10.1016/j.conengprac.2022.105299

5. Norouzi, A., **Shahpouri, S.**, Gordon, D., Shahbakhti, M. and Koch, C.R., 2023.

194

Safe deep reinforcement learning in diesel engine emission control. Proceedings of the Institution of Mechanical Engineers, Part I: Journal of Systems and Control Engineering, p.09596518231153445. DOI: https://doi.org/10.1177/09596518231153445

6. Mohammad, A., Rezaei, R., Hayduk, C., Delebinski, T., **Shahpouri, S.** and Shahbakhti, M., 2023. Physical-oriented and machine learning-based emission modeling in a diesel compression ignition engine: Dimensionality reduction and regression. International Journal of Engine Research, 24(3), pp.904-918. DOI: https://doi.org/10.1177/14680874211070736

A.1.2 Submitted Papers

1. **Shahpouri, S.**, Koch, C.R. and Shahbakhti, M., Tailpipe NO_x emissions modeling of a heavy duty diesel truck using deep learning models, Applied Energy, Submitted to Applied Energy on 2 June, 2023.

2. **Shahpouri, S.**, Gordon, R., Koch, C.R. and Shahbakhti, M., Transient Emission Modeling of a Hydrogen-Diesel Engine Using Hybrid and Machine Learning Methods, International Journal of Engine Research, Submitted to International Journal of Engine Research on 7 June, 2023.

A.2 Refereed Conference Papers in Proceedings [2, 68, 214, 215]

1. **Shahpouri, S.**, Norouzi, A., Hayduk, C., Rezaei, R., Shahbakhti, M. and Koch, C.R., 2021. Soot emission modeling of a compression ignition engine using machine learning. IFAC-PapersOnLine, 54(20), pp.826-833, DOI: https://doi.org/10.1016/j.ifacol.2021.11.274

2. Norouzi, A., **Shahpouri, S.**, Gordon, D., Winkler, A., Nuss, E., Abel, D., Andert, J., Shahbakhti, M. and Koch, C.R., 2022. Machine Learning Integrated with Model Predictive Control for Imitative Optimal Control of Compression Ignition Engines. IFAC-PapersOnLine, 55(24), pp.19-26. DOI: https://doi.org/10.1016/j.ifacol.2022.10.256

3. Mohammad, A., Rezaei, R., Hayduk, C., Delebinski, T.O., **Shahpouri, S.** and Shahbakhti, M., 2021. Hybrid physical and machine learning-oriented modeling approach to predict emissions in a diesel compression ignition engine (No. 2021-01-0496). SAE Technical Paper. DOI: https://doi.org/10.4271/2021-01-0496

A.3 Technical Presentations & workshops (refereed abstract)

1. **Shahpouri, S.**, Norouzi, A., Hayduk, C., Fandakov, A., Rezaei, R., Koch, C.R. and Shahbakhti, M., Modeling of a single fuel hydrogen spark ignition and a dual-fuel diesel-hydrogen engines. Combustion Institute – Canadian Section (CICS). 6 pages. (2022). Ottawa.

2. **Shahpouri, S.**, Norouzi, A., Hayduk, C., Fandakov, A., Rezaei, R., Koch, C.R. and Shahbakhti, M., Laminar Flame Speed Modeling of Hydrogen, Methanol and Ammonia Using Machine Learning of Machine Learning, *Canadian Society for Mechanical Engineering International Congress (CSME)*, June 5-8, 2022, Edmonton, Canada.

3. **Shahpouri, S.**, Norouzi, A., Hayduk, C., Fandakov, A., Rezaei, R., Koch, C.R. and Shahbakhti, M., Machine Learning Modeling of Soot Emissions in a Medium Duty Diesel Engine, *Canadian Society for Mechanical Engineering International Congress (CSME)*, June 5-8, 2022, Edmonton, Canada.

4. Norouzi, A., **Shahpouri, S.**, Gordon, D., Winkler, A., Nuss, E., Abel, D., Koch, C.R. and Shahbakhti, M., Deep Learning and Nonlinear Model Predictive Control Integration for Compression Ignition Engine Emission Reduction, *Canadian Society for Mechanical Engineering International Congress (CSME)*, June 5-8, 2022, Edmonton, Canada.

5. Norouzi, A., **Shahpouri, S.**, Gordon, D., Winkler, A., Nuss, E., Abel, D., Koch, C.R. and Shahbakhti, M., Deep Reinforcement Learning for Emission Control in Diesel Engines, *Canadian Society for Mechanical Engineering International Congress (CSME)*, June 5-8, 2022, Edmonton, Canada.

Appendix B: Thesis Files

Following files were used for this dissertation arranged in the tables.

B.1 Chapter 2 source files

:

Table B.1: Chapter 2 source files

File Type	File Name	Description
Experimental datasets	SS_Diesel_Edata.csv	Engine-out steady-state soot emission dataset for the compression ignition diesel engine
	SS_H2Diesel_Edata.csv	Engine-out steady-state NOx and soot emission dataset for compression ignition hydrogen-diesel engine.
	T_H2Diesel_Edata.csv	Engine-out transient NOx emission dataset for compression ignition hydrogen-diesel engine.
	Tailpipe_Edata.rar	Tailpipe transient NOx emission dataset for heavy-duty truck on-road emissions.
Figure Files	SH2engine.drawio	Figure 2.2 source file
	H2DieselExpSetupt.drawio	Figure 2.3 source file
	Inj_timing.drawio	Figure 2.4 source file
	Aftertreatment_Sch.drawio	Figure 2.6 source file

B.2   Chapter 3 source files

:

Table B.2: Chapter 3 source files

File Type	File Name	Description
LFS datasets	`LFS_H2.csv`	Hydrogen LFS dataset
	`LFS_CH3OH.csv`	Methanol LFS dataset
	`LFS_NH3.csv`	Ammonia LFS dataset
	`LFS_FuelCombination.csv`	Fuel combination LFS dataset
LFS ML Models	`H2_ANN.mat`	Hydrogen ANN LFS model
	`H2_SVM.mat`	Hydrogen SVM LFS model
	`CH3OH_ANN.mat`	Methanol ANN LFS model
	`CH3OH_SVM.mat`	Methanol SVM LFS model
	`NH3_ANN.mat`	Ammonia ANN LFS model
	`NH3_SVM.mat`	Ammonia SVM LFS model
	`FuelCombination_ANN.mat`	Fuel combination ANN LFS model
	`FuelCombination_SVM.mat`	Fuel combination SVM LFS model
LFS MATLAB scripts	`LFS_H2.m`	MATLAB script for hydrogen LFS calculation
	`LFS_CH3OH.m`	MATLAB script for methanol LFS calculation
	`LFS_NH3.m`	MATLAB script for ammonia LFS calculation
	`LFS_FuelCombination.mat`	MATLAB script for fuel combination LFS calculation

B.3   Chapter 4 source files

:

Table B.3: Chapter 4 source files

File Type	File Name	Description
Diesel Engine Physical model	`Diesel_Soot.gtm`	GT Power physical model for diesel engine
	`GTmodel_outputs_Diesel.csv`	GT Power physical model steady-state outputs
Feature Selection Files	`FeatureSelection_ExpertKnowledge.csv`	Feature selection with expert knowledge
	`FeatureSelection_LASSO.r`	R code for LASSO feature selection algorithm
ML models scripts	`BlackBox_Soot_Diesel.r`	Black-box soot emissions ML models scripts for diesel engine
	`GrayBox_Soot_Diesel.r`	Gray-box soot emissions ML models scripts for diesel engine

B.4   Chapter 5 source files

:

Table B.4: Chapter 5 source files

File Type	File Name	Description
Engine Physical models	`Diesel_H2_Engine.gtm`	GT Power physical model for hydrogen-diesel engine
	`H2_Engine.gtm`	GT Power physical model for hydrogen engine
	`LFS.dll`	ML LFS model embedded in GT power model
Feature Selection Files	`FS_ExpertKnowledge.csv`	Feature selection with expert knowledge
	`FS_LASSO.r`	R script for LASSO feature selection algorithm
ML models codes	`Soot_Blackbox_ANN.mat`	Black-box soot emissions ANN model MATLAB code for hydrogen-diesel engine
	`Soot_Graybox_ANN.mat`	Gray-box soot emissions ANN model MATLAB code for hydrogen-diesel engine
	`Soot_Graybox_GPR.mat`	Gray-box soot emissions GPR model MATLAB code for hydrogen-diesel engine
	`Soot_Graybox_SVM.mat`	Gray-box soot emissions SVM model MATLAB code for hydrogen-diesel engine
	`NOx_Blackbox_ANN.mat`	Black-box NOx emissions ANN model MATLAB code for hydrogen-diesel engine
	`NOx_Graybox_ANN.mat`	Gray-box NOx emissions ANN model MATLAB code for hydrogen-diesel engine
	`NOx_Graybox_GPR.mat`	Gray-box NOx emissions GPR model MATLAB code for hydrogen-diesel engine
	`NOx_Graybox_SVM.mat`	Gray-box NOx emissions SVM model MATLAB code for hydrogen-diesel engine

B.5   Chapter 6 source files

:

Table B.5: Chapter 6 source files

File Type	File Name	Description
Engine Physical model	`H2Diesel_T.gtm`	GT Power physical model for hydrogen-diesel engine
	`H2Diesel_Outputs.csv`	GT Power physical model outputs for hydrogen-diesel engine
	`LFS.dll`	ML LFS model embedded in GT power model
Feature Selection Files	`FS_ExpertKnowledge.csv`	Feature selection with expert knowledge
	`FS_LASSO.r`	R script for LASSO feature selection algorithm
	`FS_algorithms.mat`	MATLAB file for feature selection algorithms
Pre-Processing Files	`DataPlotting.m`	MATLAB code for processing and plotting experimental data
	`Diesel_inj_fit.mat`	MATLAB function for injection mass calculation from diesel DOI
	`H2_inj_fit.mat`	MATLAB function for calculating injection mass from from hydrogen DOI
ML models codes	`SS_BB.mat`	Black-box SSM NOx emissions model MATLAB code for hydrogen-diesel engine
	`SS_GB.mat`	Gray-box SSM NOx emissions model MATLAB code for hydrogen-diesel engine
	`QSS_BB.mat`	Black-box QSSM NOx emissions model MATLAB code for hydrogen-diesel engine
	`QSS_GB.mat`	Gray-box QSSM NOx emissions model MATLAB code for hydrogen-diesel engine
	`BB_GRU.mat`	Black-box TSM GRU NOx emissions model MATLAB code for hydrogen-diesel engine
	`GB_GRU.mat`	Gray-box TSM GRU NOx emissions model MATLAB code for hydrogen-diesel engine
	`BB_LSTM.mat`	Black-box TSM LSTM NOx emissions model MATLAB code for hydrogen-diesel engine
	`GB_LSTM.mat`	Gray-box TSM LSTM NOx emissions model MATLAB code for hydrogen-diesel engine

B.6   Chapter 7 source files

:

Table B.6: Chapter 7 source files

File Type	File Name	Description
Pre-Processing Files	`Pre-Processing1.m`	MATLAB script for processing of the experimental data
	`Pre-Processing2.m`	MATLAB script for processing and normalizing of the experimental data
	`Pre-Processing1.py`	Phyton script for processing of the experimental data
	`Pre-Processing2.py`	Phyton script for processing and normalizing of the experimental data
DL models codes	`LSTM_5par.mat`	MATLAB code for Tailpipe NOx emissions LSTM model with 5 input features
	`LSTM_7par.mat`	MATLAB code for Tailpipe NOx emissions LSTM model with 7 input features
	`LSTM_9par.mat`	MATLAB code for Tailpipe NOx emissions LSTM model with 9 input features
MATLAB scripts	`Run_tailpipeNox.m`	MATLAB script for running Tailpipe NOx emissions models
	`Cumulative.m`	MATLAB script for calculating cumulative performance metrics

Appendix C: Publicly shared files

The LFS ML-based models and datasets from Chapter 3 and the tailpipe NOx emission dataset from Chapter 7 are shared online for the use of other reasearchers:

- https://github.com/saeidshahpouri/LFS

    - **Descriptions:** LFS datasets and ML models developed in Chapter 3 are found online. These include the LFS datasets as well as ML codes for H_2, CH_3OH, NH_3 and $H_2+CH_3OH+NH_3$ fuels. Table C.1 shows the examples of the LFS datasets for different fuels.

    - **Related Papers:** [1, 4, 5]

- https://github.com/saeidshahpouri/LFS.

    - **Descriptions:** The temporary password for the dataset file is `Tailpipe_NOx_UofA`. This dataset includes ambient temperature (degree Celsius), vehicle speed (km/h), engine speed (rpm), engine torque (N.m), fuel consumption (L/h) and tailpipe NOx emissions (ppm). Table C.2 shows sample data from the first five rows of this dataset.

    - **Related Papers:** [6]

Table C.1: Examples of the laminar flame speed datasets for H_2, CH_3OH, and NH_3 fuels available at https://github.com/saeidshahpouri/LFS

Fuel	Temperature (K)	Pressure (bar)	Residual Gas Fraction	Lambda (-)	Laminar Flame Speed (m/s)
H_2	600	30	0	1	3.613
	600	30	0	1.1	2.911
	600	30	0	1.2	2.330
	600	30	0	1.3	1.858
	600	30	0	1.4	1.469
CH_3OH	600	30	0	1	0.612
	600	30	0	1.1	0.524
	600	30	0	1.2	0.441
	600	30	0	1.3	0.368
	600	30	0	1.4	0.305
NH_3	600	30	0	1	0.117
	600	30	0	1.1	0.0930
	600	30	0	1.2	0.0652
	600	30	0	1.3	0.0421
	600	30	0	1.4	0.027

Table C.2: Examples of tailpipe NOx emissions dataset available at https://era.library.ualberta.ca/items/3a48b032-ec7e-41d9-b562-7985c504345c

Ambient air temperature (°C)	Vehicle speed (km/h)	Engine speed (rpm)	Engine torque (N.m)	Fuel consumption (L/h)	Tailpipe NOx emissions (ppm)
0.6	100.3	1162.9	2373.2	41.9	211.8
0.6	101.1	1162	2374.9	41.9	234.5
0.59	101	1165.2	2368.47	41.93	237.9
0.59	101.23	1165.35	2368.17	41.93	236.1
0.59	101.05	1166.5	2374.02	42.89	227.75